

COMPREHENSIVE INVESTIGATION OF SELECTED URANIUM COMPOUNDS WITH  
APPLICATION FOR CLEAN ENERGY

A Thesis Submitted to the College of  
Graduate and Postdoctoral Studies  
In Partial Fulfillment of the Requirements  
For the Degree of Doctor of Philosophy  
In the Department of Physics and Engineering Physics  
University of Saskatchewan  
Saskatoon

By  
Jayangani Inoka Ranasinghe

© Copyright Jayangani Inoka Ranasinghe, July 2022. All rights reserved.

"Unless otherwise noted, copyright of the material in this thesis belongs to the author"

## Permission to use

In presenting this thesis in partial fulfillment of the requirements for a postgraduate degree from the University of Saskatchewan, I agree that the Libraries of this University may make it freely available for inspection. I further agree that permission for copying of this thesis in any manner, in whole or in part, for scholarly purpose may be granted by the professors who supervised my thesis work or, in their absence, by the Head of the Department or the Dean of the College in which my thesis work was done. It is understood that any copying or publication or use of this thesis or part thereof for financial gain shall not be allowed without my written permission. It is also understood that due recognition shall be given to me and to the University of Saskatchewan in any scholarly use which may be made of any material in my thesis.

Requests for permission to copy or to make other use of material in this thesis in whole or part should be addressed to:

Department of Physics and Engineering Physics  
University of Saskatchewan  
116 Science Place, Rm 163  
Saskatoon, SK, S7N 5E2  
Canada

And

College of Graduate and Postdoctoral Studies  
University of Saskatchewan  
116 Thorvaldson Building  
110 Science Place  
Saskatoon, SK S7N 5C9  
Canada

## Abstract

The focus of this thesis mainly revolves investigation of the thermal properties of triuranium octoxide ( $U_3O_8$ ), uranium di-aluminide ( $UAl_2$ ),  $U_3O_8$ -Mo, and  $U_3O_8$ -Al nuclear fuels. They have significant importance in the nuclear industry related to their fuel applications for research and test reactors. This study is carried out mainly using density functional theory (DFT) based calculations within the first principles framework to bring an insight into the molecular level contribution to their heat transport. Furthermore, an experimental evaluation is performed with  $U_3O_8$ ,  $U_3O_8$ -Mo, and  $U_3O_8$ -Al, and these results are compared with the theoretical predictions.

The theoretical calculations on  $U_3O_8$  reveal that the strong anharmonicity in the Grüneisen parameter is the origin of its low thermal conductivity. Furthermore, the directional dependence of the group velocity triggers the anisotropic nature of its thermal conductivity. This work experimentally demonstrated a significant thermal conductivity enhancement in  $U_3O_8$  with added Al or Mo. The experimental band gap measurements and the DFT-based computational predictions on the electronic and optical properties proved  $U_3O_8$  to be a semiconductor with an indirect bandgap.

The structural and mechanical properties and the time-dependent thermal conductivities of  $UAl_2$  are assessed computationally. The research findings reveal that both the acoustic and optical modes of the phonon vibrations give a considerable impact on total thermal conductivity. Furthermore, the electronic contribution to the total thermal conductivity in  $UAl_2$  is shown to be getting more robust with increasing temperature.

## Acknowledgement

I would like to thank my supervisors, Dr. Barbara Szpunar and Prof. Jerzy Szpunar, for this opportunity, guidance, and continuous support throughout this journey. In addition, this would not be successful without your understanding and patience with me. Special thanks to my advisory committee, Professors Andrei Smolyakov (Committee chair), Alexandre Koustov, Masoud Ghezelbash, and Kelly Timothy (Cognate member) for their encouragement, constructive comments, and discussions.

My sincere thanks to all the present and past colleagues in the Advanced Materials and Renewable Energy (AMRE) research group, especially Dr. Linu Malakkal, Dr. Ericmoore Jossou, Dotun Oladimeji, and Murali Krishnakumar, for their unconditional support whenever I needed. I would also like to thank all the faculty and staff members in the Department of Physics and Engineering Physics, and the Department of Mechanical Engineering, University of Saskatchewan.

I am grateful for the assistance and guidance received from Prof. Lukas Bichler and Dr. Anil Prasad at the University of British Columbia for the support in fabricating the fuel samples, and Dr. Ramaswami Sammynaiken at Saskatchewan Structural Sciences Centre (SSSC) and Prof. Noble Scott at Department of Mechanical Engineering, University of Saskatchewan for the assistance in powder sample characterization and measurements. In addition, the funding supports received from NSERC and the University of Saskatchewan is greatly appreciated. I would like to thank Westgrid, Compute Canada, and the University of Saskatchewan (Plato) for their high-performance computing facilities. Further, Cameco Inc. Ltd. is highly appreciated for providing me required  $U_3O_8$  powders.



*In memory of my loving husband.....*

## LIST OF TABLES

1.1	Theoretical densities of several selected uranium compounds used in dispersion type fuel applications.....	10
2.1	The weights of the starting powder materials used to prepare the specimens of pure $U_3O_8$ , $U_3O_8$ -Al (with 10, 15 and 20 vol% of $U_3O_8$ in Al) and $U_3O_8$ -Mo (with 7.5 and 12.5 vol% of Mo in $U_3O_8$ ). The weights are given in grams and total of 25 grams in each composition is prepared for ball milling.....	31
3.1	Sintering conditions and the final densities, and the density as a percentage of the theoretical density (TD%) for the sintered samples with different $U_3O_8$ concentrations.....	50
3.2	Optimized lattice parameters (in Å) of the orthorhombic phase of $U_3O_8$ with nonmagnetic (NM) and spin-polarized (SP) conditions. The literature works of Yun <i>et al.</i> <sup>119</sup> and Brincat <i>et al.</i> <sup>144</sup> , have conducted with Ferromagnetic (FM) conditions while Wen <i>et al.</i> <sup>120</sup> used an antiferromagnetic (AFM) structure.....	59
3.3	Elastic constants ( $C_{ij}$ ) of $\alpha$ - $U_3O_8$ (in GPa) .....	60
3.4	Calculated bulk modulus ( $B_X$ ), shear modulus ( $S_X$ ), Young's modulus ( $Y_X$ ) (in GPa), Poisson ratio ( $\nu_X$ ), and the Debye temperature ( $\theta$ ) (in K) of $\alpha$ - $U_3O_8$ . The subscript $X$ denotes the Voigt ( $V$ ) <sup>151</sup> , Reuss <sup>152</sup> ( $R$ ) and Hill <sup>153</sup> ( $H$ ) approximations.....	62
3.5	The diffusivities ( $\alpha$ ) and the specific heat capacities ( $C_P _{LF}$ ) of $U_3O_8$ -Al and $U_3O_8$ -Mo samples measured using laser flash technique. The calculated specific heat capacities according to the Neumann-Kopp rule ( $C_P _{NK}$ ) also given for	73

comparison. Konings *et al.*<sup>156</sup>, Brooks *et al.*<sup>161</sup>, and Rasor *et al.*<sup>160</sup> were referred for the literature specific heat data on U<sub>3</sub>O<sub>8</sub>, Al and Mo, respectively.....

4.1	Predictions for lattice parameter $a$ (Å), relative energy $\Delta E$ (per UAl <sub>2</sub> in eV), magnetic moment $\mu_B$ of U atom (per UAl <sub>2</sub> in $\mu_B$ ) for ferromagnetic (FM), spin-polarized non-magnetic (SP), antiferromagnetic (AFM) and non-magnetic (NM) configurations using GGA method.....	89
4.2	The recommendations for the temperature dependences of the volume change ( $\Delta V\%$ ), linear thermal expansion coefficient ( $\alpha_L(T)$ in $10^{-6} \text{ K}^{-1}$ ), density ( $\rho(T)$ in $\text{g cm}^{-3}$ ), and the bulk modulus ( $B(T)$ in GPa) for the temperature range 0 to 1500 K.....	95
5.1	Predicted structural parameters ( $a, b$ and $c$ ), magnetic moments ( $\mu_B$ ), band gap ( $E_g$ ) and bulk modulus (B) of $\alpha$ -U <sub>3</sub> O <sub>8</sub> .....	119

## LIST OF FIGURES

1.1	An example for an induced fission reaction in $^{235}\text{U}$ sparked by a thermal neutron. In this case, the excited $^{236}\text{U}$ due to the absorption of the neutron ( $\frac{1}{0}n$ ) splits into two smaller nuclei ( $^{141}\text{B}$ and $^{92}\text{K}$ ) along with three neutrons releasing a very large amount of energy.....	2
2.1	Positions of electrons (Blue dots) and nuclei (Red circles) in a many-body system.....	15
2.2	Flowchart of the self-consistent functional for ground state Schrödinger equation when the atomic positions of the system are known .....	21
2.3	The planetary ball mill apparatus (Torrey Hills Technologies, USA) located at Department of Mechanical Engineering, University of Saskatchewan.....	32
2.4	(a) Thermal Technology spark plasma sintering system located at university of British Columbia, Canada, and (b) Schematic diagram of Spark Plasma Sintering (SPS).....	33
2.5	Torbal density measurement kit and the electronic scale used in the density measurements of the solid specimens .....	34
2.6	Schematic illustration of Bragg's law.....	36
2.7	Bruker D8 Discover X-Ray diffractometer at Department of Mechanical Engineering, University of Saskatchewan.....	36
2.8	Different types of signals generated by electron irradiation in a Scanning Electron Microscope (SEM).....	38
2.9	The SU-6600, Hitachi field emission SEM equipped with the oxford Instruments Nordlys EDX detector located at Department of Mechanical Engineering, University of Saskatchewan.....	38

2.10	(a) The discovery laser flash apparatus (DLF-1/EM-1300) used in the thermal conductivity measurements, (b) Schematic diagram of the laser flash apparatus.	40
3.1	Powder XRD diffraction patterns of (a) pure $U_3O_8$ (b) $U_3O_8$ -Al and (c) $U_3O_8$ -Mo samples prepared by SPS technique .....	51
3.2	The SEM micrographs of pure $U_3O_8$ samples fabricated by SPS technique (a) at 900 K with 94.1TD% and (b) at 1000 K with 97.8TD%. .....	52
3.3	The SEM images of the pellets having (a) 15vol% $U_3O_8$ -Al with 91.7TD% (b) 15vol% $U_3O_8$ -Al with 96.6TD%, (c) 20vol% $U_3O_8$ -Al with 93.5TD%, and (d) 30vol% $U_3O_8$ -Al with 90.1TD%. The light grey areas correspond to the $U_3O_8$ phase and dark regions are the aluminum.....	53
3.4	The SEM images of $U_3O_8$ -Mo pellets of (a) 8.2vol% with 97.5TD% (b) 12.5vol% with 97.8TD%. The light grey areas are the $U_3O_8$ phase, and the dark black are the Mo phase.....	54
3.5	The EDX (a) micrograph, (b) spectrum showing the quantitative composition, and distribution maps of elements (c) uranium and (d) oxygen within the pure $U_3O_8$ sample with 97.8TD%.....	55
3.6	(a) EDX micrograph of 15vol% $U_3O_8$ -Al pellet (96.6TD%), (b) EDX spectrum with the quantitative composition, and the distribution maps of the elemental composition (c) uranium, (d) oxygen and (e) aluminum. ....	56
3.7	The EDX (a) micrograph, (b) spectrum showing the quantitative composition, and distribution maps of elements (c) uranium, (d) oxygen and (c) molybdenum within the $U_3O_8$ -Mo sample with 12.5vol% Mo with 97.8TD%.....	57
3.8	(a) Phonon bandstructure along the first Brillouin zone, and (b) the phonon density of states, of $\alpha$ - $U_3O_8$ .....	63

3.9	Temperature dependent thermal conductivity of pure $U_3O_8$ . The yellow, green, and purple dashed lines show the DFT predictions on [100], [010], and [001] directions, and they are labeled as $\kappa_{ph}^x$ , $\kappa_{ph}^y$ and $\kappa_{ph}^z$ . Black solid line with solid triangles represents the average of them. The red solid triangles and black solid diamonds are the measured thermal conductivities of the respective 97.8TD% and 94.1TD% samples after the porosity correction. The corresponding open markers shows the respective thermal conductivities when the specific heat is taken from Ref. 156 .....	64
3.10	Specific heat capacity of $U_3O_8$ samples with 97.8TD% (red solid triangles) and 94.1TD% (black solid diamonds) measured using laser flash technique and according to Ref. 162 (open black circles) .....	66
3.11	Mean free paths of $U_3O_8$ as a function of vibrational frequency at 300 K.....	68
3.12	(a) The directional dependence of optical and acoustic mode contributions to the lattice thermal conductivity of $U_3O_8$ at 300 K, and (b) the behaviour of the temperature dependence of the total acoustic and optical mode contributions from 300 to 1000 K.....	69
3.13	Group velocities ( $v_g$ ) of lattice vibrations in $U_3O_8$ along [100], [010] and [001] direction as a function of vibrational frequency.....	70
3.14	Frequency dependent (a) phonon scattering rates and the (b) Grüneisen Parameter ( $\gamma$ ) of $U_3O_8$ .....	72
3.15	Thermal conductivities of $U_3O_8$ -Al pellets with 30vol% (yellow), 20vol% (purple) and 15vol% (blue) of $U_3O_8$ . The corresponding solid lines go through the data when $C_p$ is measured using the laser flash technique (LF) while the dashed lines connect the evaluated thermal conductivities using calculated $C_p$ according to the Numann-Kopp (NK) rule. (b) $U_3O_8$ -Mo pellets with 8.2vol% (green) and 12.5vol% (red) of Mo. Experimental thermal conductivity of pure	75

	U <sub>3</sub> O <sub>8</sub> is also given (in black) for the clarity of the enhancement achieved in U <sub>3</sub> O <sub>8</sub> -Al and U <sub>3</sub> O <sub>8</sub> -Mo pellets. All the given values are corrected to 100TD% using Eq. (3.25).....	
3.16	Thermal conductivities of U <sub>3</sub> O <sub>8</sub> -Mo pellets with 8.2vol% (green) and 12.5vol% (red) of Mo. Experimental thermal conductivity of pure U <sub>3</sub> O <sub>8</sub> is also given (in black) for the clarity of the enhancement achieved in U <sub>3</sub> O <sub>8</sub> -Al and U <sub>3</sub> O <sub>8</sub> -Mo pellets. All the given values are corrected to 100TD% using Eq. (3.25).....	76
3.17	Thermal diffusivity of (a) pure U <sub>3</sub> O <sub>8</sub> with 97.8TD% (blue triangle) and 94.1TD% (green diamond) and (b) 15vol% U <sub>3</sub> O <sub>8</sub> -Al with 96.6TD% (black triangle) and 91.7TD% (red diamond), measured using laser flash technique.....	77
3.18	Thermal conductivity of pure U <sub>3</sub> O <sub>8</sub> with 97.8TD% (blue triangles) and 94.1TD% (green squares) and (b) 15vol% U <sub>3</sub> O <sub>8</sub> -Al with 96.6TD% (black triangles) and 91.7TD% (red diamonds). The solid marks in both figures represent the thermal conductivities evaluated with diffusivity and specific heat data measured by laser flash (LF) technique, while the corresponding open marks show those when evaluated with the specific heat data taken from Konings <i>et al.</i> <sup>156</sup> (for pure U <sub>3</sub> O <sub>8</sub> ) or calculated according to the NK rule (for 15 vol%U <sub>3</sub> O <sub>8</sub> -Al).....	79
3.19	Thermal conductivity of 15vol% U <sub>3</sub> O <sub>8</sub> -Al with 96.6TD% (black triangles) and 91.7TD% (red diamonds). The solid marks represent the thermal conductivities evaluated with diffusivity and specific heat data measured by laser flash (LF) technique, while the corresponding open marks show those when evaluated with the specific heat data taken from Konings <i>et al.</i> <sup>156</sup> (for pure U <sub>3</sub> O <sub>8</sub> ) or calculated according to the NK rule (for 15vol%U <sub>3</sub> O <sub>8</sub> -Al).....	80
4.1	Conventional unit cell of UAl <sub>2</sub> structure at ground state. Solid green spheres represent the Uranium atoms, and the yellow solid spheres represent the Al atoms.....	88

4.2	Calculated Phonon spectra for FM phase of $\text{UAl}_2$ along the high symmetry directions. The right-hand side panel gives the partial density of states of phonons originated from U and O atoms .....	90
4.3	Calculated Helmholtz free energy (in eV) as a function of unit cell volume (in $\text{\AA}^3$ ) between the temperatures 0 and 1500 K in 100 K steps. Each solid line represents the fit to the Birch-Murnaghan equation of states. The minimum point on each fit is shown by the (black) cross mark. The dashed (black) line is only a guideline to the eye.....	85
4.4	The temperature dependence of the (a) volume expansion relative to optimized volume at 0 K, (b) Linear thermal expansion coefficient (c) Density, and (d) isothermal bulk modulus. The smooth curves are guidelines to the eye.....	94
4.5	Specific heat $C_p$ and $C_v$ of $\text{UAl}_2$ as a function of temperature. The green and blue lines represent the respective electronic ( $C_p^{el}$ ) and lattice/harmonic ( $C_v^{ph}$ ) contributions to $C_v$ . Black cross marks show the sum of the harmonic and anharmonic contributions to the lattice heat capacity. The black solid line gives the $C_p^{ph}$ calculated by QHA. Red line is the total heat capacity ( $C_p^{ph} + C_p^{el}$ ).....	97
4.6	The phonon contribution $\kappa_{ph}$ to the total thermal conductivity evaluated using the iterative solution (black solid line) and the relaxation time approximation $\kappa_{ph}$ -CRTA (black dashed line). The acoustic ( $\kappa_{ph}$ -Acoustic) and optical ( $\kappa_{ph}$ -Optical) contributions are given by black solid lines with solid triangles and diagonals respectively. Mei <i>et al.</i> <sup>52</sup> results are shown by red crosses.....	99
4.7	Mode contributions of the (a) group velocities ( $v_g$ ) and (b) lifetimes of phonon-phonon scatterings at 300 K. The transverse (TA1 and TA2) and longitudinal acoustic modes are represented by black, red, and yellow plus marks while all the optical modes are shown by blue circles.....	100



4.8	(a) the averaged Grüneisen parameter (b) the mode contributions of the Grüneisen parameter at 300 K. The TA1, TA2 and LA modes are shown by black, red and yellow cross marks. All optical modes are represented by blue circles.....	102
4.9	Lattice thermal conductivity cumulation ( $\kappa_{L,cumulation}$ ) as a function of mean free path (MFP). Red, green, yellow, and purple lines show the cumulation at 300, 500, 1000 and 1500 K respectively.....	103
4.10	Temperature dependence of relative electrical conductivity ( $\sigma/\tau_e$ ),.....	104
4.11	Temperature dependence of scattering time ( $1/\tau_e$ ).....	106
4.12	Temperature dependence of absolute resistivity ( $\rho$ ) of $UAl_2$ .....	106
4.13	Total thermal conductivity of $UAl_2$ . The red dashed lines with circles and diagonals show the respective lattice ( $\kappa_{ph}$ ) and electronic ( $\kappa_e$ ) contributions to the total thermal conductivity predicted in this work. Red solid line gives the total thermal conductivity ( $\kappa_{Tot} = \kappa_{ph} + \kappa_e$ ). The same interpretation is valid for the green color which shows the predictions by Mei <i>et al.</i> <sup>52</sup> . The black solid triangle represents the experimental prediction at 300 K by Armbruster <i>et al.</i> <sup>199</sup> . The black solid squares show the experimental work by Park <i>et al.</i> <sup>201</sup> .....	107
5.1	(a) XRD diffraction pattern of as received $U_3O_8$ powder measured by Chromium $K\alpha$ radiation. By comparing the JCPDS database, corresponding planes of $U_3O_8$ for the observed peaks are shown in the figure. (b) SEM image of mixed (4wt%) $U_3O_8$ -KCl powder sample. ....	116
5.2	(a) Ground state energies of $\alpha$ - $U_3O_8$ relative to the FM-GGA scheme. (Energy of the AFM-GGA structure with respect to the FM-GGA state is 0.06 eV. Hence it is not visible) (b) Crystal structure of $\alpha$ - $U_3O_8$ (Amm2) (c) Atoms on the $z = 0$ plane. Green color U1 and U2 atoms are the inequivalent uranium atoms. Oxygens are given in red circles.....	118

5.3	The pDOS (left) and the band structure (right) of $U_3O_8$ with (a) GGA, (b) GGA+U, and (c) GGA+U+SOC conditions.....	120
5.4	Charge density plot on (001) plane. X and Y shows relatively low electron densities between U-O bonds.....	122
5.5	Components of (a) Real ( $\epsilon_1$ ) and (b) imaginary ( $\epsilon_2$ ) parts of dielectric function. The insets of both (a) and (b) are a comparison of respective average values of this study with the results from a system with AFM state by Wen <i>et al.</i> <sup>120</sup> .....	124
5.6	Comparison of (a) real ( $\epsilon_1$ ) and (b) imaginary ( $\epsilon_2$ ) parts of dielectric function of $U_3O_8$ with our previous calculation on $UO_2$ <sup>214</sup> . Experimental data are taken from ref. <sup>251</sup> .....	125
5.7	(a) absorption coefficient- $\alpha(\omega)$ (b) optical conductivity- $\sigma(\omega)$ , (c) refractive index- $n(\omega)$ , and (d) loss-function- $L(\omega)$ of $\alpha-U_3O_8$ . The average of $\alpha(\omega)$ and $\sigma(\omega)$ are shown in black dashed line and the $xx$ , $yy$ and $zz$ components are given by red, yellow, and green solid lines respectively.....	128
5.8	Measured reflectance spectra for $U_3O_8$ -KCl mixture samples (a) 1wt% of $U_3O_8$ (red), (b) 2wt% of $U_3O_8$ (green), and (c) 4wt% of $U_3O_8$ (blue).....	129
5.9	Tauc's plots for the observed reflection data with $n = 2$ for (a) 1wt%, (b) 2wt% and (c) 4wt% samples.....	131
6.1	Dispersion relations of phonon vibrations in molybdenum. Solid line in the figure represents the results of the current work and empty circles are from literature.....	138
6.2	The predicted total (black solid line) and the projected partial electron densities of states (DOS) of Mo. The red, green and the blue dashed lines represent the	138

contributions from respective  $4d$ ,  $4p$  and  $5s$  electrons. The purple dotted line is to show the integrated number of electrons.....

6.3 The electron scattering rates of electron-phonon scattering at 300 (blue), 500 (red), and 1500 (black) evaluated using EPW code..... 140

6.4 The electron relaxation time ( $\tau_e$ ) as a function of temperature. Here,  $\tau_e$  at each temperature is taken as an average of those with the electron energies are  $< k_B T$ , where  $k_B$  is the Boltzmann constant..... 140

6.5 (a) The electrical conductivity of Mo with respect to the electron relaxation time ( $\sigma/\tau_e$ ), and (b) The calculated electrical resistivity as a function of temperature. Experimental data from Desai *et al.*<sup>259</sup>, Tye *et al.*<sup>261</sup>, and Taylor *et al.*<sup>262</sup>, and ab-initio predictions from Martin *et al.*<sup>260</sup>, are given for comparison..... 141

6.6 The calculated results for  $\kappa_e$  (red dashed line), and the  $\kappa_{Tot}$  (black solid line), of molybdenum. Here,  $\kappa_{Tot}$  is taken as the algebraic sum of  $\kappa_e$  and  $\kappa_{ph}$ , where phonon contributions are taken from Wen *et al.*<sup>263</sup>..... 142

6.6 The effective thermal conductivity in  $U_3O_8$ -Mo fuels with 8.2vol% and 12.5vol%. The blue square and red diamonds represent our experimental data published in Ranasinghe *et al.*<sup>253</sup> The calculated effective values are taken using the Bruggeman model..... 145

## LIST OF ABBREVIATIONS

AFM	Antiferromagnetic
AGR	Advanced gas-cooled graphite-moderated reactor
ATR	Advanced Test Reactor
CANDU	Canada Deuterium Uranium reactors
B3LYP	Becke, three parameter, Lee-Yang-Parr functional
BMEOS	Birch-Murnaghan equation of state
BTE	Boltzmann transport equation
BSE	Back-scattered electrons
BWR	Boiling water reactors
BoltzTraP	Boltzmann Transport Properties
CRTA	Constant relaxation time approximation
DFT	Density functional theory
DFT+U	Hubbard-U method
DMFT	Dynamical mean-field theory
DOE	Department of energy
DOS	Density of states
EDX	Energy Dispersive X-Ray Analysis
EPW	Electron-Phonon coupling using Wannier functions
FM	Ferromagnetic
FP-LAPW	Full-potential linearized augmented plane-wave method
GFR	Gas-cooled fast reactor
GGA	Generalized gradient approximation
GIF	Generation IV International Forum
HEU	High enriched uranium
HSE	Heyd-Scuseria-Ernzerhof functional
IAEA	International atomic energy agency
IFC	Interatomic force constants

LDA	Local density approximation
LFR	Lead-cooled fast reactor
LEU	Low enriched uranium
LF	Laser Flash
LWR	Light water reactor
NK	Numann-Kopp rule
MFP	Mean free path
MITR	Massachusetts Institute of Technology Research Reactor
Mo	Molybdenum
MOX	Mixed oxides
MSR	Molten salt reactor
MURR	University of Missouri Research Reactor
NIR	Near Infrared
NM	Nonmagnetic
ORNL	Oak Ridge National Laboratory
pDOS	Phonon density of states
PBE	Perdew, Burke and Ernzerhof functional
PBEsol	Perdew-Burke-Ernzerhof for solids functional
PECS	Pulsed electric current sintering
PIP	Polymer Infiltration and Pyrolysis
PW91	Perdew and Wang
PWR	Pressurized water reactors
PZ	Perdew-Zunger functional
SP	Spin-polarized
QE	Quantum ESPRESSO
QHA	Quasiharmonic approximation
RERTR	Reduced Enrichment for Research and Test Reactors
RTA	Relaxation time approximation
SCF	Self-consistent functional
SCWR	Supercritical water-cooled reactor
SE	Secondary electrons

SEM	Scanning electron microscope
SFR	Sodium-cooled fast reactor
SOC	Spin-orbital coupling
SPS	Spark plasma sintering
SRL	Savannah River Laboratory
TD	Theoretical Density
UV	Ultraviolet
VHTR	Very high-temperature reactor
vol%	Volume percentage
VWN	Vosko-Wilk-Nusair
wt%	Weight percentage
XANES	X-ray absorption near-edge spectroscopy
XPS	X-ray photoelectron spectra
XRD	X-ray diffraction

## LIST OF SYMBOLS

$B$	bulk modulus
$C_P$	specific heat
$C_P _{LF}$	measured specific heat capacities from Laser Flash technique
$C_P _{NK}$	specific heat capacities according to the Neumann-Kopp rule
$C_{ij}$	Elastic constants
$C_V$	specific heat at constant volume
$d$	lattice space in a solid
$e$	electron charge
$E_g$	band gap
$E$	energy eigenvalue
$\vec{E}_\beta$	electric field along the direction $\beta$
$E_{HK}[n(\vec{r})]$	total energy function of the system under the Hohenberg-Kohn definition
$E_{KS}[n(\vec{r})]$	total energy function of the system under the Kohn-Sham definition
$E_H[n(\vec{r})]$	interaction energy due to Hartree potential (Hartree term)
$E_{XC}$	exchange correlation energy
$E_{XC}^{LDA}$	exchange correlation energy under local density approximation
$E_{XC}^{B3LYP}$	B3LYP exchange correlation functional
$E_X^{HF}$	exchange energy with the Hartree-Fock approximation
$E_X^{LDA}$	exchange energy under local density approximation
$E_X^{B88}$	Becke 88 exchange functional
$E_C^{PW91}$	correlation energy under PW91 approximation

$f_j(\vec{q}, \omega)$	phonon distribution function of the phonons with mode $j$ , wave vector $\vec{q}$ , and angular frequency $\omega$
$f_j^0(\vec{q}, \omega)$	phonon distribution function according to the Bose-Einstein statistics
$f_{n\vec{k}}$	distribution function of electrons
$F(V, T)$	Helmholtz free energy function of a system with volume $V$ and at temperature $T$
$F_{el}(V, T)$	electronic contribution to the free energy of a system with volume $V$ and at temperature $T$
$F_{ph}(V, T)$	phonon contribution to the free energy of a system with volume $V$ and at temperature $T$
$F_{HK}[n(\vec{r})]$	universal density functional defined by Hohenberg-Kohn theorem
$G(T, p)$	Gibbs free energy of a system at temperature $T$ and pressure $p$
$\vec{H}$	magnetic field
$\hat{H}$	Hamiltonian operator
$\vec{J}_{ph}$	The amount of total heat flow per unit volume due to all the phonon vibrations
$\vec{k}$	electron wave vector
$k_B$	Boltzmann constant
$K_{max}$	magnitude of the largest $K$ vector in the plane-wave expansion
$L$	sample thickness in the thermal conductivity measurements
$L_0$	Lorenz number
$L(\omega)$	energy-loss function
$m_e$	electron mass
$m_{LF}$	mass of the specimen
$M_I$	mass of the $I^{\text{th}}$ nucleus
$n$	diffraction order of XRD
$n(\vec{r})$	electron density at the position $\vec{r}$
$n^0(\vec{r})$	ground-state electron density at $\vec{r}$
$n(\omega)$	refractive index



$P$	porosity volume fraction in a specimen
$Q$	Thermal energy of the pulsed laser beam
$\vec{r}_i$	position vector of the $i^{\text{th}}$ electron
$\vec{R}_I$	position vector of the $I^{\text{th}}$ nucleus
$R_{MT}$	radius of the smallest atomic sphere
$S$	Shear modulus
$S_{\gamma\beta}$	Seebeck coefficient
$t_{1/2}$	time taken to rear surface temperature reaches 50% of its maximum value
$T_0$	kinetic energy of the system under independent particle approximation
$\hat{T}_e$	kinetic energy operator for the electrons
$\hat{T}_n$	kinetic energy operator for the nuclei
$T_n$	kinetic energy of nuclei
$\hat{V}_{ee}$	potential energy operator for the Coulomb repulsion between electron pairs
$V_{ext}$	potential on electrons due to fixed nuclei
$\hat{V}_{ext}$	potential energy operator for the
$V_{en}$	potential energy due to the Coulomb interaction between electrons and nuclei
$\hat{V}_{en}$	potential energy operator for the Coulomb interaction between electrons and nuclei
$V_H(\vec{r})$	Hartree potential at the position $\vec{r}$
$\hat{V}_H(\vec{r})$	Hartree potential operator
$V_{nn}$	potential energy due to the Coulomb repulsion between pairs of nuclei
$\hat{V}_{nn}$	potential energy operator for the Coulomb repulsion between pairs of nuclei
$V_X$	exchange interaction potential energy
$\hat{V}_X(\vec{r})$	operator for the exchange interaction potential energy

$V_{XC}$	exchange correlation potential
$W_{air}$	weight of the specimen when it is placed on the upper pan
$W_{water}$	weight of the specimen when it is immersed in the water
$W^I$	isotropic scattering rates of the three-phonon scattering
$W^+$	three-phonon absorption scattering rates
$W^-$	scattering rates of the three-phonon emission process
$Y$	Young's modulus
$Z_I$	atomic number of the $I^{\text{th}}$ nucleus
$\alpha_L(T)$	linear thermal expansion coefficient
$\alpha(T)$	thermal diffusivity
$\alpha(\omega)$	absorption coefficient
$\gamma$	Grüneisen parameter
$\nabla n(\vec{r})$	gradient of the electron density
$\nabla T$	thermal gradient
$\nabla^2$	Laplace operator
$\nabla^2_{\vec{r}_i}$	Laplace operator acting on electrons
$\nabla^2_{\vec{R}_I}$	Laplace operator acting on nuclei
$\varepsilon(\omega)$	frequency dependent dielectric function of a material
$\varepsilon_i$	energy eigenvalues of the single electron systems
$\varepsilon_1(\omega)$	frequency dependent real part of the dielectric function
$\varepsilon_2(\omega)$	frequency dependent imaginary part of the dielectric function
$\varepsilon_0$	dielectric permittivity of vacuum/free space
$\varepsilon_{XC}^{GGA}$	exchange correlation energy under generalized density approximation
$\theta$	incident angle of the radiation in XRD
$\Theta$	Debye temperature
$\kappa_e$	electronic contribution of thermal conductivity

$\kappa_{eff}$	effective thermal conductivity of a mixture of materials
$\kappa_{exp}$	measured thermal conductivity
$\kappa_{ph}$	thermal conductivity caused by phonon vibrations
$\kappa_{100TD\%}$	corrected thermal conductivity to 100% theoretically dense sample
$\lambda_{XRD}$	wavelength of the radiation used in XRD
$\lambda, \lambda'$ and $\lambda''$	phonons involved in three-phonon scattering
$\mu_B$	magnetic moments
$v_g$	group velocity
$\vec{v}_j(\vec{q})$	group velocity of the phonon in the branch $j$ with the wave vector $\vec{q}$
$v_l$	longitudinal sound velocity
$v^m$	average sound velocity
$\vec{v}_{n\vec{k}}$	group velocity of the electrons
$v_s$	shear sound velocity
$\nu_X$	Poisson's ratio
$\rho_i$	density of the specimen labelled as $i$
$\sigma$	electrical conductivity tensor
$\sigma(\omega)$	optical conductivity
$\Sigma_{nk}''$	electron self-energy
$\tau_j(\vec{q}, \omega)$	relaxation time of the phonon in the $j^{\text{th}}$ branch with frequency $\omega$ , and the wave vector $\vec{q}$
$\tau_j^0$	phonon relaxation time within CRTA
$\phi_i(\vec{r}_i)$	single-particle electron wave function
$\Phi_3$	third-order part of the interatomic potential
$\Psi_{MB}(\vec{r}_1, \vec{r}_2, \dots; \vec{R}_1, \vec{R}_2, \dots)$	Many body wave function for the electrons and nuclei
$\Psi_{MB}(\vec{r}_1, \vec{r}_2, \dots)$	Many body wave function for the electrons
$\omega_j(\vec{q})$	angular frequency of the phonon in the branch $j$ with the wave vector $\vec{q}$

$\Omega$	unit cell volume of the crystal
$\hbar$	reduced Plank constant
$\Delta_j$	a measure of the deviation of the heat current from CRTA

## TABLE OF CONTENTS

Permission to use .....	I
Abstract .....	II
Acknowledgement .....	III
List of tables.....	V
List of figures.....	VII
List of abbreviations .....	XV
List of symbols.....	XVIII
<a href="#">Chapter 1: Introduction</a> .....	1
1.1 Basics of nuclear industry .....	1
1.2 History of nuclear industry .....	3
1.3 History of nuclear fuels.....	3
1.4 Motivation for this work .....	4
1.5 Thesis objectives.....	8
1.6 Thesis outline .....	9
<a href="#">Chapter 2: Methodology</a> .....	11
2.1 Computational Methodology .....	11
2.1.1 Many-body problem.....	12
2.1.1.1 Hartree-like approximation.....	14
2.1.1.2 Hartree-Fock approximation.....	15
2.1.2 Density Functional Theory (DFT).....	15
2.1.2.1 Hohenberg-Kohn theorems.....	15
2.1.2.2 Kohn-Sham equations.....	16
2.1.2.3 The Exchange-correlation energy ( $E_{XC}$ ) .....	19
2.1.2.4 Limitations of DFT and DFT+U method.....	21
2.1.3 Thermal transport in crystalline solids.....	21
2.1.3.1 Lattice thermal conductivity ( $\kappa_{ph}$ ).....	22
2.1.3.2 Electron transport properties.....	26
2.2 Experimental procedure .....	28

2.2.1	Powder sample preparation .....	28
2.2.2	Sintering of the pellets.....	29
2.2.3	Density measurement of the sintered specimens.....	32
2.2.4	X-ray diffraction.....	33
2.2.5	Scanning electron microscopy and EDX .....	35
2.2.6	Thermal conductivity measurement.....	37

[Chapter 3:](#) DFT and experimental study on the thermal conductivity of  $U_3O_8$  and  $U_3O_{8-x}$ ; (X=Al and Mo)..... 40

3.0	Abstract.....	42
3.1	Introduction.....	43
3.2	Methodology .....	46
3.2.1	Computational details.....	46
3.2.2	Experimental procedure .....	47
3.2.2.1	Fabrication of the samples .....	47
3.2.2.2	Characterization of the pellets .....	48
3.2.2.3	Thermal conductivity measurement.....	56
3.3	Results and Discussion .....	56
3.3.1	Structural and mechanical properties of $U_3O_8$ .....	56
3.3.2	Lattice dynamics .....	61
3.3.3	Anisotropic thermal conductivity of $U_3O_8$ .....	63
3.3.4	Thermal conductivity of $U_3O_8$ -Al and $U_3O_8$ -Mo .....	72
3.3.5	The effect of porosity on thermal diffusivity and conductivity .....	76
3.4	Conclusion .....	79

[Chapter 4:](#) Density functional theory study of the structural, mechanical, and thermal conductivity of uranium dialuminide ( $UAl_2$ )..... 80

4.0	Abstract.....	81
4.1	Introduction.....	82
4.2	Computational details .....	83
4.3	Results and discussion .....	85

4.3.1	Optimized structure at ground state .....	85
4.3.2	Lattice dynamics and thermomechanical properties .....	88
4.3.3	Thermal transport properties .....	96
4.3.3.1	Phonon thermal conductivity .....	96
4.3.3.2	Electronic thermal contribution and the total thermal conductivity .....	101
4.4	Conclusion .....	107
 <u>Chapter 5:</u> Comprehensive study on the electronic and optical properties of $\alpha$ - $U_3O_8$ .....		108
5.0	Abstract .....	109
5.1	Introduction.....	110
5.2	Computational and experimental methodology .....	111
5.2.1	Computational details.....	111
5.2.2	Experimental Details .....	113
5.3	Results and Discussion .....	115
5.3.1	Structural, electronic, and optical property simulation.....	115
5.3.2	Experimental band gap .....	127
5.4.	Conclusion .....	130
 <u>Chapter 6:</u> Electronic transport in pure molybdenum and the effective thermal conductivity of $U_3O_8$ -Mo .....		131
6.0	Abstract.....	132
6.1	Introduction.....	133
6.2	Computational details .....	134
6.3	Results and discussion .....	135
6.3.1	Ground state properties .....	135
6.3.2	Electron scattering rates and the relaxation time .....	137
6.3.3	Electrical resistivity.....	139
6.3.4	Electronic thermal contribution ().....	140
6.3.5	Effective thermal conductivity of $U_3O_8$ -Mo fuels: ().....	141
6.4	Conclusion .....	144

<a href="#">Chapter 7: Concluding remarks</a> .....	145
7.1 Conclusions.....	145
7.2 Suggestions for future works .....	147
REFERENCES .....	149
<a href="#">Appendix A: Copyright agreements</a> .....	173



# Chapter 1

## Introduction

The nuclear industry plays a vital role in many sectors, including supplying electricity for civilian applications, producing neutrons for materials' research and testing purposes, and producing radioisotopes for the medical sector. Importantly, nuclear power is one of the most potent forms of energy that can meet the ever-increasing global electricity demand<sup>1</sup> and is also a significant contributor to realizing the dream of net-zero emissions. To improve the efficiency and safety of current and future reactor designs while minimizing the environmental impacts, it is crucial to engage in a wide range of research, from the fundamental level of materials studies to safety demonstrations of the nuclear reactors. This project primarily investigates the fundamental physics of the thermal properties of the selected nuclear fuel materials utilized in fission reactors. This chapter briefly covers the background of the nuclear industry, the project's motivation, and the relevance and importance of the current work to the nuclear industry.

### 1.1 Basics of nuclear industry

Fission and fusion are two nuclear reactions that release enormous energy by splitting unstable nuclei or combining light nuclei, respectively. Since this project primarily focuses on fission fuels, the discussion always refers to nuclear fission reactors.

The fission process occurs in nature through the decay of radioactive isotopes. However, such a random and uncertain process is not suitable for any useful reactor application. The fission reactor core consists of the nuclear fuel materials that undergo fission reactions (also called the fissile material), and uranium is the most widely used fissile material in current commercial nuclear reactors.<sup>2</sup> Among the isotopes of uranium ( $^{234}\text{U}$ ,  $^{235}\text{U}$ , and  $^{238}\text{U}$ ), only  $^{235}\text{U}$  is fissile, but its abundance is only 0.7% of natural uranium. Figure 1.1 shows one of the possible fission reactions in  $^{235}\text{U}$  when bombarded either with a thermal or a fast neutron. The absorption of the neutron

into  $^{235}\text{U}$  creates  $^{236}\text{U}$ , an unstable isotope of uranium. Then it splits spontaneously into two lighter elements called fission products (e.g.,  $^{92}\text{Kr}$  and  $^{141}\text{Ba}$ ), releasing two to three free neutrons and a large amount of energy ( $\sim 200$  MeV). The released neutrons can trigger further fissions, thus ensuring a sustained chain reaction that eventually ensures the required production of heat, neutrons, or radioisotopes depending on the reactor's purpose.

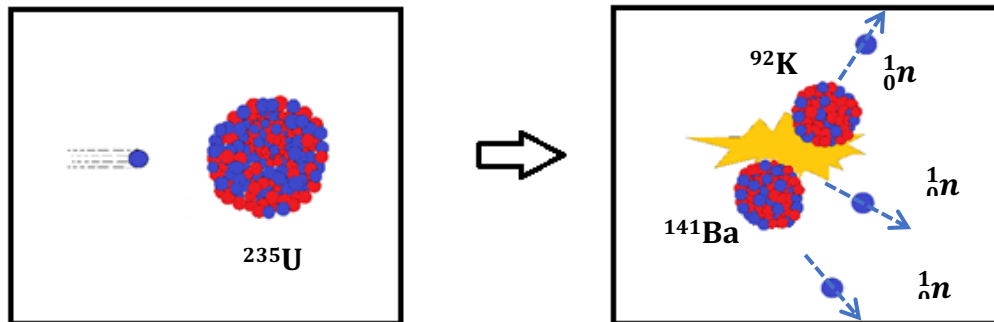


**Figure 1.1:** An example of an induced fission reaction in  $^{235}\text{U}$  sparked by a thermal neutron. In this case, the  $^{236}\text{U}$ , excited due to the absorption of the neutron ( $\frac{1}{0}n$ ), splits into two smaller nuclei ( $^{141}\text{B}$  and  $^{92}\text{K}$ ) along with three neutrons releasing a very large amount of energy.

Nuclear reactors can be classified as power reactors, research and test reactors, and propulsion reactors. The primary purpose of power reactors is to produce enough heat to make steam that spins a turbine to run electric-power generators. The 2020 edition of RDS-1 (Reference Data Series No. 1) released by the international atomic energy agency (IAEA)<sup>3</sup> reveals that, by the end of 2019, there were 443 commercial power plants worldwide with a total net installed power capacity of 392 GW(e). In addition, 54 reactors with a combined capacity of 57 GW(e) were under construction, and 109 plants with 114 GW(e) of power were planned. On the other hand, the research and test reactors are primarily designed to generate neutrons for advancing materials' research, produce radioisotopes for the medical sector, or use them for training, improvement, and development purposes in the nuclear industry.<sup>4</sup> Due to the wide range of their design purposes, research and test reactors operate with different power densities, neutron flux levels, and operating

temperatures. For example, high-performance research reactors are needed to perform neutron scattering experiments, high levels of radioisotope production, or to investigate fast neutron damages. Consequently, they are operated at high power levels and fission densities that can exceed the conditions in power reactors.<sup>4</sup> Despite that, basic irradiation experiments or low-scale radioisotopes production can be done in reactors operated at a low power density.<sup>4</sup> The third category, propulsion reactors, are the ones designed for naval applications. In these reactors, steam generated through the fission process is used to spin propeller turbines to run ships and submarines.

## **1.2 History of nuclear industry**

The history of the nuclear industry begins with the accidental discovery of X-rays by Wilhelm Roentgen in 1895.<sup>5</sup> However, it took several decades for scientists to discover the process of building up reactors using nuclear fission energy. The first fission reaction was demonstrated by a pair of German scientists, Otto Hahn and Fritz Strassman, in 1938.<sup>6</sup> Since this discovery happened during World War II, the focus of nuclear fission research was to develop a practical nuclear weapon. As a result, the first nuclear reactor design, Chicago Pile-1, was established to produce the required fissile atoms to make an atomic bomb.<sup>6,7</sup> However, peaceful applications of nuclear power became a significant focus sooner with the end of the war.<sup>6-8</sup> By the mid-1950s, the primary goal of nuclear research was to develop the required technology to generate electricity at the commercial level. These endeavours led to the world's first commercial nuclear power station, the Shipping port Reactor (Pennsylvania, USA), operational in 1957. Eventually, many other commercial power reactors, research and test reactors, as well as military applications with advanced technology were developed.

## **1.3 History of nuclear fuels**

The fuel element is essentially one of the primary components of a nuclear reactor because it is the ultimate energy source to facilitate electricity generation. Additionally, thermo-physical properties of fuels under regular operation and in accident scenarios govern the reactor's

performance, including its efficiency, reliability, and safety. Numerous fuel designs have been developed throughout the nuclear power industry's history based on the experience of prevailing technology, reactor type, and the limitations identified from the previous real accidents.<sup>5,7,9-12</sup>

Pure metallic uranium is the first and the most basic type of fuel ever employed in nuclear applications;<sup>13</sup> examples are: Manhattan Project, EBR-I, early MAGNOX reactors, and early CANDU reactors. A mixture of metallic and oxide forms of uranium<sup>10</sup> has been used in the world's first nuclear reactor, Chicago Pile I. Metallic uranium nitride has been applied in several nuclear space applications<sup>14,15</sup> and Russian fast reactors.<sup>16</sup> Mixed-Oxides (MOX) fuels, mostly a mixture of plutonium dioxide and Urania, are used in commercial reactors.<sup>16</sup> Later, uranium dioxide (UO<sub>2</sub>)<sup>17,18</sup> became the most widely used fuel in commercial reactors. However, the most recent nuclear reactor accident, the Fukushima disaster in 2011, revealed severe safety issues with the UO<sub>2</sub> and zircalloy cladding system.<sup>17,18</sup> Hence a great deal of attention is focused on improving the reactor core design by altering the existing fuel and cladding materials, such that the new design can not only withstand the loss of coolant for a long time but also improve the efficiency.<sup>19</sup> Therefore, several accident-tolerant fuel (ATF) concepts are being investigated<sup>20,21</sup> to mitigate the risk associated with the existing reactor core design.

There are numerous other fuels dominantly designed for research and test reactor applications. Primarily, dispersion type<sup>22</sup> (fissile phase is dispersed in a metallic matrix) and monolithic plate-type fuels are widely used in research and test reactors. Most widely used research reactor fuels are dispersion-type fuels made with uranium aluminide (U-Al),<sup>23,24</sup> uranium silicide (U<sub>3</sub>Si<sub>2</sub>),<sup>24,25</sup> or tri-uranium-octoxide (U<sub>3</sub>O<sub>8</sub>)<sup>24,26</sup> in an aluminum matrix. Further, development efforts are undertaken for new dispersion type fuel systems with U-Mo alloys with high uranium density.<sup>27-</sup>

32

## 1.4 Motivation for this work

This research project aims to investigate the thermal properties of two uranium compounds namely, U<sub>3</sub>O<sub>8</sub> and UAl<sub>2</sub>. Further, it is planned to study the enhancement of the thermal properties

of  $U_3O_8$  when mixed with metallic Al and Mo at different concentrations. The reasons for selecting these materials are as follows:

$U_3O_8$  is an abundant nuclear material found in the natural uranium ore, nuclear fuel cycle (known as yellowcake), and used nuclear waste deposits. Besides,  $U_3O_8$ -Al dispersion fuels are currently used in the High Flux Isotope Reactor (HFIR)<sup>33</sup> and have been used in several other decommissioned research reactors including Puerto Rico Nuclear Center Reactor (PRNC), Oak Ridge Research Reactor (ORR), and High Flux Beam Reactor (HFBR).<sup>34</sup> The applicability of pure  $U_3O_8$  as a power reactor fuel is limited due to many reasons, including its low thermal conductivity. Besides that, experimental, and theoretical investigations report that the current power reactor fuel  $UO_2$  oxidizes to  $U_3O_8$  at high temperature.<sup>35,36</sup> Therefore, the fuel elements in nuclear power reactors may contain  $U_3O_8$ , especially in accident scenarios where the reactor core exceeds the normal operating temperature. Hence, understanding the fundamental properties of  $U_3O_8$  is essential to evaluate the performance of current commercial fuel under accident conditions. One primary limitation of  $U_3O_8$  as a nuclear fuel has been its low thermal conductivity ( $2.01 \text{ W m}^{-1} \text{ K}^{-1}$  at 300 K).<sup>37-39</sup> So far, several techniques to enhance thermal conductivity have been successfully tested with other nuclear fuels (*e.g.*,  $UO_2$ , UN, and  $U_3Si_2$ ). For example, thermal conductivity improvement in  $UO_2$  is actively tested for doped conditions with high thermal conduction additives like silicon carbide (SiC),<sup>40</sup> beryllium oxide (BeO),<sup>41</sup> diamond,<sup>42</sup> and molybdenum (Mo).<sup>43</sup> However, the applicability of similar methodologies in  $U_3O_8$  has not been investigated. Hence, it is worthy of scrutinizing the feasibility of developing enhanced thermal conduction fuels using  $U_3O_8$  and metallic additives.

Furthermore, the interest in investigating the optical properties of  $U_3O_8$  was motivated by its possible recycling applications. The United States department of energy (DOE) has commenced a research and development project called the “Depleted uranium uses”<sup>44</sup> to investigate the practical applications of depleted uranium and other leftover materials from the conversion of depleted  $UF_6$ . The main goal of this project was the conservation of resources and to study the relative cost-effectiveness compared with their disposal. There are several other investigations on possible recycling methods, such as using them in radiation shielding applications,<sup>44</sup> catalysts for the destruction of air pollutants,<sup>44</sup> and uranium oxide semiconductors.<sup>45</sup> Oak Ridge National Laboratory (ORNL) engaged in finding the feasibility of using uranium oxides in semiconductor

applications, particularly in solar cells and other electronic devices (*e.g.*, integrated circuits). These proposals were driven due to the comparative material properties of uranium oxides (*e.g.*,  $\text{UO}_2$  and  $\text{U}_3\text{O}_8$ ) with conventional semiconductors such as Si, Ge, and GaAs. For instance, the optical band gap of  $\text{UO}_2$  is in the appropriate range for solar cell applications;  $\text{UO}_2$  and  $\text{U}_3\text{O}_8$  can withstand much higher operating temperatures ( $\sim 2500$  K) compared with Si or GaAs ( $\sim 473$  K), hence suitable in space applications. Supporting these investigations, Meek *et al.*<sup>45,46</sup> successfully fabricated photovoltaic devices using  $\text{UO}_2$  and  $\text{U}_3\text{O}_8$ . However, more research and investigations are needed to confirm their commercial uses. Therefore, it is imperative to study the fundamental semiconductor properties of  $\text{U}_3\text{O}_8$  to support its innovative novel applications.

Continuous interest and the advantages of low enriched uranium (LEU) research reactor fuels inspired our investigation of the high uranium density material,  $\text{UAl}_2$ . Meanwhile, there are extensive efforts to develop low enriched  $\text{UAl}_2$ -Al fuels for the new Brazilian Multipurpose Reactor (RMB)<sup>47</sup> and Pakistan Research Reactor-1<sup>48</sup> targeting the productivity improvements of  $^{99}\text{Mo}$  and the proliferation concerns with highly enriched research reactor fuels. The proliferation risk of fissile materials has always been a significant concern since the beginning of the atomic era. The majority of the research reactors, until the late 1970s, were built with technology that required highly enriched uranium (HEU) fuels as high as 90% and beyond, due to many advantages, including longer time before refueling, higher neutron flux, and a more compact core. However, to guard against the malicious use and possible threat of weapon proliferation due to HEU, an international program called Reduced Enrichment for Research and Test Reactors (RERTR)<sup>22,25,49</sup> was launched by the Department of Energy, USA, in 1978. Since then, various national and international supportive projects have been initiated parallel with RERTR. The objective of that effort was to develop the required technologies to convert all HEU cores to LEU fuels without reducing the experimental performance, capacity, and safety aspects of the station. Many of the HEU fuels, when the program began, were dispersion types with aluminum matrices. It is technically possible to convert these HEU cores to LEU if  $^{235}\text{U}$  content can be kept approximately the same. There are two main approaches to accomplishing this goal: One is increasing the uranium density in the fuel, and the other way is increasing the fissile (uranium) volume in the matrix. The former approach is feasible with high-density uranium compounds. Some of the uranium compounds that can be developed to use in LEU levels are given in Table 1.1.<sup>48,50</sup> Dispersion fuels of  $\text{UAl}_x$  alloys (a mixture of  $\text{UAl}_2$ ,  $\text{UAl}_3$ , and  $\text{UAl}_4$ ) in aluminum matrix<sup>51-</sup>

<sup>53</sup> with a uranium density of 1.7 g. cm<sup>-3</sup> were widely used in research and test reactors with high enrichment before launching the RERTR program, and it has already been developed to use in LEU level. Given that, having the highest density in the uranium aluminide family, UAl<sub>2</sub> should provide better uranium density in the form of UAl<sub>2</sub>-Al. Ultimately, it ensures high thermal conductivity with more Al included. Due to the abovementioned importance, UAl<sub>2</sub> has driven our interest in investigating their properties.

**Table 1.1:** Theoretical densities and uranium densities of candidate fuels in dispersion type fuel applications.<sup>48,50</sup>

Compound	Theoretical density (g. cm <sup>-3</sup> )	Uranium density (g. cm <sup>-3</sup> )
UAl <sub>4</sub>	6.0	4.1
UAl <sub>3</sub>	6.8	5.1
UAl <sub>2</sub>	8.1	6.6
U <sub>3</sub> Si <sub>2</sub>	12.2	11.3
U <sub>3</sub> Si	15.3	14.8
U <sub>6</sub> Fe	17.4	17.0
U – 10wt%Mo	17.2	16.4
U	19.0	19.0

## 1.5 Thesis objectives

Thermal conductivity is one of a nuclear fuel's most critical properties because it determines the heat transfer, operating temperature, efficiency, and reactor safety. The main objective of this project is to investigate the thermomechanical properties of  $U_3O_8$ ,  $UAl_2$ ,  $U_3O_8-Al$ , and  $U_3O_8-Mo$  compounds by employing computational or experimental methodologies. We planned to explore the thermal transport in these compounds in a broad range of temperatures by first principles simulations based on density functional theory (DFT).<sup>54,55</sup> In this project, the first principles codes, namely, ShengBTE,<sup>56</sup> BoltzTraP (Boltzmann Transport Properties),<sup>57</sup> EPW (Electron-Phonon coupling using Wannier functions),<sup>58</sup> and Phonopy<sup>59</sup> will be utilized with QE (Quantum ESPRESSO).<sup>60</sup> The samples were sintered using the novel Spark plasma sintering (SPS) technique to experimentally validate the computationally determined thermal conductivity results. The structural and chemical analysis will be done using X-ray diffraction (XRD)<sup>61</sup>, Energy Dispersive X-Ray Analysis (EDX),<sup>62</sup> and scanning electron microscope (SEM)<sup>62</sup> techniques. Thermal conductivity will be measured using the laser flash apparatus.<sup>63</sup> Similarly, the computationally determined optical properties of  $\alpha-U_3O_8$  will be validated experimentally using the diffuse reflectance method.

In brief, the main objectives of the project are:

1. To evaluate thermomechanical properties of  $U_3O_8$  using first principles simulation methodologies based on DFT.
2. To experimentally determine the thermal conductivity of pure  $U_3O_8$  and analyze the effect of metal additives, Al, and Mo, on its thermal properties.
3. To evaluate thermomechanical properties of  $UAl_2$  using first principles simulation methodologies based on DFT.
4. To investigate the electronic and the optical properties of  $U_3O_8$  using first principles simulation methodologies and its optical band gap experimentally.
5. To evaluate the thermal transport properties of the additive material Mo, using first principles simulation methodologies based on DFT.



## 1.6 Thesis outline

The accomplishments related to the objectives listed above are presented in detail in the following chapters of this manuscript-based thesis. The thesis contains seven chapters, as outlined below:

- **Chapter 1** contains the overview, motivation, rationale for ATF concepts selection, and research objectives.
- **Chapter 2** gives a brief introduction to the DFT and its implementation in the simulation packages employed for this project in evaluating the properties of the selected materials. In addition, the experimental methodologies used for the preparation of  $U_3O_8$ ,  $U_3O_8$ -Al and  $U_3O_8$ -Mo samples and their characterization are described.

The results of the current research are presented in chapters 3 to 7 as follows:

- In **Chapter 3**, a detailed investigation of the lattice thermal transport in  $\alpha$ - $U_3O_8$ , and the experimental study on the effect of Mo and Al additives on the thermal transport in  $\alpha$ - $U_3O_8$  are presented. Research findings presented in this chapter are published in the *Journal of Nuclear Materials*.
- The thermomechanical properties of  $UAl_2$  are evaluated using DFT and discussed in **Chapter 4**. Electronic and lattice contributions to thermal transport are assessed and compared. The research findings presented in this chapter are published in the *Journal of Nuclear Materials*.
- DFT analysis on the optical properties of  $\alpha$ - $U_3O_8$  is reported in **Chapter 5**. The diffuse reflectance method is used to determine the optical bandgap experimentally. This work is published in the *Journal of Computational Material Sciences*.
- **Chapter 6** focuses on the thermomechanical properties of the additive materials Al and Mo. This work is conducted using DFT-based theoretical techniques, and both the electronic and lattice heat transport components are evaluated. The findings will be published in the *Journal of solid-state sciences* in the future.

- The theoretical investigation of thermal transport in Mo is discussed in *Chapter 7*. Also discussed are the effective thermal conductivities in U<sub>3</sub>O<sub>8</sub>-Mo fuels with 8.2vol% and 12.5vol% Mo predicted using an empirical model.
- Finally, the overall summary, originality of the current work, and suggestions for future work are described in *Chapter 8*.

## Chapter 2

### Methodology

In this work, the properties of two nuclear fuel materials ( $\text{U}_3\text{O}_8$  and  $\text{UAl}_2$ ) and two metallic additives ( $\text{U}_3\text{O}_8\text{-Al}$  and  $\text{U}_3\text{O}_8\text{-Mo}$ ) are evaluated theoretically within the framework of the first principles and using experimental techniques. The first part of this chapter (Sec. 2.1) outlines the computational approaches used to achieve the research objectives, followed by the experimental procedures (Sec. 2.2) applied for fuel pellet fabrication, characterization, thermal conductivity measurements, and the bandgap measurements.

#### 2.1 Computational Methodology

The macroscopic properties of crystalline solids can be understood by analyzing the internal forces acting on their electrons and nuclei. In principle, it can be precisely evaluated by solving the corresponding Schrödinger equation of the system<sup>64</sup>. However, the Schrödinger equation for a real system with an order of  $10^{23}$  particles is very complex and challenging to solve, even on the most powerful supercomputers. Therefore, various methodologies with different approximations have been tried out by many scientists throughout history. While simple systems (*e.g.* Hydrogen atom) have been solved analytically<sup>64,65</sup>, for complicated systems, the “Nearly free electron method” or “Tight-binding method”<sup>65</sup> have been used. However, those methods are based on approximations at different levels, their solutions are far or less accurate when applied to complex systems. When both the accuracy and the efficiency are considered, DFT (Hohenberg and Kohn, 1964)<sup>66</sup> is one of the most successful methods to accurately solve the Schrödinger equation of many systems required in the fields of solid-state sciences, chemistry, and materials sciences. In this thesis, all the theoretical findings have been achieved within the framework of DFT in the *ab-initio* technique. The rest of this section (Sec. 2.1) briefly discusses the quantum mechanical interpretation of matter (many-particle problem), various levels of historic approximations used to

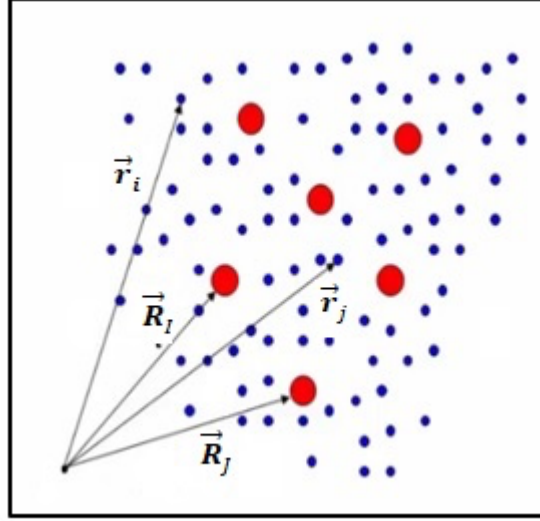


**Figure 2.1:** Positions of electrons (blue points) and nuclei (red circles) in a many-body system.

solve the Schrödinger equation of a system, the basics of the DFT, and the computational background of calculating the thermal transport.

### 2.1.1 Many-body problem

Consider a solid system composed of electrons and nuclei with respective masses of  $m_e$  and  $M_I$  (with atomic number  $Z_I$ ), located at  $\vec{r}_i$  and  $\vec{R}_I$ , as shown in Fig. 2.1. In the absence of external electric and magnetic fields, its Hamiltonian ( $\hat{H}$ ) can be written as

$$\hat{H} = \underbrace{-\frac{\hbar^2}{2} \sum_I \frac{\nabla_{\vec{R}_I}^2}{M_I}}_{\hat{T}_n} + \underbrace{\frac{-\hbar^2}{2} \sum_i \frac{\nabla_{\vec{r}_i}^2}{m_e}}_{\hat{T}_e} + \underbrace{\frac{-1}{4\pi\epsilon_0} \sum_{I,i} \frac{e^2 Z_I}{|\vec{R}_I - \vec{r}_i|}}_{\hat{V}_{en}} + \underbrace{\frac{1}{8\pi\epsilon_0} \sum_{i \neq j} \frac{e^2}{|\vec{r}_i - \vec{r}_j|}}_{\hat{V}_{ee}} + \underbrace{\frac{1}{8\pi\epsilon_0} \sum_{I \neq J} \frac{e^2 Z_I Z_J}{|\vec{R}_I - \vec{R}_J|}}_{\hat{V}_{nn}}, \quad (2.1)$$

where the lower-case subscripts  $i, j$  and the upper-case subscripts  $I, J$  respectively, represent electrons and nuclei in the system. Otherwise mentioned, the summations run over each electron

and nucleus. The constants  $\hbar$ ,  $\epsilon_0$ , and  $e$ , are the reduced Plank constant, the permittivity of vacuum, and the electron charge, respectively. The first ( $\hat{T}_n$ ) and second ( $\hat{T}_e$ ) terms in the right-hand side (RHS) of the equation respectively represent the operators for the kinetic energies of nuclei and electrons. The other three terms, labeled as  $\hat{V}_{en}$ ,  $\hat{V}_{ee}$ , and  $\hat{V}_{nn}$ , are the potential energy operators for the Coulomb interaction between electrons and nuclei, pairs of electrons, and pairs of nuclei, respectively.

Further, the corresponding time-independent Schrödinger equation of the system is

$$\hat{H}\Psi_{\text{MB}}(\vec{r}_1, \vec{r}_2, \dots; \vec{R}_1, \vec{R}_2, \dots) = E\Psi_{\text{MB}}(\vec{r}_1, \vec{r}_2, \dots; \vec{R}_1, \vec{R}_2, \dots), \quad (2.2)$$

where  $\Psi_{\text{MB}}(\vec{r}_1, \vec{r}_2, \dots; \vec{R}_1, \vec{R}_2, \dots)$  is the wave function (or the Many-body wave function) for the system of electrons and nuclei, and  $E$  denotes the energy eigenvalue for the corresponding state represented by  $\Psi_{\text{MB}}(\vec{r}_1, \vec{r}_2, \dots; \vec{R}_1, \vec{R}_2, \dots)$ .

The first approximation applied to reduce the dimensionality of this problem is the Born-Oppenheimer/adiabatic approximation<sup>67,68</sup>. This approach applies the impact of the mass difference between nuclei and electrons to reduce the complexity of the Hamiltonian. Since the nuclei are much heavier than the electrons, the former moves in a much longer time scale than the latter. This behaviour safely permits us to assume that only the electrons in the system move while the nuclei stay still at their equilibrium positions. This approximation makes the kinetic energy term of the nuclei ( $T_n$ ) in Eq. (2.1) zero and the potential energy due to Coulomb repulsion among nuclei ( $V_{nn}$ ), a constant. Further, the potential energy from the electron-nuclear interaction ( $V_{en}$ ) can be treated as a perturbation from a fixed external potential ( $V_{ext}$ ). With that description, Eq. (2.1) can be rewritten as:

$$\hat{H} = \hat{T}_e + \hat{V}_{ee} + \hat{V}_{ext}, \quad (2.3)$$

where  $\hat{V}_{ext}$  is the operator for the potential energy of electrons created by the fixed nuclei. Further, this assumption eliminates the  $\vec{R}_I$  dependence of the many-body wave function. Hence, the many-body wave function  $\Psi_{\text{MB}}(\vec{r}_1, \vec{r}_2, \dots; \vec{R}_1, \vec{R}_2, \dots)$  becomes  $\Psi_{\text{MB}} = \Psi_{\text{MB}}(\vec{r}_1, \vec{r}_2, \dots)$ , a function of only  $\vec{r}_i$ .

### 2.1.1.1 Hartree-like approximation

The subsequent primary step in solving the many-body equation is the independent-electron approximation. There are two main types of independent-electron approximations “*non-interacting*” (Hartree-like) and “Hartree-Fock”<sup>66,69–71</sup>. The former takes the electrons as free, which means that the electrons do not have Coulomb interaction with each other, except agreeing with Pauli’s principle. Therefore, if  $\phi_i(\vec{r}_i)$  represents the single-particle wave function of the  $i^{\text{th}}$  electron, the probability ( $n(\vec{r})$ ) of simultaneously finding electron 1 at position  $\vec{r}_1$ , electron 2 at position  $\vec{r}_2$ , and so forth (*i.e.*, the electron density) is given by

$$n(\vec{r}) = |\Psi_{\text{MB}}(\vec{r}_1, \vec{r}_2, \dots)|^2 = \sum_i |\phi_i(\vec{r}_i)|^2. \quad (2.4)$$

Therefore, the many-body wave function and the system’s total energy can be respectively written as in Eq. (2.5) and (2.6).

$$\Psi_{\text{MB}}(\vec{r}_1, \vec{r}_2, \vec{r}_3, \dots) = \phi_1(\vec{r}_1)\phi_2(\vec{r}_2)\phi_3(\vec{r}_3) \dots \quad (2.5)$$

$$E = \varepsilon_1 + \varepsilon_2 + \varepsilon_3 \dots \quad (2.6)$$

where  $\varepsilon_i$  are the energy eigen solutions of the single electron systems with the condition  $\varepsilon_1 < \varepsilon_2 \dots < \varepsilon_N$ .

However, the Coulomb interaction term of the electrons cannot be simply removed for simplicity because it is of the same order of magnitude as the other terms. Therefore,  $V_{ee}$  is replaced with the Coulomb interaction potential defined by the Hartree potential  $V_H(\vec{r})$ , which is defined as

$$V_H(\vec{r}) = \int \frac{n(\vec{r}')}{|\vec{r} - \vec{r}'|} d^3r'. \quad (2.7)$$

Consequently, the single-particle wave function  $\phi_i(\vec{r})$  is given by

$$\left[ -\frac{\hbar^2}{2m_e} \nabla^2 + \hat{V}_{ext}(\vec{r}) + \hat{V}_H(\vec{r}) \right] \phi_i(\vec{r}) = \varepsilon_i \phi_i(\vec{r}). \quad (2.8)$$

### 2.1.1.2 Hartree-Fock approximation

The Born-Oppenheimer and the Hartree-like approximations simplify the many-body problem, but these steps cannot be counted as very successful approaches because of two main drawbacks. The first issue is not being able to replace the exact form of the Coulomb term. The second one is the violation of the anti-symmetry condition by its wave function and disobeying Pauli's exclusion principle. In the Hartree-Fock approximation (1930), electrons are considered independent particles. However, it incorporates the missing Coulomb interactions (exchange term) and the antisymmetric condition by the new wave function representation as a Slater determinant. According to this new definition, the single-particle wave function,  $\phi_i(\vec{r})$ , satisfies the orthogonal condition. The minimization of total energy leads to the Hartree-Fock equation:

$$\left[ -\frac{\hbar^2}{2m_e} \nabla^2 + \hat{V}_{ext}(\vec{r}) + \hat{V}_H(\vec{r}) + \hat{V}_X(\vec{r}) \right] \phi_i(\vec{r}) = \varepsilon_i \phi_i(\vec{r}), \quad (2.9)$$

where the exchange interaction ( $\hat{V}_X(\vec{r})$ ) term is given by

$$\hat{V}_X(\vec{r}) = \int \frac{\phi_j^*(\vec{r}') \phi_j(\vec{r}')}{|\vec{r} - \vec{r}'|} d^3r'. \quad (2.10)$$

## 2.1.2 Density Functional Theory (DFT)

The next level solution to the many-body problem is the DFT. This method is primarily based on two theorems, postulated by Hohenberg and Kohn in 1964<sup>66</sup> and mainly focuses on reducing the dimensionality of the problem by replacing the many-electron picture with the electron density of the system.

### 2.1.2.1 Hohenberg-Kohn theorems

The two postulates in Hohenberg-Kohn theorems are; (i) the total energy of a system is a unique functional of the electron density  $n(\vec{r})$ , and (ii) the ground-state electron density gives its minimal value<sup>66</sup>. According to the theorems mentioned above, a system cannot have two different potentials which give the same ground-state electron density,  $n^0(\vec{r})$ .

By applying the Hohenberg-Kohn theorem, the Schrödinger equation can be rearranged as given in Eqs (2.11) - (2.13),

$$\hat{H}\Psi_{MB} = E_{HK}[n(\vec{r})]\Psi_{MB}, \quad (2.11)$$

$$E_{HK}[n(\vec{r})] = \underbrace{\langle \Psi_{MB} | \hat{T} + \hat{V}_{e-e} | \Psi_{MB} \rangle}_{F_{HK}[n(\vec{r})]} + \langle \Psi | \hat{V}_{\text{ext}} | \Psi \rangle, \quad (2.12)$$

$$E_{HK}[n(\vec{r})] = F_{HK}[n(\vec{r})] + \int V_{\text{ext}}(\vec{r})n(\vec{r})d\vec{r}, \quad (2.13)$$

where  $E_{HK}[n(\vec{r})]$  is the functional of  $n(\vec{r})$  defined by Hohenberg-Kohn theorems and denotes the energy eigenvalue of the system,  $F_{HK}[n(\vec{r})]$  is the unique (universal) density functional indicated by the Hohenberg-Kohn theorem.  $F_{HK}[n(\vec{r})]$  is called a universal functional because it does not carry any system-dependent parameters: for example, it does not contain any factors representing the crystal structure, type of atoms, or atomic coordinates<sup>55,72</sup>.

### 2.1.2.2 Kohn-Sham equations

Even though Hohenberg-Kohn theorem clarifies the way of solving the many-body Schrödinger equation, it does not specify the way forward with  $F_{HK}[n(\vec{r})]$ , yet *Kohn-Sham equations*<sup>73</sup> are the practical method of deriving the ground-state electron density. Before going to define Kohn-Sham equations, it needs to mention here that the exchange potential term ( $V_X$ ) and the Hartree potential term ( $V_H$ ) in Eq. (2.9) do not fully replace  $V_{ee}$  since the Slater determinant itself cannot represent the exact wave function. The energy gap between the real and the defined systems is called the *correlation energy*. This term is enclosed to the *exchange-correlation energy* ( $E_{XC}[n(\vec{r})]$ ) of the Kohn-Sham equations; hence well represents the exact energy of the system.

With this new technique, the system's energy given in Eq. (2.13) can be rewritten in the format of

$$E_{KS}[n(\vec{r})] = T_0 + \int V_{\text{ext}}(\vec{r})n(\vec{r})d\vec{r} + E_H[n(\vec{r})] + E_{XC}[n(\vec{r})], \quad (2.14)$$

where  $T_0$  is the kinetic energy under independent particle approximation, and  $E_H[n(\vec{r})]$  is the Hartree energy. The Hartree term comprises the Coulomb interaction energy of the electron density  $n(\vec{r})$  due to  $V_H(\vec{r})$ , and it is evaluated as



$$E_H[n(\vec{r})] = \frac{1}{2} \int d\vec{r} d\vec{r}' \frac{n(\vec{r})n(\vec{r}')}{|\vec{r}-\vec{r}'|}. \quad (2.15)$$

In order to get the ground-state solutions, one can minimize Eq. (2.14), which yields

$$\frac{\delta E_{KS}[n(\vec{r})]}{\delta \phi_i(\vec{r})} = \frac{\delta T_0}{\delta \phi_i(\vec{r})} + \left[ \frac{\delta E_{ext}}{\delta n(\vec{r})} + \frac{\delta E_H}{\delta n(\vec{r})} + \frac{\delta E_{XC}[n(\vec{r})]'}{\delta n(\vec{r})} \right] \frac{\delta n(\vec{r})}{\delta \phi_i(\vec{r})} = 0. \quad (2.17)$$

Finally, the many-body Schrödinger equation is reformulated using non-interacting particles' wave functions, and this representation is called the Kohn-Sham Schrödinger equations, which can be written as

$$(H_{KS} - \varepsilon_i) \phi_i(\vec{r}) = 0 \quad (2.18)$$

where  $H_{KS}$  is the effective Kohn-Sham Hamiltonian defined by

$$H_{KS} = T_0 + V_{eff}, \quad (2.19)$$

with the effective potential  $V_{eff}$  being

$$V_{eff} = V_{ext} + V_H + V_{XC}. \quad (2.20)$$

Here,  $V_{XC}$  represents the *exchange-correlation* potential.

The biggest challenge in the DFT method is the exact form of  $E_{XC}[n(\vec{r})]$ , which is an unknown term to date. However, DFT has a practical method for solving Kohn-Sham equations: it employs a self-consistent iterative technique with pre-defined specific approximations as  $E_{XC}[n(\vec{r})]$ . Figure 2.2 illustrates the flowchart of the full Self-consistent functional (SCF) method. As illustrated, SCF is usually started with an initial guess,  $n^1(\vec{r})$ , as the electron density. This  $n^1(\vec{r})$  is then used to find the Kohn-Sham Hamiltonian and build the corresponding Kohn-Sham Schrödinger equations. Consequently, the solution to the Kohn-Sham Schrödinger equations yields the wave function  $\phi_i(\vec{r})$ , updating the electron density to  $n(\vec{r})$ . If  $n^1(\vec{r})$  and  $n(\vec{r})$  are not equal, a second Kohn-Sham Hamiltonian is derived for  $n(\vec{r})$ . This loop will continue until the convergence of the electron density is achieved.

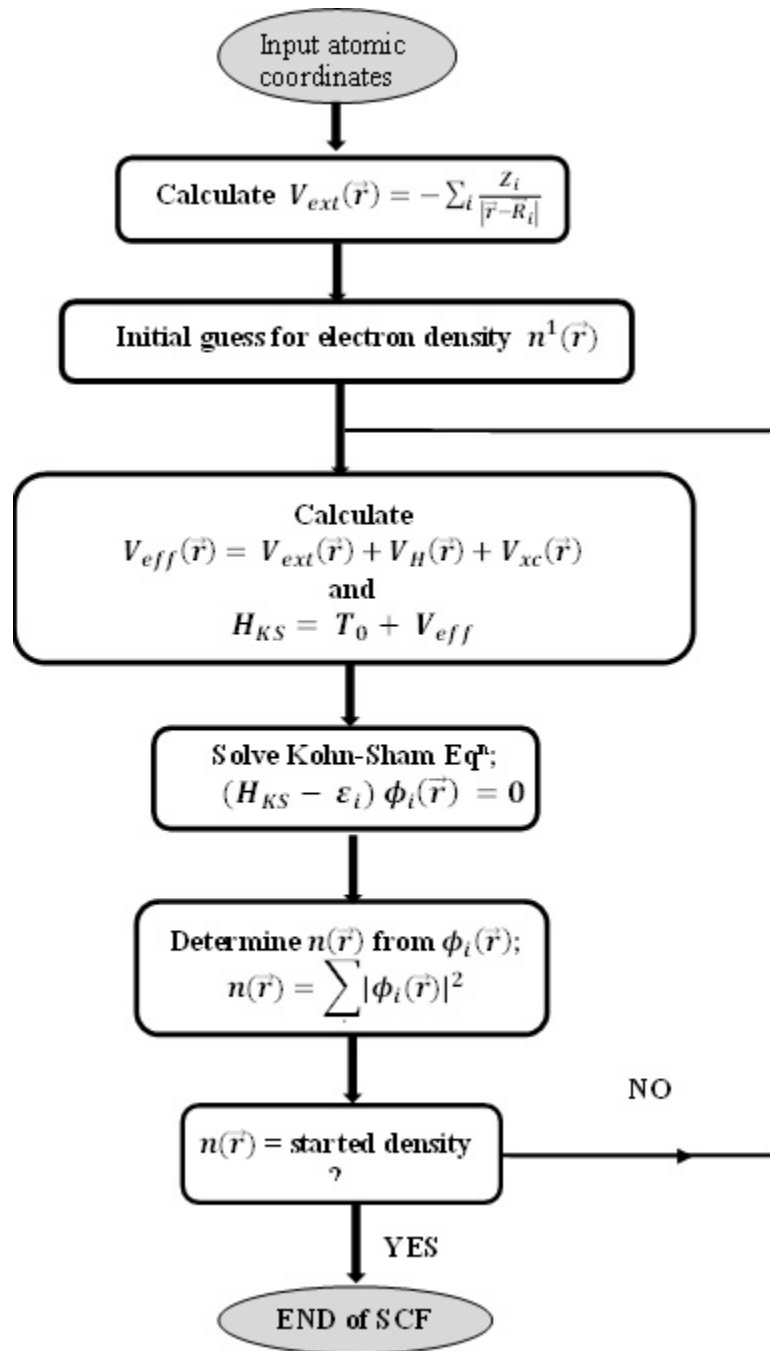


**Figure 2.2:** Flowchart of the self-consistent functional for ground state Kohn-Sham Schrödinger equation when the atomic positions of the system are known.

### 2.1.2.3 The Exchange-correlation energy ( $E_{XC}$ )

With widespread success and popularity, DFT is successfully applied to examine various material properties. However, as mentioned earlier, DFT demands approximations for  $E_{XC}$  term to practically solve the Kohn-Sham equations. With that said, the accuracy of the predicted properties depends on how closely these exchange-correlation functional replace the actual system is. Today, many types of different functionals are available to replace  $E_{XC}$ . Some examples are local density approximation (LDA), generalized gradient approximation (GGA), meta-GGA, and semiempirical hybrid functionals<sup>54,55,74</sup>.

#### (i) Local density approximation (LDA)

LDA is the simplest and one of the widely used approximations to replace  $E_{XC}$  in solid-state materials<sup>74</sup>. In this approach, electrons in solids are considered to behave within the limits of a homogeneous gas, and hence, the exchange-correlation is considered as a function of the local electron density only. The exchange-correlation in LDA ( $E_{XC}^{LDA}$ ) holds the analytic form given in Eq. (2.21),

$$E_{XC}^{LDA} = \int n(\vec{r}) \epsilon_{XC}^{hom}(n(\vec{r})) d\vec{r}. \quad (2.21)$$

Here  $\epsilon_{XC}^{hom}$  is the energy per electron at point  $\vec{r}$  due to the homogenous electron density  $n(\vec{r})$  in the neighborhood. Perdew-Zunger (PZ)<sup>75</sup> and Vosko-Wilk-Nusair (VWN)<sup>76</sup> are two widely used formalisms for LDA. In general, LDA performs poorly for systems with electron densities far from homogeneity, such as solids with strongly correlated electrons. Furthermore, it underestimates the lattice parameters in many solids because this approximation overestimates chemical bonding strength.

#### (ii) Generalized gradient approximation (GGA) and meta-GGA

LDA assumes the electron density as a uniform quantity, but it decreases slowly along the atom's radial direction in real systems. This density variation is considered to some extent in Generalized gradient approximation (GGA). GGA performs relatively better when the electron densities substantially deviate from the homogenous condition or otherwise when the LDA functionals fail. In GGA, the exchange-correlation functionals ( $E_{XC}^{GGA}$ ) are built, including the electron density

variation as a gradient function; hence it is a functional of both the local electron density and its gradient ( $\nabla n(\vec{r})$ ) as given in Eq. (2.22),

$$E_{XC}^{GGA} = \int n(\vec{r}) \epsilon_{XC}^{GGA}(n(\vec{r}), \nabla n(\vec{r})) d\vec{r}. \quad (2.22)$$

Here  $\epsilon_{XC}^{GGA}$  is the energy per electron at point  $\vec{r}$  due to the electron density  $n(\vec{r})$  and its gradient  $\nabla n(\vec{r})$  as given by corresponding approximation. While numerous types of GGA type functionals are available today, the three of the most popular types in use are PBE (Perdew, Burke, and Ernzerhof)<sup>77</sup>, PW91 (Perdew and Wang)<sup>78</sup>, PBEsol (Perdew-Burke-Ernzerhof for solids)<sup>79</sup> and B88 (Becke)<sup>79</sup>.

There is another level of GGA form called meta-GGA, which contains the Laplacian of the electron density ( $\nabla^2 n(\vec{r})$ ) or the kinetic energy density within the exchange-correlation formalism. Hence it can outperform GGA predictions occasionally. However, meta-GGA functionals need extra care with weakly interacting systems because they are more sensitive to the integration grid. The analytical form of meta-GGA functionals are in the form of

$$E_{XC}^{GGA} = \int n(\vec{r}) \epsilon_{XC}^{GGA}(n(\vec{r}), \nabla^2 n(\vec{r})) d\vec{r}. \quad (2.23)$$

### (iii) Hybrid functional

The Hybrid approach was first immersed in 1993 with the formation of B3LYP (Becke, three parameter, Lee-Yang-Parr) functional<sup>80,81</sup>. It was formed by linearly combining a part of the exact exchange term in the Hartree-Fock method with one or more terms from the exchange and correlation term. The weight of each of the hybrid functionals was usually assigned arbitrarily, but in a way, they can well reproduce some experimental properties of the system. For example, the B3LYP functionals have the following form,

$$E_{XC}^{B3LYP} = E_{XC}^{LDA} + a(E_X^{HF} - E_X^{LDA}) + b\Delta E_X^{B88} + c\Delta E_C^{PW91}. \quad (2.24)$$

where  $a$ ,  $b$ , and  $c$  are semiempirical parameters to be determined by fitting the experimental data,  $\Delta E_X^{B88}$  is the Becke's 1988 gradient functional correction,  $\Delta E_C^{PW91}$  is the Perdew's and Wang's 1991 functional,  $E_X^{HF}$  denotes the Hartree-Fock, exchange energies, and  $E_X^{LDA}$  represents the local

density approximation. Other popular hybrid functionals are PBE0<sup>82,83</sup>, HSE (Heyd-Scuseria-Ernzerhof)<sup>84</sup>, and Meta-hybrid GGA<sup>85,86</sup>.

#### 2.1.2.4 Limitations of DFT and DFT+U method

Despite the accuracy and the applicability of DFT enhanced with the improvements of the exchange-correlation functionals, it still suffers from qualitative failures of predicted properties in some materials. These failures are dominant with the predicted electron and magnetic properties when the system has strongly correlated electrons (*i.e.*, materials with localized *d*- and *f*-electrons). Some of the most common failures are underestimating the energy band gaps or even predicting metallic ground state for insulators (*e.g.*, UO<sub>2</sub>), poor predictions of vacancy formation energies, reaction barrier heights, and magnetic order<sup>55,72,74</sup>. These problems are mostly traced back to the deficiencies in treating the localized electrons and static correlation by the exchange-correlation functionals. Some of the available approaches to minimize these issues are the hybrid functionals (discussed above), Hubbard-U method (DFT+U)<sup>87</sup> or dynamical mean-field theory (DMFT)<sup>88</sup>. Applying the DFT+U method for electric and magnetic properties predictions in complex uranium compounds like U<sub>3</sub>O<sub>8</sub> is more prevalent when considering the calculation cost, feasibility, and the accuracy of the results. Hence DFT+U technique is used to evaluate the bandgap of U<sub>3</sub>O<sub>8</sub> in the current work. In this approach, an on-site parameter (Hubbard U) is added to the Hamiltonian to improve the effect of missing Coulomb interaction among the strongly correlated electrons.

#### 2.1.3 Thermal transport in crystalline solids

The heat transport in crystalline materials is performed by the vibrations of its atoms and electrons. However, having only a few free electrons to move, the thermal conductivity in semiconductors is mainly carried out by the atomic vibrations called phonons ( $\kappa_{ph}$ ). In contrast, the electronic heat transport ( $\kappa_e$ ) contribution plays a significant role in metallic materials. There are three metallic systems (UAl<sub>2</sub>, Mo, and Al) and one semiconductor (U<sub>3</sub>O<sub>8</sub>) involved in our project. Further, one of our objectives is to investigate their thermal transport properties using first principles methods, and it is achieved by solving the Boltzmann transport equation (BTE) using several simulation

packages: ShengBTE<sup>56</sup> and Phonopy<sup>59</sup> packages are used in the calculation of  $\kappa_{ph}$  and EPW<sup>58</sup> and BoltzTraP<sup>57</sup> codes are applied in the evaluation of  $\kappa_e$ . The theory and the workflow behind the above packages are described in the rest of this subsection, Sec. 2.1.3.

### 2.1.3.1 Lattice thermal conductivity ( $\kappa_{ph}$ )

The amount of heat current carried by phonon vibrations can be estimated by evaluating the rate of change of phonon distribution function  $f_j(\vec{q}, \omega)$  of the phonons with mode  $j$ , wave vector  $\vec{q}$ , and angular frequency  $\omega$ . The amount of total heat flow per unit volume due to all the phonon vibrations ( $\vec{J}^{Ph}$ ) in the crystal is given by Eq. (2.25)<sup>56,89,90</sup>,

$$\vec{J}_{ph} = \frac{1}{\Omega} \sum_{j, \vec{q}} \hbar \omega_j(\vec{q}) \vec{v}_j(\vec{q}) f_j(\vec{q}, \omega). \quad (2.25)$$

where  $\Omega$  is the unit cell volume,  $\vec{v}_j(\vec{q})$  and  $\omega_j(\vec{q})$  denote the group velocity and the frequency of the phonon in the branch  $j$  at the wave vector  $\vec{q}$ , respectively. The group velocity is the gradient of the dispersion relation, which is given by Eq. (2.26),

$$\vec{v}_j(\vec{q}) = \frac{\partial \omega_j}{\partial \vec{q}}. \quad (2.26)$$

At the thermal equilibrium,  $f_j(\vec{q}, \omega)$  can be represented by the Bose-Einstein statistics<sup>65</sup>,  $f_j^0(\vec{q}, \omega)$ . Boltzmann transport theory describes the statistical behaviour of the deviation of the distribution function from its equilibrium state under the thermal gradient of  $\nabla T$ . According to this theory, the rate of change of phonons in a small volume is caused by the diffusion of the phonons due to the thermal gradient and their different types of scattering processes, such as phonon-phonon, phonon-electron, phonon-impurity, and boundary scatterings. In a steady state, there must be no net change to the number of phonons in the considered volume portion of the system. Therefore, the rate of change of distribution function due to the drift of the phonons ( $\left. \frac{\partial f_j(\vec{q}, \omega)}{\partial t} \right|_{\text{diffusion}}$ ) should have canceled by the rate of their scatterings ( $\left. \frac{\partial f_j(\vec{q}, \omega)}{\partial t} \right|_{\text{scattering}}$ ) as stated in Eq. (2.27)<sup>56,91</sup>,

$$\left. \frac{\partial f_j(\vec{q}, \omega)}{\partial t} \right|_{\text{steady}} = \left. \frac{\partial f_j(\vec{q}, \omega)}{\partial t} \right|_{\text{diffusion}} + \left. \frac{\partial f_j(\vec{q}, \omega)}{\partial t} \right|_{\text{scattering}} = 0. \quad (2.27)$$

where  $\left. \frac{df_j(\vec{q}, \omega)}{dt} \right|_{\text{steady}}$  denotes the rate of change of distribution function at steady state and  $t$  is the time. The term  $\left. \frac{\partial f_j(\vec{q}, \omega)}{\partial t} \right|_{\text{diffusion}}$ , which gives the rate of change of distribution function due to diffusion or motion of the phonon, can be written as:

$$\left. \frac{\partial f_j(\vec{q}, \omega)}{\partial t} \right|_{\text{diffusion}} = -\frac{\partial}{\partial t} [\nabla f_j(\vec{q}, \omega) \cdot \mathbf{v}_j(\vec{q})] \quad (2.28)$$

$$\left. \frac{\partial f_j(\vec{q}, \omega)}{\partial t} \right|_{\text{diffusion}} = -\nabla T \cdot \vec{\mathbf{v}}_j(\vec{q}) \frac{\partial f_j(\vec{q}, \omega)}{\partial T}. \quad (2.29)$$

It leads to Eq. (2.30), which is known as the BTE of the phonons at a steady state with no external forces,

$$\left. \frac{\partial f_j(\vec{q}, \omega)}{\partial t} \right|_{\text{scatering}} = \nabla T \cdot \vec{\mathbf{v}}_j(\vec{q}) \frac{\partial f_j(\vec{q}, \omega)}{\partial T}. \quad (2.30)$$

The exact solution to this problem in actual cases is very hard. The historical approach to solving this equation is the constant relaxation time approximation (CRTA)<sup>89,92</sup>, which needs to be applied within the limits of linear phonon dispersion condition, very low system temperature (below room temperature), and small phonon frequencies in the system.

Under the CRTA, the scattering term is defined as

$$\left. \frac{\partial f_j(\vec{q}, \omega)}{\partial t} \right|_{\text{scatering}} = \frac{f_j(\vec{q}, \omega) - f_j^0(\vec{q}, \omega)}{\tau_j(\vec{q}, \omega)}, \quad (2.31)$$

where  $\tau_j(\vec{q}, \omega)$  is the relaxation time of the phonon in the  $j^{\text{th}}$  mode with frequency  $\omega$  and the wave vector  $\vec{q}$ .

However, the conditions that satisfy CRTA do not follow them in real cases, especially beyond the room temperature. Therefore, Eq. (2.31) does not correctly describe the scattering term when the system is at high temperature. The iterative method, which is the methodology used in this thesis, gives a more accurate approach to evaluating the scattering term and solving the BTE for many practical cases. The rest of this section briefly show up the main steps in the iterative method.

The strategy of this technique is to rearrange the linear BTE with a new variable and find that variable in an iterative calculation. First, we break the phonon distribution function into two parts, equilibrium ( $f_j^0(\vec{q}, \omega)$ ) and nonequilibrium ( $f_j'(\vec{q}, \omega)$ ):

$$f_j(\vec{q}, \omega) = f_j^0(\vec{q}, \omega) + f_j'(\vec{q}, \omega). \quad (2.32)$$

In most practical cases,  $\nabla T$  is small enough so that  $f_j'(\vec{q}, \omega)$  can be expanded to the first order of  $\nabla T$ . Then,  $f_j'(\vec{q}, \omega)$  can be defined in terms of a nonequilibrium parameter  $g_j(\vec{q})$  as given in Eq. (2.33),

$$f_j'(\vec{q}, \omega) = -\frac{df_j^0(\vec{q}, \omega)}{dT} g_j(\vec{q}). \quad (2.33)$$

Note here that the nonequilibrium parameter  $g_j(\vec{q})$  depends on  $\nabla T$  linearly. Further, since  $df_j^0(\vec{q}, \omega)/dT = f_j^0(f_j^0 + 1)/k_B T$ , Eq. (2.33) yields

$$f_j'(\vec{q}, \omega) = -\frac{f_j^0(f_j^0 + 1)}{k_B T} g_j(\vec{q}). \quad (2.34)$$

In the iterative method, the function  $g_j(\vec{q})$  is taken as<sup>56,92</sup>

$$g_j(\vec{q}) = -\mathbf{F}_j(\vec{q}) \cdot \nabla T, \quad (2.35)$$

where  $\mathbf{F}_j(\vec{q})$  is the function to be solved iteratively.

Consequently, Eq. (2.25) can be rewritten in terms of  $\mathbf{F}_j(\vec{q})$  as

$$\vec{J}_{ph} = \frac{1}{\Omega} \sum_{j, \vec{q}} \hbar \omega_j(\vec{q}) \vec{v}_j(\vec{q}) \left[ f_j^0 - \mathbf{F}_j(\vec{q}) \cdot \nabla T \frac{df_j^0}{dT} \right]. \quad (2.36)$$

The heat current is also linked to the thermal gradient according to the Fourier's Law: *i.e.*, if the thermal gradient goes along the  $\beta$ -direction, the effective thermal current across the surface with  $\alpha$ -direction ( $J_{ph\alpha}$ ) is given by

$$J_{ph\alpha} = -\sum_{\beta} \kappa_{\alpha\beta} (\nabla T)^{\beta}, \quad (2.37)$$



where the proportionality constant  $\kappa_{\alpha\beta}$  is the thermal conductivity tensor along the  $\alpha$ -direction when  $\nabla T$  is along the  $\beta$ -direction.

Since there is no heat flow without a thermal gradient, the first term of Eq. (2.36) is zero; hence by comparing Eq. (2.36) and (2.37),  $\kappa_{ph\alpha\beta}$  can be defined as

$$\kappa_{ph\alpha\beta} = \frac{1}{k_B T^2 \Omega N} \sum_{j,q} f_j^0 (f_j^0 + 1) (\hbar\omega)^2 \vec{\mathbf{v}}^\alpha \mathbf{F}_j^\beta(\vec{\mathbf{q}}). \quad (2.38)$$

Here  $N$  is the number of  $q$  points in the  $\Gamma$ -centered  $q$  mesh.

The used version of the ShengBTE<sup>56</sup> simulation package involves only the two- and three-phonon scatterings. With that said,  $\mathbf{F}$  is taken as  $\mathbf{F}_j = \tau_j^0 (\vec{\mathbf{v}} + \Delta_j)$ , where  $\tau_j^0$  is the relaxation time (or inverse of the scattering time) within CRTA and  $\Delta_j$  is a measure of how much the deviation of the heat current from CRTA.

More explicitly,  $\tau_j^0$  and  $\Delta_j$  are computed considering the three-phonon absorption ( $W^+$ ), emission ( $W^-$ ), and isotropic ( $W^I$ ) scattering rates as given in Eq. (2.39) and Eq. (2.40):

$$\Delta_j = \frac{1}{N} \sum_{\lambda'\lambda''}^+ W_{\lambda\lambda'\lambda''}^+ \left[ \frac{\omega''}{\omega} \mathbf{F}_{\lambda''} - \frac{\omega'}{\omega} \mathbf{F}_{\lambda'} \right] + \frac{1}{N} \sum_{\lambda'\lambda''}^- \frac{1}{2} W_{\lambda\lambda'\lambda''}^- \left[ \frac{\omega''}{\omega} \mathbf{F}_{\lambda''} + \frac{\omega'}{\omega} \mathbf{F}_{\lambda'} \right] + \frac{1}{N} \sum_{\lambda'} W_{\lambda\lambda'} \left[ \frac{\omega'}{\omega} \mathbf{F}_{\lambda'} \right] \quad (2.39)$$

$$\frac{1}{\tau_j^0} = \frac{1}{N} \left( \sum_{\lambda'\lambda''}^+ W_{\lambda\lambda'\lambda''}^+ + \sum_{\lambda'\lambda''}^- \frac{1}{2} W_{\lambda\lambda'\lambda''}^- + \sum_{\lambda'} W_{\lambda\lambda'}^I \right). \quad (2.40)$$

where  $\lambda, \lambda'$ , and  $\lambda''$  represent the phonon modes involved in the three-phonon scattering process.

The scattering rates are calculated using Fermi's golden rule<sup>64,93</sup>

$$W^x = \frac{2\pi}{\hbar} |\langle f | \Phi_3 | i \rangle|^2 \delta(E_f - E_i), \quad (2.41)$$

where  $x = +, -, \text{ or } I$ , and  $\Phi_3$  represents the third-order part of the interatomic potential.

The iterative calculation starts with a zeroth-order approximation,  $\mathbf{F}_j = \tau_j^0 \vec{\mathbf{v}}$ , *i.e.*, the value under CRTA. The calculation loop runs until the relative change in the conductivity tensor is less than a

considerable value (default is  $10^{-5}$ ). Usually, in systems with strong Umklapp scattering, the iterative method gives a less than 10% correction compared with the CRTA value. However, this can greatly impact high thermal conductive materials like diamond.

### 2.1.3.2 Electron transport properties

Electrical and thermal perturbations create electrical and thermal currents in metallic materials. The correlation between the generated electric current density along the  $\alpha$ -direction ( $\vec{J}_\alpha^E$ ) and the temperature gradient  $\nabla T$  along  $\beta$ -direction is given by<sup>94</sup>

$$\vec{J}_\alpha^E = \sigma_{\alpha\beta} \vec{E}_\beta - \sigma_{\alpha\gamma} S_{\gamma\beta} \nabla_\beta T. \quad (2.42)$$

Here  $\sigma_{\alpha\beta}$  denotes the electrical conductivity tensor,  $\vec{E}_\beta$  stands for the electric field, and  $S$  is the Seebeck coefficient which is the ratio of the voltage gradient to the temperature gradient when the electric current is zero.

Similar to the heat current due to phonons, it is possible to define the electric current associated with electrons ( $\vec{J}_\alpha^E$ ), as defined in Eq. (2.43),

$$\vec{J}_\alpha^E = e \sum_{n\vec{k}} f_{n\vec{k}} \vec{v}_{n\vec{k}}^\alpha, \quad (2.43)$$

where  $\vec{v}_{n\vec{k}}$  is the group velocity of the electrons with electron band index  $n$  and wave vector  $\vec{k}$ , and  $f_{n\vec{k}}$  is the distribution function of electrons.

Like the phonon distribution function, electron distribution depends on three processes; diffusion due to temperature gradients, scattering influenced by external electric ( $\vec{E}$ ) or magnetic ( $\vec{H}$ ) fields, and scatterings. Therefore, the rate of change of total distribution at the equilibrium can be expressed as:

$$\left. \frac{\partial f_{n\vec{k}}}{\partial t} \right|_{\text{diffusion}} + \left. \frac{\partial f_{n\vec{k}}}{\partial t} \right|_{\text{field}} + \left. \frac{\partial f_{n\vec{k}}}{\partial t} \right|_{\text{scattering}} = 0, \quad (2.44)$$

$$\left. \frac{\partial f_{n\bar{k}}}{\partial t} \right|_{\text{scattering}} = -\vec{v}_{n\bar{k}}^\alpha \cdot \frac{\partial f_{n\bar{k}}}{\partial \vec{r}_\alpha} + \frac{e}{\hbar} \left[ \vec{E}_\alpha + \frac{1}{c} (\vec{v}_{n\bar{k}} \times \vec{H})_\alpha \right] \cdot \frac{\partial f_{n\bar{k}}}{\partial \vec{k}_\alpha}. \quad (2.45)$$

In the absence of the magnetic field and within the limits of CRTA, one can obtain the linear BTE as

$$-\vec{v}_{n\bar{k}}^\alpha \cdot \frac{\partial f_{n\bar{k}}}{\partial T} \nabla T - e \vec{v}_{n\bar{k}}^\alpha \cdot \frac{\partial f_{n\bar{k}}}{\partial \varepsilon} \vec{E}_\alpha = \frac{f_{n\bar{k}} - f_0}{\tau_{e n\bar{k}}}, \quad (2.46)$$

where  $\tau_{e n\bar{k}}$  is the relaxation time of electrons due to electron-phonon scatterings.

By replacing the  $f_{n\bar{k}}$  in Eq. (2.43) from that in Eq. (2.46), one can define the electric conductivity tensor  $\sigma_{\alpha\beta}$  as

$$\sigma_{\alpha\beta} = \frac{e^2}{\Omega} \sum_{n,\bar{k}} \frac{\partial f_{n\bar{k}}}{\partial \varepsilon} \vec{v}_{n\bar{k}}^\alpha \cdot \vec{v}_{n\bar{k}}^\beta \tau_{e n\bar{k}}, \quad (2.47)$$

where  $\Omega$  is the crystal volume.

Once the electrical conductivity tensor is known, the electron contribution to the thermal conductivity ( $\kappa_e$ ) can be derived using the Wiedemann-Franz law<sup>95</sup> given in Eq. (2.48),

$$\kappa_e = \sigma L_0 T. \quad (2.48)$$

Here  $L_0$  is a constant known as the Lorenz number, and it is assumed here to be equal to the theoretical value of  $2.44 \times 10^{-8} \text{ W } \Omega \text{ K}^{-2}$ .

The BoltzTraP simulation package<sup>57</sup> provides the pathway to calculate the electric conductance within the constant relaxation time ( $\sigma/\tau_e$ ) approximation, and the EPW code<sup>58</sup> evaluates the temperature dependence of  $\tau_e$ , paving the way to estimate  $\kappa_e$  through Wiedemann-Franz law.

## 2.2 Experimental procedure

### 2.2.1 Powder sample preparation

Three types of fuel pellets, *i.e.*, pure  $U_3O_8$ ,  $U_3O_8$ -Al, and  $U_3O_8$ -Mo, with different volume compositions, are prepared. The respective weights of the raw powders needed to make each set of pellets are given in Table 2.1. The planetary ball mill apparatus (manufactured by Torrey Hills Technologies, USA) shown in Fig. 2.3 was utilized to mix the powders in order to make sure they are homogeneously spread. The powder of different compositions was loaded into the stainless-steel jar, along with stainless steel balls, keeping the ball to powder weight ratio at 10:1 and ethanol was added as the mixing aid media. Ethanol is non-reactive with  $U_3O_8$ , aluminum, or molybdenum and evaporates quickly at room temperature. Then the sealed jar was placed in the ball mill apparatus and milled for an hour with a rotating speed of 200 rpm (rounds per minute). After

**Table 2.1:** The weights of the starting powder materials used to prepare the specimens of pure  $U_3O_8$ ,  $U_3O_8$ -Al (with 10, 15 and 20 vol% of  $U_3O_8$  in Al) and  $U_3O_8$ -Mo (with 8.2 and 12.5 vol% of Mo in  $U_3O_8$ ). The weights are given in grams and total of 30 grams in each composition is prepared for ball milling.

Composition	Weight (gram)		
	$U_3O_8$	Al	Mo
Pure $U_3O_8$	30.00	-	-
10vol% $U_3O_8$ -Al	7.64	22.36	-
15vol% $U_3O_8$ -Al	10.55	19.45	-
20vol% $U_3O_8$ -Al	13.04	16.96	-
$U_3O_8$ -8.2vol%Mo	27.03	-	2.97
$U_3O_8$ -12.5vol%Mo	25.52	-	4.48

milling, the balls were removed, and the mixture solution was transferred to Petri dishes. After that, the powder mixtures were left in a fume hood to get dried before transferring them to sealable containers until the fabrication of the final pellets were done.



**Figure 2.3:** The planetary ball mill apparatus (Torrey Hills Technologies, USA) located at Department of Mechanical Engineering, University of Saskatchewan.

## 2.2.2 Sintering of the pellets

Spark plasma sintering (SPS), or pulsed electric current sintering (PECS), is a novel fabrication technique that can be utilized to solidify many types of powder materials. This technique uses a uniaxial force and a pulsed direct current with high heating and cooling rates to consolidate powder materials under a low-pressure close to atmospheric pressure<sup>96</sup>. There are many advantages of SPS over the other conventional sintering methods, especially the easy handling, the possibility of sintering high density pellets, short sintering time, and the low power consumption<sup>97</sup>. The application of SPS in nuclear fuel fabrication is already reported earlier. High-quality samples with high densification and good thermal conductivity were obtained for fuel candidates like  $\text{ThO}_2$ <sup>98,99</sup>,  $\text{ThO}_2\text{-SiC}$ <sup>100</sup>,  $\text{ThO}_2\text{-diamond}$ <sup>100</sup>,  $\text{UO}_2$ <sup>101-104</sup>,  $\text{UO}_2\text{-SiC}$ <sup>40,104</sup>,  $\text{UO}_2\text{-Mo}$ <sup>105,106</sup> and  $\text{UO}_2\text{-diamond}$ <sup>42,107</sup>.

All the samples investigated in this work were made using the Thermal Technology spark plasma sintering system (Fig. 2.4a) at the University of British Columbia, Canada. When sintering, the required portion (around 5 g, in this work) of each powder mixture is loaded into the graphite die-punch system and placed between hydraulic rams. Sintering of the powder is initiated and controlled by heating the die-punch system by simultaneous application of an electric current and pressure (Fig. 2.4b). The temperature, pressure, heating rate, and cooling rate of the samples were optimized to obtain high densification in the pellets. The sintered pellets were polished lightly using silica sheets and cleaned with alcohol to remove the graphite foil. After that, the samples were sealed until the characterization of structure and thermal conductivity measurements can be done.

(a)



(b)

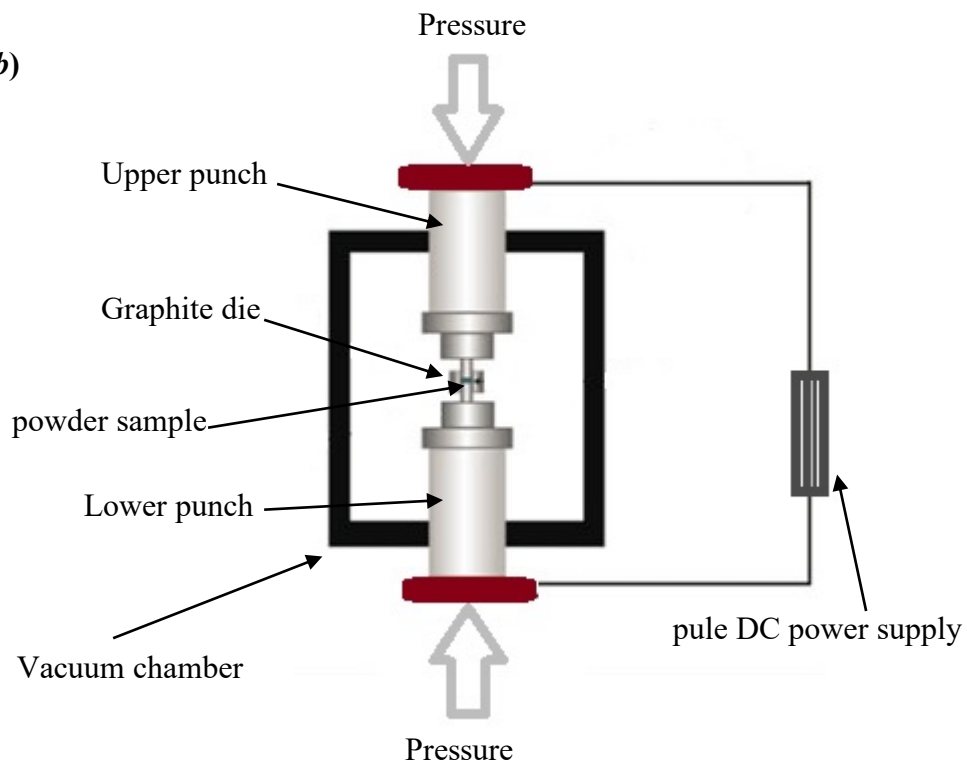


**Figure 2.4:** (a) Thermal Technology spark plasma sintering system located at university of British Columbia, Canada, and (b) Schematic diagram of Spark Plasma Sintering (SPS).

### 2.2.3 Density measurement of the sintered specimens

The densities of the sintered pellets ( $\rho_i$ ) were determined using the Torbal density measurement kit shown in Fig. 2.5. This approach is based on Archimedes' principle and is designed to evaluate densities of solid and liquid materials. The equation used to calculate the densities ( $\rho_i$ ) of the specimens is

$$\rho_i = \frac{W_{air}}{W_{air} - W_{water}}, \quad (2.49)$$

where  $W_{air}$  is the weight readings when the sample is placed on the upper pan, and  $W_{water}$  is the weight of the specimen when it is immersed in the water. The average of five measurements is taken as the final density for improving the accuracy of measurements.

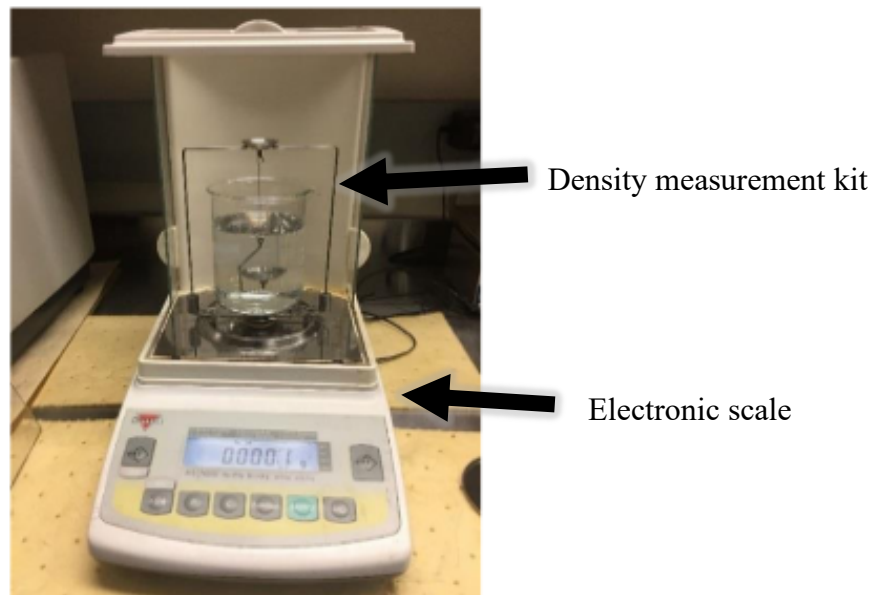


**Figure 2.5:** Torbal density measurement kit and the electronic scale used in the density measurements of the solid specimens.



## 2.2.4 X-ray diffraction

X-ray diffraction is an extensively used technique for identifying and characterizing virtually any type of single (powder) or polycrystalline material. It can be successfully employed to identify several crystalline properties, including the phase composition, orientation of grains, lattice parameters, and crystal structures. XRD technique extensively relies on the constructive interference of the elastically scattered electromagnetic waves (X-rays) by the electrons of the investigated sample. The X-rays are generated by the X-ray tube, and the monochromatic radiation characteristic for the used cathode is used in experiments. The X-rays interfere with the electrons of the atoms in the sample and generate diffraction maxima through constructive interference if Bragg's law given by Eq. (2.50) is satisfied:

$$2d\sin\theta = n\lambda_{XRD} \quad (2.50)$$

Here,  $d$ ,  $\theta$ ,  $n$ , and  $\lambda_{XRD}$  are respectively, the lattice space, incident angle of the radiation, diffraction order, and the wavelength of the radiation (Fig. 2.6).

This study employed the XRD scans to characterize the structure of powder and sintered samples using a Bruker D8 Discover X-ray diffractometer (Fig. 2.7) with chromium  $K_\alpha$  radiation ( $\lambda = 2.2898 \text{ \AA}$ ). All the scans were done from  $20^\circ$  to  $110^\circ$  angle with a step size of 0.01 and a speed of 600 seconds per step. Obtained diffraction spectra were analyzed using *X'Pert HighScore Plus* software tool to identify the main phases, and impurities in the samples.

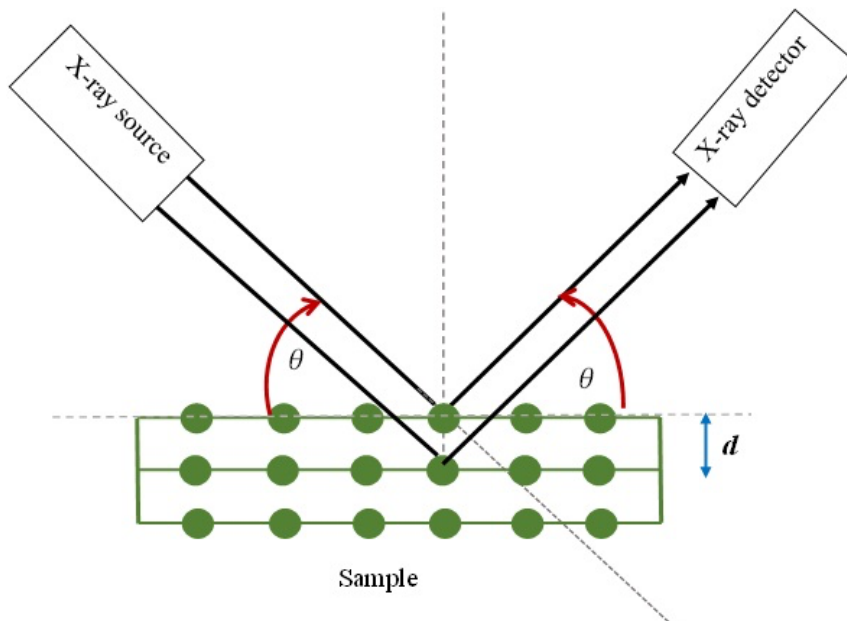


**Figure 2.6:** Schematic illustration of Bragg's law.

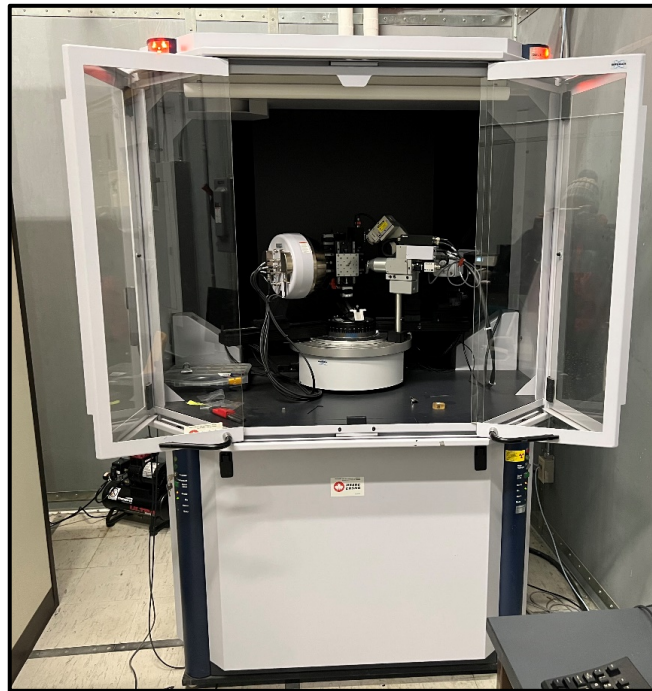


**Figure 2.7:** Bruker D8 Discover X-Ray diffractometer at Department of Mechanical Engineering, University of Saskatchewan.

### **2.2.5 Scanning electron microscopy and EDX**

Scanning electron microscopy (SEM) is a powerful technique to investigate a wide range of solid materials. It uses a focused electron beam to scan the surface of the specimen. When that primary beam strikes the sample's surface, it generates many signals through the Auger electrons (AE), emissions of secondary electrons (SE), backscattered electrons (BSE), X-rays, cathodoluminescence, specimen current, and transmitted electrons (see Fig. 2.8) providing different information about the specimen. SE is generated when the irradiated primary beam dislodges atomic electrons from the specimen's surface. Usually, they are used to obtain information about the topology of the sample's surface. Energy-dispersive X-ray spectroscopy (EDX) is used during SEM analysis to acquire additional information about the material composition. When irradiated by the primary electron beam, it can knock off electrons from the inner shells of atoms on the sample's surface. Those electron vacancies can then attract high-energy electrons from outer shells emitting their energy difference in the form of X-rays. These X-rays have specific information about the types of elements and their concentrations within the surface layer of the specimen. Hence, qualitative and quantitative analyses of the chemical information of the sample can be obtained. All the powder samples and the sintered pellets used in this work are analyzed using the SU 6600 Hitachi field emission SEM equipped with an EDX detector (Fig. 2.9), and the operating conditions are given in Chapter 3.

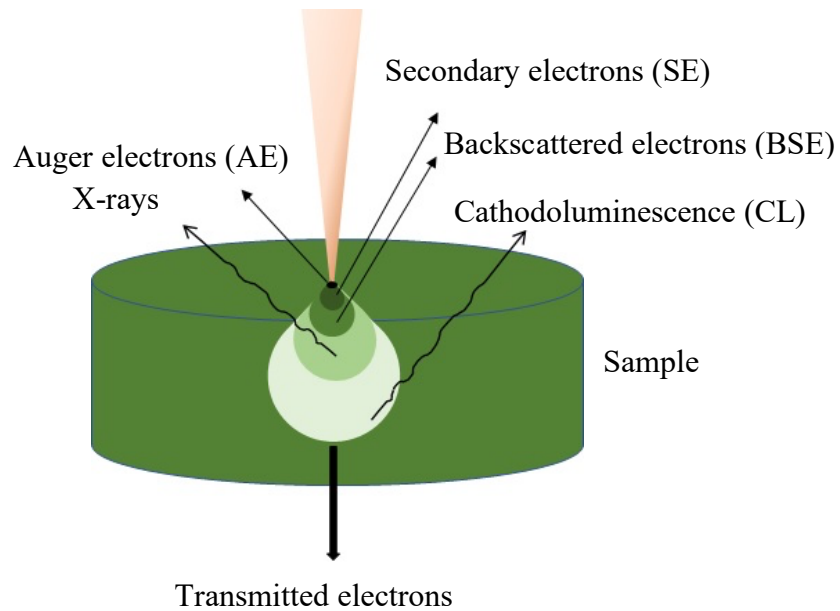


**Figure 2.8:** Different types of signals generated by electron irradiation in a Scanning Electron Microscope (SEM).



**Figure 2.9:** The SU-6600, Hitachi field emission SEM equipped with the Oxford Instruments Nordlys EDX detector located at Department of Mechanical Engineering, University of Saskatchewan.

## 2.2.6 Thermal conductivity measurement

Thermal conductivity and the thermal diffusivity of the sintered  $U_3O_8$ ,  $U_3O_8$ -Al, and  $U_3O_8$ -Mo pellets are measured using the discovery laser flash apparatus (DLF-1/EM-1300) in Fig. 2.10. In this instrument, the thermal conductivity is measured under a controlled atmosphere, and the sample needs to have a circular ( $\sim 12$  mm diameter) cross-section with up to 10 mm uniform thickness.

The prepared specimens are placed in the furnace and then irradiated with a very short laser pulse on its front surface (Fig.2.11). It causes a temperature rise in the front surface, and eventually, the heat is transferred to the rear surface of the specimen at a speed proportional to its thermal conductivity. The temperature raising data of the rear surface is recorded by an optical sensor with a very fast thermal response. The output data are used to evaluate the thermal diffusivity  $\alpha(T)$ , given by the Parkers relation in Eq. (2.51),

$$\alpha(T) = 0.1388 L^2/t_{1/2}, \quad (2.51)$$

where  $L$  is the thickness in meters, and  $t_{1/2}$  (in seconds) is when the rear surface temperature reaches 50% of its maximum value. Further, the specific heat  $C_p$  of materials can be calculated using

$$C_p(T) = \frac{Q}{m_{LF} \Delta T}, \quad (2.52)$$

where  $Q$  is the energy of the pulsed laser beam, which can be determined by comparing the maximum value of temperature rise with that of reference,  $m_{LF}$  is the mass of the specimen, and  $\Delta T$  is the maximum temperature rise. In the LF technique, evaluation of  $C_p(T)$  is done by the comparative method, comparing the maximum temperature rise in the sample to that of a known reference sample. Furthermore, both the reference and unknown samples are measured under the same conditions in a single run; hence the energy given to both the systems is the same. Then, the specific heat of the unknown sample ( $C_p(T)_S$ ) can be estimated by Eq. (2.53),

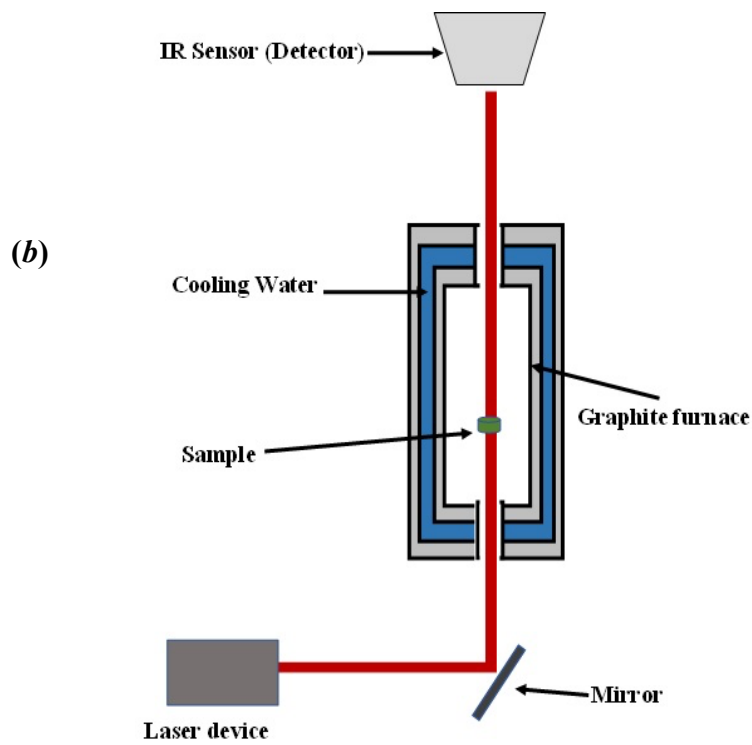


**Figure. 2.10:** (a) The discovery laser flash apparatus (DLF-1/EM-1300) used in the thermal conductivity measurements, and (b) Schematic diagram of the laser flash apparatus.

$$C_p(T)_S = \frac{C_p(T)_R \cdot m_R \cdot \Delta T_R}{m_S \Delta T_S}, \quad (2.53)$$

where  $R$  denotes the known reference sample, and  $S$  stands for the unknown system.

Finally, the thermal conductivity ( $\kappa$ ) is calculated using Eq. (2.54),

$$\kappa(T) = \rho(T) \cdot \alpha(T) \cdot C_p(T). \quad (2.54)$$

## Chapter 3

### **DFT and experimental study on the thermal conductivity of $U_3O_8$ and $U_3O_{8-X}$ ; (X=Al and Mo)**

This chapter presents and discusses the experimental and computational investigation of the thermal properties of  $U_3O_8$ . Thermal transport via lattice vibrations was predicted using first principles calculations unified with BTE. An extensive investigation of the phonon mode contribution on group velocity, mean free path, and scattering rates was revealed to disclose phonon transport's underlying mechanism in  $U_3O_8$ . The computational results were compared with the experimental measurement on pure  $U_3O_8$  samples prepared by the SPS technique. Thermal conductivity of  $U_3O_8$ -Al dispersion type fuels was evaluated using the high-dense samples prepared by SPS technique. Furthermore, the thermal conductivity enhancement in  $U_3O_8$  pellets with added Mo particles was demonstrated. In brief, this chapter accomplishes this project's first and second objectives by evaluating the thermal properties of  $U_3O_8$ ,  $U_3O_8$ -Al, and  $U_3O_8$ -Mo fuels.

The research findings described in this chapter have been published as follows:

Ranasinghe, J.I., Malakkal, L., Szpunar, B., Prasad, A., Jossou, E., Szpunar, J.A., Bichler, L., DFT and experimental study on the thermal conductivity of  $U_3O_8$  and  $U_3O_{8-X}$ ; (X=Al and Mo), *Journal of Nuclear Materials*, 549, (2021).

Section 3.2.2.3 (Density measurement) in the original publication is removed here as it is described in Sec. 2.2.3 with more details. Further, the Eqs. 3.1, 3.2, 3.3, and 3.4 in the original publication are removed as they are included and described in Sec. 2.26 in the current dissertation. The contribution of the Ph.D. candidate are as follows; (1) Preparation of the powder samples for SPS sintering, (2) Characterization of the powder samples and the sintered pellets using XRD, SEM, and EDX. (3) Measuring the thermal conductivities using laser flash technique, (4) Evaluation of the thermal properties of  $U_3O_8$  using computational methodologies along with Phonopy, ShengBTE, and QE simulation packages, (5) Analysis of the data, and (6) Writing the manuscript



for the Journal of Nuclear Materials. The coworkers and the supervisors reviewed the work before the publication.

# DFT and experimental study on the thermal conductivity of $U_3O_8$ and $U_3O_8-X$ ; (X=Al and Mo)

Jayangani. I. Ranasinghe<sup>a</sup>, Linu Malakkal<sup>b</sup>, Barbara Szpunar<sup>a</sup>, Anil Prasad<sup>c</sup>, Ericmoore Jossou<sup>b</sup>, Jerzy A. Szpunar<sup>b</sup>, and Lukas Bichler<sup>c</sup>

<sup>a</sup>Department of Physics and Engineering Physics, University of Saskatchewan, CA

<sup>b</sup>Department of Mechanical Engineering, University of Saskatchewan, CA

<sup>c</sup>School of Engineering University of British Columbia-Okanagan Kelowna, CA

## 3.0 Abstract

This article reports a theoretical and experimental investigation of the phonon thermal conductivity ( $\kappa_{ph}$ ) of  $\alpha-U_3O_8$  in the temperature range of 300 K to 1000 K. The theoretical calculations of the  $\kappa_{ph}$  were performed via the density functional theory (DFT) unified with the Boltzmann transport equation (BTE). An extensive investigation of the mode-wise scattering rate, group velocity ( $v_g$ ), and the Grüneisen parameters ( $\gamma$ ) were also conducted. The theoretically predicted values of the thermal conductivity of  $U_3O_8$  were compared by measuring the thermal conductivity using the transient method on samples sintered using the spark plasma sintering technique (SPS). In addition to the thermal properties of  $U_3O_8$ , an investigation on the effect of the addition of aluminum (Al) and molybdenum (Mo) is also reported. Our theoretical prediction corroborated the larger directional dependence of  $\kappa_{ph}$  in  $U_3O_8$ ; for example, at 300 K, they are 0.97, 0.67, and 3.05  $W m^{-1} K^{-1}$  along [100], [010], and [001] directions, respectively. The average value of  $U_3O_8$  decreases as a function of temperature from 1.57  $W m^{-1} K^{-1}$  at 300 K to 0.49  $W m^{-1} K^{-1}$  at 1000 K. The reason for the low thermal conductivity in  $U_3O_8$  has been explained by evaluating the mode-dependent scattering rates and  $\gamma$ . Also, the prediction of  $v_g$  corroborated the larger directional dependence of  $\kappa_{ph}$ . Finally, the effect of Al (with 15, 20, and 30vol% of  $U_3O_8$  in Al matrix) and Mo (with 8.2 and 12.5vol% of Mo in  $U_3O_8$ ) on the thermal conductivity of  $U_3O_8$  has been reported. At 300 K, thermal conductivities of  $U_3O_8$ -Al samples with 15, 20, and 30vol% of  $U_3O_8$  dispersions are 50.91, 33.79, and 16.53  $W m^{-1} K^{-1}$ , respectively. Moreover, the samples with 8.2 and 12.5vol% of Mo reported 59% and 104% respective thermal conductivity

enhancement at ~300 K. Ultimately, this work determined the possibility of sintering  $U_3O_8$  based nuclear fuels using SPS and demonstrated the thermal conductivity enhancement of  $U_3O_8$  with Al and Mo additives.

### 3.1 Introduction

Triuranium octaoxide,  $U_3O_8$ , is an essential material in the nuclear industry due to reasons such as its applicability as a research reactor fuel and a form of dry storage for spent nuclear fuels. Despite the importance, investigations on its thermal conductivity are sparse and limited to the experimental works reported by Pillai *et al.*<sup>37</sup>, Noda *et al.*<sup>39</sup>, Weisensee *et al.*<sup>108</sup>, and Schulz *et al.*<sup>109</sup>. Nevertheless, those studies have been conducted on relatively high-porous samples fabricated by conventional sintering techniques, and the data have been corrected for 100% theoretical (100%TD) values using different theoretical and experimental models. However, the accuracy of these corrected predictions depends on how well the sample specifications, such as the shape of the pores and the concentration, match the applied model's conditions. Producing a sample that fits a model is very difficult; hence these results will contain errors compared to the actual conductivity of 100%TD  $U_3O_8$ . It is well demonstrated that the first-principles calculations based on density functional theory (DFT) can be used to accurately predict the thermal conductivities of a vast range of materials, including ceramics and metals. Moreover, it can also be utilized to predict the thermal conductivity of materials with various conditions such as with (or without) impurities, defects, and boundary scattering. There are numerous first-principles investigations on nuclear fuels' thermal conductivity, such as  $UO_2$ <sup>110–112</sup>,  $ThO_2$ <sup>98,113,114</sup>,  $U_3Si_2$ <sup>115,116</sup>, and  $UN$ <sup>117</sup>, but to date, there are no reports on  $U_3O_8$ . In line with this thought, this work investigates the thermal conductivity and the fundamental mechanisms of thermal transport in high-quality, bulk, single-crystal  $U_3O_8$  in the low-temperature phase with orthorhombic structure ( $\alpha$ - $U_3O_8$ ), using first-principles methods. Several studies show that conventional methods like localized general approximation (LDA) or generalized gradient approximation (GGA) could not predict the correct electronic properties in many actinides oxides with a strongly correlated electronic configuration like  $\alpha$ - $U_3O_8$ ,<sup>118–121</sup>. However, it is a well-known fact that using DFT+U scheme or hybrid functional for lattice dynamic calculations for strongly correlated systems is

computationally very demanding. Besides, in this work on  $\alpha$ - $\text{U}_3\text{O}_8$ , the third-order and the second-order interatomic force constants (IFCs) evaluations using the DFT+U scheme were highly challenging due to convergence issues. Moreover, several previous works had accurately calculated the phonon dispersion relation, thermal transport, and the defect energies of several actinide oxides using LDA and GGA methodologies<sup>110,122–125</sup>. With this confidence, this work is performed using the LDA scheme without including the Hubbard-U.

Investigations on  $\text{U}_3\text{O}_8$ -Al dispersion fuels emerged with the Reduced Enrichment for Research and Test Reactors (RERTR) program, paving a way to increase the uranium density so that the target of low enriched uranium fuels (with less than 20% of  $\text{U}^{235}$ ) could be achieved. Since late 1950, several previous publications reported successful fabrication procedures for  $\text{U}_3\text{O}_8$ -Al dispersion fuels in commercial levels<sup>34,126–129</sup>. Oak Ridge National Laboratory (ORNL) has used a hot rolling method followed by cold pressing the ball-milled mixture of  $\text{U}_3\text{O}_8$  and aluminum powders to produce fuel plates with up to 39vol% (75wt%)  $\text{U}_3\text{O}_8$  loadings<sup>34,126</sup>. They also investigated the effects of the mechanical integrity against the irradiation performances with different oxide concentrations, fuel dimensions, and various preparation conditions of the fuel<sup>126</sup>. The developed fuels with 17vol% (35wt%) and 35vol% (55wt%) were used in several reactors. However, technical failures have occurred when  $\text{U}_3\text{O}_8$  loading exceeds 35vol% (55wt%)<sup>34</sup>. NUKEM (Federal Republic of Germany) has been involved in this project since late 1978 and has reported several methodologies<sup>127</sup>. More importantly, their initial step started from scratch by making  $\text{U}_3\text{O}_8$  from  $\text{UF}_6$  and then sintering the pellets at 1673 K achieving up to 2.2 U-g  $\text{cm}^{-3}$ . CERCA (France) reported the preparation procedure for up to 3.2 U-g. $\text{cm}^{-3}$  (60wt% of uranium) in the pellet<sup>127</sup>. In their method, starting  $\text{U}_3\text{O}_8$  was fabricated by calcinating  $\text{UO}_2$  powder and then sintered in the air at 1673 K<sup>127</sup>. Peacock *et al.*<sup>128</sup> reported the powder metallurgy process at SRL (Savannah River Laboratory) to achieve 12vol% (32wt%) to 39 vol% (75wt%) with less than 20vol% of voids. Despite the success of all these traditional methods, they have some limitations, such as long preparation time and high sintering temperature.

During the last two decades, the spark plasma sintering (SPS) technique gained industrial attention due to its advantages, such as the ability to consolidate both ceramic and metallic powders, rapid heating rates, low sintering temperatures, and short sintering time compared with conventional fabrication methods. Moreover, SPS enables the fabrication of microstructure with a smaller grain

size (compared to conventional sintering), resulting in improved mechanical strength and toughness of sintered pellets. Furthermore, the SPS technique provides a near-final-shape to the pellet, demanding less post-grinding work to achieve its final shape, which is highly appreciated in the nuclear industry as it reduces the problematic hazardous dust of radioactive materials. The SPS densification procedure for  $\text{UO}_2$  is presented by Ge *et al.*<sup>130</sup>, where they have achieved 96% of theoretical density (96TD%) in the sample sintered at 1323 K with only 30 s holding time. However, according to Timothy *et al.*<sup>131</sup>, industrial up-scaling of SPS requires further developments in the die-design configurations and tooling materials to facilitate large-scale production. Malakkal *et al.*<sup>98,99</sup>, reported a systematic study on the optimization of the sintering parameters to achieve 95TD% in  $\text{ThO}_2$  via SPS. Furthermore, the SPS technique has been utilized to successfully fabricate composite candidates of accident tolerant fuels, such as  $\text{UO}_2\text{-SiC}$ <sup>40,104</sup>,  $\text{UO}_2\text{-diamond}$ <sup>42,107</sup>,  $\text{UO}_2\text{-CNT}$ <sup>132,133</sup>,  $\text{UN-U}_3\text{Si}_2$ <sup>133</sup>, and  $\text{UN-ZrN}$ <sup>134</sup>. Nevertheless, the feasibility of this process for manufacturing mixed oxide fuels such as  $(\text{U-Pu})\text{O}_2$ <sup>135</sup> has been explored. However, its applicability to  $\text{U}_3\text{O}_8$  and  $\text{U}_3\text{O}_8\text{-Al}$  materials has not yet been explored to date. Therefore, this work applies the SPS process to fabricate pure  $\text{U}_3\text{O}_8$  and its dispersions in aluminum matrixes ( $\text{U}_3\text{O}_8\text{-Al}$ ) with different uranium concentrations. Furthermore, an experimental investigation of the thermal conductivities of the sintered samples was carried out via the laser flash (LF) technique. The results are compared with our DFT predictions and available previous experimental records.

One challenging property of  $\text{U}_3\text{O}_8$  preventing its applications as a power reactor fuel is its low thermal conductivity<sup>37,39,108</sup>. However, the limitation of the low thermal conductivity can be solved using modern advancement methodologies such as adding high thermal conductive additives. For example, one of our recent works reveals that a 56% increase in thermal conductivity of  $\text{ThO}_2$  can be achieved by adding 5vol% of SiC<sup>99</sup>. Fabrication of  $\text{U}_3\text{O}_8\text{-SiC}$  Cermet (Ceramics in a metallic matrix) fuels using the Polymer Infiltration and Pyrolysis (PIP) technique is already discussed and can be found in Singh *et al.*<sup>136</sup>. Molybdenum (Mo) is an attractive potential candidate as a secondary additive material mainly because of its high thermal conductivity, high melting point, and relatively low neutron cross-section<sup>137,138</sup>. Therefore, it is worth studying the thermal conductivity improvement in  $\text{U}_3\text{O}_8\text{-Mo}$  composites, which will benefit future fuel applications. With this view, our work focuses on the fabrication of  $\text{U}_3\text{O}_8\text{-Mo}$  composites with 8.2vol% and 12.5vol% Mo using SPS, and their thermal conductivity enhancement is investigated.

The paper is organized as follows. Section 3.2 gives the critical parameters used in the DFT calculation and the experimental methodology for SPS, sample characterization, and the thermal conductivity investigation. Next, section 3.3 presents and discusses our DFT results and the experimental observations on the thermal conductivity of  $U_3O_8$ ,  $U_3O_8$ -Al, and  $U_3O_8$ -Mo fuels prepared by SPS. Finally, the main findings of this work are summarized in section 3.4.

## 3.2 Methodology

### 3.2.1 Computational details

In this work, the structural optimization was carried out using the plane-wave pseudopotential technique implemented in the Quantum ESPRESSO<sup>60</sup> package. Norm-conserved pseudopotentials in the local density approximation (LDA) with Perdew-Zunger functional<sup>75</sup> were used to define the electrons' exchange-correlation interactions. Initial lattice parameters given by Loopstra *et al.*<sup>139</sup> were used for structural optimization. Total energy convergence is obtained with a plane wave cutoff energy of 140 Ry and  $8 \times 8 \times 13$  Monkhorst-Pack sampling ( $k$ -mesh) grid. For structural relaxation, the tolerance for forces on each atom was set less than  $10^{-10}$  meV.Å<sup>-1</sup> along with 1.63 eV smearing of the partial occupancies in the Methfessel-Paxton (mp) method. The calculation of the second and the third-order IFCs is required to solve the Boltzmann transport equation as they are the essential inputs for ShengBTE code<sup>56</sup>. As mentioned in the introduction, it is computationally expensive to include the Hubbard-U correction and the spin-orbit coupling because it involves many supercells (44 for the second- and 828 for the third-order IFCs) with a large number of atoms, and was challenging to converge the system. Therefore, no Hubbard-U corrections or the spin-orbit coupling were included in this work. The harmonic second-order IFC is constructed using 44 displaced-supercells originated from a  $2 \times 2 \times 2$  supercell with 88 atoms using Phonopy package<sup>59</sup>. The third order IFC is evaluated by considering up to the fourth nearest neighbor interaction to ensure that the results are well converged. Finally, the generated IFCs are used to solve the linearized Boltzmann-Transport equation (BTE) in the temperature range from 300 to 1000 K by using the ShengBTE code<sup>56</sup>.

## 3.2.2 Experimental procedure

### 3.2.2.1 Fabrication of the samples

$\alpha$ - $\text{U}_3\text{O}_8$  powder used in this work was supplied by Cameco, Canada, and Al (99.8% pure) and Mo (99% pure) powders were received from Sigma Aldrich with a purity greater than 99.9%. These powders were characterized using X-ray diffraction (XRD) with Cu  $K\alpha$  radiation, scanning electron microscopy (SEM), and Energy-dispersive X-ray spectroscopy (EDX). The SEM analysis confirmed that the particle sizes of  $\text{U}_3\text{O}_8$  powder range between 1-2.5  $\mu\text{m}$ , and it is, on average 40  $\mu\text{m}$  and 50  $\mu\text{m}$  for Al and Mo, respectively. As received  $\text{U}_3\text{O}_8$  powders were directly used to prepare pure  $\text{U}_3\text{O}_8$  pellets. Three sets of  $\text{U}_3\text{O}_8$ -Al mixtures (15vol%, 20vol%, and 30vol% of  $\text{U}_3\text{O}_8$  in aluminum) and two sets of  $\text{U}_3\text{O}_8$ -Mo mixed powders (8.2vol% and 12.5vol% of Mo in  $\text{U}_3\text{O}_8$ ) were prepared. Ball milling was used to ensure the mixture's homogenous distribution. It was conducted in a stainless-steel jar keeping the powder (in grams) to ball ratio 10:1 and using ethanol as the process control media. Each powder batch was milled for one hour with a speed of 200 rpm and then dried in a fume hood. Prepared powders were observed using XRD to confirm that no impurities were introduced during the ball milling process.  $\text{U}_3\text{O}_8$  powders and each set of dried powder mixtures were sintered in an argon atmosphere using the SPS system located at the University of British Columbia (Kelowna, BC). Approximately 5 g of each powder is filled in a graphite SPS die of internal diameter 12.7 mm to prepare ~3-5 mm thick cylindrical shape pellets. A thin layer of graphite foil (~0.125 mm) was used at the die wall and the punching interfaces to prevent the friction and interaction between the powder and the SPS tooling. The applied sintering conditions for the samples used in this work are listed in Table 3.1.

**Table 3.1:** Sintering conditions and the final densities, and the density as a percentage of the theoretical density (TD%) for the sintered samples with different U<sub>3</sub>O<sub>8</sub> concentrations.

Sample type	Composition	Temp. (K)	P (MPa)	Cooling rate (K min <sup>-1</sup> )	Heating rate (K min <sup>-1</sup> )	Holding time (min)	Density (g cm <sup>-3</sup> )	TD%
1 U <sub>3</sub> O <sub>8</sub>	100%U <sub>3</sub> O <sub>8</sub>	1000	60	100	100	0.5	8.13	97.8
2 U <sub>3</sub> O <sub>8</sub>	100%U <sub>3</sub> O <sub>8</sub>	900	50	200	100	5.0	7.90	94.1
3 U <sub>3</sub> O <sub>8</sub> -Al	30vol%U <sub>3</sub> O <sub>8</sub>	873	60	100	100	0.5	3.95	90.1
4 U <sub>3</sub> O <sub>8</sub> -Al	20vol%U <sub>3</sub> O <sub>8</sub>	873	60	100	100	0.5	3.58	93.5
5 U <sub>3</sub> O <sub>8</sub> -Al	15vol%U <sub>3</sub> O <sub>8</sub>	873	60	100	100	0.5	3.42	96.6
6 U <sub>3</sub> O <sub>8</sub> -Al	15vol%U <sub>3</sub> O <sub>8</sub>	723	60	100	100	5.0	3.25	91.7
7 U <sub>3</sub> O <sub>8</sub> -Mo	8.2vol%Mo	973	60	100	100	5.0	8.25	97.5
8 U <sub>3</sub> O <sub>8</sub> -Mo	12.5vol%Mo	973	60	100	100	5.0	8.35	97.8

### 3.2.2.2 Characterization of the pellets

As listed in Table 3.1, eight samples with different U<sub>3</sub>O<sub>8</sub> concentrations were used and each of these-received pellet was ground using silicon carbide (SiC) grit papers to remove the graphite foil and to make its surfaces flat and smooth. Then, the cleaned pellets were characterized using XRD, SEM, and EDS techniques. The XRD diffraction patterns of the as-received U<sub>3</sub>O<sub>8</sub> powders and the sintered pure U<sub>3</sub>O<sub>8</sub> samples are illustrated in Fig. 3.1a. The peaks in the spectra matched the orthorhombic phase of U<sub>3</sub>O<sub>8</sub>. Figure 3.1b and c compare the XRD patterns of the fabricated specimens of U<sub>3</sub>O<sub>8</sub>-Al and U<sub>3</sub>O<sub>8</sub>-Mo with their original powders. No additional characteristic peaks other than that of the starting powders (*i.e.*, U<sub>3</sub>O<sub>8</sub>, Mo, or Al) were present, demonstrating the absence of impurities or reaction products in the sintered pellets.



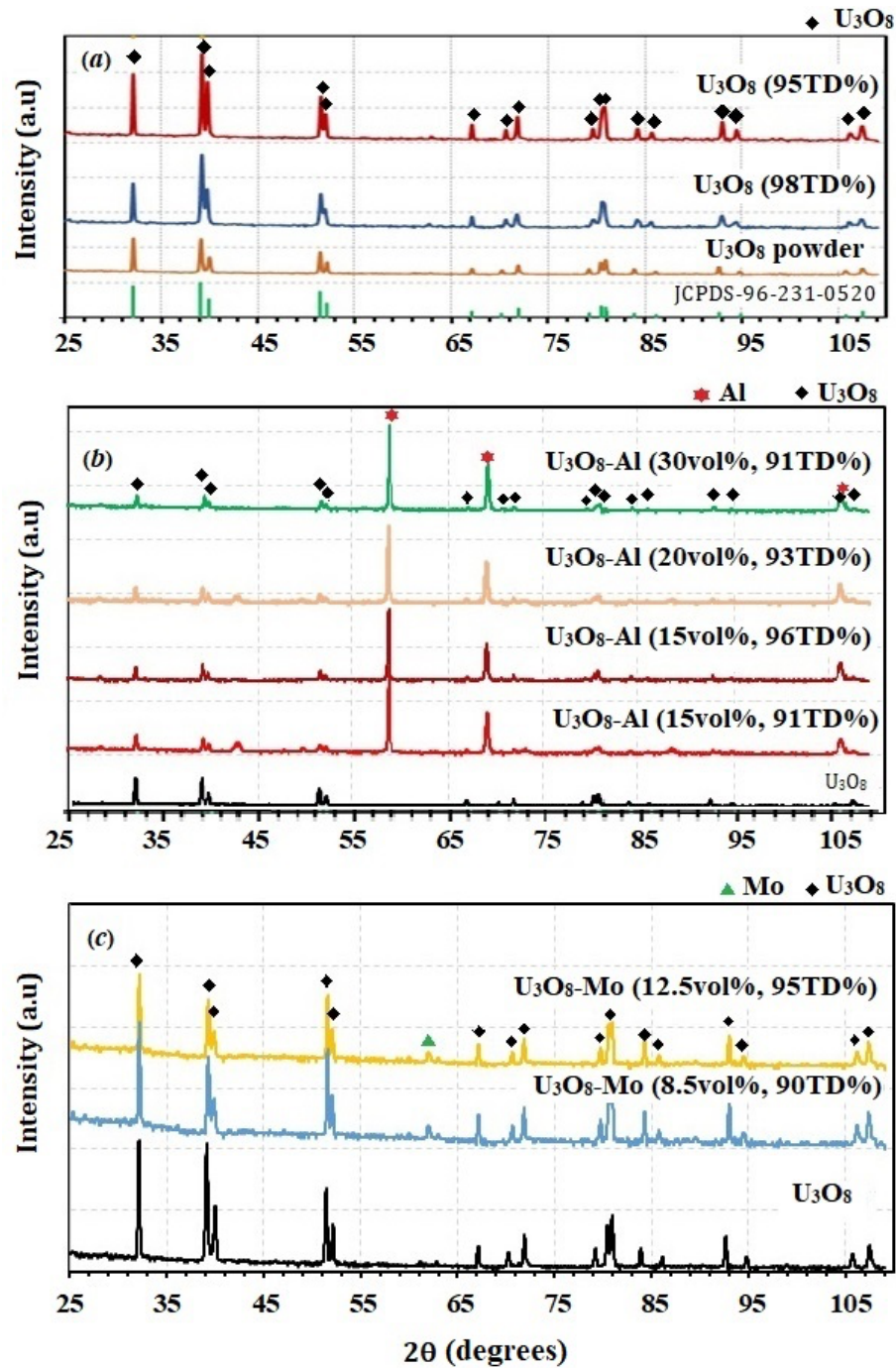


**Figure 3.1:** Powder XRD diffraction patterns of (a) pure  $U_3O_8$  (b)  $U_3O_8$ -Al and (c)  $U_3O_8$ -Mo samples prepared by SPS technique.

The micrographs, given in Fig. 3.2*a*, and *b* reveal the surface morphologies of the two pure  $U_3O_8$  pellets sintered at 900 K and 1000 K. Their densities were found to be 94.1TD% and 97.6 TD%. The morphology of the sample sintered at 900 K shows the densification as well as the formation of closed void structures, which is an intermediate step of sintering. The SEM micrograph of the pellet fabricated at 1000 K reveals that the grain growth has started. Additionally, only fewer voids are available indicating the high density of the sample. The typical distribution of  $U_3O_8$  particles within Al matrixes can be seen in Fig. 3.3*a*, *b*, *c*, and *d* where  $U_3O_8$  particles mostly form discontinuous channels (light grey areas) while large consolidations can be seen in some places. The channels in the samples with 15vol% and 20vol% of  $U_3O_8$  are found to be preferentially making Al islands (dark black areas) and formed along island-boundaries. The continuity and the thickness of the channels improve with increasing the  $U_3O_8$  concentration. Further, the images demonstrate an inhomogeneous distribution of  $U_3O_8$  particles within the fabricated pellets of  $U_3O_8$ -Al. This suggests that the aluminum is not homogeneously distributed within the precursor mixture. In contrast, the  $U_3O_8$ -Mo exhibits a more homogenous spread of Mo additives (dark black spots) across both the pellet with 8.2vol% Mo (Fig. 3.4*a*) and 12.5vol% Mo (Fig. 3.4*b*). Additionally, they do not show interconnection among Mo spots, rather in isolated and evenly distributed Mo particles.

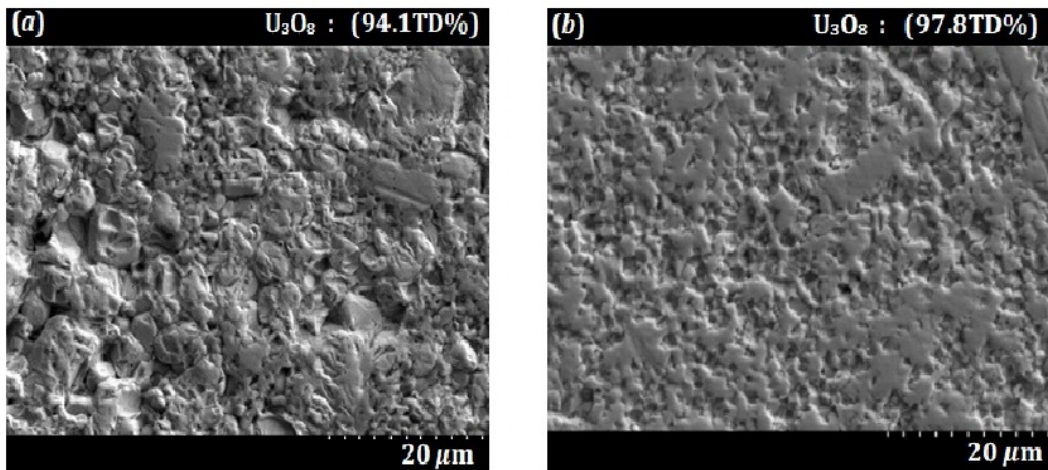


**Figure. 3.2:** The SEM micrographs of pure  $U_3O_8$  samples fabricated by SPS technique (*a*) at 900 K with 94.1TD% and (*b*) at 1000 K with 97.8TD%.

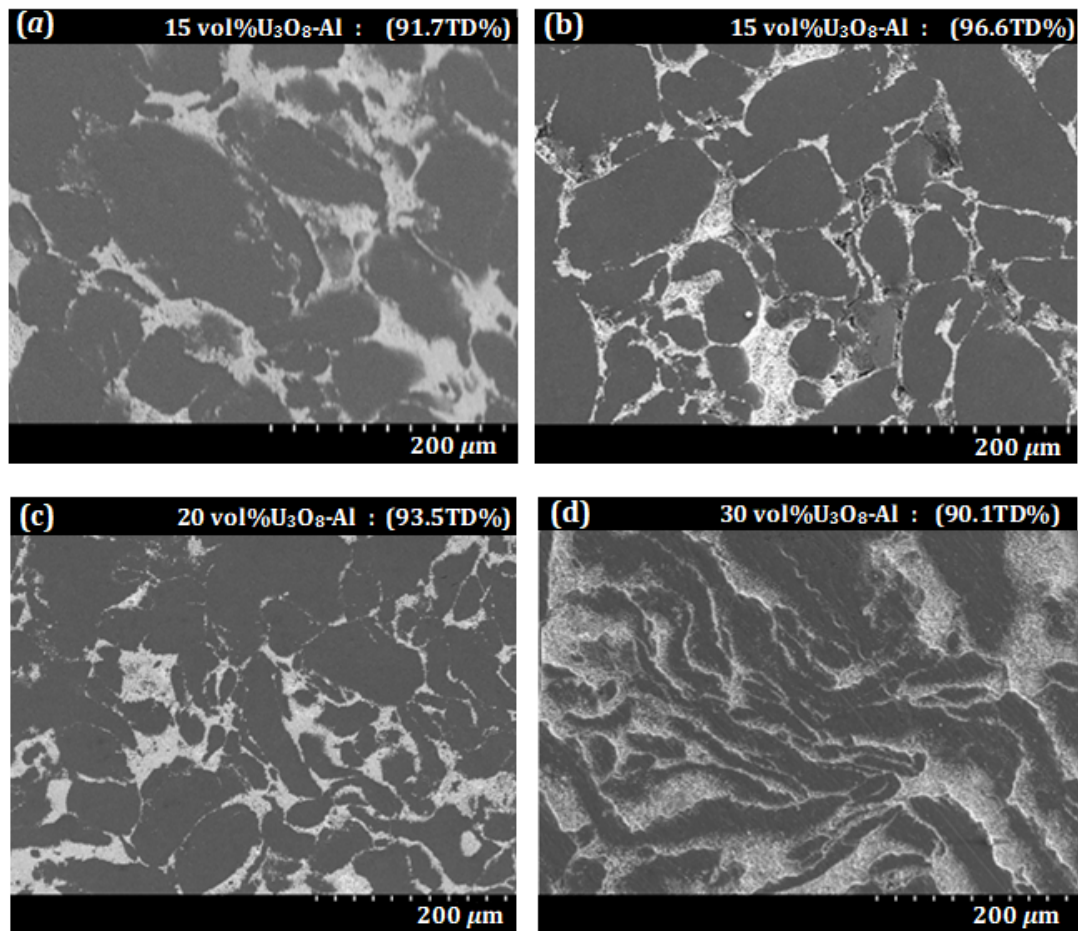


**Figure 3.3:** The SEM images of the pellets having (a) 15vol%U<sub>3</sub>O<sub>8</sub>-Al with 91.7TD% (b) 15vol%U<sub>3</sub>O<sub>8</sub>-Al with 96.6TD%, (c) 20vol%U<sub>3</sub>O<sub>8</sub>-Al with 93.5TD%, and (d) 30vol%U<sub>3</sub>O<sub>8</sub>-Al with 90.1TD%. The light grey areas correspond to theU<sub>3</sub>O<sub>8</sub> phase and dark regions are the aluminum.

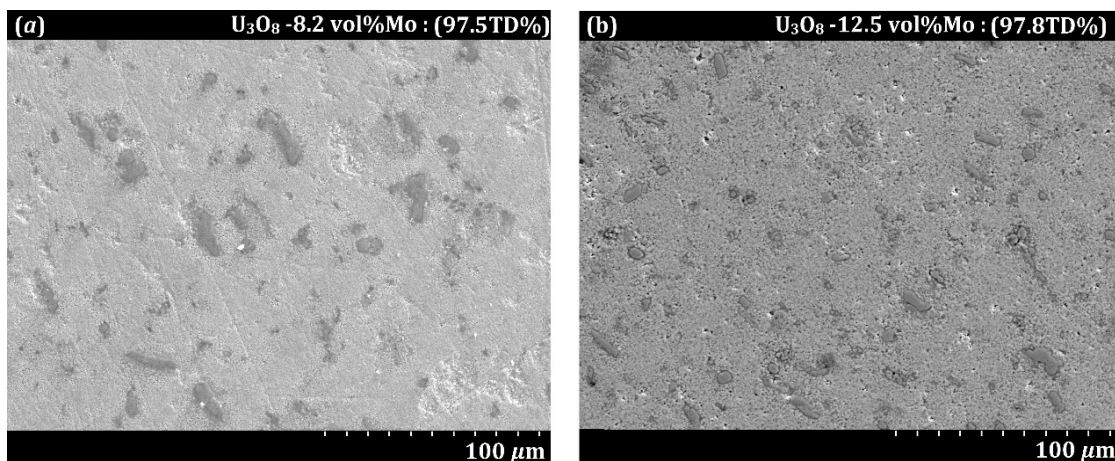


**Figure 3.4:** The SEM images of  $U_3O_8$ -Mo pellets of (a) 8.2vol% with 97.5TD% (b) 12.5vol% with 97.8TD%. The light grey areas are the  $U_3O_8$  phase, and the dark black are the Mo phase.

EDX images and the distribution maps give information on the constituent elements in a sample surface. Hence their locations can be used to analyze the particle distribution within the surface. The EDX analysis, conducted on the samples of  $U_3O_8$  (with 97.8TD%), 15vol% $U_3O_8$ -Al (with 96.6TD%), and  $U_3O_8$ -Mo with 12.5vol%Mo (with 97.8TD%), are given in Fig. 3.5, 3.6, and 3.7. The EDX spectrums (Fig. 3.5b, 3.6b, and 3.7b) did not detect any foreign particles except their original elements supporting the purity of the sintered pellets. The analysis of distribution maps in Fig. 3.6c, d, and e confirms that  $U_3O_8$  particles are in the discontinuous channels around aluminum island boundaries. Further, the uniform distribution of Mo particles within the  $U_3O_8$  matrix is shown in the EDX distribution maps, as given in Fig. 3.7c, d, and e.



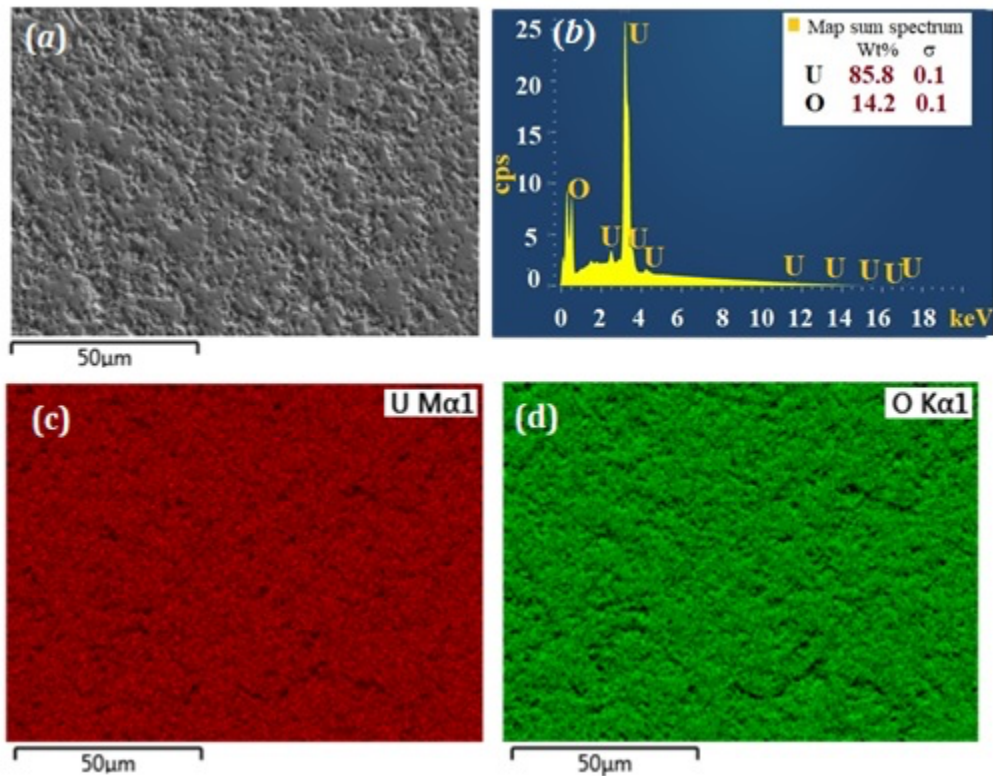


**Figure 3.5:** The EDX (a) micrograph, (b) spectrum showing the quantitative composition, and distribution maps of elements (c) uranium and (d) oxygen within the pure  $U_3O_8$  sample with 97.8 TD%.

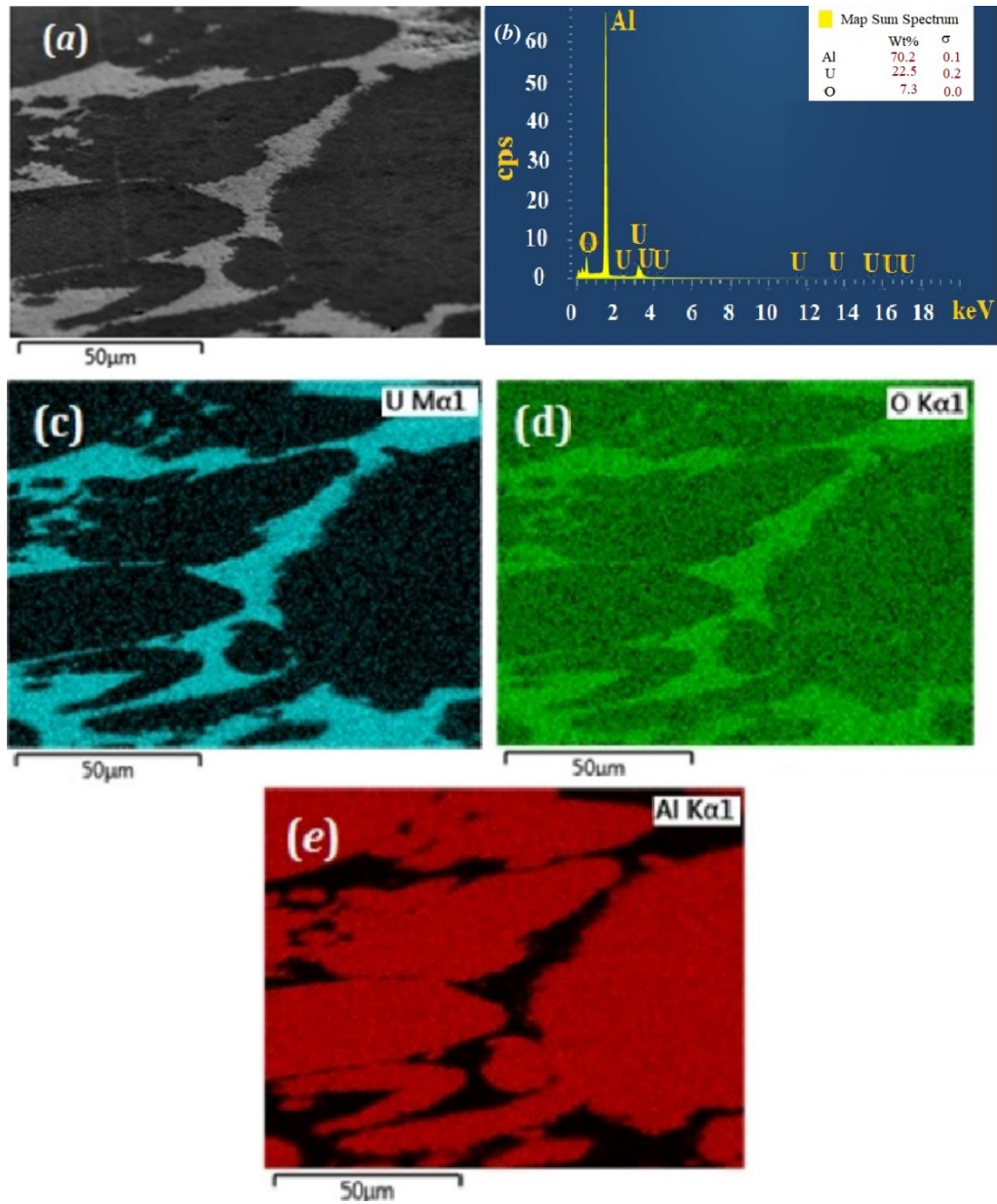


**Figure 3.6:** (a) EDX micrograph of 15vol%U<sub>3</sub>O<sub>8</sub>-Al pellet (96.6TD%), (b) EDX spectrum with the quantitative composition, and the distribution maps of the elemental composition (c) uranium, (d) oxygen and (e) aluminum.

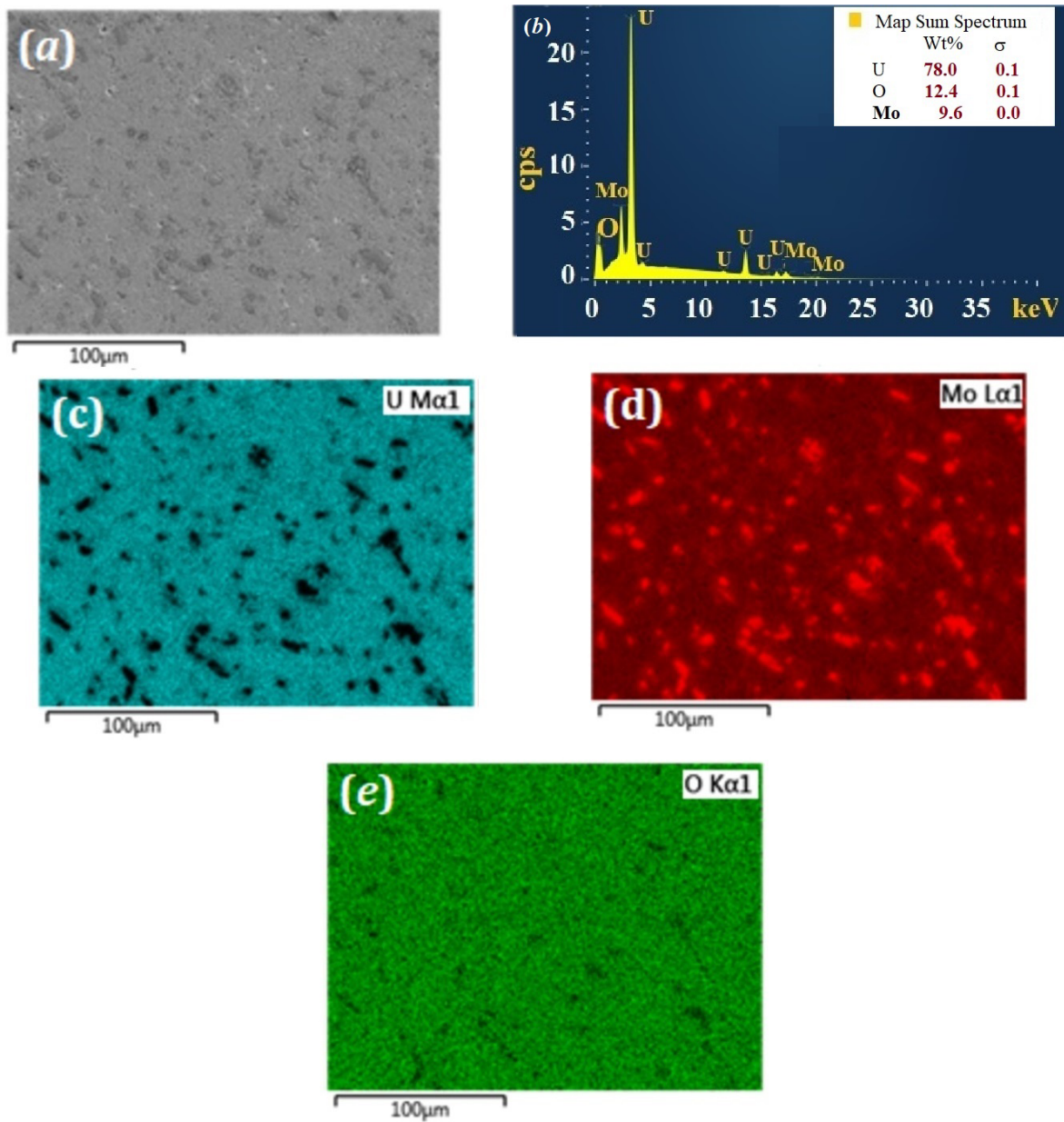


**Figure 3.7:** The EDX (a) micrograph, (b) spectrum showing the quantitative composition, and distribution maps of elements (c) uranium, (d) oxygen and (e) molybdenum within the  $U_3O_8$ -Mo sample with 12.5vol% Mo with 97.8TD%.

### 3.2.2.3 Thermal conductivity measurement

The thermal conductivity of a material can be evaluated as a function of temperature using the relation given in Eq. (2.55). In this work, the LF technique is used to evaluate  $\alpha$  and  $C_p$  of the prepared samples in the temperature range from 300 to 1000 K. Measured  $\alpha$  and  $C_p$ , along with the sample densities, were employed in Eq. (2.55) to evaluate the corresponding temperature-dependent thermal conductivities. The samples were finely polished to get flat and smooth surfaces. After that, the samples' top and bottom sides were coated with a thin layer of graphite to facilitate better absorption and emission of the LF. The measurements were conducted under the argon atmosphere. The system is vacuumed before sending the argon gas. The XRD diffraction patterns of each of the samples are observed after the experiment to confirm that no chemical reactions or composition changes occurred during the thermal conductivity measurement. The methodology for evaluating  $\alpha$  and  $C_p$  in the LF technique is described below.

In this technique, the temperature-dependent diffusivities were evaluated using the Parkers relations as given in Eq. (2.52), and for  $C_p$ , Eq. (2.53) was employed. The required thicknesses for  $\alpha(T)$  measurements were taken as an average of five measurements, and their standard deviations were within 0.01 mm. However, the density variation due to the thermal expansion during the temperature range considered for this work is negligible ( $\sim 1.08\%$ )<sup>140</sup> in  $U_3O_8$ ; hence has not been considered.

## 3.3 Results and Discussion

### 3.3.1 Structural and mechanical properties of U3O8

Table 3.2. summarizes the optimized lattice constants for  $\alpha$ - $U_3O_8$  along with available experimental and theoretical results. Our predictions overestimate  $a$  and  $c$  respectively by  $\sim 6$  and  $3\%$ , and underestimate  $b$  by  $\sim 2\%$  compared with the experimental values. It is a well-known fact that the LDA usually underpredicts the lattice parameters due to over binding the system. However, with the limitations of the current work due to the assumptions of disregarding the magnetic state and discounting the coulomb corrections for strongly correlated electrons, the



overall agreement of our structural parameters with earlier experimental observations and theoretical predictions is acceptable.

Elastic constants ( $C_{ij}$ ) provide valuable information on the mechanical properties and mechanical stability of materials. In this work, the elastic constants of  $\alpha$ - $U_3O_8$  are estimated according to the stress-strain method<sup>141,142</sup> using the optimized structural parameters. The predicted 9 independent parameters, analogous to the orthorhombic structure, are presented in Table 3.3. It is found that our predictions fulfill the stability conditions specified by Born criteria<sup>143</sup>, demonstrating the mechanical stability of the structure. Previous records on mechanical properties of  $\alpha$ - $U_3O_8$  are limited to the DFT work done by Brincat *et al.*<sup>144</sup>, which has been done using the finite displacement method. They have conducted GGA and GGA+U calculations concerning two space groups (namely,  $Cmmm$  and  $Amm2$ ) of  $\alpha$ - $U_3O_8$  and have achieved somewhat different values compared with the current work. The acceptability of their predictions on the  $Amm2$  space group is questionable because of the imaginary vibrational frequencies in their optimized structure. Besides, the observed deviation from the calculation done on the  $Cmmm$  space group is not surprising due to the methodological differences added to the structural inequality.

**Table 3.2:** Optimized lattice parameters (in Å) of the orthorhombic phase of  $U_3O_8$  with nonmagnetic (NM) and spin-polarized (SP) conditions. The literature works of Yun *et al.*<sup>119</sup> and Brincat *et al.*<sup>144</sup>, have conducted with Ferromagnetic (FM) conditions while Wen *et al.*<sup>120</sup> used an antiferromagnetic (AFM) structure.

	LDA NM (SP)	GGA+U+SOC FM	GGA AFM	GGA+U AFM	HSE	GGA	GGA + U FM	GGA+U	Exp.
<i>a</i>	7.14	7.20	6.82	6.83	6.65	7.22	6.60	7.22	6.72
<i>b</i>	11.74	11.61	11.87	12.12	11.86	11.60	13.06	11.59	11.97
<i>c</i>	4.27	4.21	4.16	4.20	4.09	4.21	4.24	4.20	4.15
Space group	<i>Amm2</i>	<i>C2mm</i>	<i>C2mm</i>			<i>Amm2</i>	<i>Cmmm</i>		
Reference	This work	119	120			144			139

**Table 3.3:** Elastic constants ( $C_{ij}$ ) of  $\alpha$ - $\text{U}_3\text{O}_8$  (in GPa).

	Method	$C_{11}$	$C_{12}$	$C_{13}$	$C_{22}$	$C_{23}$	$C_{33}$	$C_{44}$	$C_{55}$	$C_{66}$
This work	LDA	376.4	198.7	31.0	329.9	27.8	546.6	22.2	24.2	15.6
<i>Amm2</i>										
Brincat <i>et al.</i> <sup>144</sup>										
<i>Cmmm</i>	GGA+U	268.0	142.2	29.2	386.3	38.6	505.9	35.7	34.3	26.3
<i>Amm2</i>	GGA+U	505.3	42.5	26.9	373.9	139.9	258.2	31.8	34.4	25.7
	GGA	523.4	27.8	30.2	245.4	198.2	248.4	32.1	31.3	33.4

The bulk ( $B$ ) and the shear ( $S$ ) moduli can be derived according to the Voigt<sup>145</sup>, Reuss<sup>146</sup> and Hill<sup>147</sup> approximations using the equations through (3.1) to (3.6):

$$B_V = \frac{1}{9}(C_{11} + C_{22} + C_{33}) + \frac{2}{9}(C_{12} + C_{13} + C_{23}) \quad (3.1)$$

$$B_R = \frac{1}{[(S_{11}+S_{22}+S_{33})+2(S_{12}+S_{13}+S_{23})]} \quad (3.2)$$

$$S_V = \frac{1}{15}(C_{11} + C_{22} + C_{33} - C_{12} - C_{13} - C_{23}) + \frac{1}{5}(C_{44} + C_{55} + C_{66}) \quad (3.3)$$

$$S_R = \frac{15}{4(S_{11}+S_{22}+S_{33})-4(S_{12}+S_{13}+S_{23})+3(S_{44}+S_{55}+S_{66})} \quad (3.4)$$

$$B_H = \frac{1}{2}(B_V + B_R) \quad (3.5)$$

$$B_H = \frac{1}{2}(S_V + S_R), \quad (3.6)$$

where  $R$ ,  $V$ , and  $H$  in each equation represent Voigt, Reuss, and Hill approximations, and  $S_{ij}$  is the inverse matrix of the elastic constant matrix, which is defined from Eq. (3.7) to (3.15):

$$S_{11} = (C_{22}C_{33} - C_{23}^2)/(C_{11}C_{22}C_{33} + 2C_{12}C_{13}C_{23} - C_{11}C_{23}^2 - C_{22}C_{13}^2 - C_{33}C_{12}^2) \quad (3.7)$$

$$S_{12} = (C_{13}C_{23} - C_{12}C_{33}) / (C_{11}C_{22}C_{33} + 2C_{12}C_{13}C_{23} - C_{11}C_{23}^2 - C_{22}C_{13}^2 - C_{33}C_{12}^2) \quad (3.8)$$

$$S_{13} = (C_{12}C_{23} - C_{22}C_{13}) / (C_{11}C_{22}C_{33} + 2C_{12}C_{13}C_{23} - C_{11}C_{23}^2 - C_{22}C_{13}^2 - C_{33}C_{12}^2) \quad (3.9)$$

$$S_{22} = (C_{11}C_{33} - C_{13}^2) / (C_{11}C_{22}C_{33} + 2C_{12}C_{13}C_{23} - C_{11}C_{23}^2 - C_{22}C_{13}^2 - C_{33}C_{12}^2) \quad (3.10)$$

$$S_{23} = (C_{12}C_{13} - C_{11}C_{23}) / (C_{11}C_{22}C_{33} + 2C_{12}C_{13}C_{23} - C_{11}C_{23}^2 - C_{22}C_{13}^2 - C_{33}C_{12}^2) \quad (3.11)$$

$$S_{33} = (C_{11}C_{22} - C_{12}^2) / (C_{11}C_{22}C_{33} + 2C_{12}C_{13}C_{23} - C_{11}C_{23}^2 - C_{22}C_{13}^2 - C_{33}C_{12}^2) \quad (3.12)$$

$$S_{44} = \frac{1}{c_{44}} \quad (3.13)$$

$$S_{55} = \frac{1}{c_{55}} \quad (3.14)$$

$$S_{66} = \frac{1}{c_{66}}. \quad (3.15)$$

Estimated  $B_X$  and  $S_X$  ( $X = V, R,$  and  $H$ ) are employed to derive Young's modulus ( $Y_X$ ), Poison's ratio ( $\nu_X$ ), and the Debye temperature ( $\theta$ ) using the expressions given from Eq. (3.16) to (3.18):

$$Y_X = 9 B_X S_X / (S_X + 3B_X) \quad (3.16)$$

$$\nu_X = (3B_X - 2S_X) / 2(3B_X + S_X) \quad (3.17)$$

$$\theta_X = \frac{h}{k} \left[ \frac{3nN\rho}{4\pi M} \right]^{\frac{1}{3}} v_X^m, \quad (3.18)$$

where  $v_X^m$  is the average sound velocity defined by Eq. (3.19),

$$v_X^m = \left[ 3 / \left( \frac{2}{v_s^3} + \frac{1}{v_l^3} \right) \right]^{1/3}. \quad (3.19)$$

Here  $v_s$  and  $v_l$  are the shear sound velocity  $v_s = \sqrt{S_X/\rho}$ , and the longitudinal sound velocity  $v_l = \sqrt{(3B_X + 4S_X)/3\rho}$  respectively.

**Table 3.4:** Calculated bulk modulus ( $B_X$ ), shear modulus ( $S_X$ ), Young's modulus ( $Y_X$ ) (in GPa), Poisson ratio ( $\nu_X$ ), and the Debye temperature ( $\theta$ ) (in K) of  $\alpha$ -U<sub>3</sub>O<sub>8</sub>. The subscript  $X$  denotes the Voigt<sup>146</sup> ( $V$ ), Reuss<sup>146</sup> ( $R$ ) and Hill<sup>147</sup> ( $H$ ) approximations.

Space group	<i>Amm2</i>	<i>Cmmm</i>	<i>Amm2</i>	<i>Amm2</i>
Methodology	LDA	GGA+U	GGA+U	GGA+U
Ref.	This work	Brincat <i>et al.</i> <sup>144</sup>	Brincat <i>et al.</i> <sup>144</sup>	Brincat <i>et al.</i> <sup>144</sup>
$B_V$	57.22	46.7	56.9	46.5
$B_R$	195.43	169.4	168.1	165.8
$B_H$	126.33	108.0	112.5	106.1
$S_V$	96.75	82.6	70.1	80.3
$S_R$	44.29	45.0	36.1	43.1
$S_H$	70.52	63.8	53.1	61.7
$Y_V$	185.63	155.9	149.1	152.8
$Y_R$	123.55	124.1	101.0	119.1
$Y_H$	178.37	160.0	137.6	155.1
$\nu_V$	-0.04	-0.05	0.06	-0.05
$\nu_R$	0.39	0.34	0.40	0.38
$\nu_H$	0.26	0.25	0.30	0.26
$\theta_V$	441.71	407.4	379.0	402.1
$\theta_R$	312.74	314.7	282.5	308.0
$\theta_H$	387.95	368.6	337.9	362.5

Calculated  $B, S, Y, \nu$ , and  $\theta$  parameters of  $\alpha$ -U<sub>3</sub>O<sub>8</sub> according to Voigt, Reuss, and Hill approximations are summarized in Table 3.4. It needs to mention here that, Brincat *et al.*<sup>144</sup> has provided the aforementioned parameters only based on the Reuss approximation and the other values given in the table are derived using their elastic constants listed in Table 3.3. The given Voigt and Reuss approximations represent the upper and lower bounds of  $B, S, Y, \nu$ , and  $\theta$  parameters, while the Hill estimate corresponds to the mean value. As it is clear from Table 3.4, the predictions from our LDA calculation based on each of the three approximations are found to compare very favorably with the literature. Moreover, our calculation on  $\theta$  is in good agreement with the value estimated using an empirical method by Pillai *et al.*<sup>37</sup> (395 K).

### 3.3.2 Lattice dynamics

Figure 3.8a represents the calculated phonon dispersions of  $\alpha$ -U<sub>3</sub>O<sub>8</sub> at 0 K temperature, and Fig. 3.8b shows the corresponding phonon density of states (pDOS) together with the partial pDOS of U and O atoms. Because of the 11-atomic unit cell, there are 33 vibrational branches, of which, 3 are acoustic and the other 30 are optical phonons. As it is clear from the figure, the dispersion relation does not have any imaginary vibrational frequencies indicating the dynamical stability of the optimized structure. Moreover, there is a small gap of 1.03 THz (34.36 cm<sup>-1</sup>) between the low- and high-frequency optical modes starting from 9.91 THz. Nevertheless, the high-frequency optical modes, above 10.94 THz, are mainly generated by oxygen vibrations and they exhibit relatively steep slopes in low-frequency modes indicating large group velocities. In most of the solids, acoustic modes dominate the thermal transport having high dispersions. However, in this case, the low-frequency optical modes interact with the acoustic channels suppressing their dispersions and eventually reducing the ability to transport heat.

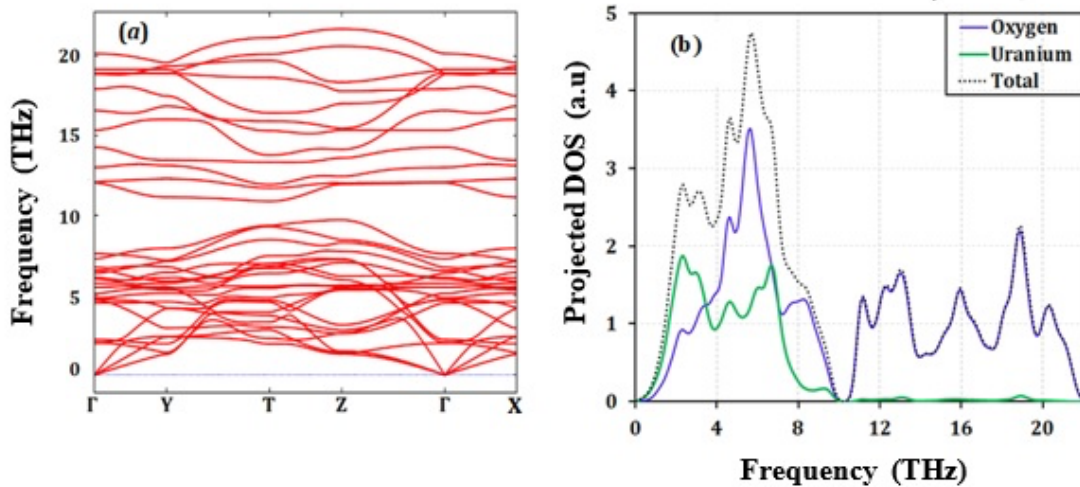


**Figure 3.8:** (a) Phonon band structure along the first Brillouin zone, and (b) the projected phonon density of states, of  $\alpha$ -U<sub>3</sub>O<sub>8</sub>.

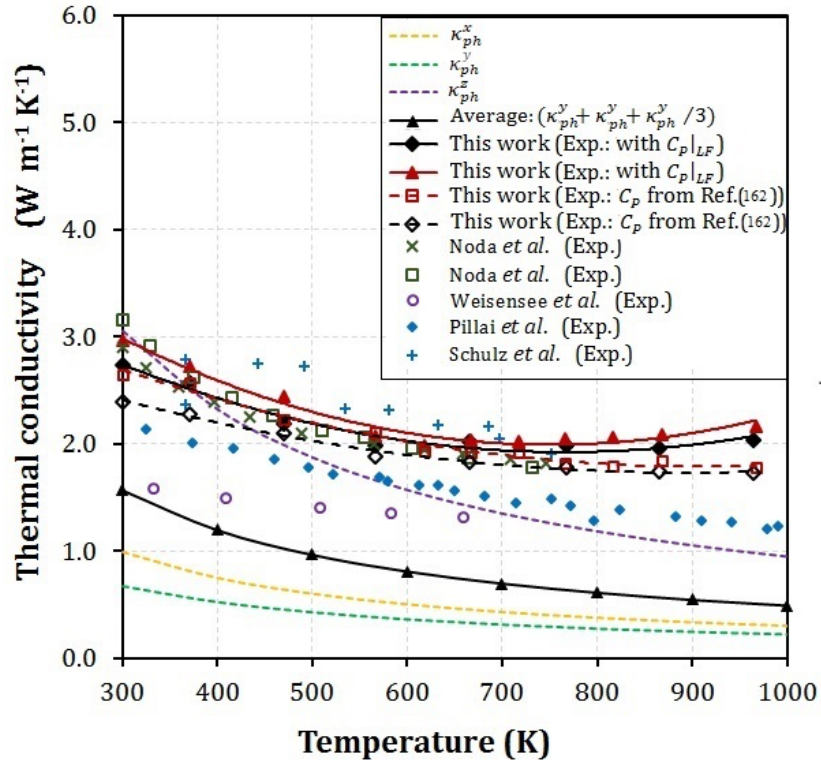


**Figure 3.9:** Temperature dependent thermal conductivity of pure  $U_3O_8$ . The yellow, green, and purple dashed lines show the DFT predictions on [100], [010], and [001] directions, and they are labeled as  $\kappa_{ph}^x$ ,  $\kappa_{ph}^y$  and  $\kappa_{ph}^z$ . Black solid line with solid triangles represents the average of them. The red solid triangles and black solid diamonds are the measured thermal conductivities of the respective 97.8TD% and 94.1TD% samples after the porosity correction. The corresponding open markers shows the respective thermal conductivities when the specific heat is taken from Ref. 156.

### 3.3.3 Anisotropic thermal conductivity of U<sub>3</sub>O<sub>8</sub>

The calculated lattice thermal conductivities ( $\kappa_{ph}$ ) of a perfect, defect-free crystal of  $\alpha$ -U<sub>3</sub>O<sub>8</sub> along [100], [010] and [001] directions (*i.e.*,  $\kappa_{ph}^x$ ,  $\kappa_{ph}^y$  and  $\kappa_{ph}^z$  respectively) and their averages  $\left(\frac{\kappa_{ph}^x + \kappa_{ph}^y + \kappa_{ph}^z}{3}\right)$  up to 1000 K are shown in Fig. 3.9. As it is clear from the figure, the calculated average thermal conductivity decreases monotonically from 1.57 W m<sup>-1</sup> K<sup>-1</sup> to 0.49 W m<sup>-1</sup> K<sup>-1</sup> when the temperature goes from 300 to 1000 K. Moreover, the results predict a strong anisotropy in thermal transport in the three crystal directions, which shows  $\kappa_{ph}^z > \kappa_{ph}^x > \kappa_{ph}^y$  relation. At 300 K,  $\kappa_{ph}^z$  (3.05 W m<sup>-1</sup> K<sup>-1</sup>) is over four times larger than  $\kappa_{ph}^y$  (0.67 W m<sup>-1</sup> K<sup>-1</sup>) and approximately three times as of  $\kappa_{ph}^x$  (0.97 W m<sup>-1</sup> K<sup>-1</sup>). This strength of the anisotropy persists almost the same throughout the entire temperature range considered in this work, showing the typical  $\kappa_{ph} \propto \frac{1}{T}$  behaviour.

To validate our theoretical predictions, calculated  $\kappa_{ph}^x$ ,  $\kappa_{ph}^y$ ,  $\kappa_{ph}^z$  and their average values were compared with the measured thermal conductivities of the pure U<sub>3</sub>O<sub>8</sub> samples with 97.8TD% and 94.1TD% which were sintered using the SPS technique. Since the sintered samples are porous, the measured values were corrected to zero porosity using the analytical model proposed by Schulz *et al.*<sup>148</sup> described by

$$\kappa_{100TD\%} = \kappa_{exp} (1 - P)^{-3/2}, \quad (3.20)$$

where  $\kappa_{100TD\%}$  and  $\kappa_{exp}$  are the respective corrected and the measured thermal conductivities, and  $P$  is the porosity volume fraction. The validity of the above model on nuclear fuels with dilute and random dispersions ( $P < 0.12$ ) is well discussed in several previous works<sup>37,148,149</sup>. The recalculated thermal conductivities and the available previous experimental data<sup>37,39,108,109</sup> are presented in Fig. 3.9. The red solid triangles and the black solid diamonds represent the zero porosity values of the measured thermal conductivities of 97.8TD% and 94.1TD% samples, respectively. All the literature data, except for Weisensee *et al.*<sup>108</sup>, have been recalculated for 100TD% using either Eq. (3.20) or modified Leob equation<sup>148</sup> ( $\kappa_{100TD\%} = \kappa_{exp} (1 - P)^{-1}$ ) depending on the porosity amount in the sample. The respective porosity volume fractions of the

samples in Pillai *et al.*<sup>37</sup> and in Noda *et al.*<sup>39</sup> were 0.11 and 0.87, hence, the same model given in Eq. (3.20) was employed. Whereas, the modified Leob equation is applied to correct the thermal conductivities observed in Schulz *et al.*<sup>109</sup> due to the high porosity found in their sample ( $P=34\%$ ). The data from Weisensee *et al.*<sup>108</sup> are not adjusted since no porosity information could be found.

As shown in Fig. 3.9, our experimental measurements agree well with the available literature works, except with Weisensee *et al.*<sup>108</sup> which has reported slightly lower values compared to ours as well as for all the other works. However, with lack of information on the sample (*i.e.*, porosity or density), it is hard to guess the underline reason for this deviation.

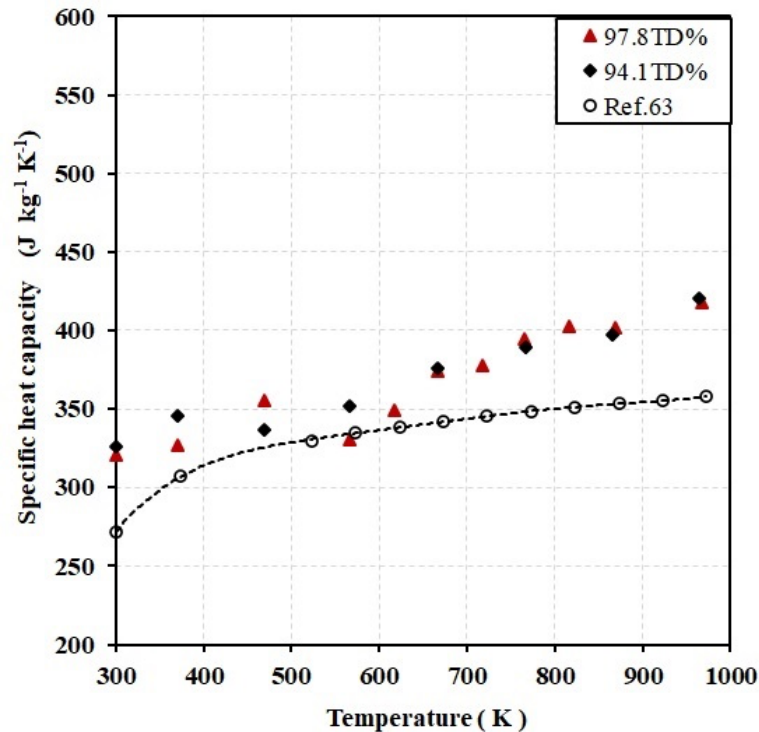


**Figure 3.10:** Specific heat capacity of  $U_3O_8$  samples with 97.8TD% (red solid triangles) and 94.1TD% (black solid diamonds) measured using laser flash technique and according to Ref. 156 (open black circles).



An important indication observed from our experiment is, it shows an increasing trend in the thermal conductivity arises within the temperature range  $\sim 450\text{-}550$  K, which is near the orthorhombic-hexagonal phase transition temperature<sup>38,150</sup>. One possible reason for this behaviour could be the increasing thermal conductivity contribution added from electrons at elevated temperatures. However, the expected electron contribution to the total thermal conductivity in  $\text{U}_3\text{O}_8$  is negligible due to its low electrical conductivity; for example, at 900 K, the electron thermal contribution should be only  $2.2 \times 10^{-4} \text{ W m}^{-1} \text{ K}^{-1}$  as estimated by Wideman-Fanz law with its low electrical conductivity of  $9.9 \text{ S m}^{-1}$ <sup>151</sup>. Therefore, the observed increased thermal conductivity behaviour cannot be attributed to the electron thermal conductivity. Another possibility is the experimental errors in our  $C_p$  measurements as explained below; In this work, the thermal conductivity is evaluated incorporating Eq. (2.55) with  $C_p$  and  $\alpha$  data measured via the LF technique. It is discussed in the literature that, the LF method can give large errors in  $C_p$  measurements when the sample undergoes phase transitions<sup>152</sup>. Because,  $\alpha\text{-U}_3\text{O}_8$  undergoes three phase transitions at 483, 568 and 850 K with  $\lambda$ -type peaks in the heat capacity<sup>153-156</sup>, it is worth to compare the previous  $C_p$  information with the current measurements. The function (Eq. (3.21)) given in Konings *et al.*<sup>156</sup> describes the baseline of the temperature dependent heat capacity of the aforementioned three phases:

$$C_p = 331.64 + 32.62 \times 10^{-3} \times T - 5.12 \times 10^6 \times T^{-2}. \quad (3.21)$$

This expression is a summary of the previous  $C_p$  measurements<sup>153-155</sup> on  $\text{U}_3\text{O}_8$  which have been conducted using adiabatic scanning calorimetry. Figure 3.10 compares the current measurements on  $C_p$  of pure  $\text{U}_3\text{O}_8$  samples with the calculated values using Eq. (3.21). It is clear that there is a considerable difference between the two readings. Especially, the deviation is much pronounced in the high-temperature region, which is the reason for the observed inclination of our measured thermal conductivity. To correct this error, the thermal conductivity is recalculated applying the evaluated  $C_p$  values using Eq. (3.21) with the corresponding  $\alpha$  and the density data from the current work. The red open squares and black open diamonds in Fig. 3.9 represent the expected thermal conductivities when  $C_p$  data are taken from Eq. (3.21) and recalculated for 100TD%. When experimental data are compared with the DFT calculations, it is noticed that the former values reasonably agree with the  $\kappa_{ph}^z$  values, especially in the low-temperature region.

Furthermore, the experimental evaluations are significantly higher than the calculated  $\kappa_{ph}^x, \kappa_{ph}^y$  as well as the average values throughout the entire temperature range of this study. With the anisotropy of heat transport revealed by DFT, it can be suspected that the aforementioned observations indicate the (001)-directional dominated orientations in the pellets. However, given the fact that the previous experimental works also have recorded similar measurements as ours, more likely our DFT calculations with LDA scheme underestimate the thermal conductivity of  $U_3O_8$ . Therefore, further investigations using different exchange-correlational functional and/or Hubbard-U model will help to improve the results. Moreover, it is discussed in recent studies that some phonons with shorter mean free paths than its atomic distances (or wavelengths) cannot treat within BTE methodology. As shown in Fig. 3.11, a considerable portion of phonon mean free paths in  $\alpha$ - $U_3O_8$  at 300 K are comparable or below the minimum atomic distance (2.05 Å), or the so called Ioffe-Regel<sup>157</sup> limit. Therefore, further investigations on the thermal conductivity contribution from wave-like propagation of phonons with a short mean free path can also support to fill the gap between measured and calculated thermal conductivities observed in this work.

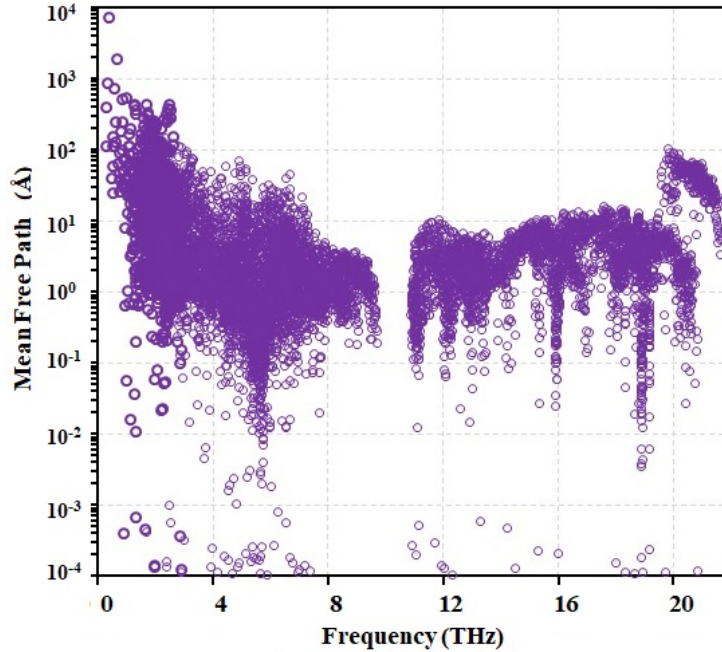


**Figure 3.11:** Mean free paths of  $U_3O_8$  as a function of vibrational frequency at 300 K.

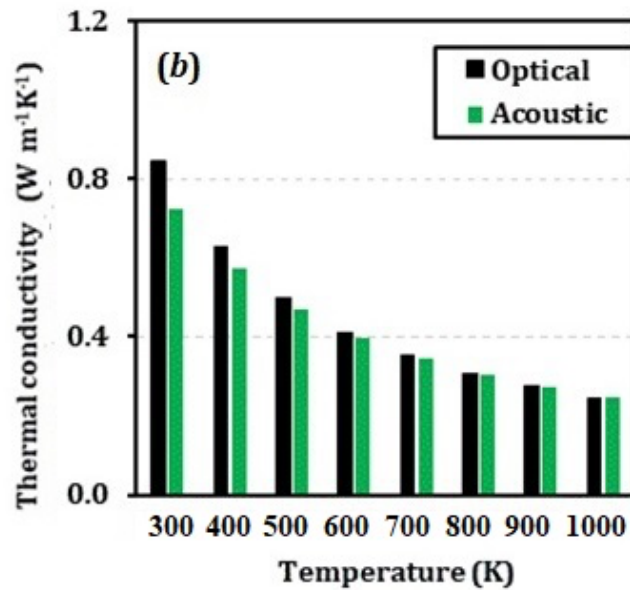
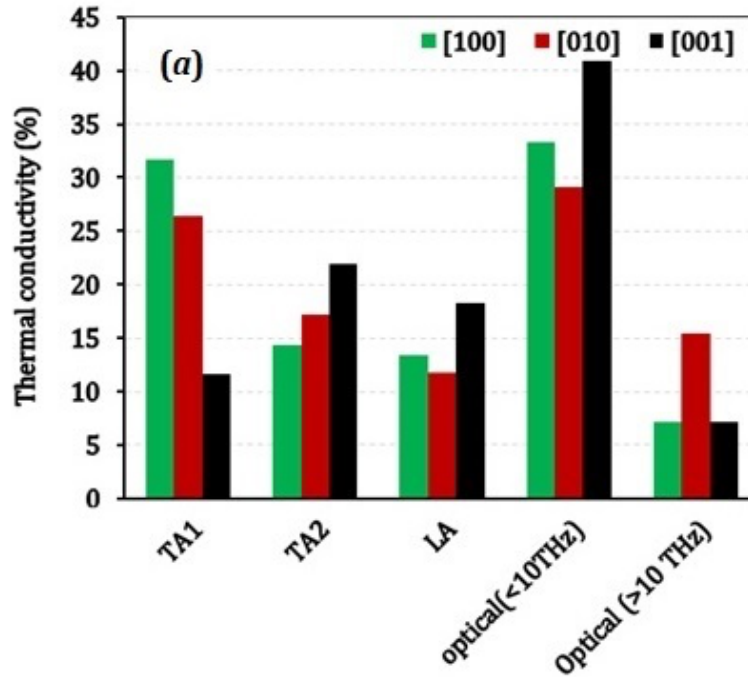


**Figure 3.12:** (a) The directional dependence of optical and acoustic mode contributions to the lattice thermal conductivity of U<sub>3</sub>O<sub>8</sub> at 300 K, and (b) the behaviour of the temperature dependence of the total acoustic and optical mode contributions from 300 to 1000 K.

Afterward, an in-depth investigation into the mechanism of phonon heat transport in  $\text{U}_3\text{O}_8$  is conducted using the results of ShengBTE<sup>56</sup>. Firstly, the mode-wise contribution to the thermal transport is evaluated at 300 K and the percentages of the directional contributions by transverse (TA1 and TA2) and longitudinal (LA) acoustic modes and the optical modes are plotted in Fig. 3.12. The total acoustic mode contribution along [100], [010], and [001] directions are 59.42, 55.36, and 51.88% respectively and that of optical phonons are 40.57, 44.63, and 48.12%. Furthermore, it is found that the optical modes with low frequencies ( $< 10$  THz) play a critical role in thermal transport especially along the [001] direction. Besides, the impact from the high-frequency optical modes also seems to be vital because they have provided 7.22, 15.45, and 7.22% contribution along [100], [010], and [001] direction. The temperature dependence of the mode contribution given in Fig. 3.12b indicates that the optical modes get much stronger with increasing temperature. All these observations indicate that the optical modes of  $\text{U}_3\text{O}_8$  are not negligible in heat transport which is a similar characteristic found in other nuclear fuels like  $\text{PuO}_2$  and  $\text{ThO}_2$ <sup>158</sup>.

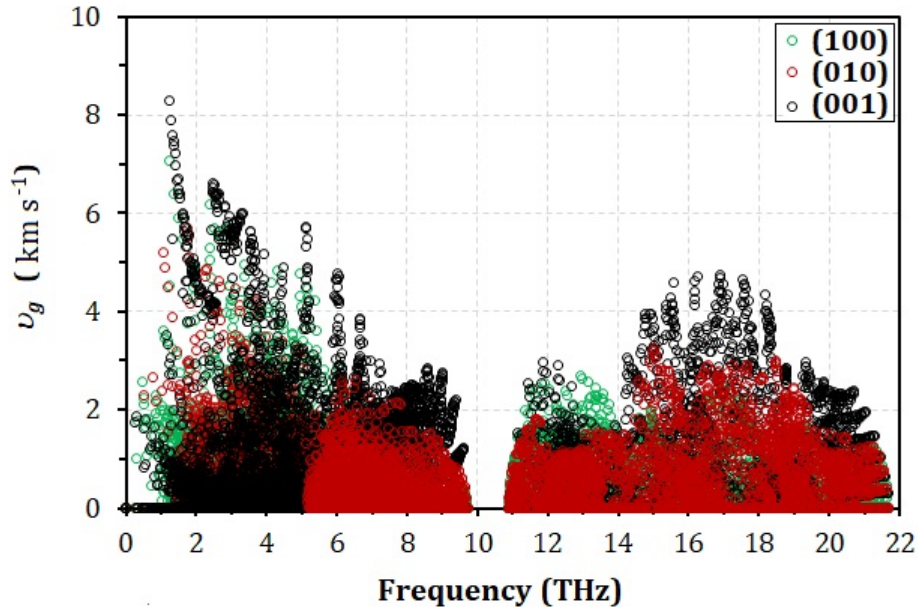


**Figure 3.13** Group velocities ( $v_g$ ) of lattice vibrations in  $\text{U}_3\text{O}_8$  along (100), (010) and (001) direction as a function of vibrational frequency.

The origin of the observed characteristics from mode dependent heat transport can be explained by the material properties such as group velocity ( $\mathbf{v}_g$ ), scattering rates and Grüneisen parameter ( $\gamma$ ). The  $\mathbf{v}_g$  of a phonon mode is directly proportional to the thermal conductivity. Hence, it can be used to get an insight into the anisotropy of heat transport. The group velocities along [100], [010], and [001] directions are calculated and plotted in Fig. 3.13. As it is clear from the figure, the  $\mathbf{v}_g$  in the [001] direction dominates the [100] and [010] components at most frequencies, and this facilitates the easy heat transport along that direction. The scattering rate (inverse of relaxation time) of the phonons is inversely proportional to the thermal conductivity, where small scattering rates imply high thermal conductivity. However, it is found that the scattering rates of acoustic and optical branches in  $\text{U}_3\text{O}_8$  (Fig. 3.14a) are comparable. Especially, the acoustic branch and the low-frequency optical modes are very similar. This facilitates an appreciable heat flow through optical modes. Our prediction for mode-dependent  $\gamma$  is given in Fig. 3.14b where the black circles show the acoustic vibrations and green and blue circles are the respective low and high-frequency optical modes. It is known that the  $\gamma$  is a measure of the strength of the anharmonicity of phonon vibrations in a material. Therefore, the higher the  $\gamma$ , the lower the thermal conductivity is. The mode dependent  $\gamma$  gives large (absolute) values indicating strong anharmonicity, hence this supports the low thermal conductivity. This anharmonicity is a result of the strong interaction between acoustic and low-frequency optical modes.

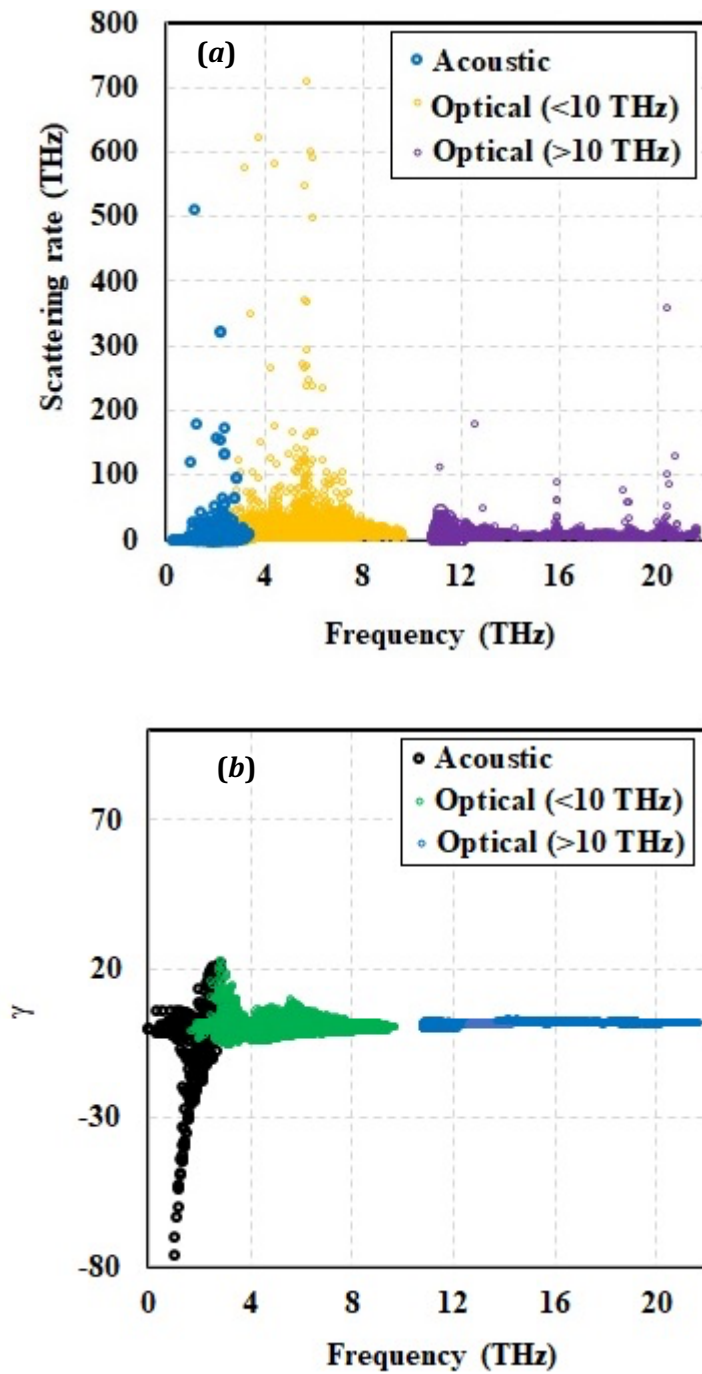


**Figure 3.14:** Frequency dependent (a) phonon scattering rates and the (b) Grüneisen Parameter ( $\gamma$ ) of  $U_3O_8$ .

**Table 3.5:** The diffusivities ( $\alpha$ ) and the specific heat capacities ( $C_P|_{LF}$ ) of  $U_3O_8$ -Al and  $U_3O_8$ -Mo samples measured using laser flash technique. The calculated specific heat capacities according to the Neumann-Kopp rule ( $C_P|_{NK}$ ) also given for comparison. Konings *et al.*<sup>156</sup>, Brooks *et al.*<sup>161</sup>, and Rasor *et al.*<sup>160</sup> were referred for the literature specific heat data on  $U_3O_8$ , Al and Mo, respectively.

T (K)	$\alpha$ ( $mm^2 s^{-1}$ )	$C_P _{LF}$ ( $J kg^{-1} K^{-1}$ )	$C_P _{NK}$ ( $J kg^{-1} K^{-1}$ )	$ \Delta C_P\% $	T (K)	$\alpha$ ( $mm^2 s^{-1}$ )	$C_P _{LF}$ ( $J kg^{-1} K^{-1}$ )	$C_P _{NK}$ ( $J kg^{-1} K^{-1}$ )	$ \Delta C_P\% $
30 $U_3O_8$ -Al					U $_3O_8$ -12.5vol%Mo				
300	5.95	601.45	555.27	8.32	300	2.37	295.30	279.36	5.70
370	5.60	610.32	579.71	5.28	371	1.93	318.54	298.83	6.60
469	5.22	650.30	608.80	6.82	471	1.65	312.66	314.61	0.62
566	4.92	685.90	636.04	7.84	569	1.45	330.20	324.42	1.78
665	4.67	710.05	664.63	6.83	667	1.25	334.56	331.65	0.87
763	4.44	752.98	694.53	8.42	767	1.05	349.47	337.63	3.51
20 $U_3O_8$ -Al					U $_3O_8$ -8.2vol%Mo				
301	13.02	655.48	639.712	2.47	300	1.82	301.17	281.10	7.14
370	12.45	673.93	664.586	1.41	370	1.48	320.42	301.20	6.38
470	11.92	712.51	697.645	2.13	470	1.31	309.46	317.61	2.57
567	11.21	755.26	730.111	3.44	568	1.14	328.04	327.68	0.11
666	10.06	798.71	765.226	4.38	667	0.96	340.74	335.10	1.68
764	9.16	842.01	802.581	4.91	766	0.83	360.88	341.05	5.81
15 $U_3O_8$ -Al (96.6TD)					U $_3O_8$ -8.2vol%Mo				
300	18.92	747.37	691.316	8.05	866	0.77	371.25	346.20	7.24
370	18.77	772.14	717.094	7.68	965	0.76	382.86	350.76	9.15
469	18.06	802.39	752.078	6.69					
567	17.22	833.61	788.133	5.77					
666	16.34	909.28	827.278	9.91					
765	15.58	925.78	869.678	6.45					
15 $U_3O_8$ -Al (91.7TD)									
300	16.82	742.39	691.32	7.39					
371	16.10	768.59	717.45	7.13					
471	15.19	797.75	752.79	5.97					
566	14.17	823.36	787.75	4.52					
667	11.45	879.62	827.69	6.27					
765	10.82	923.08	827.69	6.09					

### 3.3.4 Thermal conductivity of U<sub>3</sub>O<sub>8</sub>-Al and U<sub>3</sub>O<sub>8</sub>-Mo

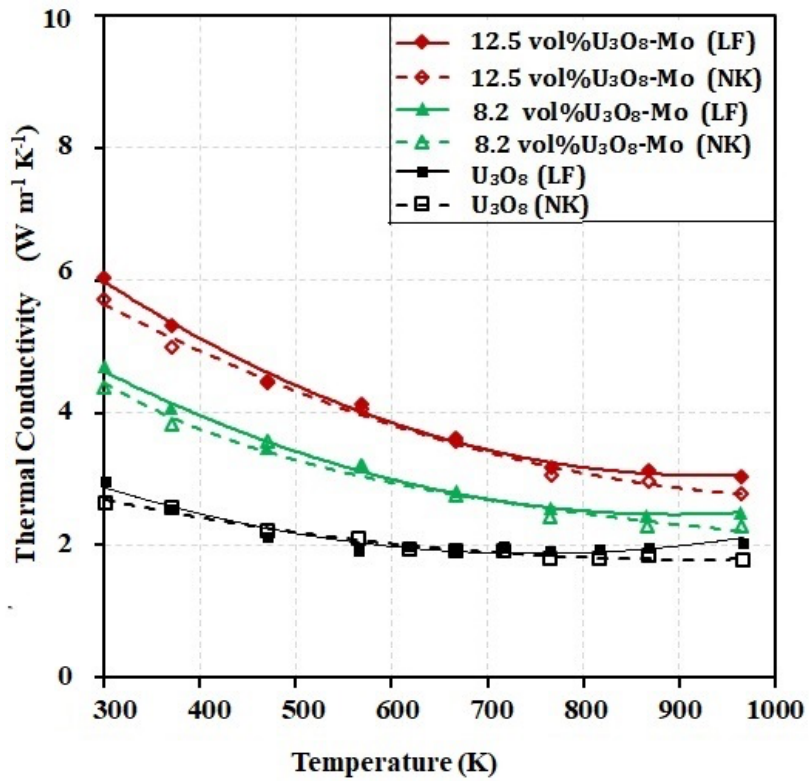
Temperature-dependent thermal conductivities of U<sub>3</sub>O<sub>8</sub>-Al mixed pellets with 30, 20, and 15vol% of U<sub>3</sub>O<sub>8</sub> and U<sub>3</sub>O<sub>8</sub>-Mo samples with 8.2 and 12.5vol% of Mo were measured, and its enhancement is compared with that of the pure U<sub>3</sub>O<sub>8</sub>. The measurements on U<sub>3</sub>O<sub>8</sub>-Al samples were conducted only up to 765 K in order to avoid the melting of aluminum. Corresponding measured  $\alpha$  and  $C_p$  data for each of the pellet are listed in Table 3.5 along with the calculated  $C_p$  values based on the Neumann-Kopp rule (NK) rule<sup>159</sup>. (*i.e.*  $C_p = \sum C_{p,i}f_i$ ; where  $C_{p,i}$  and  $f_i$  are the specific heat capacity and the mass fraction of the  $i^{\text{th}}$  phase) using the literature data on Mo<sup>160</sup>, Al<sup>161</sup> and U<sub>3</sub>O<sub>8</sub><sup>156</sup>. As can be seen from Table 3.5, the specific heat capacities of our work deviate from those evaluated using the NK rule within 10%. There may be several reasons for this deviation; one is the uncertainties and the difficulties linked with the LF technique, as examples, the practical difficulties of having exactly similar geometries or sizes in both the pellet and the reference, and the unavoidable errors added to the emissivity with evaporating the sprayed graphite coating when increasing the temperature, can be specified. Further, the considerable difference in  $C_p$  of U<sub>3</sub>O<sub>8</sub> compared with Al and Mo is challenging in LF method. Another difficulty is associate with the phase transitions of U<sub>3</sub>O<sub>8</sub> as mentioned in Sec 3.3.3.

Figure 3.15 presents the thermal conductivities of U<sub>3</sub>O<sub>8</sub>-Al samples with 15 (96.6TD%), 20 (93.5TD%), and 30vol% (90.1TD%) of U<sub>3</sub>O<sub>8</sub> after the porosity correction with Eq. (3.20). The blue, purple, and yellow solid lines go through the respective thermal conductivities when  $C_p$  is measured using the LF technique, whilst the corresponding dashed lines connect the points estimated with the calculated  $C_p$  data according to the NK rule. It is clear from the figure that there is a significant enhancement in thermal conductivity of the U<sub>3</sub>O<sub>8</sub>-Al pellets compared to that of pure U<sub>3</sub>O<sub>8</sub>, but not surprising due to a large amount of high thermal conductive aluminum. This enhancement remains considerably the same even in the high temperature region, which is a favorable quality for nuclear fuel application. However, the thermal conductivity considerably deteriorates with increasing the amount of U<sub>3</sub>O<sub>8</sub>. As an example, at 300 K, the respective experimental values when  $C_p$  is measured with the LF method are 50.91, 33.79, and 16.53 W m<sup>-1</sup> K<sup>-1</sup> in the 15, 20, and 30vol% U<sub>3</sub>O<sub>8</sub>-Al samples. They are 47.11, 32.98, and 15.26 W m<sup>-1</sup> K<sup>-1</sup> when NK rule is used to evaluate the  $C_p$ . Temperature-dependent thermal conductivity



data of  $U_3O_8$ -Al for the concentrations considered here were not available in the literature. However, the experimental value, given by Copeland *et al.*<sup>126</sup> ( $56.32 \text{ W}\cdot\text{m}^{-1}\cdot\text{K}^{-1}$ ) for 30vol% $U_3O_8$  at 332 K, is in good agreement with our work.

The thermal conductivities of Mo added fuel pellets are measured up to 1000 K, and the corrected values for 100TD% are given in Fig. 3.16. The red and the green series are for the pellets with 8.2vol% (with 97.5TD%) and 12.5vol% (with 97.8TD%) Mo concentrations, respectively. The shown data with solid diamonds and triangles represent the evaluations with measured  $C_p$  and  $\alpha$ , whilst the corresponding open marker points represent the estimations using calculated  $C_p$  (according to the NK rule) and measured  $\alpha$ . As shown in the figure, the thermal conductivities of both the samples are found to be increased relative to that of pure  $U_3O_8$ . The highest enhancement is found in the sample with 12.5vol% of Mo; its thermal conductivity is  $6.04 \text{ W m}^{-1} \text{ K}^{-1}$  at 300 K and  $3.04 \text{ W m}^{-1} \text{ K}^{-1}$  at 965 K. When Mo concentration is only 8.2vol%, those values reduced to 4.70 and  $2.49 \text{ W m}^{-1} \text{ K}^{-1}$ , respectively. However, the NK rule method gives slightly lower values compared to the aforementioned enhancements with only 5.72 (at 300 K) and  $2.77 \text{ W m}^{-1} \text{ K}^{-1}$  (965 K) in high Mo sample (12.5vol% Mo). They are respectively 4.38 and  $2.28 \text{ W m}^{-1} \text{ K}^{-1}$  in 8.2vol% Mo pellet at the aforementioned low and high temperatures.



**Figure 3.16:** Thermal conductivities of U<sub>3</sub>O<sub>8</sub>-Mo pellets with 8.2vol% (green) and 12.5vol% (red) of Mo. Experimental thermal conductivity of pure U<sub>3</sub>O<sub>8</sub> is also given (in black) for the clarity of the enhancement achieved in U<sub>3</sub>O<sub>8</sub>-Al and U<sub>3</sub>O<sub>8</sub>-Mo pellets. All the given values are corrected to 100TD% using Eq. (3.20).

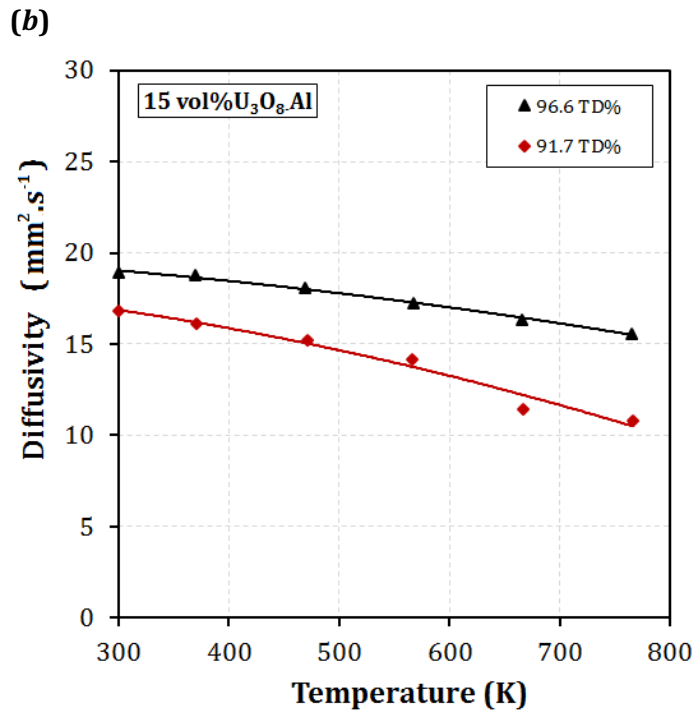
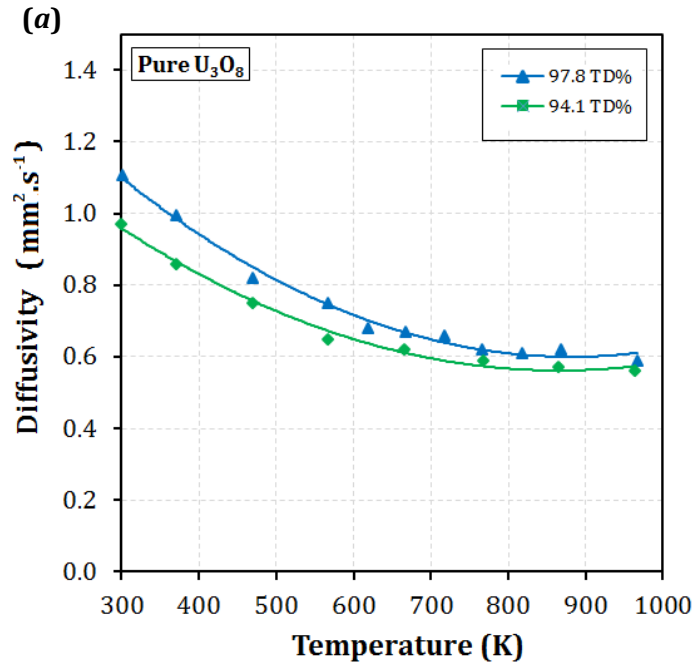


**Figure 3.17:** Thermal diffusivity of (a) pure  $U_3O_8$  with 97.8TD% (blue triangle) and 94.1TD% (green diamond) and (b) 15vol%  $U_3O_8-Al$  with 96.6TD% (black triangle) and 91.7TD% (red diamond), measured using laser flash technique.

### 3.3.5 The effect of porosity on thermal diffusivity and conductivity

To determine how the porosity controls the thermal diffusivity and thermal conductivity, the respective measured data of two of the pure  $U_3O_8$  (with 97.8TD% and 94.1TD%) and two of 15vol% $U_3O_8$ -Al (96.5TD% and 91.7TD%) samples were compared. As shown in Fig. 3.17a, and b, the most important observation is that the thermal diffusivity decreases with increasing the porosity. In the case of pure  $U_3O_8$ , the effect is much pronounced in the low-temperature region, but it fades at the high-temperature end. However, in  $U_3O_8$ -Al, it remains significant throughout the whole temperature range of this work.

The measured thermal conductivities of the respective pellets without the porosity corrections are shown in Fig. 3.18 and 3.19. The solid and the open blue triangles in Fig. 3.18 represent the measured thermal conductivities of the 97.8TD% pellet when  $C_p$  is measured using the LF method and when taken from Konings *et al.*<sup>156</sup>, respectively. The green squares show the respective experimental values for the pure  $U_3O_8$  sample with 94.1TD%. The solid and open black (red) triangles (diamonds) in Fig. 3.19 represent the data for 96.5TD% (91.7TD%) sample when  $C_p$  is evaluated with the LF method or with literature data, respectively. Comparing both Fig. 3.18 and 3.19, it can be stated that there is an inverse relationship between porosity on thermal conductivity similar to  $\alpha$ . Therefore, high densification is important in nuclear fuel pellets to assure high thermal conductivity. Additionally, there is a noticeable gap between measured thermal conductivities in the two samples of  $U_3O_8$  (with 97.8TD% and 94.1TD%) at the low-temperature region, yet the difference reduces with increasing temperature. Contrary, in  $U_3O_8$ -Al pellets, this gap becomes much pronounced with increasing temperatures.

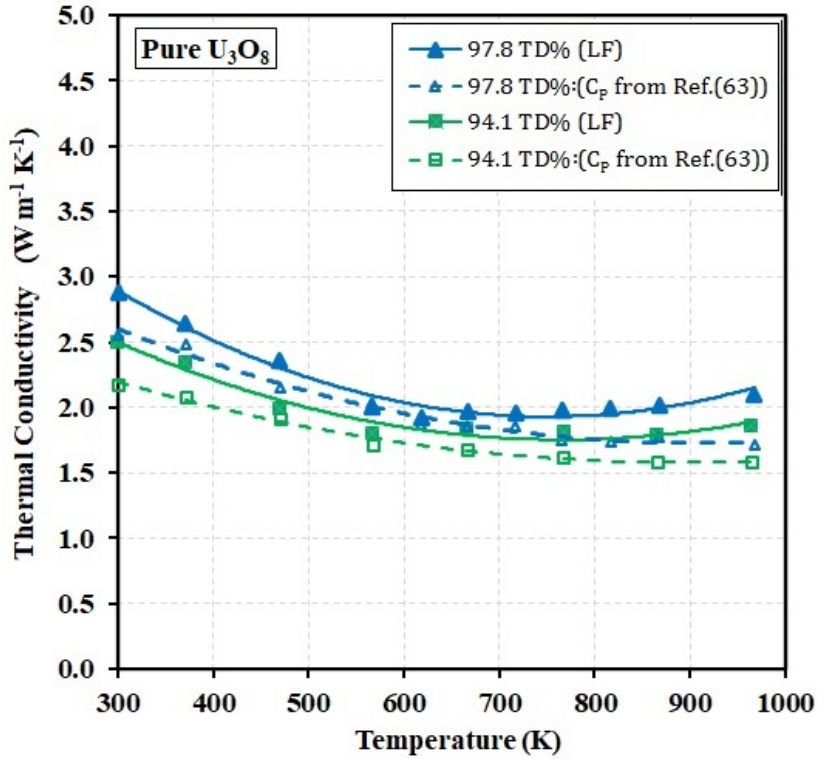


**Figure 3.18:** Thermal conductivity of pure U<sub>3</sub>O<sub>8</sub> with 97.8TD% (blue triangles) and 94.1TD% (green squares) and The solid marks in both figures represent the thermal conductivities evaluated with diffusivity and specific heat data measured by laser flash (LF) technique, while the corresponding open marks show those when evaluated with the specific heat data taken from Konings *et al.*<sup>156</sup> (for pure U<sub>3</sub>O<sub>8</sub>) or calculated according to the NK rule (for 15vol%U<sub>3</sub>O<sub>8</sub>-Al).

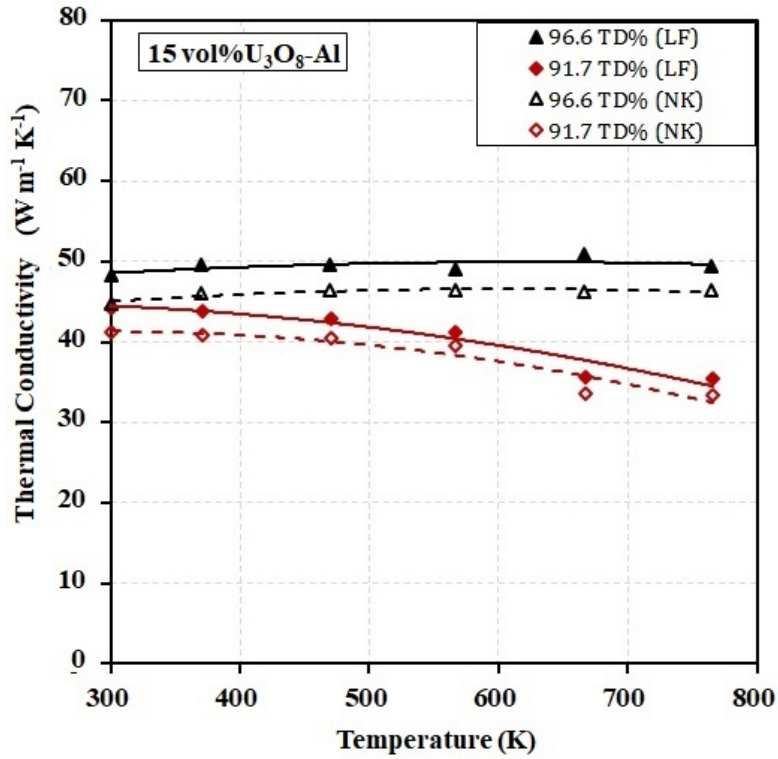


**Figure 3.19:** Thermal conductivity of 15vol%  $U_3O_8$ -Al with 96.6TD% (black triangles) and 91.7TD% (red diamonds). The solid marks represent the thermal conductivities evaluated with diffusivity and specific heat data measured by laser flash (LF) technique, while the corresponding open marks show those when evaluated with the specific heat data taken from Konings *et al.*<sup>156</sup> (for pure  $U_3O_8$ ) or calculated according to the NK rule (for 15vol% $U_3O_8$ -Al).

### 3.4 Conclusion

For the first time, a detailed study of the lattice thermal transport in  $\alpha$ - $\text{U}_3\text{O}_8$  using DFT based simulation techniques is reported. Strong anisotropy in thermal conductivity is predicted and is attributed to the directional dependence of the group velocity. The low thermal conductivity of  $\alpha$ - $\text{U}_3\text{O}_8$  is primarily due to its strong anharmonicity as indicated by the mode-wise analysis of the Grüneisen parameter. Besides, the mode-wise calculation of the thermal conductivity reveals a substantial optical mode contribution to heat transport. The theoretical results are compared with experimental investigations conducted using pure  $\text{U}_3\text{O}_8$  samples prepared by the SPS technique. This work also sheds light on the possibility of using the SPS technique to fabricate high-density  $\text{U}_3\text{O}_8$ -Al and  $\text{U}_3\text{O}_8$ -Mo samples. For example,  $\text{U}_3\text{O}_8$ -Al samples with 30vol% of  $\text{U}_3\text{O}_8$  and  $\text{U}_3\text{O}_8$ -Mo samples with 12.5vol% Mo have respective densities of 90.1TD% and 97.8TD%. The thermal conductivity of  $\text{U}_3\text{O}_8$ -Mo with 8.2vol% and 12.5vol% Mo concentrations respectively are 6.04 and 4.70  $\text{W m}^{-1} \text{K}^{-1}$  at 300 K and 3.04 and 2.49  $\text{W m}^{-1} \text{K}^{-1}$  at 965 K which is higher than the traditional reactor fuel  $\text{UO}_2$ . Finally, both the  $\text{U}_3\text{O}_8$ -Al and  $\text{U}_3\text{O}_8$ -Mo pellets have shown significant thermal conductivity enhancement and can be used as potential fuels in future reactors.

## Chapter 4

### **Density functional theory study of the structural, mechanical, and thermal conductivity of uranium dialuminide (UAl<sub>2</sub>)**

This chapter presents and discusses the results related to a part of this project's third objective, which is the evaluation of thermomechanical properties of UAl<sub>2</sub> using first principles simulation methodologies based on DFT. This work reproduced structural and mechanical properties using first principles methodologies. Further, the phonon dynamics were evaluated using the Phonon and shengBTE codes together with QE, while the electron transport properties were studied employing the EPW simulation package. For the first time, the temperature dependence of electron relaxation time and the electronic thermal conductivities are presented here. Interestingly, our predictions are within acceptable limits compared to the literature data.

The research findings discussed in this chapter have been published as follows:

Ranasinghe, J.I., Malakkal, L., Jossou, E., Szpunar, B., Szpunar, J.A., Density functional theory study of the structural, mechanical and thermal conductivity of uranium dialuminide (UAl<sub>2</sub>), *Journal of Nuclear Materials*, 540, (2020).

The contributions of the Ph.D. candidates:

The entire computational evaluation reported in this paper is performed by PhD candidate under the supervision of Dr. Barbara Szpunar. Further, the analysis of the results and writing the first draft of the manuscript were done by the candidate. Finally, both the supervisors reviewed the work before publication.



# Density functional theory study of the structural, mechanical, and thermal conductivity of uranium dialuminide (UAl<sub>2</sub>)

J. I. Ranasinghe<sup>1</sup>, L. Malakkal<sup>2</sup>, E. Jossou<sup>2</sup>, B. Szpunar<sup>1</sup> and J.A. Szpunar<sup>2</sup>

<sup>1</sup> Department of Physics and Engineering Physics, University of Saskatchewan, CA

<sup>2</sup> Department of Mechanical Engineering, University of Saskatchewan, CA

## 4.0 Abstract

This work presents a systematic study on the structural, mechanical, and thermal conductivity of uranium dialuminide (UAl<sub>2</sub>) using the *ab initio* calculation, based on the density functional theory (DFT). The structural and mechanical properties such as the volume expansion, thermal expansion coefficient, density variation, and the bulk modulus of UAl<sub>2</sub> as a function of temperature (between 300 K and 1500 K) are evaluated within quasiharmonic approximation (QHA). The total thermal conductivity ( $\kappa_{Tot}$ ) of UAl<sub>2</sub> as a function of temperature was predicted considering both the lattice thermal conductivity ( $\kappa_{ph}$ ) and the electronic contribution ( $\kappa_e$ ). The  $\kappa_{ph}$  was estimated using the harmonic and anharmonic interatomic force constants by solving the Boltzmann Transport Equation (BTE). Whereas the  $\kappa_e$  was evaluated using the Wiedemann-Franz law. The absolute value of electrical conductivity ( $\sigma$ ) required for the Wiedemann-Franz law was evaluated employing the BoltzTraP code and the Electron-Phonon Wannier (EPW) code. In addition to the total thermal conductivity  $\kappa_{Tot} = \kappa_e + \kappa_{ph}$ , the mode-dependent phonon scattering rates and the group velocities, as well as their impacts on the lattice thermal conductivity, are discussed in detail. The results obtained demonstrated that  $\kappa_{Tot}$  of UAl<sub>2</sub> decreased with increasing temperature up to 600 K and then remained nearly invariant at  $\sim 5.9 \text{ W m}^{-1} \text{ K}^{-1}$  up to 1500 K. Moreover, a large optical mode contribution (31% at 300 K) to the  $\kappa_{ph}$  was predicted for UAl<sub>2</sub>.

## 4.1 Introduction

Uranium-aluminide alloys (U-Al alloys) mainly consist of three binary intermetallic compounds, namely  $UAl_2$ ,  $UAl_3$ , and  $UAl_4$ . U-Al alloys dispersed in aluminum (Al) matrices are used in several research reactors, namely MURR (University of Missouri Research Reactor), MITR (Massachusetts Institute of Technology Research Reactor), and ATR (Advanced Test Reactor) in the United States. As a fuel, the U-Al system has been extensively studied in many areas such as fuel preparation<sup>162–164</sup>, burnup properties<sup>165,166</sup>, fission product behaviour<sup>50,167,168</sup>, and the corrosion behaviour of spent fuels in the dry storages<sup>50,169,170</sup>. Moreover, the applicability of pure  $UAl_3$  and  $UAl_2$  binary systems in the form of dispersions in Al matrices also have been examined for research reactors<sup>163,164,166</sup>. However, investigations on its applicability in commercial power reactors have hardly been considered despite the fact that they have many favourable qualities as an accident tolerant fuel for future reactors. Specially  $UAl_2$ , which is the focus of this work, has high uranium density ( $6.64 \text{ U-g.cm}^{-3}$ )<sup>29</sup>, high thermal conductivity at both low ( $11.04 \text{ W m}^{-1} \text{ K}^{-1}$  at 300 K)<sup>52</sup> and high temperature ( $9.3 \text{ W m}^{-1} \text{ K}^{-1}$  at 1000 K)<sup>52</sup>, and high melting point (1863 K)<sup>29</sup>. Further, it has been found that  $UAl_2$ -Al shows exceptional resistance to fission gas bubble formation and the possibility of reducing fuel swelling by controlling the porosity<sup>171</sup>. Thus, the applicability of  $UAl_2$  in commercial reactors is worth to be evaluated. Apart from being a nuclear fuel, U-Al compounds have greatly interested many investigators because of the critical interaction kinetics between U and Al. Many research and test reactor fuels are formed by dispersing uranium compounds (*e.g.*, Uranium molybdenum (U-Mo)<sup>172,173</sup>, uranium silicide ( $U_3Si_2$  and  $U_3Si$ )<sup>23,174,175</sup> and tri-uranium octaoxide ( $U_3O_8$ )<sup>23,176,177</sup>) in aluminum matrixes. It has been shown that, during the irradiation, the uranium compounds react with the Al matrixes forming an interaction layer that may be composed of U-Al binary compounds such as  $UAl_2$ ,  $UAl_3$ , and  $UAl_4$ <sup>28,178–181</sup>. In-pile and post-irradiation tests of those fuels show a considerable reduction of thermomechanical properties because of the enhanced porosity and fuel swelling due to the interaction layer<sup>171</sup>. Therefore, the availability of accurate thermomechanical properties of U-Al compounds is beneficial for evaluating the applicability of many fuel candidates in the nuclear industry.

In this work, our focus is to study the thermomechanical properties of  $UAl_2$  using first principle methods based on density functional theory (DFT). After the first report in 1950<sup>182</sup>, many experimental and theoretical studies have been performed to investigate the properties of  $UAl_2$ .

Several studies suggest that it crystallizes in  $Fd\bar{3}m$  space group having a  $MgCu_2$  type cubic Laves lattice<sup>182–184</sup>. Experimental and theoretical works on phase diagram<sup>185</sup>, electronic structure<sup>51,180</sup>, and magnetic properties<sup>186</sup> also have been conducted. Room temperature elastic constants have been evaluated by measuring the sound velocities using an ultrasonic technique by Narasimham *et al.*<sup>187</sup>. Mei *et al.*<sup>52,180</sup> reports several thermomechanical properties, including thermal expansion, specific heat, and thermal conductivity, based on ab initio molecular dynamics (AIMD) and empirical method studies. However, these studies are limited to a maximum temperature of 1000 K, which is insufficient to evaluate the fuel behaviour in severe accidents. Hence, a detailed study on thermomechanical properties over a wide temperature range, which is essential in safer nuclear applications, is still rare. In that context, we provide a systematic investigation on the thermomechanical properties controlled by both phonon-phonon and the electron-phonon interactions in the temperature range from 300 K to 1500 K by using first principles calculations. The electron-electron scattering is ignored here, for the reason that it is not important at temperatures higher than the Debye temperature ( $\theta_D$ ) ( $\theta_D$  is  $\sim 300$  K for  $UAl_2$ <sup>188</sup>). We further conduct an indepth study on the phonon contribution ( $\kappa_{ph}$ ) to the total thermal conductivity ( $\kappa_{Tot}$ ) as well as its mode dependency. To our knowledge, there are no previous experimental or theoretical studies on the temperature dependence of the electron relaxation time ( $\tau_e$ ) for the electron-phonon scattering process, which is essential in evaluating the electron thermal transport. In this work, we provide a fully *ab-initio* calculation of  $\tau_e$  over a wide temperature range for the first time. Further, the absolute values of electronic contribution to the total thermal conductivity ( $\kappa_e$ ) are predicted. The rest of this paper is organized as follows; Section 4.2 describes the calculation procedures focusing on the calculation method and parameters used for the investigation. In section 4.3, we discuss the findings of this work and compare them with available literature. Finally, the conclusions in the section 4.4 summarize the highlights of the study.

## 4.2 Computational details

First-principles calculations were performed using the DFT as implemented in the Quantum ESPRESSO (QE) simulation package<sup>60</sup>. The pseudopotential of the U and Al are norm conserved, and the exchange and correlation is based on the generalized gradient approximation (GGA) with

PBEsol (Perdew-Burke-Ernzerhof <sup>77</sup> for solids). Previous studies <sup>52,180,181</sup> have shown that satisfactory results of the bulk properties for UAl<sub>2</sub> were obtained without the Hubbard U parameter and the spin-orbit coupling (SOC). Thus, in this work, Hubbard U corrections and the SOC were not incorporated. The structural optimization of the UAl<sub>2</sub> was obtained using the converged wave vector grid of 8×8×8 Monkhorst-Pack sampling (*k*-mesh) and the plane wave energy cutoff of 1632.7 eV. The criteria for the electronic energy convergence and the tolerance for forces on each atom was respectively set a value of 10<sup>-7</sup> eV.Å<sup>-1</sup> and 10<sup>-9</sup> eV. To estimate the magnetic ordering, of UAl<sub>2</sub> we compared the ground state energies of non-magnetic (NM), spin-polarized (SP), ferromagnetic (FM), antiferromagnetic (AFM) configurations.

The temperature dependent mechanical and thermal properties (at constant pressure) of UAl<sub>2</sub> were evaluated using the Quasi-Harmonic Approximation (QHA)<sup>189</sup> as implemented with the Phonopy<sup>59</sup> simulation package. The Birch-Murnaghan equation of state (BMEOS)<sup>190</sup> is then used to fit the calculated energy-volume data and hence to evaluate the temperature dependent thermal properties as explained in respective sections where applicable. In this work, the phonon contribution to the thermal conductivity was predicted by solving the Boltzmann transport equation (BTE) using the ShengBTE<sup>56</sup> simulation package based on the second (harmonic force constant) and third order (anharmonic force constant) interatomic force constants (IFCs). The harmonic force constant is calculated using the direct approach based on the finite displacement method as implemented in the Phonopy package<sup>59</sup>. We achieved the convergence of the harmonic force constant with a 3×3×3 supercell of the primitive cell. The calculation of the third-order force constants was performed on a 3×3×3 supercell, and the force cutoff distance was set to the fourth nearest neighboring atoms to ensure the convergency of the results.

Since UAl<sub>2</sub> is a metallic compound, the thermal transport due to electron-phonon scattering cannot be ignored. We used BoltzTrap<sup>57</sup> and Electron-Phonon Wannier (EPW)<sup>58</sup> codes to evaluate the  $\kappa_e$  as a function of temperature as explained below. First, the temperature-dependent electrical conductivity relative to the electron relaxation time ( $\sigma/\tau_e$ ) is evaluated using the rigid band approximation within the framework of Boltzmann transport theory using the Fourier interpolation of the electronic band structure of UAl<sub>2</sub> with FM conditions as implemented in the BoltzTrap package<sup>57</sup>. In this method, it requires to use a denser *k*- mesh for the non-self-consistent calculation for accurate results. Hence, we used a much denser *k*- mesh in the non-self-consistent calculation

and the results presented in this work are for a  $50 \times 50 \times 50$  mesh where we have achieved the convergency of the calculated  $\sigma/\tau_e$ . In order to obtain the absolute values of  $\sigma$ , the temperature dependent  $\tau_e$  is required and this can be derived from the electron-phonon coupling matrix as implemented in EPW<sup>58</sup> code. However, EPW code is not yet implemented for magnetic materials, hence we assumed NM conditions in the calculation of  $\tau_e$ . First, we calculated the electron self-energy using the matrix elements of the electron-phonon interaction by combining the Quantum Espresso code<sup>60</sup> with the EPW package<sup>58</sup>. In order to calculate the electron-phonon matrix elements, we employed the density functional perturbation theory (DFPT) along with the Wannier interpolation technique as implemented in EPW package. An inner frozen window of 9.0 to 11.0 eV and outer disentanglement window of 0.0 to 20.0 eV including 28 Wannier functions with the projections of U-*f*, U-*d* and Al-*p<sub>x</sub>* are used to construct the maximally-localized Wannier functions (MLWF). The convergence of the disentanglement and the Wannierization is achieved under  $10^{-10} \text{ \AA}^2$ . The electron and phonon states are first calculated on coarse grids of  $6 \times 6 \times 6$  in and then interpolated to finer meshes via MLWFs with finer unshifted grids of  $24 \times 24 \times 24$  in both *k*- and *q*-meshes to ensure the convergence of  $\tau_e$ . The electron-phonon matrix elements are evaluated up to the temperature of 1500 K and they are used to derive the temperature dependent  $\tau_e$  as discussed in the Sec. 4.3.5. Thereafter, the Wiedemann-Franz law is used extract  $\kappa_e$  as a function of temperature from 300 K to 1500 K.

## 4.3 Results and discussion

### 4.3.1 Optimized structure at ground state

As shown in Fig. 4.1, the conventional unit cell of  $\text{UAl}_2$  consists of eight U and sixteen Al atoms located at Wyckoff positions  $(0, 0, 0)$ ;  $(0.25, 0.25, 0.25)$  and  $(5/8, 5/8, 5/8)$ ,  $(5/8, 3/8, 3/8)$ ,  $(3/8, 5/8, 3/8)$ ,  $(3/8, 3/8, 5/8)$  respectively<sup>183</sup>. Table 4.1 lists the optimized structural parameters and relative energies ( $\Delta E$ ) for different magnetic phases (NM, FM, SP, and AFM) along with the known literature data. The magnetic moment  $\mu_B$ , and  $\Delta E$  are given for one formula unit of  $\text{UAl}_2$ . Among all the four states the FM phase has the lowest energy suggesting that the FM phase is the

energetically most favourable state. This observation is consistent with the previous experimental and theoretical publications<sup>52,180,181</sup>.

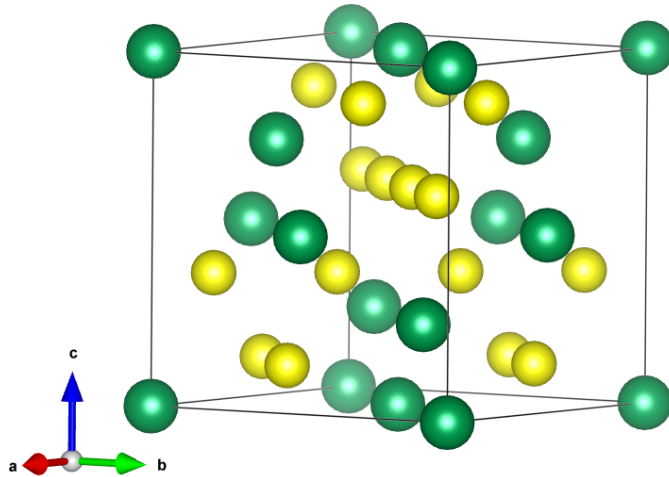


**Figure 4.1:** Conventional unit cell of UA<sub>12</sub> structure at ground state. Solid green spheres represent the Uranium atoms, and the yellow solid spheres represent the Al atoms.

**Table 4.1:** Predictions for lattice parameter  $a$  (Å), relative energy  $\Delta E$  (per Ual<sub>2</sub> in eV), magnetic moment  $\mu_B$  of U atom (per Ual<sub>2</sub> in  $\mu_B$ ) for ferromagnetic (FM), spin-polarized non-magnetic (SP), antiferromagnetic (AFM) and non-magnetic (NM) configurations using GGA method.

	$a$ (Å)	$\Delta E$ (eV)	$\mu_B$	Ref.
FM	7.789	0.00	3.35	This work
	7.712		2.64	180
SP	7.561	0.42		This work
AFM	7.561	0.79	2.81	This work
	7.632		1.34	180
NM	7.561	1.22		This work
	7.624			180
Exp.	7.76			184
	3.14			191

Moreover, the lattice parameter of 7.79 Å for the FM state is in excellent agreement with the experimental value (7.76 Å) reported by Katz *et al.*<sup>184</sup>. The computed total magnetic moment per U atom, 3.35  $\mu_B$ , concurs with the experimental moment of 3.14  $\mu_B$  reported by Burzo *et. Al.*<sup>186</sup>. To further validate the structure parameters used in this work, we compared the first nearest neighbour (1NN) interatomic distance with their experimental data in the literature. The respective predictions for 1NN distances between U-U, Al-Al and U-Al atoms are 3.33, 2.72 and 3.12 Å respectively, also shows an excellent agreement with Rundle *et al.*<sup>183</sup>.

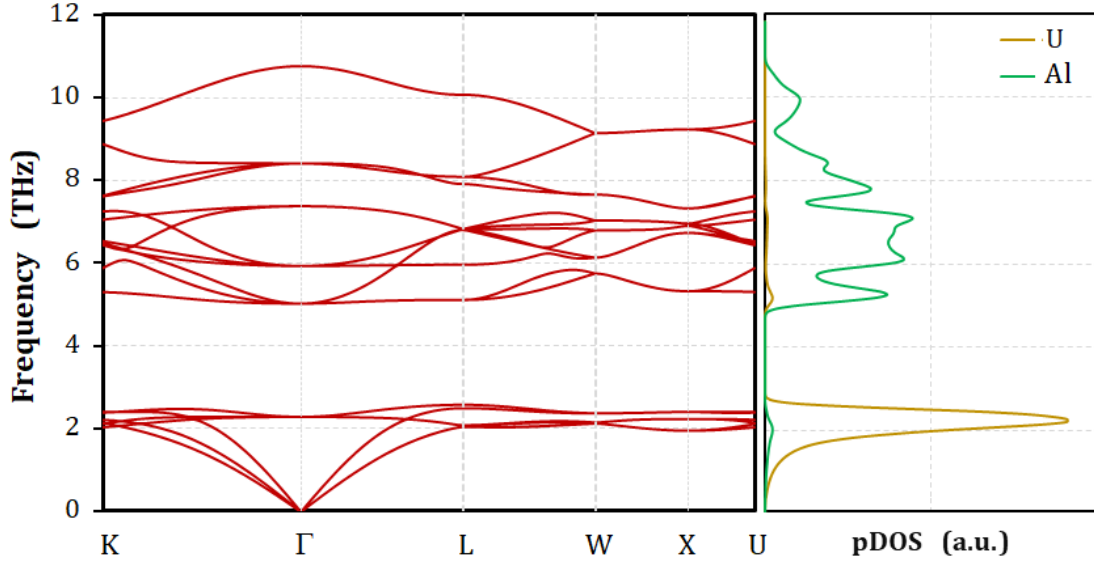


**Figure 4.2:** Calculated Phonon spectra for FM phase of  $\text{UAl}_2$  along the high symmetry directions. The right-hand side panel gives the partial density of states of phonons originated from U and O atoms.

### 4.3.2 Lattice dynamics and thermomechanical properties

Phonon dispersion spectra of crystalline solids give valuable information about the dynamical stability and thermal transport properties of the structure. In this work, the finite difference method is used to determine the harmonic phonon dispersion curve along the high symmetry path for the FM phase of  $\text{UAl}_2$  (Fig. 4.2). The three phonon branches starting from the  $\Gamma$  point are the acoustic phonons, and the other 15 branches represent the optical phonons. The phonon dispersion curve shows a clear gap between 2.9 and 5.6 THz frequencies and below the bandgap, three of the optical branches overlap with the acoustic modes far from the  $\Gamma$  point. The gaps of dispersions are usually attributed to the atomic mass difference which eventually will restrain the optical-acoustic phonon interaction above the gap. Further, the absence of negative phonon frequency indicates that the structure is dynamically stable. The calculated phonon spectrum is in fair agreement with the work



done by Mei *et. al.*<sup>180</sup>. From phonon partial density of states, it is clear that the heavy U atoms are likely to play the major role in the low-frequency region, while the Al atoms trigger the high-frequency vibrations.

Once the phonon dispersion spectrum is evaluated over the first BZ, it can be used to derive the energy  $E_{ph}$  of the system using Eq. (4.1),

$$E_{ph} = \sum_{\mathbf{q},\nu} \hbar\omega_{\mathbf{q},\nu} \left[ \frac{1}{2} + \frac{1}{\exp\left(\frac{\hbar\omega_{\mathbf{q},\nu}}{k_B T}\right) - 1} \right], \quad (4.1)$$

where  $\hbar$  is the reduced Plank constant,  $\omega_{\mathbf{q},\nu}$  is the vibration frequency of a phonon with wave vector  $\mathbf{q}$  and the mode  $\nu$ , and  $k_B$  is the Boltzmann constant. Note that,  $E_{ph}$  depends on both the phonon frequency and the temperature of the system. Further, it can be used to evaluate the specific heat at constant volume ( $C_V$ ) according to the relation

$$C_V = k_B \sum_{\mathbf{q},\nu} \left\{ \left[ \frac{\hbar\omega_{\mathbf{q},\nu}}{k_B T} \right]^2 \frac{\exp\left(\frac{\hbar\omega_{\mathbf{q},\nu}}{k_B T}\right)}{\left(\exp\left(\frac{\hbar\omega_{\mathbf{q},\nu}}{k_B T}\right) - 1\right)^2} \right\}, \quad (4.2)$$

where all the terms in the equation have the same meaning as in Eq. (4.1). In order to evaluate the temperature dependence of thermal expansion, Bulk modulus, and the density of Ual<sub>2</sub>, we analysed the Helmholtz free energy function, as explained below.

The total Helmholtz free energy function  $F(V, T)$  of a system is

$$F(V, T) = U(V) + F_{el}(V, T) + F_{ph}(V, T), \quad (4.3)$$

where  $U(V)$  is the static energy of the system at 0 K, and  $F_{el}(V, T)$  is the electronic contribution to the free energy which can be evaluated by the electronic bandstructure calculation according to the Fermi-Dirac statistics. However, it has been shown that the effect of  $F_{el}(V, T)$  on the EOS is negligible at the temperatures well below the melting<sup>191–194</sup>. Therefore, electronic excitations are not considered in the thermal expansion, bulk modulus, and density calculations.  $F_{ph}(V, T)$  is the phonon contribution to the free energy at volume  $V$  and temperature  $T$  and can be given as

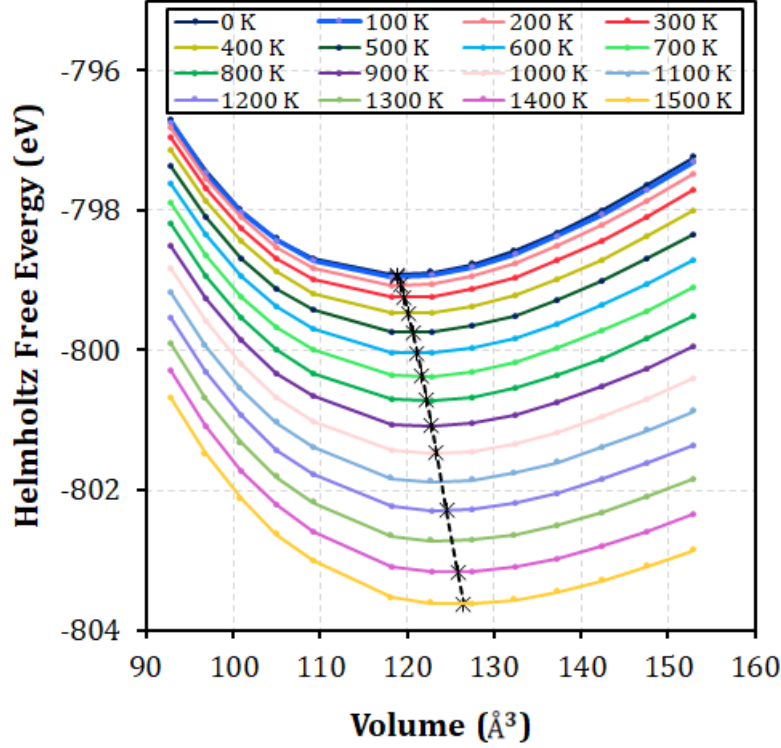


**Figure 4.3:** Calculated Helmholtz free energy (in eV) as a function of unit cell volume (in  $\text{\AA}^3$ ) between the temperatures 0 and 1500 K in 100 K steps. Each solid line represents the fit to the Birch-Murnaghan equation of states. The minimum point on each fit is shown by the (black) cross mark. The dashed (black) line is only a guideline to the eye.

$$F_{ph}(V, T) = \frac{1}{2} \sum_{q,\nu} \hbar\omega_{q,\nu} + k_B T \sum_{q,\nu} \ln \left\{ 1 - \exp \left( -\frac{\hbar\omega_{q,\nu}}{k_B T} \right) \right\} \quad (4.4)$$

We first computed the corresponding  $F(V, T)$  for 14 cells around the equilibrium volume with lattice parameters differed by  $\pm 0.1 \text{\AA}$  steps from the original optimized structure. The calculated energy-volume data is fitted to the third-order BMEOS<sup>194</sup> which eventually gives the Bulk modulus and the equilibrium volume.

The Gibbs free energy  $G(T, p)$  of a system is defined by the thermodynamic relation

$$G(T, p) = \min_V \{ U(V) + F_{ph}(V, T) + pV \}. \quad (4.5)$$

This equation says that  $G(T, p)$  can be obtained by finding the global minima of the function  $\{U(V) + F_{ph}(V, T) + pV\}$  by changing the volume at constant pressure. We employed QHA to evaluate the corresponding  $G(T, p)$  over the temperature range from 0 to 1500 K. Thereafter the lattice contribution to the heat capacity at constant pressure,  $C_p^{ph}(T, p)$ , is derived using the thermodynamic relation

$$C_p^{ph}(T, p) = -T \frac{\partial^2 G(T, p)}{\partial T^2}. \quad (4.6)$$

Figure 4.3 illustrates the  $F(V, T)$  Vs  $V$  curves fitted to BMEOS at different temperatures. The points represented by red crosses on each curve are the corresponding  $G(T, p)$  and the equilibrium volume at the corresponding temperature.

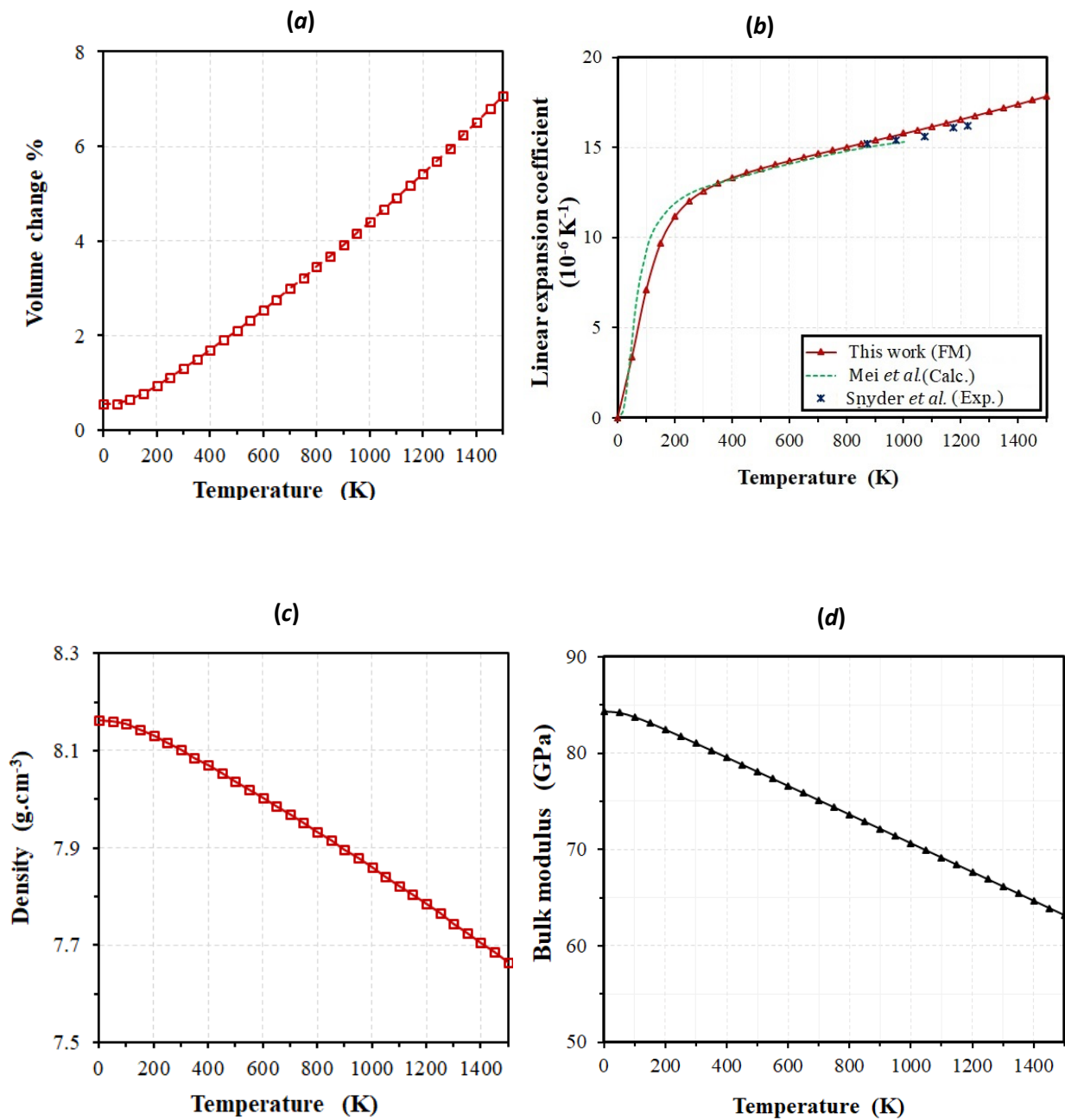


**Figure 4.4.** The temperature dependence of the (a) volume expansion relative to optimized volume at 0 K, (b) Linear thermal expansion coefficient (c) Density, and (d) isothermal bulk modulus. The smooth curves are guidelines to the eyes.

---

**Table 4.2:** The recommendations for the temperature dependences of the volume change ( $\Delta V\%$ ), linear thermal expansion coefficient ( $\alpha_L(T)$  in  $10^{-6} \text{ K}^{-1}$ ), density ( $\rho(T)$  in  $\text{g cm}^{-3}$ ), and the bulk modulus ( $B(T)$  in GPa) for the temperature range 0 to 1500 K.

---

$$\Delta V\% = 6 \times 10^{-13}T^4 - 2 \times 10^{-9}T^3 + 4 \times 10^{-6}T^2 + 0.0018T + 0.48$$

$$\alpha_L(T) = -2 \times 10^{-17}T^6 + 10^{-13}T^5 - 4 \times 10^{-10}T^4 + 4 \times 10^{-7}T^3 - 3 \times 10^{-4}T^2 + 0.1T - 0.28$$

$$\rho(T) = 7 \times 10^{-17}T^5 - 4 \times 10^{-13}T^4 + 7 \times 10^{-10}T^3 - 6 \times 10^{-7}T^2 - 8 \times 10^{-5}T + 8.17$$

$$B(T) = \begin{cases} 85.89 - 10^{-3}T - 10^{-6}T^2, & 300 > T > 0 \\ 85.93 - 0.0006T, & 1500 > T > 300 \end{cases}$$


---

We utilized the obtained equilibrium volumes at a different temperature to predict the percentage volume changes ( $\Delta V\%$ ) which can be evaluated using  $\Delta V\% = \left[ \frac{V(T) - V(0)}{V(0)} \times 100\% \right]$  as shown in Fig. 4.4a. This analysis gives only 8.3 % volume expansion in  $\text{UAl}_2$  when the temperature rises through 300 to 1500 K. Knowing the volume changes upon the temperature, we evaluated the volume ( $\alpha_V$ ) and the linear ( $\alpha_L$ ) thermal expansion coefficients using  $\alpha_L(T) = \frac{1}{3} \alpha_V(T) = \frac{1}{3V(T)} \left( \frac{\partial V(T)}{\partial T} \right)$ . In Fig. 4.4b we show the calculated  $\alpha_L$  up to 1500 K along with available references from literature for comparison. Our prediction is in good agreement with the experimental work by Snyder *et al.*<sup>195</sup> at the high-temperature region. The minor deviation from Mei *et al.*<sup>52</sup>, both at high and low temperature regions, might be due to the different exchange-correlations used in the studies. The unit cell volume is converted to the molar volume, thereby the percentage of the density variation is predicted (see Fig. 4.4c). For this calculation, we have used the molar mass as 291.9 g. QHA technique simultaneously provides the isothermal bulk moduli as it is a fitting parameter to the BMEOS. As shown in Fig. 4.4d, the bulk modulus shows inverse dependence with the temperature and has been softened by  $\sim 22.03\%$  from 300 to 1500 K.

Since there are no literature works which gives the bulk modulus for higher temperatures, we compared our prediction at 300 K with the derived bulk modulus from the experimental work done by Narasinmham *et al.*<sup>187</sup>. In their work, they have measured the elastic constant at 300 K and the stress-strain method gives the bulk modulus as 82.93 GPa, which shows good agreement with this work (81.02 GPa at 300 K). Moreover, we utilized the results given in Fig. 4.4*a, b, c* and *d* to find the recommendations for their polynomial fits as provided in Table 4.2.

The temperature dependence of heat capacities at constant pressure and at constant volume for isotropic defect-free bulk UAl<sub>2</sub> are displayed in Fig. 4.5. The black dashed line indicates the high-temperature classical limit of the phonon contribution to the specific heat at constant volume ( $C_V^{ph}$ ), which is  $3nR$ , where  $n$  is the number of atoms and  $R$  is the universal gas constant. At high temperature, the calculated  $C_V^{ph}$  shows excellent agreement with classical limit, while  $C_P^{ph}$  (the phonon contribution to the specific heat at constant pressure) increases monotonously. At temperatures below  $\sim 200$  K, the difference between  $C_V^{ph}$  and  $C_P^{ph}$  is insignificant, which is not surprising since the anharmonic effects are minimum. We evaluated the  $C_V$  contribution due to structural changes using  $9\alpha_L^2 B(T, P)VT$ , and it exactly matches with the difference between  $C_P^{ph}$  and  $C_V^{ph}$  confirming the reliability of our work. We compared our results of  $C_P$  with similar work done by Mei *et. al.*<sup>180</sup> with excellent agreement with us. We also evaluated the electronic contribution of specific heat,  $C_P^{el}$ , and it is shown by the green line in Fig. 4.5 (the evaluation method will be given later on this report in section 4.3.5.2.) The results fit the linear equation  $C_P^{el} = 0.0069T$ , hence we predict the electronic constant  $\gamma$  as  $6.9 \text{ mJ. mol. K}^{-2}$ . The total  $C_P = C_P^{ph} + C_P^{el}$ , which represents by the red solid line, continues to increase with temperature and reaches  $95.59 \text{ mJ. mol. K}^{-2}$  at 1500 K which can be understood by the increasing anharmonicity.

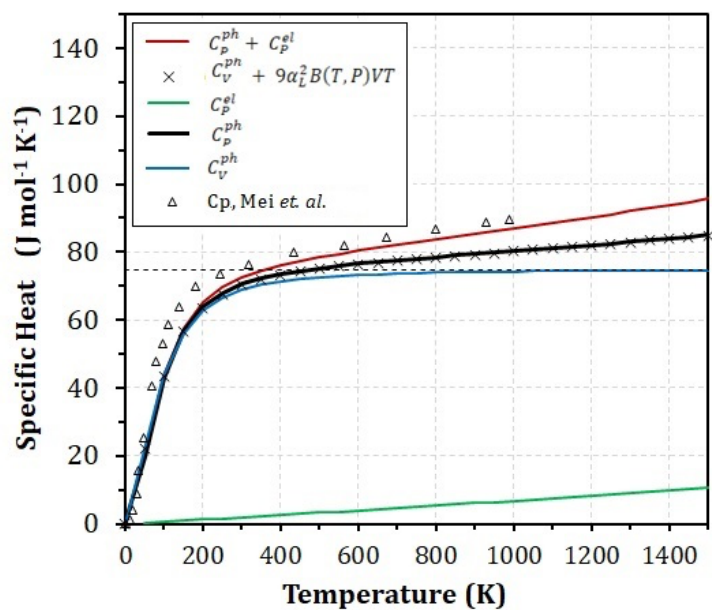


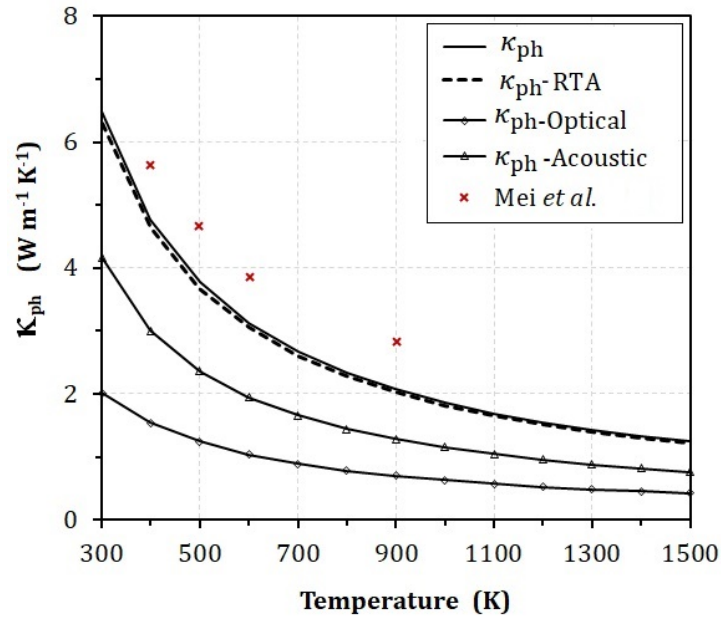
**Figure 4.5:** Specific heat  $C_P$  and  $C_V$  of  $\text{UAl}_2$  as a function of temperature. The green and blue lines represent the respective electronic ( $C_P^{el}$ ) and lattice/harmonic ( $C_V^{ph}$ ) contributions to  $C_V$ . Black cross marks show the sum of the harmonic and anharmonic contributions to the lattice heat capacity. The black solid line gives the  $C_P^{ph}$  calculated by QHA. Red line is the total heat capacity ( $C_P^{ph} + C_P^{el}$ ).

### 4.3.3 Thermal transport properties

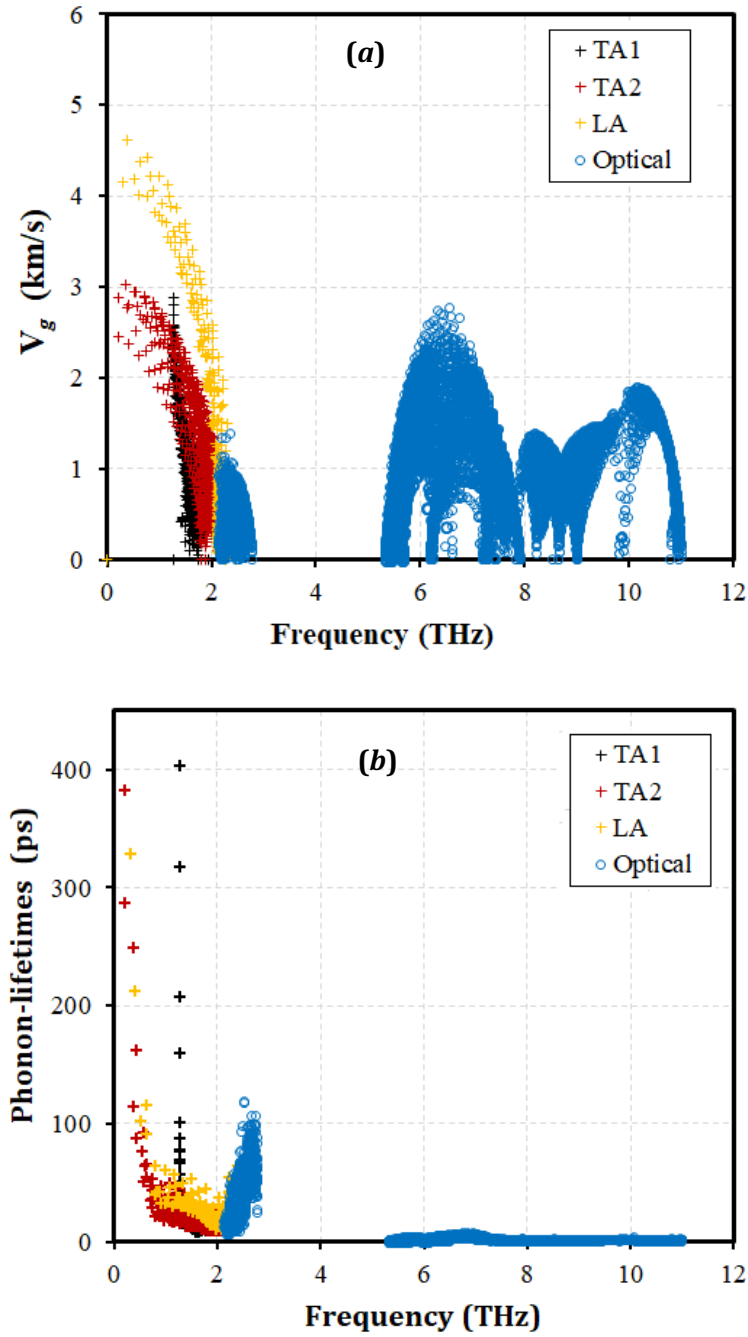
#### 4.3.3.1 Phonon thermal conductivity

Figure 4.6 describes the temperature dependence of the  $\kappa_{ph}$  for the FM phase of  $\text{UAl}_2$ , obtained using an iterative solution to the linearized BTE. The value of  $\kappa_{ph}$  represents the intrinsic conductivity of a perfect crystal by considering three-phonon scattering and isotropic scattering. The predicted  $\kappa_{ph}$  compared reasonably well with the previous prediction made by Mei *et al.*,<sup>52</sup> using AIMD method. As expected, the  $\kappa_{ph}$  decreased with increasing temperature due to enhanced phonon-phonon interaction and is isotropic in  $x, y$ , and  $z$  directions. Moreover, we evaluated the  $\kappa_{ph}$ , using the constant relaxation time approximation (CRTA) and found very similar results with the iterative solution. This observation can be described as follows: between the Normal- and Umklapp processes, the latter is dominant when the temperature is above  $\theta_D$ . However, in the CRTA method, both the normal- and Umklapp- scatterings are incorrectly treated as resistive in accordance with Mattheissen's rule<sup>56</sup> and this assumption typically predicts much lower thermal conductivities than the actual values. The error caused by CRTA is considered and treated by the iterative method ensuring more accurate results. Therefore, the CRTA method can accurately predict the full solution only when the Umklapp process dominates which could be the possible reason for the observation in this work. In addition to the total lattice thermal conductivity, we also predicted the contribution from the acoustic modes and the optical modes separately. It was worth noting that the optical modes contributed to 31% of the total lattice thermal conductivity as previously observed in other materials such as  $\text{UO}_2$ <sup>196</sup>,  $\text{CeO}_2$ <sup>197</sup> and  $\text{ThO}_2$ <sup>98</sup>.





**Figure 4.6:** The phonon contribution  $\kappa_{ph}$  to the total thermal conductivity evaluated using the iterative solution (black solid line) and the relaxation time approximation  $\kappa_{ph}$ -RTA (black dashed line). The acoustic ( $\kappa_{ph}$ -Acoustic) and optical ( $\kappa_{ph}$ -Optical) contributions are given by black solid lines with solid triangles and diagonals respectively. Mei *et al.*<sup>52</sup> results are shown by red crosses.



**Figure 4. 7:** Mode contributions of the (a) group velocities ( $v_g$ ) and (b) lifetimes of phonon-phonon scatterings at 300 K. The transverse (TA1 and TA2) and longitudinal acoustic modes are represented by black, red and yellow plus marks while all the optical modes are shown by blue circles.

To gain insight into the fundamental physics of thermal transport of  $\text{UAl}_2$ , the mode wise group velocities ( $v_g$ ) and the lifetimes of phonons are plotted in Fig. 4.7. As expected, the group velocity of the acoustic phonons is higher than those of optical phonons. The maximum group velocities of TA1, TA2 and LA branches are 2.89, 3.03 and 4.62  $\text{km.s}^{-1}$  respectively. Phonon lifetimes also showed similar trends as  $v_g$ . The phonon lifetime of the acoustic vibrations at 0.21, 0.31 and 1.27 THz were 382.41, 329.26 and 402.81 ps respectively. Whereas, the longest lifetime of the optical vibrations (maximum of 118.3 ps), lied between 2.18 and 2.57 THz, while all other high-frequency optical modes had a lifetime below 10 ps. Hence having both the large group velocities and longer scattering time, the acoustic modes dominate over the optical contribution in the thermal transport.

Grüneisen parameter ( $\gamma$ ) the measure of the strength of the anharmonicity of a material is another important characteristic that determines the lattice thermal conductivity. It is well known that the lifetime of Umklapp process is inversely proportional to  $\gamma^2$ , which means higher the value of  $\gamma$ , the smaller the heat transport. Figure 4.8a illustrates that the average  $\gamma$  increases as a function of temperature, suggesting a decrease in thermal transport. Additionally, Fig. 4.8b indicates that the mode-wise contributions of the  $\gamma$  at 300 K varied between -0.50 and 2.10.

Finally, the dependence of the normalized cumulative  $\kappa_{ph}$  on phonon MFP at 300 K, 500 K, 1000 K and 1500 K are described in Fig. 4.9. The normalized  $\kappa_{ph}$  increases with the increase in MFP. At 300 K, a significant contribution ( $\sim 80\%$ ) to the  $\kappa_{ph}$  is given by the phonons with MFP between 76 nm to 1  $\mu\text{m}$  and at 1500 K, this range reduces to 20 nm to 300 nm.

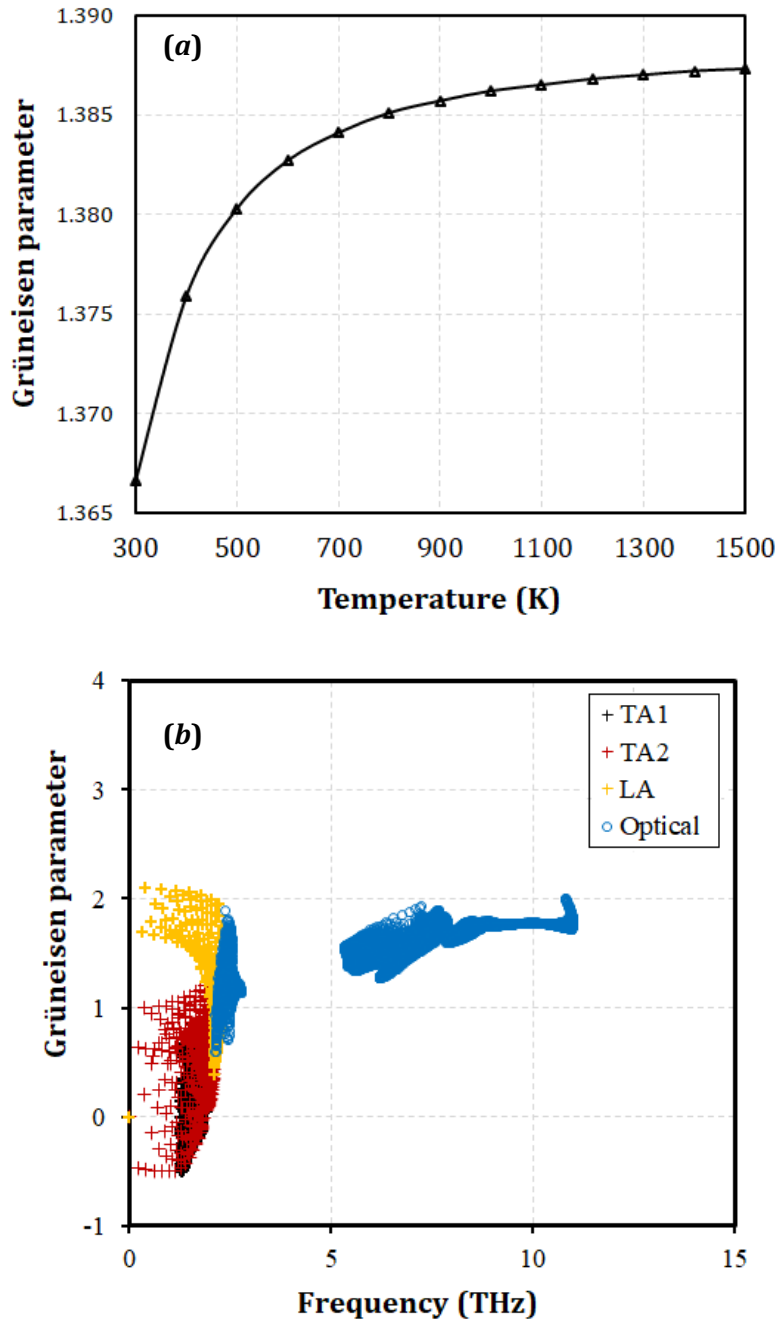


**Figure 4.8:** (a) the averaged Grüneisen parameter (b) the mode contributions of the Grüneisen parameter at 300 K. The TA1, TA2 and LA modes are shown by black, red and yellow cross marks. All optical modes are represented by blue circles.

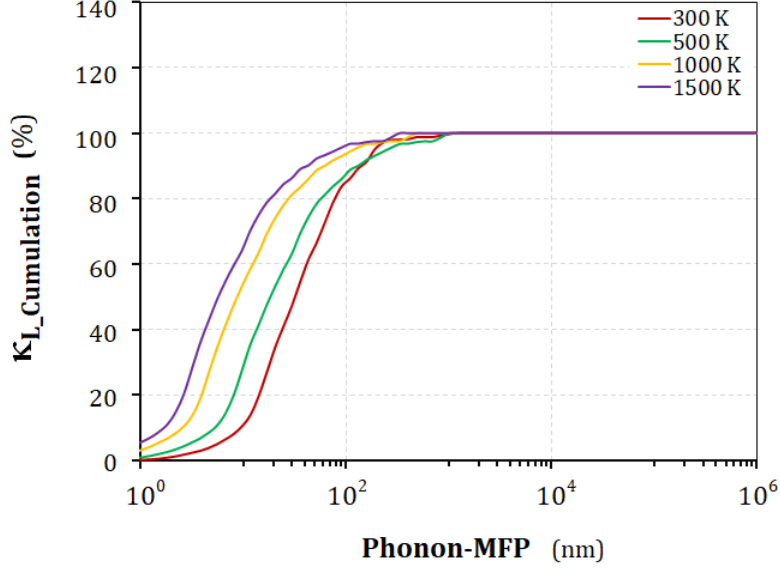


**Figure 4.9:** Lattice thermal conductivity cumulation ( $\kappa_{ph\_cumulation}$ ) as a function of mean free path (MFP). Red, green, yellow, and purple lines show the cumulation at 300, 500, 1000 and 1500 K respectively.

#### 4.3.3.2 Electronic thermal contribution and the total thermal conductivity

The temperature dependence of  $C_p^{el}$  and the electrical conductivity ( $\sigma$ ) are given by the relations in Eq. (4.7) and (4.8):

$$C_p^{el}(T, \mu) = \int (\epsilon - \mu) n(\epsilon) \left[ -\frac{\partial f_{ik}(T, \mu)}{\partial \epsilon} \right] d\epsilon \quad (4.7)$$

$$\sigma(T, \mu) = \frac{e^2}{\Omega} \int \sum_{i\mathbf{k}} v_{i\mathbf{k},\alpha} v_{i\mathbf{k},\beta} \tau_{i\mathbf{k}} \left[ -\frac{\partial f_{ik}(T, \mu)}{\partial \epsilon} \right] d\epsilon. \quad (4.8)$$

where the symbols  $\mu$ ,  $e$ ,  $\Omega$ ,  $\epsilon$ , and  $f$  represent the chemical potential, electron charge, unit cell volume, energy eigenvalue, and the Fermi distribution function respectively,  $n(\epsilon) = \int \sum_i \delta(\epsilon - \epsilon_{i,\mathbf{k}}) \frac{d\mathbf{k}}{8\pi^3}$  is the number of conduction electrons per unit volume which can be derived

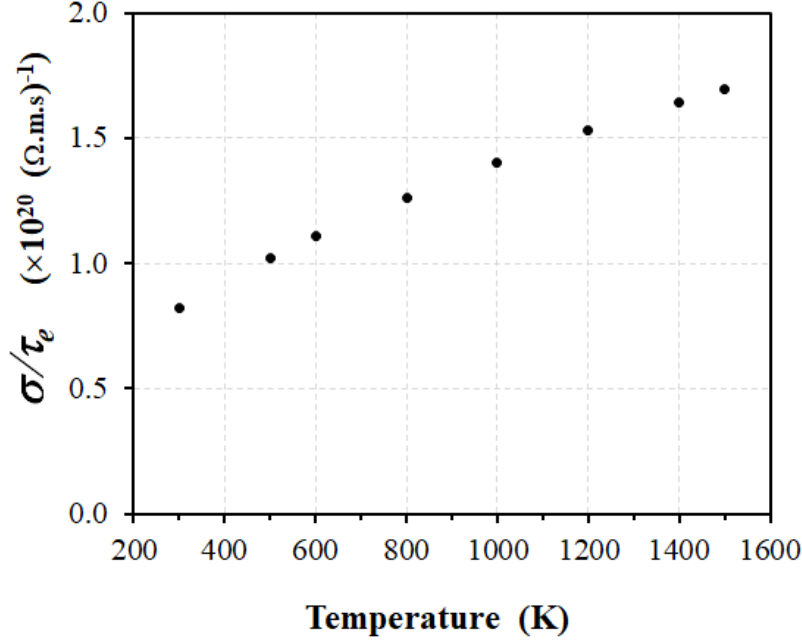


**Figure 4.10:** Temperature dependence of the electrical conductivity with respect to electron relaxation time ( $\sigma/\tau_e$ ).

from the electron density of states, and the group velocity  $v_{ik,\alpha} = \frac{1}{\hbar} \frac{\partial \epsilon_{ik}}{\partial k_\alpha}$  is evaluated as the first derivative of the electronic bands. In all the terms,  $i$  represents the band index and  $\mathbf{k}$  stands for the wave vector. First, the BTE is solved for the FM state of  $\text{UAl}_2$  within the constant relaxation time (CRTA) and rigid band approximations using the BoltzTraP code<sup>57</sup>, and  $\sigma$  and  $C_p^{el}$  are evaluated according to Eqs. (4.7) and (4.8). The results of  $C_p^{el}$  are shown in Fig. 4.5 and explained in the section 3.2.1. Figure 4.10a shows the predicted electrical conductivity over the temperature range from 300 to 1500 K relative to the electron relaxation time ( $\sigma/\tau_e$ ). Within this temperature region  $\sigma/\tau_e$  varies from  $0.82 (\Omega \cdot \text{m} \cdot \text{s})^{-1}$  (at 300 K) to  $1.64 (\Omega \cdot \text{m} \cdot \text{s})^{-1}$  (at 1500 K) showing a linear progression. However, this behaviour is valid only with CRTA and the exact  $\tau_e(T)$  is essential for an absolute  $\sigma$  behaviour. It is known that the relaxation time is the inverse of the scattering time (also known as the linewidth) and the electron scattering time is proportional to the imaginary part of the electron self-energy ( $\Sigma_{nk}''$ ). Therefore, when the electron self-energy is available,  $\tau_e$  can be derived using the relation,

$$\tau_e = \frac{\hbar}{2\Sigma_{nk}}. \quad (4.9)$$

In this work, the electron-self energies are evaluated for the NM phase of  $\text{UAl}_2$  using the EPW code<sup>58</sup> and then the relaxation times are calculated using Eq. (4.9). Figure 4.11 illustrates our predictions for the inverse of the relaxation time as a function of temperature and it shows a linear dependence on  $T$  which can be fitted to the equation,  $\frac{1}{\tau_e} = 0.0008T + 0.0011 (\times 10^{15} \text{s}^{-1})$ . It is important to note here that, the resultant relaxation time is taken as the average of those with energies  $|\epsilon - \epsilon_F| < k_B T$ . Furthermore, since the electron-phonon coupling in FM materials are stronger than to the NM phase, it limits the relaxation time resulting higher scattering rates. Therefore  $\frac{1}{\tau_e}$  for the FM phase of  $\text{UAl}_2$  should be higher than to the values shown in Fig. 4.11. Knowing the values of  $\sigma/\tau_e$  and  $\tau_e$ , the absolute values of  $\sigma$  and hence the electrical resistivity ( $\rho$ ) were evaluated. As shown in Fig. 4.12, we observe a continuous increase in  $\rho$  over the temperature range studied, and the best fit polynomial to the data is given in the Table 4.2. Compared with literature, our predictions are in a fair agreement<sup>198–200</sup> below 300 K. However, the current work overestimates  $\rho$  at higher temperatures compared to previously reported values by Mei *et al.*<sup>52</sup> and Wire *et al.*<sup>200</sup>. One of the possible reasons for this disagreement can be originated from the error made in the present work by using NM phase for calculating the relaxation time. Deviation from Mei *et al.*<sup>52</sup> is referred to the methodological differences between the two calculations where they used a semi-empirical method to evaluate the relaxation time by linear fitting with the experimental  $\rho$  by Armbrüster *et al.*<sup>199</sup>. For the discrepancy with Wire *et al.*<sup>200</sup>, the impact by the uncertainty of the results due to the metallurgical quality of their samples as well as the other unavoidable experimental errors also needs to be considered.

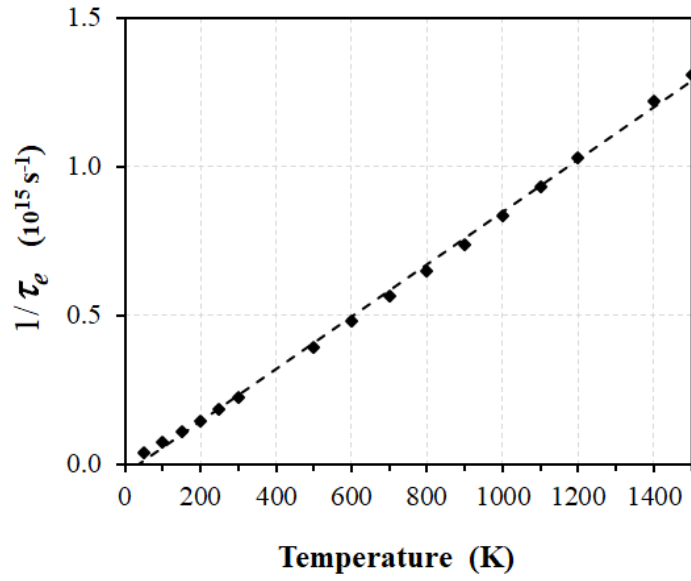


**Figure 4.11:** Temperature dependence of scattering time ( $1/\tau_e$ ).

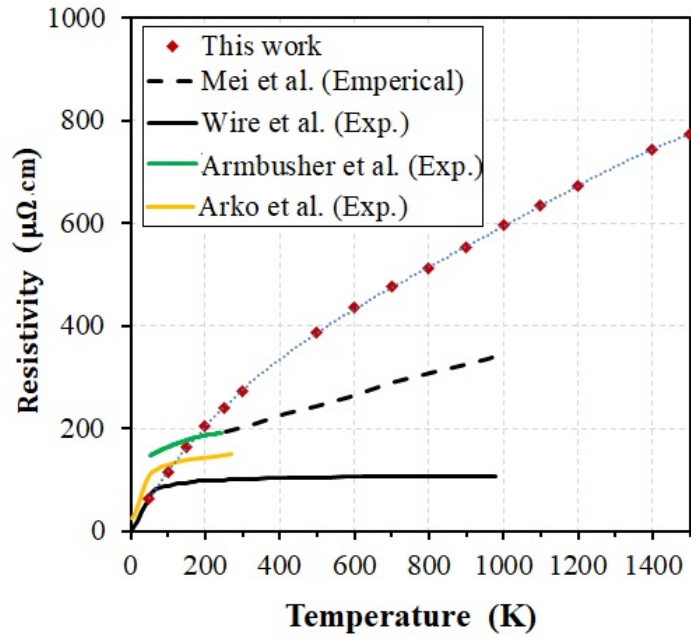


**Figure 4.12:** Temperature dependence of absolute resistivity ( $\rho$ ) of  $\text{UAl}_2$ .



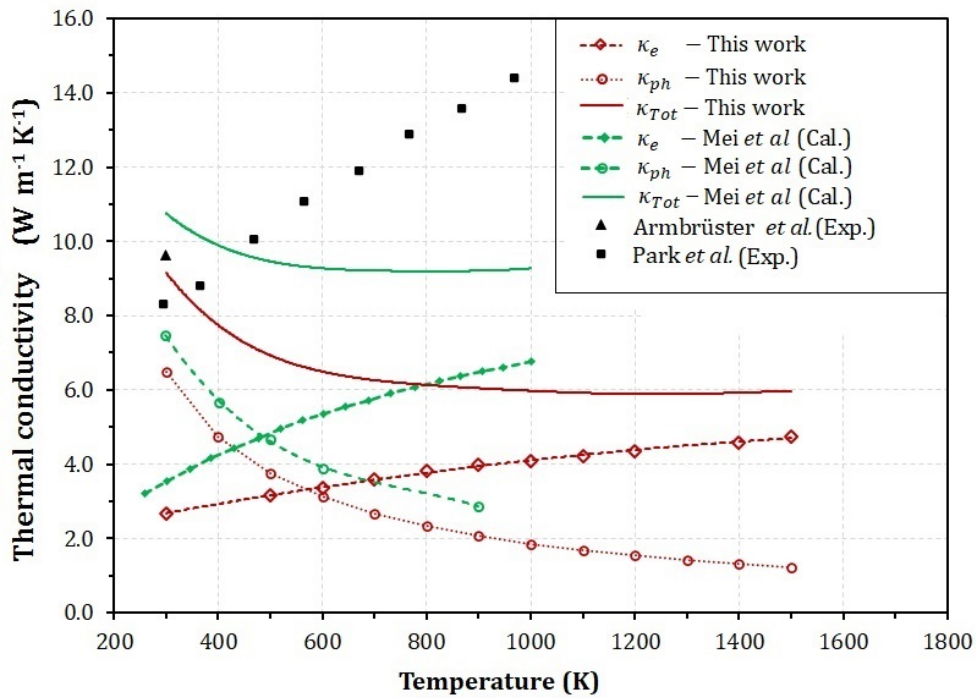


**Figure 4.13:** Total thermal conductivity of  $\text{UAl}_2$ . The red dashed lines with circles and diagonals show the respective lattice ( $\kappa_{ph}$ ) and electronic ( $\kappa_e$ ) contributions to the total thermal conductivity predicted in this work. Red solid line gives the total thermal conductivity ( $\kappa_{Tot} = \kappa_{ph} + \kappa_e$ ). The same interpretation is valid for the green color which shows the predictions by Mei *et al.*<sup>52</sup>. The black solid triangle represents the experimental prediction at 300 K by Armbruster *et al.*<sup>199</sup>. The black solid squares show the experimental work by Park *et al.*<sup>201</sup>.

Electrical conductivity couples with electronic thermal conductivity via Wiedemann-Franz law<sup>95</sup>,

$$\kappa_e = L_0 \sigma T \quad (4.10)$$

where  $L_0$  is an empirical parameter called Lorentz number and for metallic materials,  $L_0 \approx \frac{\pi^2}{3} \left[ \frac{k_B}{e} \right]^2 = 2.45 \times 10^{-8} \text{ W } \Omega \text{ K}^{-2}$ . Having predicted  $\sigma$  as explained before, we evaluated the electronic thermal conductivity using Eq. (4.10). As shown in Fig. 4.13,  $\kappa_e$  increases with temperature and this variation can be fitted to a second-order polynomial (Table 4.2). It was found that the value at 300 K ( $2.68 \text{ W m}^{-1} \text{ K}^{-1}$ ) increases by  $\sim 43\%$  when the temperature rises to 1500 K ( $4.73 \text{ W m}^{-1} \text{ K}^{-1}$ ). Analogous with the underestimation of our  $\sigma$  as explained before, the results of  $\kappa_e$  has been underestimated compared to Mei *et al.*<sup>52</sup>. Thereafter, the total thermal conductivity  $\kappa_{Tot}$  is calculated as the algebraic summation of  $\kappa_{ph}$  and  $\kappa_e$ , which is the red solid line in Fig. 4.13. We found that total thermal conductivity decreases over the temperature range from 300 K ( $9.16 \text{ W m}^{-1} \text{ K}^{-1}$ ) to 600 K ( $6.49 \text{ W m}^{-1} \text{ K}^{-1}$ ) showing a 29% reduction and then becomes almost a plateau ( $5.97 \text{ W m}^{-1} \text{ K}^{-1}$ ) which has reduced only by 5% by 1500 K. A similar trend is observed in Mei *et al.*,<sup>52</sup> however, they have overestimated  $\kappa_{Tot}$  compared to ours mainly due to their overestimation of  $\kappa_e$ . Our prediction for  $\kappa_{Tot}$  at 300 K ( $9.16 \text{ W m}^{-1} \text{ K}^{-1}$ ) is in very good agreement with the experimental works reported by Armbrüster *et al.*<sup>199</sup> ( $9.64 \text{ W m}^{-1} \text{ K}^{-1}$ ) and Park *et al.*<sup>201</sup> ( $8.28 \text{ W m}^{-1} \text{ K}^{-1}$ ). However, our results disagree with the predictions by Park *et al.*<sup>201</sup> at higher temperatures where they have observed an increasing trend in  $\kappa_{Tot}$  over all the temperatures up to 1000 K. There are two main causes for this discrepancy; As mentioned earlier, since the current work overestimates  $\rho$ , the estimated  $\kappa_e$  as well as  $\kappa_{Tot}$  can be smaller than the expected values. The other reason for the disagreement can be attributed to the possible experimental errors. For an example, it is well discussed in the literature that having pure single crystals of  $\text{UAl}_2$  is a major challenge because of the chemical reaction of  $\text{UAl}_2 + \text{Al} \rightarrow \text{UAl}_3$ , which is difficult to avoid in most of the cases. Therefore, high thermal conductive  $\text{UAl}_3$  impurities can be the reason for observing a higher thermal conductivity in experimental works relative to the calculated values.

## 4.4 Conclusion

In summary, we have systematically investigated the thermomechanical properties which are thermal expansion, density, and bulk modulus of  $\text{UAl}_2$  using QHA, and their temperature dependence functions have been predicted. Further, we carried out a comprehensive, fully *ab initio* method to evaluate the total thermal conductivity including the absolute electronic part of thermal conductivity. This work gives the thermal conductivity of bulk samples of pure  $\text{UAl}_2$  for temperatures in the range from 300 to 1500 K. Regarding the phonon-assisted thermal transport, we found that both the iterative and relaxation time approximation methods were able to accurately predict the lattice thermal conductivity. Mode dependent analysis shows a strong contribution from acoustic as well as optical modes, where the exact contributions are 69% ( $4.17 \text{ W m}^{-1} \text{ K}^{-1}$ ) and 66.2% ( $0.76 \text{ W m}^{-1} \text{ K}^{-1}$ ) from acoustic and 31.0% ( $2.01 \text{ W m}^{-1} \text{ K}^{-1}$ ) and 33.8% ( $0.47 \text{ W m}^{-1} \text{ K}^{-1}$ ) from optical vibrations at 300 and 1500 K respectively. Apart from that, the temperature-dependent electron scattering rates (which is the inverse of the relaxation time) associated with the electron-phonon scattering has been predicted for the first time using an *ab initio* method. It directly proportional to the temperature; the corresponding values at 300 and 1500 K are  $0.22 \times 10^{-15} \text{ s}^{-1}$  and  $1.31 \times 10^{-15} \text{ s}^{-1}$ , respectively. Finally, this work predicts a stable total thermal conductivity of around  $5.9 \text{ W m}^{-1} \text{ K}^{-1}$  after 600 K. With this conclusion, we note here that the thermal conductivity of  $\text{UAl}_2$  performs well over the traditional fuel  $\text{UO}_2$  indicating the possibility of testing them in power reactors.

## Chapter 5

### Comprehensive study on the electronic and optical properties of $\alpha$ - $U_3O_8$

This chapter covers the fourth objective of the thesis. It presents DFT-based computational results on optical properties of  $U_3O_8$  obtained using WIEN2k software package. Apart from the electronic structure investigation, it also presents a comprehensive work on real and imaginary parts of the dielectric tensor, absorption coefficient, optical conductivity, refractive index, and Loss-function. Further, this chapter describes the experimental work on bandgap investigation based on the diffuse reflectance spectra (DRS) method.

The research findings reported in this chapter have been published as follows:

Ranasinghe, J.I., Malakkal, L., Jossou, E., Szpunar, B., Szpunar, J.A., Comprehensive study on the electronic and optical properties of  $\alpha$ - $U_3O_8$ , Computational Materials Science, 171, (2020).

The contribution of the Ph.D. candidate are:

(1). Performing the DFT based calculation on electronic and optical properties (2). Analysis of the data, (3). Powder sample characterization and experimental measurement of the bandgap, (4). Manuscript preparation. The supervisors reviewed the full work before publication.

# Comprehensive study on the electronic and optical properties of $\alpha$ - $U_3O_8$

Jayangani I. Ranasinghe\*<sup>a</sup>, Linu Malakkal<sup>b</sup>, Ericmoore Jossou<sup>b</sup>, Barbara Szpunar<sup>a</sup>, and Jerzy A. Szpunar<sup>b</sup>

<sup>a</sup>*Department of Physics and Engineering Physics, University of Saskatchewan, CA*

<sup>b</sup>*Department of Mechanical Engineering, University of Saskatchewan, CA*

## 5.0 Abstract

Triuranium octoxide ( $U_3O_8$ ), the most stable form of uranium oxide, is an important material that finds application in the nuclear industry. The understanding of the electronic, magnetic, and optical properties of  $U_3O_8$  is essential for these advanced applications. Therefore, in this work, we have performed the density functional theory (DFT) study to investigate the structural, electronic, magnetic, and optical properties of the low-temperature orthorhombic phase of  $U_3O_8$  ( $\alpha$ - $U_3O_8$ ) within the generalized gradient approximation (GGA) by using WIEN2k software package. To capture the highly correlated nature of  $5f$  electrons in uranium atoms, an on-site Coulomb repulsion term (Hubbard- $U$ ) of 4.5 eV was considered. Further, the effect of spin orbital coupling (SOC) on the electronic structure and band gap of  $\alpha$ - $U_3O_8$  is demonstrated. Work functions ( $\phi$ ) were evaluated for the planes (001), (100), (010) and (111) using the first principles code Quantum ESPRESSO (QE). This study verifies the importance of SOC on structural, electronic, and optical properties of  $\alpha$ - $U_3O_8$  and claims for an indirect theoretical band gap- $E_g$  of 2.03 eV, verifying the semiconductor behaviour. The optical anisotropy is analyzed through the frequency-dependent optical properties, namely, the real and imaginary parts of the dielectric tensor ( $\epsilon_1(\omega)$  and  $\epsilon_2(\omega)$ ), absorption coefficient ( $\alpha(\omega)$ ), optical conductivity ( $\sigma(\omega)$ ), refractive index ( $n(\omega)$ ), and Loss-function ( $L(\omega)$ ). By comparing the Fermi energy and the vacuum level energy, the work functions for the planes (100), (001), (010) and (111) are predicted as 6.31, 6.73, 7.01, and 7.03 eV, respectively. Furthermore, in this article, we present our experimental investigation of  $E_g$  based on the diffuse reflectance spectra (DRS) method. Measured DRS of three powder samples are analyzed using the Kubelka-Munk model. Three powder samples, namely 1wt%, 2wt%, and 4wt%

of  $\text{U}_3\text{O}_8$  diluted with KCl show that  $\text{U}_3\text{O}_8$  exhibits semiconducting behaviour with indirect band gaps of 1.86, 1.81, and 1.72 eV, respectively.

## 5.1 Introduction

Uranium dioxide or Urania ( $\text{UO}_2$ ) is the primary fuel in most commercial light water nuclear power reactors<sup>202–204</sup>. Therefore, the uranium-oxygen system has been the subject of numerous theoretical and experimental studies for decades<sup>202,205–207</sup>. Depending on the temperature and the oxygen partial pressure in the environment,  $\text{UO}_2$  exists in several hyper-stoichiometric solid oxides<sup>208–210</sup>. Among these hyper-stoichiometric solid oxides, tri-uranium octoxide ( $\text{U}_3\text{O}_8$ ) is the most stable oxidation state of  $\text{UO}_2$ . During the oxidation of  $\text{UO}_2$  to  $\text{U}_3\text{O}_8$ , the volume expands by nearly 36%, which is determinantal for the integrity of the fuel element and cladding<sup>211</sup>. Since  $\text{U}_3\text{O}_8$  is the most stable oxide of Urania and undergoes only minimal volume expansion,  $\text{U}_3\text{O}_8$  is considered the safest material for storing nuclear wastes<sup>211</sup>. Moreover,  $\text{U}_3\text{O}_8$  is also used as dispersed fuels for research reactors<sup>23,212,213</sup>.  $\text{U}_3\text{O}_8$  mainly has three different crystalline phases; the ground state  $\alpha$  and  $\beta$  (obtained only under special circumstances<sup>214</sup>) phases, and the high temperature  $\gamma$  phase<sup>208,209</sup>. The X-ray powder diffraction and neutron diffraction investigations revealed an orthorhombic structure for  $\alpha$  and  $\beta$  phases,<sup>139,214</sup> and a hexagonal structure for the  $\gamma$  phase.<sup>214</sup> Among these three phases, the semiconducting behaviour of  $\alpha$ - $\text{U}_3\text{O}_8$  is well established,<sup>45,46,120,215</sup> and several previous investigations verify the possibility of making its photovoltaics<sup>45,46,216</sup>. For example, T. Meek and co-workers<sup>45</sup> have successfully designed a Schottky diode of  $\text{U}_3\text{O}_8$ . Also, there have been several experimental and theoretical investigations on mechanical,<sup>144,211</sup> electronic<sup>119,120,144</sup> thermophysical,<sup>37,144,217,218</sup> and oxidation behaviour<sup>119,120,211</sup> of  $\text{U}_3\text{O}_8$ . However, the results obtained from these studies appear to be scattered. For example, the theoretical and experimental results on bandgap- $E_g$  varied between 0 to 2.34 eV<sup>119,120,211,219</sup>. Moreover, some studies suggest  $\text{U}^{4+}/\text{U}^{6+}$  mix valency state<sup>119,120,220</sup> for uranium, while other investigations propose  $\text{U}^{5+}/\text{U}^{6+}$ .<sup>144</sup> Also, some studies predict the magnetic state of  $\text{U}_3\text{O}_8$  to be ferromagnetic (FM) and others predict antiferromagnetic (AFM) configurations.<sup>119,120,144</sup> The main reason for such scattered data in the theoretical predictions can be due to the negligence of the effect of spin-orbital coupling effect (SOC).

To resolve these aberrations, we have performed a systematic investigation of the electronic, magnetic, and optical properties of  $U_3O_8$  using the density functional theory (DFT)<sup>221</sup> by including the spin-orbital coupling (SOC). Besides, the work functions of the (001), (100), (010), and (111) surfaces were also evaluated. Furthermore, we have also performed the experimental determination of the  $E_g$  using the diffuse reflectance spectra (DRS) measurement<sup>222–224</sup>. All the presented theoretical and experimental results in this work will fill the information gaps on the properties of  $\alpha$ - $U_3O_8$  available within the literature database. Also, the results may enable the scientists in nuclear and semiconductor industry in the design of commercial level devices.

## 5.2 Computational and experimental methodology

### 5.2.1 Computational details

Theoretical investigations on electronic structure and optical properties were carried out utilizing the full-potential linearized augmented plane-wave (FP-LAPW) method using WIEN2k package<sup>225</sup>. In the first stage of the calculation, we optimized the size of the Monkhrst-Pack scheme  $k$ -mesh and the plane wave cut-off-  $R_{MT}K_{max}$  in order to achieve the energy convergence. The terms  $R_{MT}$  and  $K_{max}$  denote the smallest atomic sphere radius and the magnitude of the largest  $K$  vector in the plane-wave expansion. The cut-off energy to separate the core and the valance electron states was set to -8 Ry. The exchange-correlation effects are treated by the Perdew-Burke-Ernzerhof (PBE)<sup>226</sup> in GGA (general gradient approximations). The convergency criteria for the self-consistent calculations is taken as  $10^{-5}$  Ry and  $10^{-4}$  (in the unit of electron charge) for the total energy and the charge density respectively. Electronic structure calculations were performed with the optimized values of  $R_{MT}K_{max}=8.5$  and  $k$ -mesh of size  $21 \times 15 \times 15$  over the first Brillouin zone (FBZ). In the second step of the simulation, the magnetic behaviour of the structure is studied by applying spin polarized non-magnetic (NM), FM and AFM conditions to the U atoms in the system. By comparing the lowest energies of the systems, it is understood that the  $U_3O_8$  structure with FM behaviour is the most stable state. Therefore, the rest of the calculation is continued applying the FM spin polarized conditions to the system. It is well known that conventional density functional schemes with generalized gradient approximation (GGA) or local density

approximation (LDA), underestimate the band gap because they do not correctly capture the strong Coulomb interaction of  $5f$  electrons of actinides. Therefore, we have adopted the GGA+U approach in which the underestimated Coulomb interaction is corrected by additional parameters (Hubbard-U and J) added on uranium atoms. Here in this study, we applied an effective value of the parameter as 4.5 eV (Hubbard U), which is accepted value to capture the electronic structure and the optical properties of  $U_3O_8$  as shown in previous studies<sup>119,120</sup>. However, the improved electron correlation by LDA or GGA+U method can converge the system in a metastable state. In order to verify that we have achieved the correct ground state, we performed many independent calculations with random (unrestricted) initial occupation matrices and seven different calculations with fixed initial diagonal matrices for the  $5f$  electron configuration in the  $U^{5+}$  atom following the procedure given by Dorado *et al.*<sup>227</sup> However, we achieved the similar ground state in all the cases which is a strong indication that metastable state can be safely excluded for  $U_3O_8$ . With the aim of finding the easy magnetization direction for SOC, the energies for four types of spin alignments along [001], [010], [100] and [111] directions are compared. It is found that the system has the lowest energy and hence, it is most stable when the magnetic direction is along [010]. Thus, in this work the electronic structure and the optical properties are studied in FM structure with spin orbital coupling added along [010] low energy direction. Furthermore, we performed the electron band structure and partial density of states (pDOS) study with and without SOC and reported its effect on the  $E_g$ .

Convergence of optical properties was tested over the k-mesh and continued with a finer mesh of size  $28 \times 20 \times 20$  which achieved the convergence of the optical properties. The work functions ( $\phi$ ) of the (001), (100), (010) and (111) surfaces were evaluated by the difference between the energy of an electron in the vacuum and the Fermi energy ( $E_F$ ). We carried out this work within DFT+U+SOC technique (with Hubbard-U 4.5 eV) using the first principles code Quantum ESPRESSO (QE)<sup>60</sup> Norm conserved fully-relativistic pseudopotentials with Perdew–Burke–Ernzerhof revised for solids (PBEsol)<sup>226</sup> exchange-correlational functional within generalized gradient approximation (GGA) are used. The energy convergence is obtained with a wave vector grid of  $4 \times 6 \times 4$  and plane wave energy cutoff of 130 Ry. Brillouin-zone integration is carried out using Gaussian broadening of 0.12 Ry. Using the fully optimized structure, (111) plane is cleaved using METADISE code<sup>228</sup> and  $1 \times 1 \times 2$  supercell of the created plane with four layers is created



using the Phonopy code<sup>59</sup> followed by a fully relaxation of the atomic positions of the resulting structure. Thereafter 20 Å vacuum is built to the z-direction using VESTA program<sup>229</sup>.

## 5.2.2 Experimental Details

The high purity powder of  $\alpha$ -U<sub>3</sub>O<sub>8</sub> was obtained from Cameco Canada. The structural characterization of the powder was performed using the X-ray diffraction (XRD) using Cu  $K\alpha$  radiation with a step size of 0.02°. The obtained powder XRD pattern (Fig. 5.1a) was compared with the JCPDS database (JCPDS 96-210-6982), and its pattern revealed the U<sub>3</sub>O<sub>8</sub> has an orthorhombic structure with Amm2 space group. After that, we prepared three samples with three different U<sub>3</sub>O<sub>8</sub> concentrations (1wt%, 2wt% and 4wt% U<sub>3</sub>O<sub>8</sub> in KCl) for measuring  $E_g$  by DRS method. These three samples were used to examine the replication of the measurements and the validity of the method. The powders were fine ground using a hand motor and a pestle made of Alumina (AlO<sub>2</sub>). Scanning electron microscopy (SEM) image given in Fig. 5.1b confirms that the particles are well distributed and in the range of 1-2.5  $\mu$ m. To ensure there is no reaction between U<sub>3</sub>O<sub>8</sub> and KCl, we performed the XRD investigations of the mixed samples however, the plots are not given here for brevity. After that, the three samples were tightly filled in Quartz cuvettes with a 1 cm path length to prevent any voids. A Dual-beam Cary 5G UV-visible-NIR spectrophotometer (Agilent Technologies, Mississauga, Canada.) was employed to measure the diffuse reflectance spectrum of each of the samples for the wavelengths ( $\lambda$ ) from 900 to 300 nm with 1 nm step intervals. The reflection spectrum measured for KCl was considered as the reference. The collected experimental data were converted to Kubelka-Munk units<sup>223,224,230</sup> and then fitted to Tauc-plot<sup>231,232</sup>.

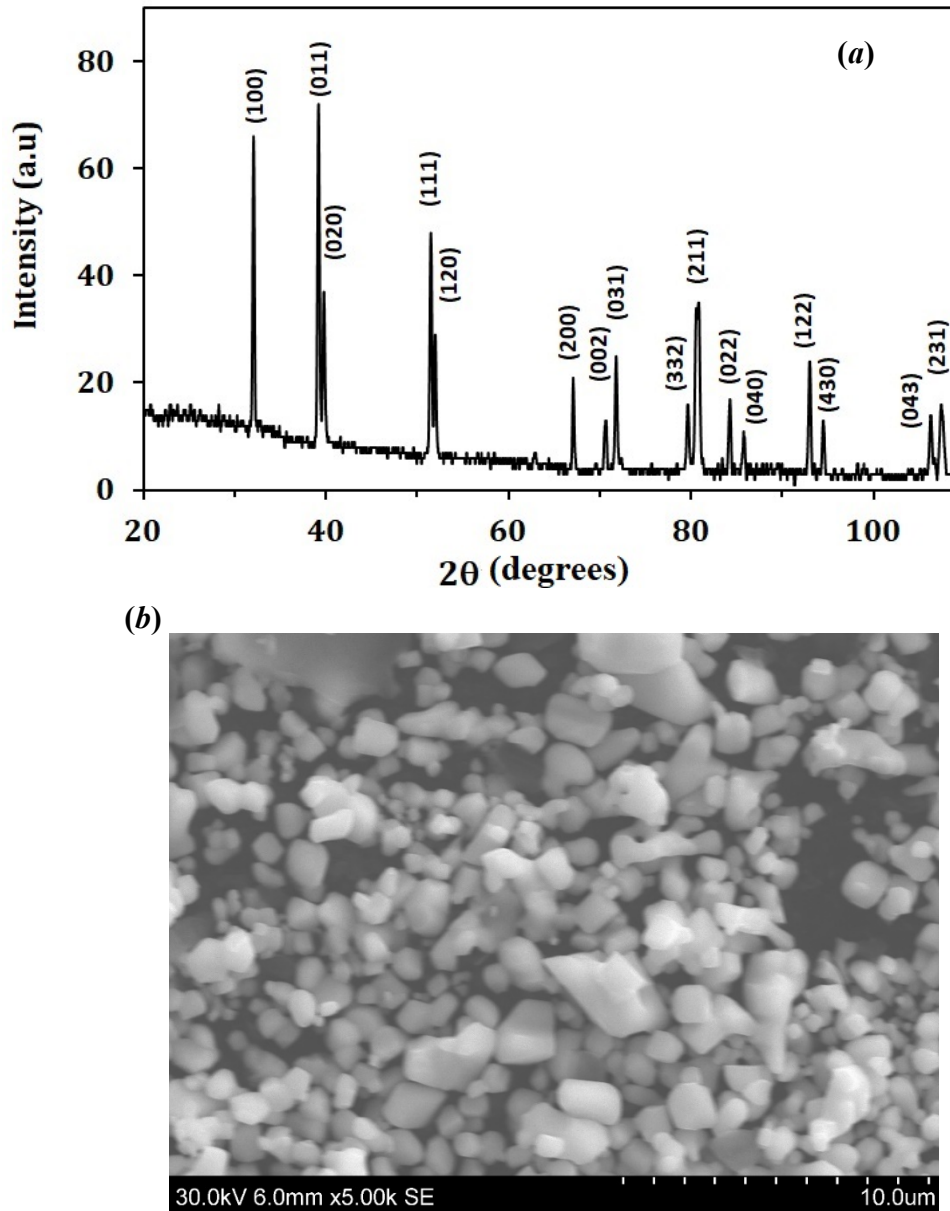


**Figure 5.1:** (a) XRD diffraction pattern of as received  $U_3O_8$  powder measured by Chromium  $K\alpha$  radiation. By comparing the JCPDS database, corresponding planes of  $U_3O_8$  for the observed peaks are shown in the figure. (b) SEM image of mixed (4wt%)  $U_3O_8$ -KCl powder sample.

## 5.3 Results and Discussion

### 5.3.1 Structural, electronic, and optical property simulation

The initial structural parameters of the  $U_3O_8$  orthorhombic structure (space group Amm2 (No. 38)) for the geometry optimization were taken from the experimental data provided by Loopstra *et al.*<sup>139</sup>. Figure 5.2a shows the comparison of the calculated ground state energy of the FM, AFM, and NM configurations via GGA, GGA+U and GGA+U+SOC methodologies. It has to be noted that the ground state energy of various cases in Fig. 5.2a are relative to the FM state under GGA scheme, and therefore the energy of the FM state under the GGA scheme is set zero. Also, the ground state energy of the AFM structure under GGA scheme with respect to the energy for FM state is 0.06 eV. It is worthwhile to note that, despite the choice of schemes FM and AFM states have comparable ground state energies, but the NM state has relatively higher energy. From the calculated ground state energies for the cases in which the SOC is considered, the FM state has the minimum energy; hence we predict that in the ground state phase  $U_3O_8$  to be FM. However, Wen *et al.*<sup>120</sup>, without considering the effect of SOC, predicted  $\alpha$ -  $U_3O_8$  to be AFM. Recently, Brincat *et al.*<sup>144</sup>, using GGA+U methodology, reported that Amm2 morphology contains minor imaginary phonon modes due to oxygen vibrations and hence is unstable. Further, they predicted that  $U_3O_8$  is paramagnetic because of the close energies obtained in both FM and AFM states. However, we argue that these minor vibrations can be weakened by including SOC as shown in several previous works based on first principles calculations<sup>233,234</sup> and equal ground state energies observed in FM and AFM states is a result of ignoring the SOC. All these findings indicate that to capture the absolute electronic and magnetic properties of  $\alpha$ -  $U_3O_8$  the SOC needs to be included. In the work done by Yun *et al.*<sup>119</sup> by including SOC, they predict FM stability of  $U_3O_8$  which is consistent with our result. We have provided the predicted structural and magnetic data in Table 5.1 whilst Fig. 5.2b and c shows the optimized lattice structure. It shows that calculated lattice parameters considering the SOC effect is in excellent agreement with experimental data with only 0.97, 0.92 and 0.90% deviations for  $a$ ,  $b$  and  $c$  respectively. This negligible change can be attributed to the fact that the experimental data are given for the room temperature structure and the simulation results are for zero Kelvin temperature. There are two types of inequivalent U atoms in the unit cell, and they are labeled as U1 and U2 in Fig. 5.2b and Fig. 5.2c.

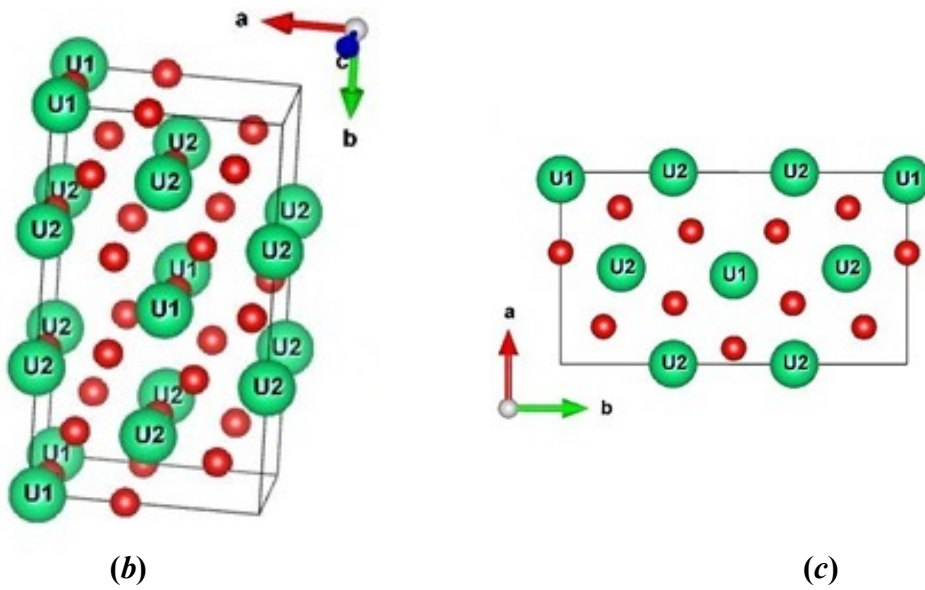
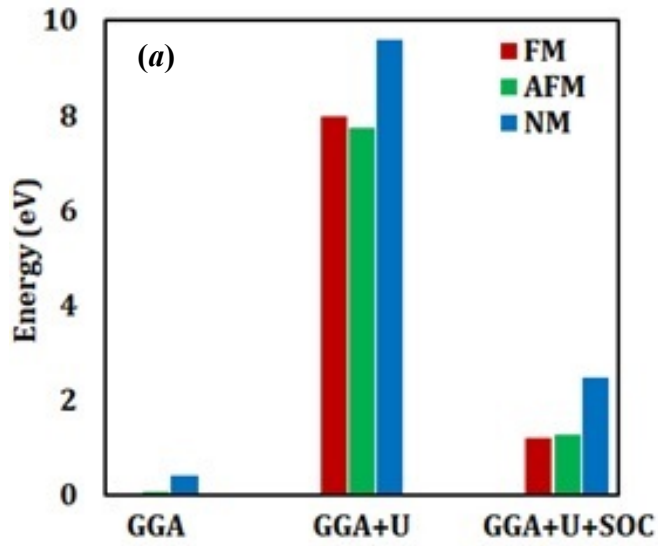


**Figure 5.2:** (a) Ground state energies of  $\alpha$ -  $\text{U}_3\text{O}_8$  relative to the FM-GGA scheme. (Energy of the AFM-GGA structure with respect to the FM-GGA state is 0.06 eV. Hence it is not visible), (b) Crystal structure of  $\alpha$ - $\text{U}_3\text{O}_8$  (Amm2), and (c) Atoms on the  $z=0$  plane. Green color U1 and U2 atoms are the inequivalent uranium atoms. Oxygens are given in red circles.

Structural optimization converged to have one U atom of type U1 and two uranium atoms of type U2. Figure 2c shows the equivalent two U atoms (U2) and the U1 are surrounded by five oxygen atoms forming two types of pentagons related to the different distances between U and O atoms.

**Table 5.1:** Predicted structural parameters ( $a$ ,  $b$  and  $c$ ), magnetic moments ( $\mu_B$ ), band gap ( $E_g$ ) and bulk modulus (B) of  $\alpha$ -U<sub>3</sub>O<sub>8</sub>.

Work	Method		$a$	$b$	$c$	$\mu_B$		$E_g$ (eV)	Space group
						U1	U2		
This work	GGA+U+SOC	FM	4.11	11.85	6.65	0.0	0.73	2.03	Amm2
	GGA + U		4.10	11.81	6.63	0.0	0.69	1.22	
	GGA		4.07	11.73	6.58	0.0	0.13	0.00	
Wen <i>et al.</i> <sup>120</sup>	HSE	AFM	4.09	11.86	6.64	0.0	1.10	0.80	C2mm
	PBE+U	AF M	4.21	11.60	7.22	0.0	1.10	1.20	
Yun <i>et al.</i> <sup>119</sup>	PW91+U+SO C	FM	4.21	11.61	7.20	0.0	1.00	0.63	C2mm
Brincat <i>et al.</i> <sup>144</sup>	PBE+U	FM	4.24	13.06	6.60	2.0	0.05	2.05	C222
He <i>et al.</i> <sup>219</sup>	Exp. PBE+U							1.76 2.43	Amm2
Loopstra <i>et al.</i> <sup>139</sup>	Exp.		4.14	11.96	6.71				Amm2

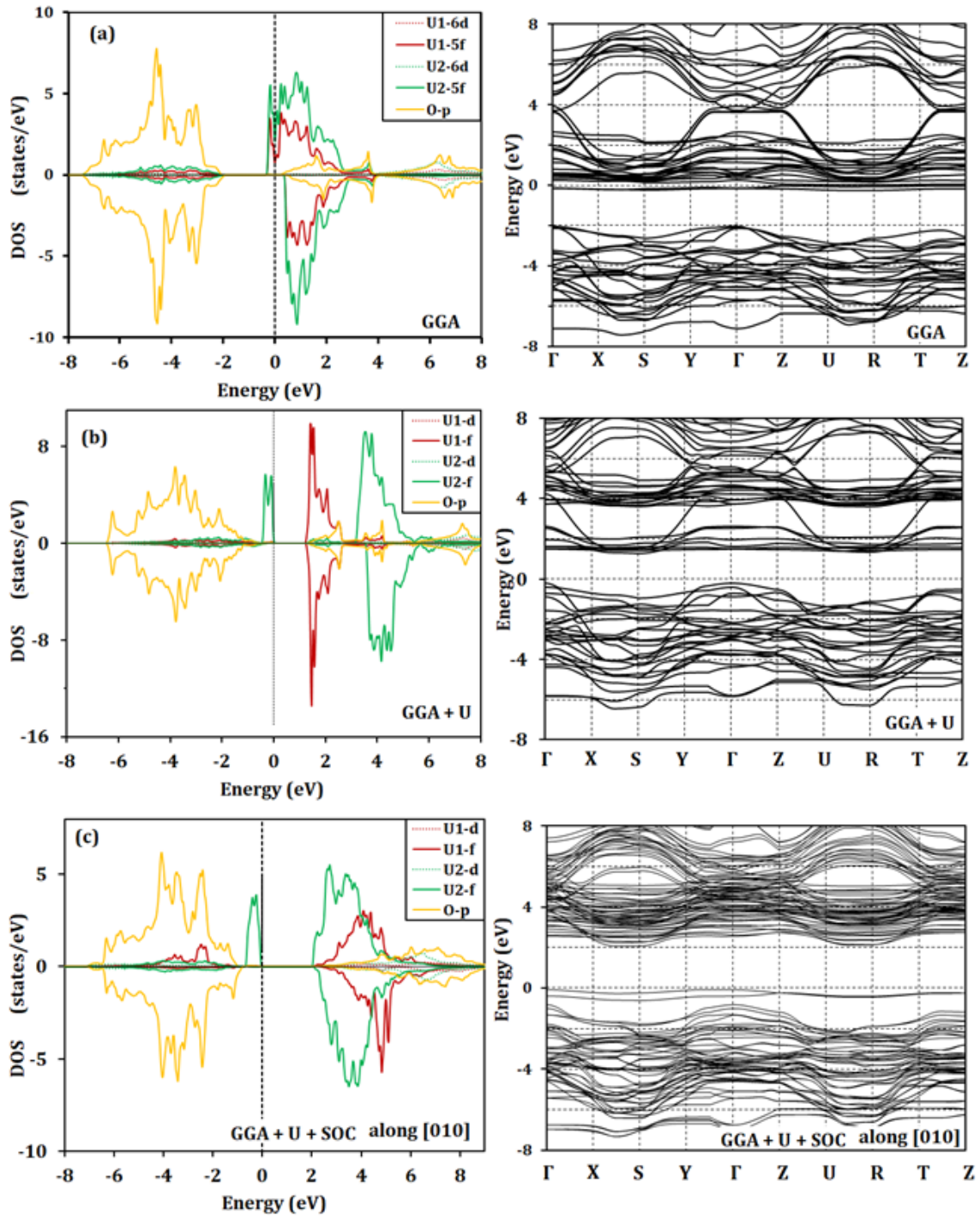


**Figure 5.3:** The pDOS (left) and the band structure (right) of  $U_3O_8$  with (a) GGA, (b) GGA+U, and (c) GGA+U+SOC conditions.

With the intention of verifying the oxidation status of the U atoms, we evaluated the magnetic moments of uranium atoms and provided in Table 5.1. We can discuss our conclusion on the oxidation behaviour as follows. In order to keep the charge neutrality, the three uranium in  $U_3O_8$  could have two possible combinations of oxidation states either as one- $U^{6+}$  and two- $U^{5+}$  or one- $U^{4+}$  and two- $U^{6+}$ . Previous XANES (X-ray absorption near-edge spectroscopy) studies at the U- $L_3$  edge<sup>235</sup> and U- $M_4$  edge<sup>236</sup> has revealed that U in  $U_3O_8$  is in  $U^{6+}/U^{5+}$  oxidation states whilst two separate theoretical investigations based on HSE (Heyd, Scuseria, and Ernzerhof hybrid functional)<sup>237</sup> and GGA functionalities supports that argument. In contrast, X-ray photoelectron spectra (XPS)<sup>238</sup> study suggests  $U^{4+}$  and  $U^{6+}$  mix valences. In this work, we observed zero magnetic moment in U1, which means that the U1 uranium atom needs to have 6+ oxidation state to agree with Hund's rule. Then the other two equivalent U2 atoms with  $0.45 \mu_B$  should share ten electrons with oxygen, making pentavalent states in U2 atoms. Thus, our study suggests having  $U^{6+}/U^{5+}$  oxidation states in uranium atoms.

Figure 5.3 illustrates the electron density of states (DOS) and the band structure of  $\alpha$ - $U_3O_8$  the results, were obtained using GGA, GGA+U and GGA+U+SOC methodologies. As shown in Fig. 5.3a, when Hubbard-U and SOC effect are neglected, the semiconducting behaviour is not detected. This predicts metallic character giving a broad  $5f$  peak crossing the Fermi level without opening any band gap. Using Hubbard-U splits the wide  $5f$  peak of U2 atoms to two narrow bands with a 3.6 eV gap while the  $5f$  bands of U1 atoms narrowed and moved toward to the higher energy region resulting 1.22 eV band gap opening. However, the reported theoretical and experimental  $E_g$  by the previous studies<sup>119,120,219</sup> and by our study (discussed in Sec. 5.3.2) is somewhat larger than this value. Hence, we examined the effect of SOC, and the results are plotted in the energy range from  $-8$  eV to 10 eV in Fig. 5.3c. From the plot, it is clear that  $\alpha$ - $U_3O_8$  is a semiconductor with indirect energy band gap 2.03 eV, which gives a better agreement with experimental observations<sup>219</sup>. Moreover, Fig. 5.3c illustrates that the valance bands are dominated by uranium  $5f$  and oxygen  $3p$  states while the conduction band is dominated by only  $5f$  electrons of both U1 and U2. In the valence band, there is a sharp narrow peak appeared close to  $E_F$  which arises from  $5f$  electrons of U2. The conduction band is dominated by the DOS of U2 atoms close to the minimum edge of the band. While the contribution of U1 atoms in the conduction bands are large within the energy range of 3 to 5 eV, oxygen contribution becomes important only after 4 eV.

Partial DOS of both U1 and U2 in Fig. 5.3c confirm that  $f$ -orbital is the principal contributor in the conduction band and the  $d$ -orbital density is negligible. For the spin-up case, there is a sharp peak due to the  $f$ -electrons of U2 atoms close to  $E_F$  in the valence band. U1 and O contribution in that peak is negligible.

The charge density counter plot is an important graphical method to understand the valence charge distribution and bonding behaviour in solids. We have employed WIEN2k<sup>225</sup> software package to get the charge density plot of the system including Hubbard U and the SOC. Figure 5.4 demonstrates the valence densities around the atoms in the (001) plane. Note that the corresponding color scheme given in the figure is in logarithmic scale. It is known that  $U_3O_8$  is not the highest oxide of uranium, and it can be further oxidized to form  $UO_3$ . The low electron density areas marked as X and Y in the plot supports the possibility of further oxidation of  $U_3O_8$ . This behaviour agrees with the finding in Yun *et al.*<sup>119</sup>.

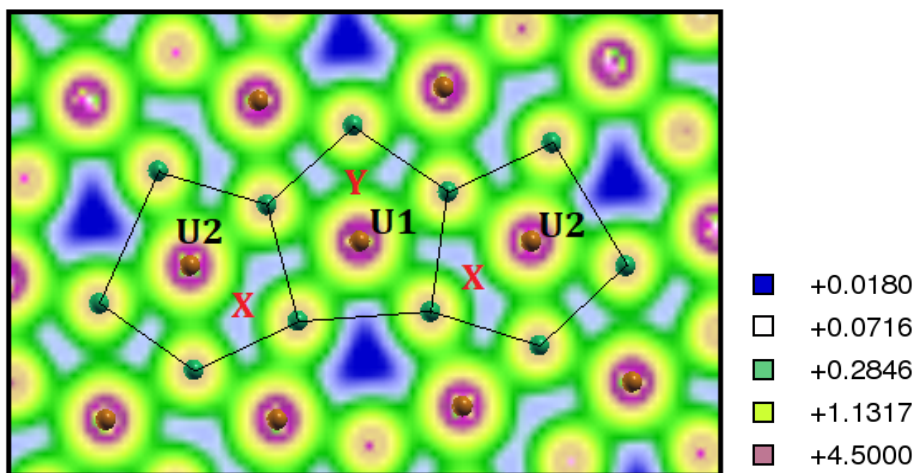


**Figure 5.4:** Charge density plot on (001) plane. X and Y shows relatively low electron densities between U-O bonds



Optical property analysis is a powerful technique to determine the suitability of a material in photovoltaic and other semiconductor applications. The optical properties of a material directly related to its complex dielectric function,  $\varepsilon(\omega) = \varepsilon_1(\omega) + i\varepsilon_2(\omega)$ , where  $\varepsilon_1(\omega)$  and  $\varepsilon_2(\omega)$  are the frequency dependent real and imaginary parts. As implemented in WIEN2k, frequency dependent  $\varepsilon_2(\omega)$  is calculated over the empty states by using Eq. (5.1)<sup>225</sup>,

$$\varepsilon_2(\omega) = \frac{4\pi e^2}{m_e^2 \omega^2} \sum_{n,n'} \int d^3k |\langle kn|p|kn'\rangle|^2 f_{kn}(1 - f_{kn'}) \delta(E_{kn} - E_{kn'} - \omega), \quad (5.1)$$

where  $e$  is the electron charge,  $m_e$  is the electron mass,  $f_{kn}$  is the Fermi distribution function, and  $p$  is the momentum matrix element between the conduction band states  $n$  and the valence band states  $n'$ . The integral in Eq. (5.1) is taken over the first Brillouin zone.

$\varepsilon_1(\omega)$  is evaluated by the Kramers-Kronig transformation as given by Eq. (5.2)<sup>225</sup>:

$$\varepsilon_1(\omega) = 1 + \frac{2}{\pi} P \int_0^\infty \frac{\varepsilon_2(\omega') \omega'}{\omega'^2 - \omega^2} d\omega'. \quad (5.2)$$

Here  $P$  implies the principal value of the integral. According to the symmetry of the orthorhombic structure, both  $\varepsilon_1(\omega)$  and  $\varepsilon_2(\omega)$  consists of three independent matrix elements as  $\varepsilon_{i_{xx}}$ ,  $\varepsilon_{i_{yy}}$ , and  $\varepsilon_{i_{zz}}$  where  $i$  is either 1 or 2<sup>225</sup>.

The dielectric function is composed of two processes named as inter-band and intra-band transitions. The intra-band contribution is important only for metallic materials; hence it is ignored in this study. Obtained results of  $\varepsilon_1$  is plotted in Fig. 5.5a as a function of energy where red, green and blue lines attribute to its  $x$ ,  $y$  and  $z$  components respectively. In general,  $\varepsilon_1(\omega)$  gives information on the strength of polarizability of materials and the figure clarifies an anisotropic behaviour of the polarization strength of  $\alpha$ -U<sub>3</sub>O<sub>8</sub>. Moreover, the graph clearly shows that the  $x$ ,  $y$  and  $z$  components of  $\varepsilon_1$  are negative in the energy ranges from 6.59 to 14.5 eV, 9.08 to 14.96 eV and 9.17 to 15.02 eV which means that the incident photons with the energies within those regions will be totally reflected showing metallic behaviour. The components of the static dielectric function  $\varepsilon_1(0)$  along  $x$ ,  $y$  and  $z$  directions are found to be 4.51, 4.08 and 4.3, which is equivalent to an average of 4.3. This average value is usually considered as the dielectric constant of a material. Figure 5.5b illustrates the behaviour of the three components of  $\varepsilon_2$  in the energy range

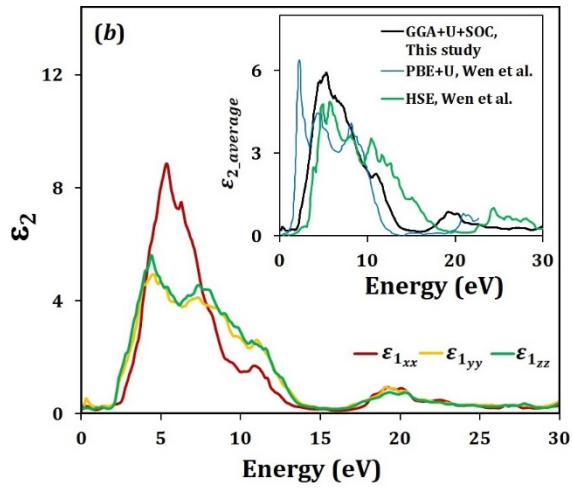
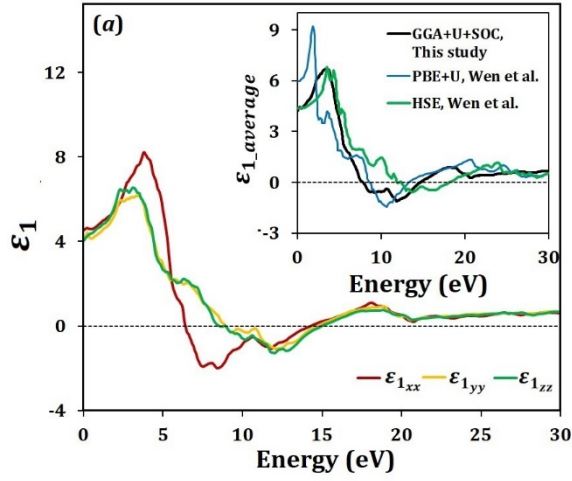


**Figure 5.5:** Components of (a) Real ( $\epsilon_1$ ) and (b) imaginary ( $\epsilon_2$ ) parts of dielectric function. The insets of both (a) and (b) are a comparison of respective average values of this study with the results from a system with AFM state by Wen *et al.*<sup>120</sup>

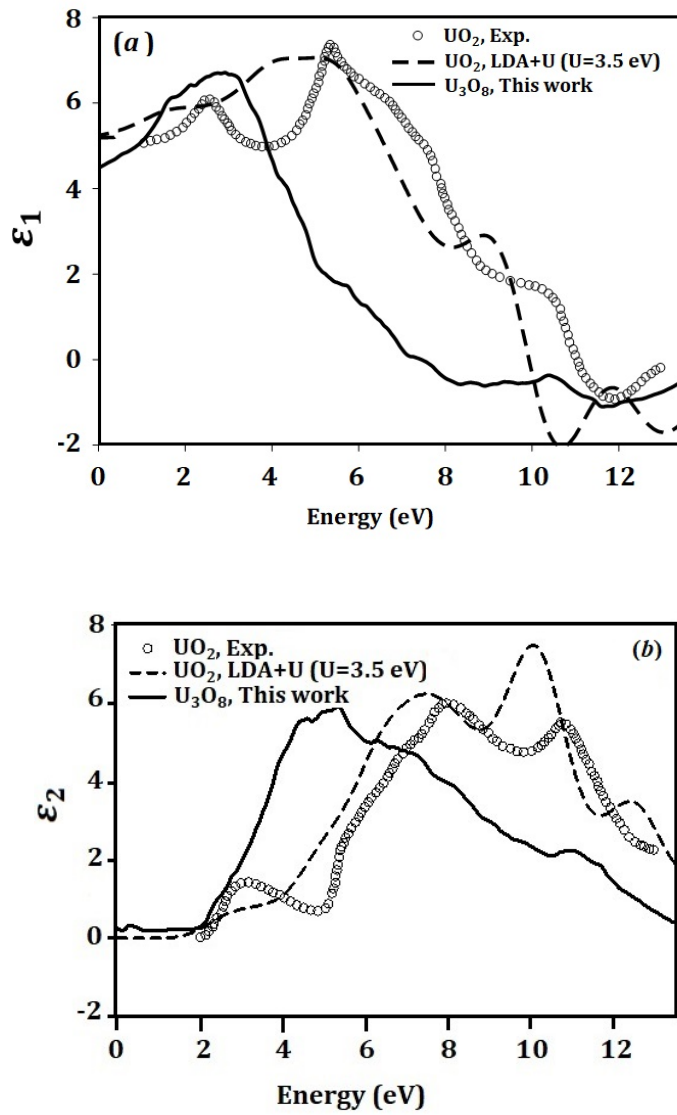


**Figure 5.6:** Comparison of (a) real ( $\epsilon_1$ ) and (b) imaginary ( $\epsilon_2$ ) parts of dielectric function of  $\text{U}_3\text{O}_8$  with our previous calculation on  $\text{UO}_2$ <sup>214</sup>. Experimental data are taken from Ref 251.

from 0 to 30 eV. It also shows anisotropic behaviour and absorption edges around 2.16, 2.03 and 2.01 eV correspondingly when an electric field is along  $x$ ,  $y$  and  $z$  directions. For the reason that  $\varepsilon_2$  is a reflection of the optical absorption strength of a material, we can predict from Fig. 5.5b that the photons with energies between  $\sim 2.01$  to 13.95 eV are well absorbed. Which means that  $U_3O_8$  is a better absorber for the ultraviolet (UV) region of the electromagnetic spectrum. The insets of Fig. 5.5a and b compare the average values of  $\varepsilon_1$  and  $\varepsilon_2$  in our study with the results of the work by Wen *et al.*<sup>120</sup>. It has to be added that Wen *et al.*<sup>120</sup> consider AFM states in their studies and the SOC is neglected. The graph shows that the predicted values by Wen *et al.*<sup>120</sup> by using screened hybrid functional has very similar behaviour as the GGA+U+SOC method. In Fig. 5.6, we compare the results of our previous work<sup>36</sup> on the dielectric spectrum of  $UO_2$  by LDA+U method using CASTEP code. Experimental data from a previous study on the dielectric function of  $UO_2$ <sup>239</sup> is given for comparison. It shows that the static dielectric function,  $\varepsilon_1(0)$  of  $U_3O_8$  which is 4.3 is less than to that of  $UO_2$  (5.4). The main peaks of  $\varepsilon_1(\omega)$ -curve in  $U_3O_8$  are shifted to the lower region of the energy axis. The calculated absorption limit of  $UO_2$  was 2.01 with  $U=3.5$  eV.

It is known that there are several other optical responses of a material, such as absorption coefficient  $\alpha(\omega)$ , optical conductivity  $\sigma(\omega)$ , refractive index  $n(\omega)$ , and energy-loss function  $L(\omega)$ , which are related to its dielectric function. The explicit expressions used in WIEN2k simulation package to derive the properties mentioned above are given in the equations (5.3) to (5.6), respectively<sup>225</sup>:

$$\alpha(\omega) = \sqrt{2}\omega \left[ \sqrt{\varepsilon_1(\omega)^2 + \varepsilon_2(\omega)^2} - \varepsilon_1(\omega) \right]^{1/2} \quad (5.3)$$

$$\sigma(\omega) = \frac{\omega \varepsilon_2}{4\pi} \quad (5.4)$$

$$n(\omega) = \left[ \frac{\sqrt{\varepsilon_1(\omega)^2 + \varepsilon_2(\omega)^2} + \varepsilon_1(\omega)}{2} \right]^{1/2} \quad (5.5)$$

$$L(\omega) = \frac{\varepsilon_2(\omega)}{\sqrt{\varepsilon_1(\omega)^2 + \varepsilon_2(\omega)^2}}. \quad (5.6)$$

Figure 5.7 shows the frequency-dependent  $\alpha(\omega)$ ,  $\sigma(\omega)$ ,  $n(\omega)$  and  $L(\omega)$  spectrums calculated by employing Eqs. (5.3) - (5.6). The absorption coefficient reflects the strength of a material to absorb

the incident light. The evaluated  $\alpha(\omega)$  spectrum has anisotropy, as shown in Fig. 5.7a. It shows similar behaviour as the imaginary part of the dielectric tensor and reveals that the best absorption occurs at the blue end of the visible spectrum and within the UV region of the electromagnetic spectrum. Further, the main absorption peaks observed at 5.1 eV, and it is 12.04 and 12.01 eV when the electric field is parallel to  $y$  and  $z$  directions, respectively. Further, this graph reflects that even though the absorption is anisotropic, the intensity of the peaks and the width of the absorption are nearly the same indicating the same absorption along all the directions. Refractive index is one of the principle characteristics of defining the electronic and optical properties of a material. The calculated three components of the refractive index spectrum using the GGA+U+SOC method are presented in Fig. 5.7c. The behaviour of  $n_{yy}$  and  $n_{zz}$  is relatively similar to each other for all the calculated photons in the energy range from 0-30 eV. The obtained static refractive indices  $n_{xx}(0)$ ,  $n_{yy}(0)$  and  $n_{zz}(0)$  are 2.11, 2.05 and 2.05 respectively. The maximum values are obtained for the photon energies in the UV region. The loss function is an indicator of the energy loss of electron when passing through a dielectric medium. Figure 5.7d represents the average values of  $L(\omega)$ , and it has a clear peak at the energy range, which matches with the minimum of conductivity  $\sigma(\omega)$ .

Work function ( $\phi$ ) can be considered as an indicator for the stability of a surface because its higher values reflect the difficulty for an electron to escape the surface. This study predicts work functions of 6.31, 6.73, 7.01 and 7.03 eV for (100), (001), (010) and (111) planes respectively. Therefore, we can predict that the planes, (010) and (111) are relatively equally stable. However, to the best of the author's knowledge, there are no previous experimental or theoretical studies to compare our results. Instead, we compared our results with the experimental evaluations of  $\text{UO}_2$  for  $\phi$  of the planes (100) and (111) by Young *et al.*<sup>240</sup> which is 5.56 and 5.66 eV respectively. This comparison indicates lower stability of  $\text{UO}_2$  compared to  $\text{U}_3\text{O}_8$ .

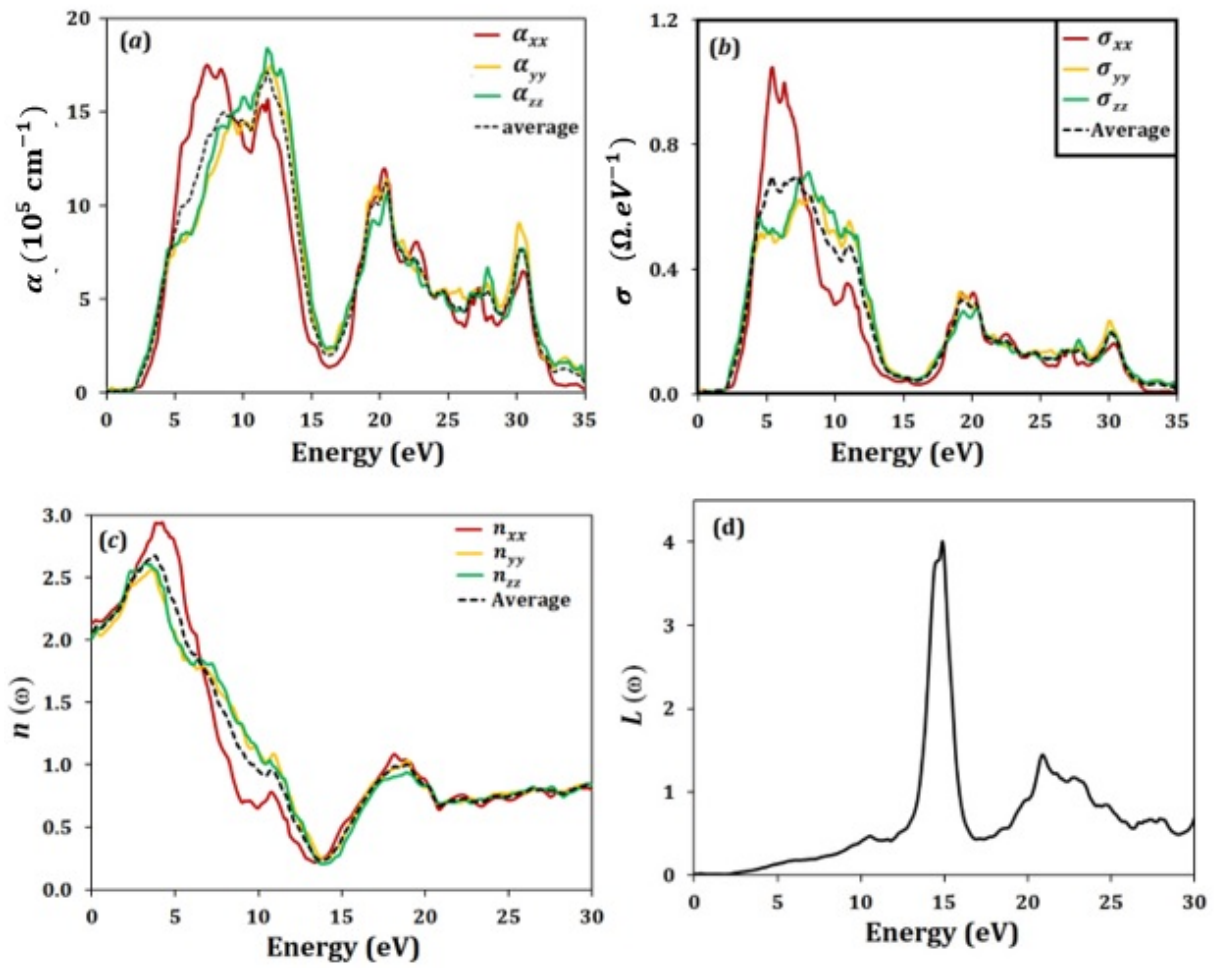


**Figure 5.7:** (a) absorption coefficient- $\alpha(\omega)$  (b) optical conductivity- $\sigma(\omega)$ , (c) refractive index- $n(\omega)$ , and (d) loss-function- $L(\omega)$  of  $\alpha$ - $U_3O_8$ . The average of  $\alpha(\omega)$  and  $\sigma(\omega)$  are shown in black dashed line and the  $xx$ ,  $yy$  and  $zz$  components are given by red, yellow, and green solid lines respectively.

### 5.3.2 Experimental band gap

We conducted the experimental investigation on  $E_g$  based on diffuse reflectance spectral (DRS) measurement<sup>224</sup>. This method is well justified to obtain optical properties of powder samples in the UV-visible, near-infrared (NIR) and mid-infrared regions and is also very useful when the normal transmission spectroscopies are difficult to obtain<sup>224,241</sup>. In most cases, a decrease of particle size and dilution (1-10%) within a non-absorbing matrix such as alkali halides (KBr, KCl, etc.) should improve the quality of the spectrum<sup>222,241</sup>. Good quality spectra allow more accurate results on  $E_g$ . In this study, we have used KCl as the dilution medium because of its optical transparency down to  $\sim 200$  nm<sup>242</sup>. The measured reflectance spectra of 1wt%, 2wt%, and 4wt% samples are presented in Fig. 5.8 as a function of incident photon wavelength ( $\lambda$ ) within the 300-800 nm range. It is clear from the plot that there is a clear absorption edge within 400 to 500 nm range in all three samples. However, with increasing the concentration of  $U_3O_8$  in the mixture, it reduces the strength of the absorption step. The minor distortion, which is visible around 600 nm,

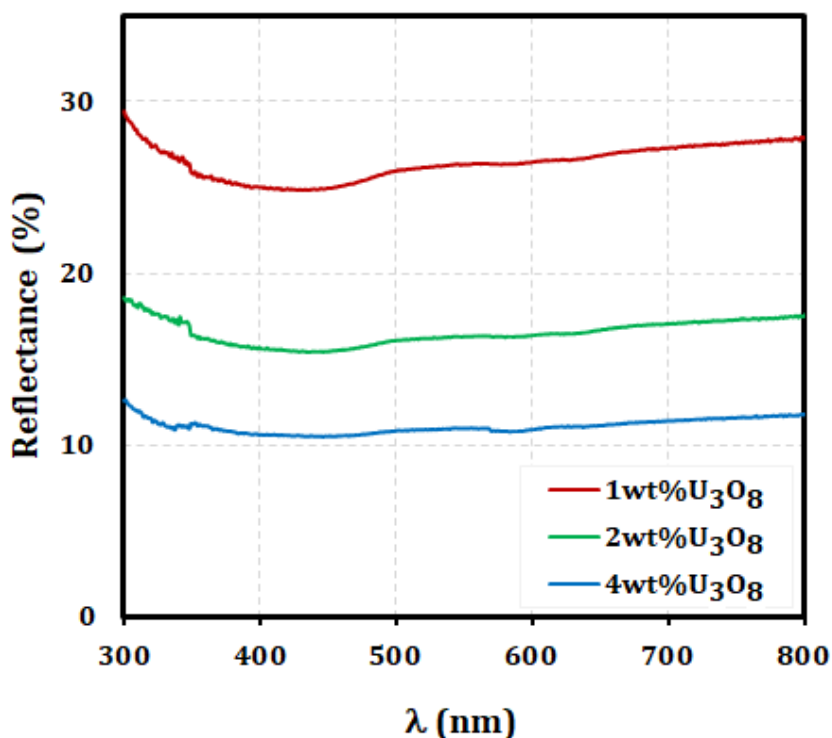


**Figure 5.8:** Measured reflectance spectra for  $U_3O_8$ -KCl mixture samples (a) 1wt% of  $U_3O_8$  (red) (b) 2wt% of  $U_3O_8$  (green) (c) 4wt% of  $U_3O_8$  (blue).

is an instrumental noise due to the grating change and should not be interpreted as a characteristic of absorption behaviour.

The collected reflection data are then converted to Kubelka-Munk<sup>223,230</sup> units by employing Kubelka-Munk function,  $F(R) = (1 - R)^2/2R$ <sup>230</sup>. The parameter  $R$  in the equation is the reflection coefficient taken from reflection measurements. The function  $F(R)$ , is approximately proportional to the absorption coefficient  $\alpha(h\nu)$  at an incident photon of energy  $h\nu$ , where  $h$  being the plank constant and  $\nu$  being the frequency of the incident photon. Energy of the incident photon has been evaluated by using well-known  $h\nu = 1240/\lambda$  relationship. In order to obtain  $E_g$ , we applied the method suggested by Davis and Mott<sup>243</sup>. In this method, modified Kubellka-Munk function is assumed to be related to the band gap  $E_g$  of the material via the relationship given by Eq. (5.7),

$$[F(R) \times h\nu] \propto [h\nu - E_g]^n. \quad (5.7)$$

It can be rearranged to be represented as the well-known Tauc relation<sup>231</sup>

$$[\alpha(h\nu) \times h\nu] = A(h\nu - E_g)^n, \quad (5.8)$$

where  $A$  is a constant independent of energy. The index  $n$  is a constant which contains information on the electron transition process related to the light absorption of the material. Precisely,  $n$  can be  $1/2$ ,  $2$ ,  $3/2$  or  $3$  for direct allowed, indirect allowed, direct forbidden or indirect forbidden transitions respectively<sup>232</sup>. According to Davis and Mott, the graph of  $[\alpha(h\nu) \times h\nu]^{1/n}$  versus  $h\nu$  gives a linear region just above the optical absorption edge, and the intercept of the extrapolation of the best fit straight line to the energy axis gives the band gap of the material. Thus, by employing this method, one can predict both  $E_g$  and the electron transition type (by the value of  $n$ ) of a semiconductor. In order to find the best fit  $n$  for the current data, we tested the behaviour of  $[\alpha(h\nu) \times h\nu]^{1/n}$  with all the possibilities of  $n$  namely  $n=1/2$ ,  $2$ ,  $3/2$  and  $3$ . We observed that, data of any of the three samples (1wt%, 2wt%, and 4wt%) do not fit to straight lines with  $n = 1/2$ ,  $3$ , or  $3/2$ , suggesting no direct-allowed, direct-forbidden or indirect-forbidden band gaps in  $U_3O_8$ . However, as shown in Fig. 5.9a, b, and c, our data fits to straight lines when  $n = 2$ , predicting an indirect behaviour of the band gap. This observation agrees with our theoretical prediction for an



indirect band gap, as discussed in section 5.3.1. The evaluated optical band gaps from the three samples by extrapolating the straight lines to the energy axis are  $1.86 (\pm 0.04)$ ,  $1.81 (\pm 0.12)$  and  $1.72 (\pm 0.19)$  eV. We compared our results with a previous experimental work by He *et al.*<sup>219</sup> carried out on uranium oxide thin films using spectroscopic ellipsometry. In their work, the authors used three different analyzing methods, namely Tauc, Cody and Tauc-Lorentz methods to evaluate  $E_g$  and have predicted 1.76, 1.67 and 1.81 eV, respectively. These are in good agreement with our results verifying our experimental method and the results.

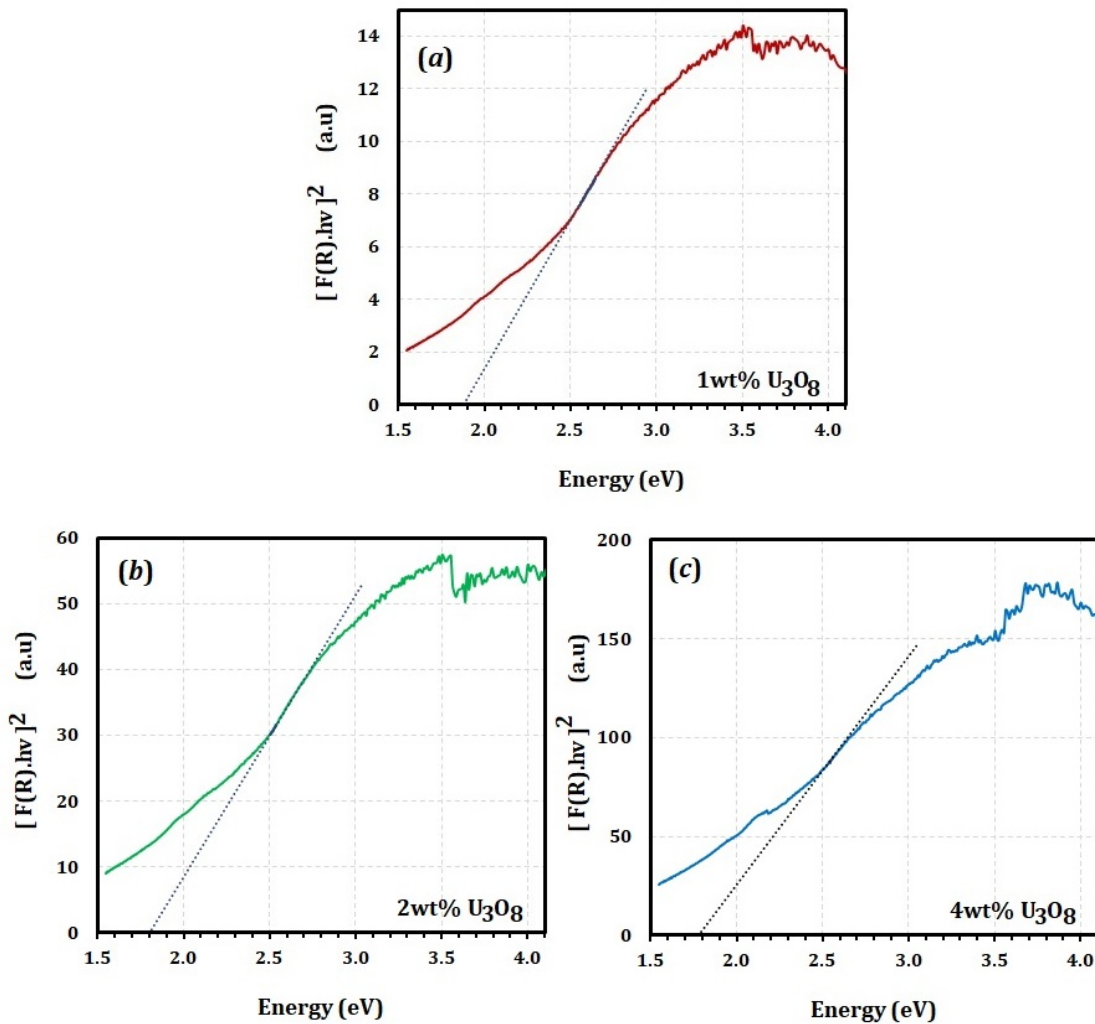


**Figure 5.9:** Tauc's plots for the observed reflection data with  $n = 2$  for (a) 1wt%, (b) 2wt% and (c) 4wt% samples.

## 5.4. Conclusion

In this work, we have performed a comprehensive investigation on the effect of Hubbard-U correction and SOC for predicting electronic, magnetic and optical properties of  $\alpha$ -U<sub>3</sub>O<sub>8</sub>. This study verifies the significance of considering the SOC in the determination of the electronic structure of  $\alpha$ -U<sub>3</sub>O<sub>8</sub>, where it predicts a band gap of 2.03 eV, which is in good agreement with experimental studies. Optical properties suggest that  $\alpha$ -U<sub>3</sub>O<sub>8</sub> is a good absorber in the UV region of the electromagnetic spectrum. Further, we have reported the experimental band gap of  $\alpha$ -U<sub>3</sub>O<sub>8</sub> by measuring the DRS of three mixtures of U<sub>3</sub>O<sub>8</sub>- KCl powders with 1wt%, 2wt% and, 3wt% U<sub>3</sub>O<sub>8</sub>. The measured band gap is indirect and has an average value of 1.80 eV. This band gap value is in the acceptable region for a material suitable for semiconductor applications even though indirect band gap behaviour is a drawback for use in photovoltaics applications.

## Chapter 6.

### **Electronic transport in pure molybdenum and the effective thermal conductivity of U<sub>3</sub>O<sub>8</sub>-Mo**

Molybdenum is one of the two metallic additives considered in this project to enhance the thermal conductivity in U<sub>3</sub>O<sub>8</sub> fuels. In Chapter 3, experimental findings on U<sub>3</sub>O<sub>8</sub>-Mo fuels with two different Mo concentrations (8.2 and 12.5vol% of Mo) are presented and discussed. In addition to that, a detailed description of the theoretical investigation of the thermomechanical properties of U<sub>3</sub>O<sub>8</sub> is given there. In this chapter, our theoretical findings on the temperature-dependent phonon and electronic contributions of thermal conductivities in Mo are presented. In addition, the effective thermal conductivity of U<sub>3</sub>O<sub>8</sub>-Mo with 8.2vol% and 12.5vol% of Mo is estimated based on the Bruggeman model employing the theoretical predictions of the thermal conductivities of U<sub>3</sub>O<sub>8</sub> and Mo. The calculated effective thermal conductivity is compared with the previous experimental data.

This work is submitted to the *Journal of Solid-State Sciences* for publication:

Ranasinghe, J.I., Szpunar, B., Szpunar, J.A., Electronic transport in pure molybdenum and the effective thermal conductivity of U<sub>3</sub>O<sub>8</sub>-Mo, Manuscript Number: SSSCIE-D-22-00419.

The contribution of the Ph.D. candidate is:

(1). Calculation of the thermal conductivity of Mo (2). Analysis of the data, (3). Manuscript preparation. The supervisors review this work before publication.

# Electronic transport in pure molybdenum and the effective thermal conductivity of U<sub>3</sub>O<sub>8</sub>-Mo

Jayangani I. Ranasinghe<sup>a\*</sup>, Barbara Szpunar<sup>a</sup>, and Jerzy A. Szpunar<sup>b</sup>

<sup>a</sup>*Department of Physics and Engineering Physics, University of Saskatchewan, CA*

<sup>b</sup>*Department of Mechanical Engineering, University of Saskatchewan, Saskatoon, CA*

## 6.0 Abstract

Molybdenum (Mo) is well identified as an excellent metallic dopant for enhancing the effective thermal conductivity in current and future accident-tolerant fuels. Our recent experimental work reports a 59% thermal conductivity gain in U<sub>3</sub>O<sub>8</sub> (at 300 K) when only 8.2vol% of Mo is added. In this work, the electronic transport properties in metallic molybdenum are systematically investigated using first principles calculations up to 1500 K. This study is conducted using EPW (electron–phonon coupling using Wannier functions), BoltzTraP (Boltzmann Transport Properties), and Phonopy codes incorporated with the Quantum ESPRESSO (QE) package. The thermal conductivities for U<sub>3</sub>O<sub>8</sub> are taken from our recent publication based on DFT calculations given in Ranasinghe *et al.*. Finally, the current work predicts the effective thermal conductivities of U<sub>3</sub>O<sub>8</sub>-Mo fuels with 8.2vol% and 12.5vol% of Mo using the Bruggeman model and compares them with our experimental measurements conducted using the laser flash technique on specimens prepared using spark plasma sintering. This work agrees within reasonable limits with our previous experimental observations.

## 6.1 Introduction

One of the safety constraints in nuclear reactors is maintaining the centerline temperature of the fuel elements below the melting point<sup>244,245</sup> all the time. Thermal conductivity of the fuel material directly impacts the centerline temperature as it controls the speed of heat flowing through the system. As a result, low thermal conductivity leads to a high thermal gradient and causes deformations and cracks in the fuel element leading to fission product release.<sup>246</sup> Besides, in accident situations such as loss of coolants, the low thermal conductivity causes an accumulation of the generated heat. This phenomenon leads to a rising fuel rod temperature, putting it at risk of melting.<sup>246</sup> The shortfalls mentioned above have led to the renewed interest in investigating high-thermal conduction fuels to replace the current nuclear fuels with low thermal conductivity. Apart from safety, high-thermal conduction fuels can also improve the efficiency of nuclear energy production.<sup>19,168,247</sup>

Among various novel concepts to enhance the thermal conductivity in nuclear fuels, metallic dopants are of great interest, not only because of the possibility of improving thermal conductivity but also due to many other advantages, including easy fabricability, reduced fission product release, and increased grain sizes.<sup>43,105,248</sup> Diamond,<sup>42,107</sup> Chromium,<sup>101,249,250</sup> and Molybdenum<sup>22,105,106,138,251,252</sup> are a few metallics that have been actively investigated as dopants in nuclear fuels to improve the thermal conductivity. As published in Ranasinghe *et al.*<sup>253</sup>, we have successfully sintered U<sub>3</sub>O<sub>8</sub>-Mo fuel pellets with 8.2vol% and 12.5vol% of Mo using spark plasma sintering. Those specimens showed, respectively, 59% (*i.e.*, 4.70 W m<sup>-1</sup> K<sup>-1</sup>) and 104% (*i.e.*, 6.04 W m<sup>-1</sup> K<sup>-1</sup>) thermal conductivity enhancement compared to pure U<sub>3</sub>O<sub>8</sub> at ~300 K (*i.e.*, 2.96 W m<sup>-1</sup> K<sup>-1</sup>) showing a significant improvement. However, no other theoretical or experimental works have been conducted on U<sub>3</sub>O<sub>8</sub>-Mo so far, which is essential for considering its commercial applicability as a future accident-tolerant fuel. Therefore, in this work, we performed a theoretical work to predict the thermal conductivity of U<sub>3</sub>O<sub>8</sub>-Mo fuels and compared them with our experimental findings in Ref. 20. In the current work, our first aim is to theoretically obtain the thermal conductivity of pure Mo. After that, it is planned to derive the thermal conductivity of U<sub>3</sub>O<sub>8</sub>-Mo, with 8.2vol% and 12.5vol% of Mo, using an empirical model. The theoretical thermal

conductivities of pure  $U_3O_8$  are taken from our previous publication,<sup>253</sup> and the details of the calculations are not discussed here to avoid repetition.

The rest of this chapter is organized as follows: Sec. 6.2 presents the calculation methodology applied to evaluate the thermal conductivity of Mo. Our predictions on the thermal conductivity of Mo and the effective thermal conductivities of  $U_3O_8$ -Mo fuels are given in Sec. 6.3. The conclusions of the work are given in Sec. 6.4.

## 6.2 Computational details

The electrical resistivity and the electronic contribution to the total thermal conductivity calculations reported in this work are performed using Density Functional Theory (DFT) based simulation packages and QE (QUANTUM Espresso).<sup>60</sup> The pseudopotential utilized in the calculation is norm-conserved, and the exchange and correlation energies are based on the Local Density Approximation (LDA) with Perdew-Zunger (PZ)<sup>75</sup> functionals. The structural optimization for the ground state of Mo was obtained for a Monkhorst-Pack sampling  $k$ -mesh of  $12 \times 12 \times 12$  and the plane wave cutoff energy of 1360.6 eV. The phonon dispersion relation is investigated to assess the dynamical stability of the optimized structure. It is analyzed within the harmonic approximation based on the supercell approach utilizing the Phonopy<sup>59</sup> code.

BoltzTrap<sup>57</sup> (Boltzmann Transport Properties) and EPW<sup>58</sup> (electron-phonon coupling using Wannier functions) codes are employed to evaluate the temperature dependence of  $\kappa_e$  as described below. First, the temperature-dependent electrical conductivity relative to the electron relaxation time ( $\sigma/\tau_e$ ) is evaluated using the rigid band approximation implemented in the BoltzTrap package. A denser  $k$ -mesh of  $50 \times 50 \times 50$  is used in the non-self-consistent calculation to assure the accuracy and the convergence of the density of states. Then, the electron self-energy is evaluated using the matrix elements of the electron-phonon interaction by combining the QE code with the EPW package. An inner frozen window with a maximum of 11.0 eV and an outer disentanglement window with an upper limit of 45.0 eV, including 8 Wannier functions (projections of  $sp3d2$ ,  $dxy$ , and  $dx^2-y^2$ ), were used to construct the maximally localized Wannier functions (MLWF). The EPW results' convergence was tested with different sizes of fine  $q$ - and  $k$ - meshes. The converged

results reported here performed with  $50 \times 50 \times 50$  regular  $q$ - and  $k$ - fine grids. Finally, the Wiedemann-Franz law<sup>95</sup> is used to derive  $\kappa_e$  as a function of temperature from 300 K to 1500 K.

## 6.3 Results and discussion

### 6.3.1 Ground state properties

Molybdenum is a magnetically neutral, transition metal with a body-centered cubic structure (space group 229).<sup>254,255</sup> As the first step, the equilibrium lattice parameters are obtained by optimizing the experimental structure as a function of the energy of the unit cell. The calculated ground state lattice parameter (3.165 Å) is well justified by available theoretical<sup>254,256</sup> and experimental<sup>255,257</sup> data with less than 1% deviation. It is well known that the phonon spectrum with no negative vibration frequencies indicates the dynamical stability of a structure; hence it was necessary to obtain meaningful results from a DFT calculation. Therefore, the optimized ground-state is used to evaluate the phonon spectrum of Mo at 300 K, and the obtained results are as shown in Fig. 6.1. The open circles in the figure are the experimental data from Zarestky *et al.*<sup>258</sup> Having only one atom in the primitive unit cell, it has three acoustic branches in the phonon dispersion spectrum, and all vibrations have positive frequencies, verifying the dynamical stability of the predicted structure at the ground state. Further, the calculated spectrum reproduced the previously reported theoretical<sup>254</sup> and experimental<sup>258</sup> data justifying the validity of our calculation.

The ground state electronic structure of Mo along the high symmetry path was determined using the QE simulation package. The obtained values of total electronic densities of states (DOS) as a function of the electron energy are shown by the solid black line in Fig. 6.2. Further, the evaluated projected partial DOS are represented by the red ( $4d$ ), green ( $4p$ ), and blue ( $5s$ ) dashed lines in the same figure. The black dashed line indicates the calculated value of the Fermi energy ( $E_F$ ). Our results confirm the metallic feature of Mo, giving a non-zero DOS dominated by  $4d$  electrons at  $E_F$ . Further, it shows a strong hybridization among the  $4d$ ,  $4p$ , and  $5s$  electrons below  $E_F$ . The integrated number of electrons as a function of energy (purple dotted line) states that there are six electrons by  $E_F$ , which agrees with the electron configuration of Mo ([Kr]  $4d^5 5s^1$ ).

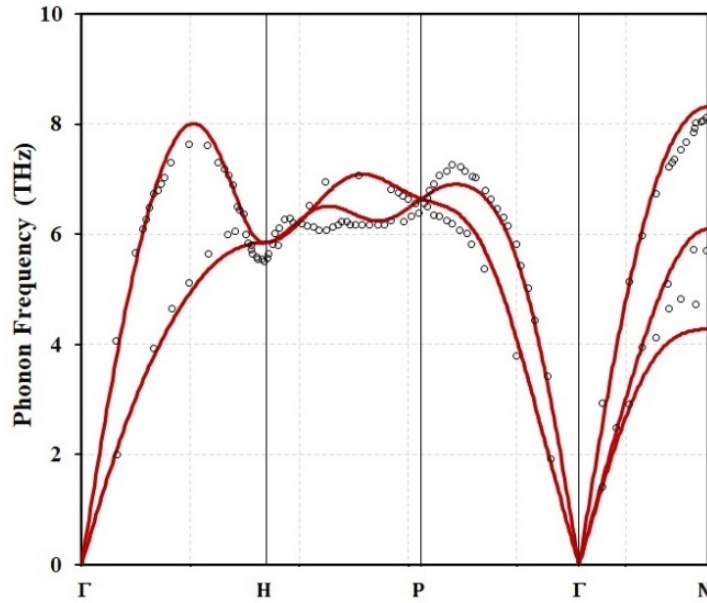


**Figure 6.1:** Dispersion relations of phonon vibrations in molybdenum. The red solid line represents the prediction from the current work and empty circles are from literature.

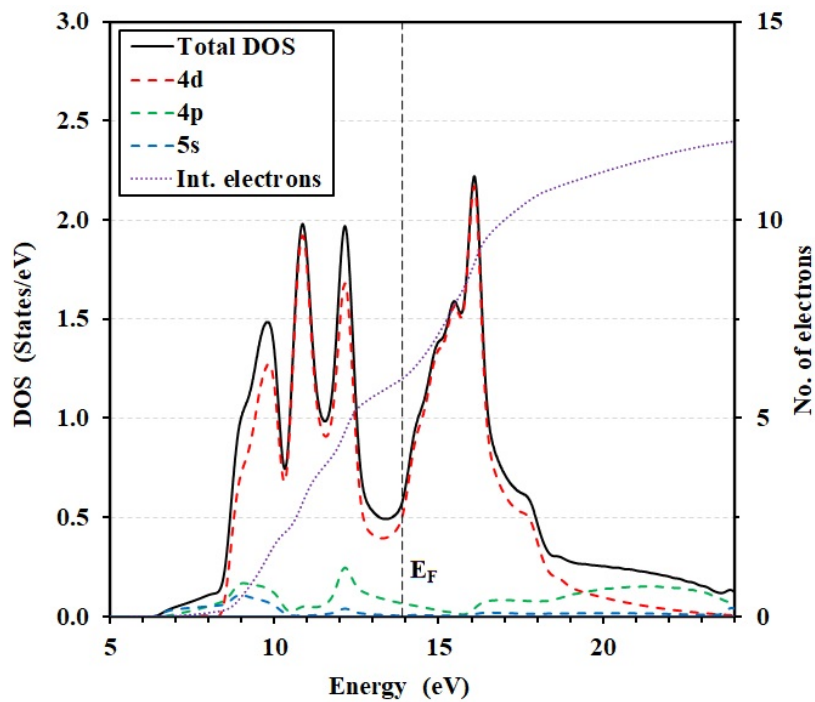


**Figure 6.2:** The predicted total (black solid line) and the projected partial electron densities of states (DOS) of Mo. The red, green and the blue dashed lines represent the contributions from respective  $4d$ ,  $4p$  and  $5s$  electrons. The purple dotted line is to show the integrated number of electrons.



### 6.3.2 Electron scattering rates and the relaxation time

In this work, the electrical resistivity ( $\sigma$ ) of Mo is evaluated using the rigid band approximation as implemented in BoltzTraP code. According to this method,  $\sigma$  is evaluated with respect to the electron relaxation time ( $\tau_e$ ); hence for the absolute values, one needs to provide the corresponding  $\tau_e$ . In most theoretical calculations conducted using BoltzTraP,  $\tau_e$  is either assumed as a constant or derived using empirical methods. In this work, the temperature dependency of  $\tau_e$  is revealed using a first principles non-empirical method as described below. However, it does not consider the anharmonic effects; hence the predicted  $\tau_e$  may have been overestimated at high temperatures.

The scattering rate is the inverse of the relaxation time ( $1/\tau_e$ ), and it relates to the imaginary part of the electron self-energy ( $\Sigma''_{nk}$ ) from Eq. (6.1),

$$\frac{1}{\tau_e} = \frac{2\Sigma''_{nk}}{\hbar}. \quad (6.1)$$

Here,  $\hbar$  is the reduced Plank constant,  $\hbar = 6.582119569 \times 10^{-16}$  eV s. In the current work, energy-dependent  $\Sigma''_{nk}$  is evaluated as implemented in the EPW package at different temperatures, and then they were employed to calculate the scattering rates using Eq. (6.1). Figure 6.3 illustrates the energy dependences of electron scattering rates at 300, 500, and 1500 K. It is clear from the figure that the scattering rate variation closely follows the electron DOS, consistent with the fact that the available phase space reflects the DOS. Further, the scattering rates are subjected to increase uniformly with raising the temperature since more phonons are excited, allowing more electron-phonon scatterings at the higher temperature.

The scattering rates were then used to evaluate the corresponding energy-dependent  $\tau_e$  at different temperatures from 300 K to 1500 K. At each temperature, the average of  $\tau_e$  with energies less than  $k_B T$  is taken as the corresponding value for that temperature  $T$ . The obtained results are presented in Fig. 6.4. It shows a strong inverse dependence on temperature, and the data well fit with the relation given in Eq. (6.2),

$$\tau_e = 8 \times 10^{-6} T^2 - 0.0218 T + 15.985 \quad (\times 10^{-15} \text{ s}). \quad (6.2)$$

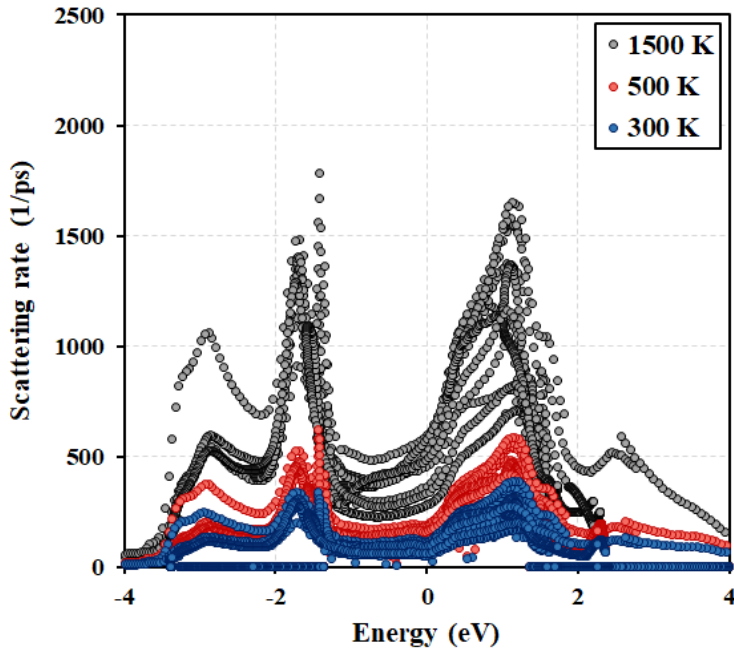


**Figure 6.3:** The electron scattering rates of electron-phonon scattering at 300 (blue), 500 (red), and 1500 (black) evaluated using EPW code.

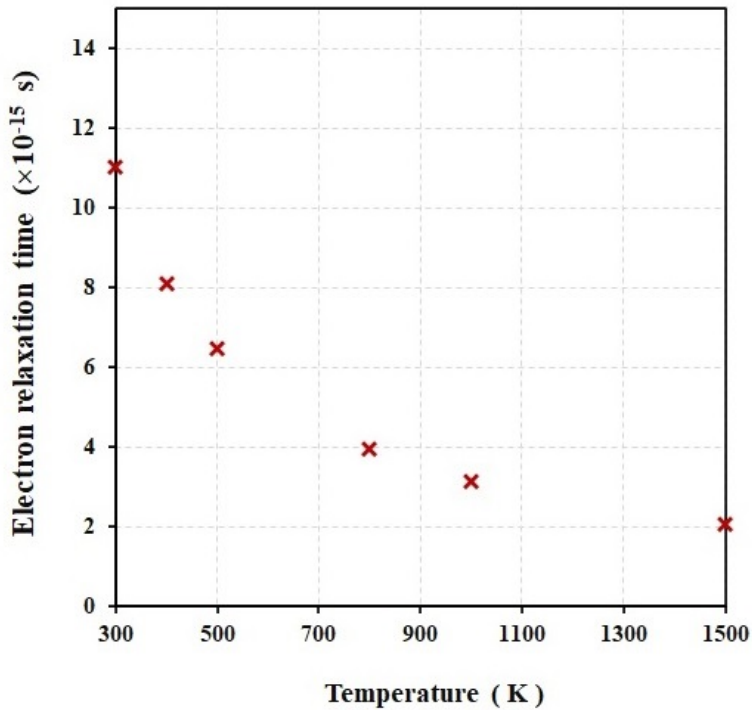


**Figure 6.4:** The electron relaxation time ( $\tau_e$ ) as a function of temperature. Here,  $\tau_e$  at each temperature is taken as an average of those with the electron energies are  $< k_B T$ , where  $k_B$  is the Boltzmann constant.

### 6.3.3 Electrical resistivity

The obtained temperature-dependent  $\sigma/\tau_e$  data using the BoltzTraP code are illustrated in Fig. 6.5a from 300 to 1500 K. It shows an increasing trend against the temperature, changing from  $15.09 (\times 10^{20} (\Omega \cdot \text{m} \cdot \text{s})^{-1})$  to  $17.07 (\times 10^{20} (\Omega \cdot \text{m} \cdot \text{s})^{-1})$  when the temperature rises from 300 K to 1500 K. Subsequently, with  $\sigma/\tau_e$  and  $\tau_e$  in hand, the absolute values of the electrical resistivities (*i.e.*, the inverse of conductivity) of Mo are evaluated. The solid black line in Fig. 6.5b shows the predicted electrical resistivity versus temperature from 300 to 1500 K. It is clear from the figure that our predictions show a reasonable agreement with the previous experimental data.<sup>259–262</sup> The obtained resistivity-temperature data from the current work can be well represented by the linear progression function given in Eq. (6.3),

$$\rho = 0.0215 T - 0.3452. \quad (6.3)$$

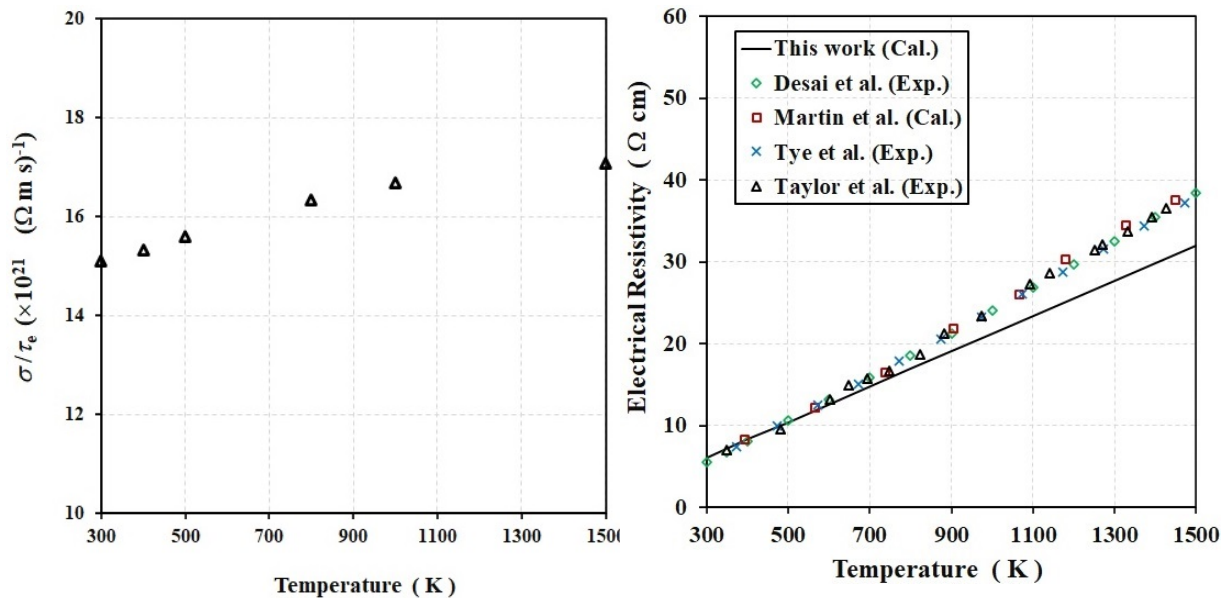


**Figure 6.5:** (a) The electrical conductivity of Mo with respect to the electron relaxation time ( $\sigma/\tau_e$ ), and (b) The calculated electrical resistivity as a function of temperature. Experimental data from Desai *et al.*<sup>259</sup>, Tye *et al.*<sup>261</sup>, and Taylor *et al.*<sup>262</sup>, and ab-initio predictions from Martin *et al.*<sup>260</sup>, are given for comparison.

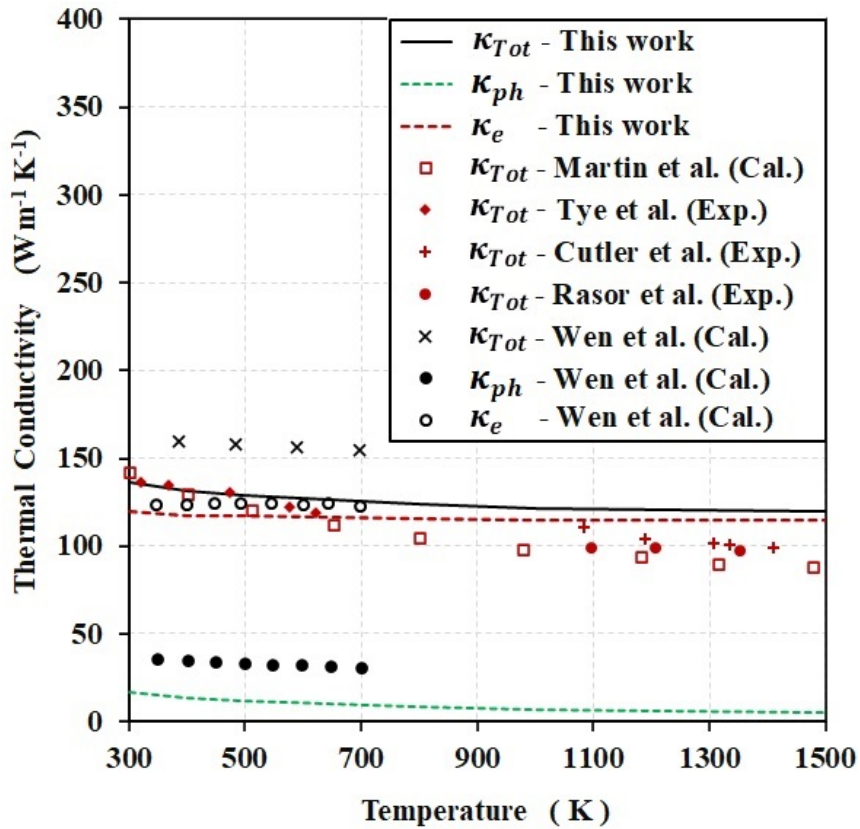


**Figure 6.6:** The calculated results for  $\kappa_e$  (red dashed line), and the  $\kappa_{Tot}$  (black solid line) of molybdenum. Here,  $\kappa_{Tot}$  is taken as the algebraic sum of  $\kappa_e$  and  $\kappa_{ph}$ , where phonon contributions are taken from Wen *et al.*<sup>263</sup>.

### 6.3.4 Electronic thermal contribution ( $\kappa_e$ )

green dashed line in Fig. 6.6). Therefore, we employed the ShengBTE<sup>56</sup> simulation package to evaluate  $\kappa_{ph}$  in Mo due to phonon-phonon, and phonon-isotope scatterings at 300 K. The harmonic IFCs required for this calculation were derived based on the supercell approach using the Phonopy code with a  $5 \times 5 \times 5$  supercell. Anharmonic IFCs were calculated using QE on a  $5 \times 5 \times 5$  supercell with the force cutoff distance to the fifth nearest neighbouring atom. The converged  $\kappa_{ph}$  of our calculation gives  $16.47 \text{ W m}^{-1} \text{ K}^{-1}$  at 300 K. However, Wen *et al.*<sup>263</sup> predict a much higher  $\kappa_{ph}$  compared to ours (e.g.  $38.77 \text{ W m}^{-1} \text{ K}^{-1}$  at 300 K), and it is hard to guess the reason behind this

discrepancy. However, Wen *et al.*<sup>263</sup> have incorporated the effect of electron-phonon scattering on  $\kappa_{ph}$  and GGA functionals, which can impact the difference. According to Wen *et al.*,<sup>263</sup>  $\kappa_{ph}$  decreases with increasing temperature according to the usual theoretical model  $\kappa_{ph} = 1/(A + BT)$ , with  $A = 2.33 \times 10^{-2} \text{ (W}^{-1} \text{ m K)}$  and  $B = 1.26 \times 10^{-5} \text{ (W}^{-1} \text{ m)}$ . In the current work, we applied the above relation to interpolate  $\kappa_{ph}$  up to 1500 K and used them to calculate the total thermal conductivity of Mo ( $\kappa_{Mo}$ ). The solid black line represents the obtained  $\kappa_{Mo}$  values in Fig. 6.6. It gives a value of  $156.86 \text{ W m}^{-1} \text{ K}^{-1}$  for  $\kappa_{Mo}$  at 300 K, and it decreases to  $138.30 \text{ W m}^{-1} \text{ K}^{-1}$  by 1500 K, showing only an 11.83% reduction. Interestingly, this deterioration primarily occurs before 800 K and is almost flat in the higher temperature end. Previous theoretical works by Martin *et al.*<sup>260</sup> (blank red square) and experimental data from Tye *et al.*<sup>261</sup> (solid red diamonds) agree with our ab-initio predictions in the lower temperature region. Cutler<sup>264</sup> (red plus) and Rasor *et al.*<sup>160</sup> (solid red circle) provide experimental thermal conductivities at higher temperatures, and the discrepancy of our data compared to theirs is always  $> 20\%$  showing a reasonable agreement. Our predictions for total thermal conductivity in Mo ( $\kappa_{Mo}$ ) can be fitted to Eq. (6.5),

$$\kappa_{Mo} = -9 \times 10^{-9} T^3 + 3 \times 10^{-5} T^2 - 0.0495 T + 168.7. \quad (6.5)$$

### 6.3.5 Effective thermal conductivity of $\text{U}_3\text{O}_8\text{-Mo}$ fuels: ( $\kappa_{eff}^{\text{U}_3\text{O}_8\text{-Mo}}$ )

There are numerous models to calculate the effective thermal conductivity of heterogeneous materials when the thermal conductivity, the volume fractions of the constituents, and the microstructures are known.<sup>265,266</sup> These models can be categorized into five fundamental groups: the parallel, series, two forms of Maxwell-Eucken, and the Effective Medium Theory (EMT).<sup>265</sup> The applicability of these models to evaluate the effective thermal conductivity of different systems, including nuclear fuel composites, is discussed in several previous works.<sup>266</sup> As per the previous reports, the series and parallel models give the lower and the upper bounds of heterogeneous materials if conduction is the only heat transfer mechanism. Maxwell-Eucken models give the upper and the lower bounds when one or more phases with sphere-like small particles are dispersed into a continuous medium. In the Maxwell-Eucken approximation, it is

assumed that the interaction between the dispersed particles and the differences in the thermal conductivity at the particle-matrix interfaces are negligible.<sup>265,267</sup> However, due to these assumptions, the Maxwell-Eucken model is accurate only with low concentrations of the embedded particles; otherwise, the predicted values may have an error of up to 10%. The EMT model (also called Bruggeman model) assumes random particle distributions within the systems, which means all the phases are mutually dispersed, having continuous locations.<sup>265</sup> When considering the constraints of all these models and the microstructural patterns reported in Ranasinghe *et al.*,<sup>253</sup> Bruggeman seems the best fit for our work to predict  $\kappa_{eff}^{U_3O_8-Mo}$ . Nevertheless, previous works show that this model gives satisfactory results with nuclear fuels like UO<sub>2</sub>-Mo and UO<sub>2</sub>-W.<sup>266</sup> Therefore, in this work, we used the Bruggeman model to evaluate the thermal conductivity of U<sub>3</sub>O<sub>8</sub>-Mo with 8.2vol% and 12.5vol% of Mo. The symbolic form of the Bruggeman is given in Eq. (6.6),

$$\kappa_{eff} = \frac{A + \sqrt{A^2 + 8k_d k_c}}{4} \quad (6.6)$$

where  $A = (3\alpha - 1)k_d - (3\alpha - 2)k_c$ . In this equation  $\kappa_c$  and  $\kappa_d$  are the thermal conductivities of the continuous phase (U<sub>3</sub>O<sub>8</sub>), and the dispersed phase (Mo) respectively, and  $\alpha$  is the volume fraction of the dispersed phase.

Figure 6.7 provides our predictions on the effective thermal conductivity distribution of Mo dispersed fuels with concentrations of 8.2 and 12.5vol.%, determined using the Bruggeman model and the predicted thermal conductivities for U<sub>3</sub>O<sub>8</sub> and Mo. The required theoretical thermal conductivity for U<sub>3</sub>O<sub>8</sub> is taken from the results presented in Ranasinghe *et al.*<sup>253</sup> As shown in Fig. 3.9, U<sub>3</sub>O<sub>8</sub> has a strong anisotropy in the thermal conductivity with  $\kappa_{ph}^z > \kappa_{ph}^x > \kappa_{ph}^y$ . Therefore, the effective thermal conductivities of U<sub>3</sub>O<sub>8</sub>-Mo also show this anisotropy. However, here we show only the calculated  $\kappa_{eff}$  relevant to  $\kappa_{ph}^z$  and  $\kappa_{ph}^{Ave}$  of U<sub>3</sub>O<sub>8</sub> for the clarity of the discussion. The blue (12.5vol% Mo) and red (8.2vol%) solid lines in Fig. 6.7 are the effective thermal conductivities when the thermal conductivity of U<sub>3</sub>O<sub>8</sub> along the [001] direction is considered. The respective dashed lines represent the effective thermal conductivities when the averaged thermal conductivity of U<sub>3</sub>O<sub>8</sub> is applied. The figure shows that our experimental results (blue squares and red diamonds) show a reasonable agreement with the current empirical estimation (red and blue solid lines).

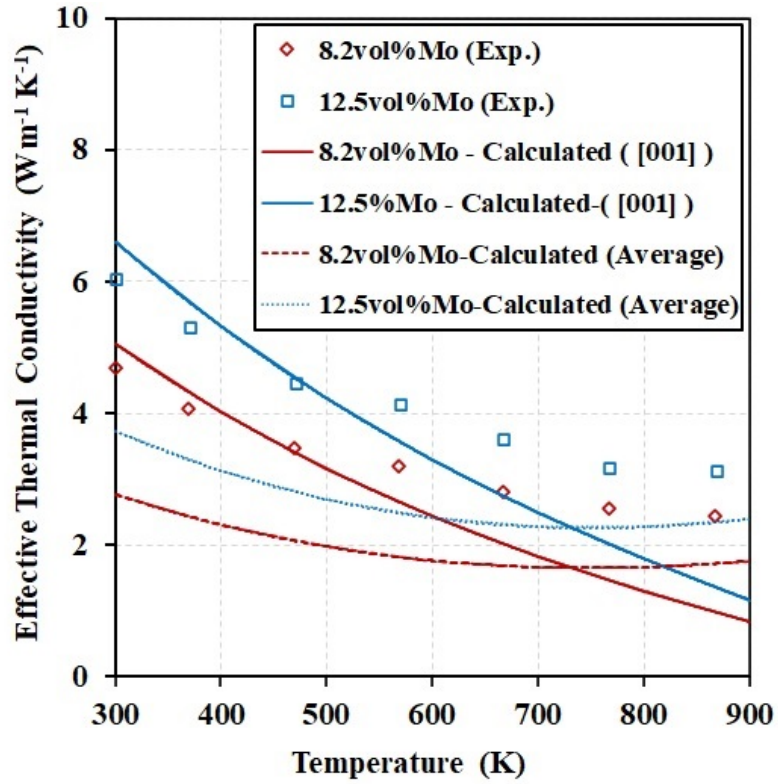


**Figure 6.7:** The effective thermal conductivity in  $U_3O_8$ -Mo fuels with 8.2vol% and 12.5vol%. The blue square and red diamonds represent our experimental data published in Ranasinghe *et al.*<sup>253</sup>. The calculated effective values are taken using the Bruggeman model.

## 6.4 Conclusion

In this work, we derived the electronic thermal conductivities of Mo by solving the linearized BTE for the electron-phonon scattering process by employing first principles methodologies. It is found here that Mo has a significant electronic thermal conductivity contribution relative to its lattice contribution and, at higher temperatures, it remains almost constant at around  $120 \text{ W m}^{-1} \text{ K}^{-1}$ . The theoretical predictions for the effective thermal conductivity in  $\text{U}_3\text{O}_8$ -Mo fuels are evaluated using the Bruggeman model. It gives  $6.05 \text{ W m}^{-1} \text{ K}^{-1}$  and  $5.01 \text{ W m}^{-1} \text{ K}^{-1}$ , respectively, with 12.5 and 8.2vol% Mo metal at 300 K. Overall, the experimental values measured using the laser flash technique reasonably agree with the calculated effective values. Finally, this work confirms the thermal conductivity enhancement in  $\text{U}_3\text{O}_8$ -Mo fuels above the current commercial fuel,  $\text{UO}_2$ .



## Chapter 7

### Concluding Remarks

This thesis aimed to examine uranium compounds of  $U_3O_8$ ,  $UAl_2$ ,  $U_3O_8-Al$ , and  $U_3O_8-Mo$ , mainly related to their nuclear reactor applications. Based on that, several primary goals were identified; First, the examination of their thermomechanical properties would use DFT techniques. Second, experiments would be conducted to study thermal transport behaviour in pure  $U_3O_8$ ,  $U_3O_8-Al$ , and  $U_3O_8-Mo$  with different metallic concentrations. Third, experimental techniques and DFT-based theoretical methods would be employed to examine the bandgap of  $U_3O_8$ , primarily based on the current interest in recycling nuclear wastes through possible electronic industry applications. Lastly, the thermal transport in the metallic additive material, Mo, would be investigated. A concise description of the background and the importance of the work is introduced in Chapter 1. The methodologies used to achieve the goals of the research work, including the background of the DFT, are briefly described in Chapter 2. Chapters 3, 4, 5, and 6 include discussions of the results of our theoretical and experimental findings. Here, the main conclusions of this thesis and the suggestions for future investigations are summarized.

#### 7.1 Conclusions

Despite the role of  $U_3O_8$  in the nuclear industry, its thermomechanical properties are neither comprehensively studied nor well established. Especially, thermal conductivity investigations are very few and limited to a couple of experimental examinations. Therefore, the need for extensive theoretical work on the thermal transport mechanism of  $U_3O_8$  is recognized. In this project, the applicability of the DFT technique for predicting the thermal conductivity of  $U_3O_8$  is demonstrated for the first time. Chapter 3 of this thesis reports the results of the DFT-based investigation on

temperature-dependent lattice thermal conductivity behaviour of  $U_3O_8$ , its mode-wise phonon contribution, phonon scattering rates, Grüneisen parameter, and the mode-wise group velocity, for the first time. Further, the temperature dependence of thermal conductivity and thermal diffusivity of pure  $U_3O_8$ ,  $U_3O_8$ -Al, and  $U_3O_8$ -Mo were experimentally measured using high-density sintered specimens prepared using the SPS technique, and the thermal conductivity enhancement when  $U_3O_8$  is incorporated with Al and Mo is quantitatively demonstrated. Based on the results discussed in Chapter 3, we conclude that the DFT technique is a powerful tool for scanning the thermal transport properties of  $U_3O_8$  and can be utilized in synergy with experimental data for a deep understanding of the underlying mechanism of the thermal conductivity. Furthermore, we conclude that the anisotropy of the thermal conductivity originated from the directional dependence of the group velocity.

Chapter 4 presents the outcomes of DFT-based study on the thermomechanical properties of the metallic fuel  $UAl_2$  for the temperature range from 300 K to 1500 K. It predicted the temperature-dependent functions of thermal expansion, bulk modulus, and the density variation over that temperature range. For the first time, this work revealed a full *ab initio* investigation of the electronic thermal contribution through the electron relaxation time of electron-phonon scattering. The research findings of this work conclude that the electronic contribution to the thermal conductivity in  $UAl_2$  increases with increasing temperature. As a result, unlike in semiconductor fuel  $UO_2$ , the resultant thermal conductivity in  $UAl_2$  is quantitatively shown to remain relatively unchanged and high up to 1500 K temperature.

Chapter 5 reports the theoretical findings on the electronic and optical properties of  $\alpha$ - $U_3O_8$  based on DFT calculations and the experimental work on the bandgap evaluation. This work proved the importance of including the Hubbard-U correction and the SOC when performing DFT-based electronic, magnetic, and optical property investigations in  $U_3O_8$ . Based on the calculated electronic band structure, this investigation theoretically demonstrated an indirect bandgap of 2.03 eV in  $\alpha$ - $U_3O_8$ . Furthermore, this work successfully employed the diffuse reflectance spectra method to evaluate the band gap using powder samples of  $U_3O_8$ , and experimental findings confirmed the indirect behaviour of the bandgap.

Chapter 6 presents the theoretical findings on the electronic contribution to thermal conductivity in Mo. This evaluation follows a fully ab-initio method to predict the relaxation time of electrons in the electron-phonon scatterings for the first time. Our findings quantitatively demonstrate that Mo's thermal conductivity is weakly dependent on the temperature in the range of 300 to 1500 K. Further, this work demonstrates that the calculated effective thermal conductivity of  $U_3O_8$ -8.2vol%Mo and  $U_3O_8$ -12.5vol%Mo fuels based on the Bruggeman model agree with our experimental thermal conductivity measurements of  $U_3O_8$ -8.2vol%Mo and  $U_3O_8$ -12.5vol%Mo specimens presented in Chap. 3.

## 7.2 Suggestions for future works

- (i) DFT-based investigation of the fission product behaviour in  $U_3O_8$  and  $UAl_2$

DFT-based calculations can be successfully used to evaluate the fission products accumulation behaviour during fuel burning and its effects on the thermomechanical properties of the fuel materials. These studies are essential in  $U_3O_8$  and  $UAl_2$  fuels to evaluate their possible safer application under actual irradiation conditions. Thus, comprehensive investigation using ab-initio methods is necessary to widen these fuels' databases.

- (ii) Evaluation of thermal transport properties in  $U_3O_8$ ,  $U_3O_8$ -Al, and  $U_3O_8$ -Mo sintered pellets after irradiation.

During their use in reactors, fuel pellets are exposed to a very harsh thermal and radiation environment and undergo many complex chemical, physical and mechanical changes, such as fission product accumulation, fission gas release, fuel swelling, and interaction with the cladding. The fuel-designing engineers need to evaluate these changes to design efficient and safe fuel types. Therefore, further experimental investigations on the thermomechanical properties of the sintered samples after irradiation exposure is suggested.

(iii) Study of corrosion behaviour of  $UAl_2$  fuels

Even though  $UAl_2$  possesses suitable thermomechanical properties as a LEU fuel, there is a known issue that Al-based fuels corrode relatively rapidly in a humid environment. Especially when metallic aluminum particles are released from the fuel, they can accumulate at intergranular locations, oxidizing to form hydrogel  $Al_2O_3 \cdot H_2O$ . Some experimental investigations have been conducted to study fuel oxidation mechanisms in  $UAl_x$  under different environmental conditions and their properties after the oxidation. DFT can provide fundamental insights into oxidation mechanisms with different environmental conditions and predict the fuel's degradation. Hence, a comprehensive, DFT-based study on fuel corrosion and its properties after corrosion is suggested as future work.

## REFERENCES

1. Fernández-Arias, P., Vergara, D. & Orosa, J. A. A global review of PWR nuclear power plants. *Applied Sciences (Switzerland)*, 10, (2020).
2. Morse, E. Analytical Methods for Nonproliferation. in *Analytical Methods for Nonproliferation*, Springer International Publishing, (2016).
3. Electricity and Nuclear Power Estimates for the Period up to 2050, Reference Data Series No. 1. *International Atomic Energy Agency*, (2021).
4. Meyer, M. K., Keiser, D. D., Jue, J.-F. & Shaber, E. *Research reactor fuels. Advances in Nuclear Fuel Chemistry* (LTD, 2020).
5. Paley, C. *Pros and Cons of Nuclear Power*. (Cavendish Square Publishing, 2015).
6. Oxlade, C. *Nuclear Energy*. Heinemann Intl Inc., (2012).
7. Mahaffey, J. A. Atomic accidents : a history of nuclear meltdowns and disasters from the Ozark Mountains to Fukushima. Pegasus Books, (2014).
8. Joyce, M. Nuclear engineering: A conceptual introduction to nuclear power. *Nucl. Eng. A Concept. Introd. to Nucl. Power*, (2017).
9. Hore-L Hore-Lacy, I. Nuclear Energy in the 21st Century. *Academic Press*, (2007).
10. Breeze, P. Nuclear Power. *Elsevier Science & Technology*, (2017).
11. Neighbour, Gareth, B. *Securing the Safe Performance of Graphite Reactor Cores.*, Royal Society of Chemistry, (2010).
12. Gandini, A. From the Chicago Pile 1 to next-generation reactors. *Enrico Fermi*, (2004).
13. Buschbeck, K. C. & Keller, C. *U Uranium: Behavior of Uranium Fuels in Nuclear Reactors. Reprocessing of Spent Nuclear Fuels*. (2013).
14. Deforest, D. L. Transient fission-gas behavior in uranium nitride fuel under proposed space applications. Air Force Inst. of Tech., Wright-Patterson AFB, OH, (1991).
15. Matthews, R. B., Chidester, K. M., Hoth, C. W., Mason, R. E. & Petty, R. L. Fabrication

- and testing of uranium nitride fuel for space power reactors. *J. Nucl. Mater.* 151, 345 (1988).
16. Zabudko, L.M., Poplavsky, V. M. Proceedings of the symposium on nitride fuel cycle technology. in Session A, JAERI-Conf , Japan, (2004).
  17. Walker, C. T. Assessment of the radial extent and completion of recrystallisation in high burn-up UO<sub>2</sub> nuclear fuel by EPMA. *J. Nucl. Mater.* 275, (1999).
  18. Wronkiewicz, D. J., Bates, J. K., Wolf, S. F. & Buck, E. C. Ten-year results from unsaturated drip tests with UO<sub>2</sub> at 90°C: Implications for the corrosion of spent nuclear fuel. *J. Nucl. Mater.* 238, (1996).
  19. Nuclear energy Agency. State-of-the-Art Report on Light Water Reactor Accident-Tolerant Fuels. *OECD*, (2018).
  20. International Atomic Energy Agency. Implementation and Effectiveness of Actions Taken at Nuclear Power Plants Following the Fukushima Daiichi Accident. *IAEA TECDOC-1930*, (2020).
  21. Charit, I. Accident Tolerant Nuclear Fuels and Cladding Materials. *Jom* 70, (2018).
  22. Williams, A. F., Leitch, B. W. & Wang, N. A microstructural model of the thermal conductivity of dispersion type fuels with a fuel matrix interaction layer. *Nucl. Eng. Technol.* 45, (2013).
  23. Ranasinghe, J. I., Jossou, E., Malakkal, L., Szpunar, B. & Szpunar, J. A. Study on Radial Temperature Distribution of Aluminum Dispersed Nuclear Fuels: U<sub>3</sub>O<sub>8</sub>-Al, U<sub>3</sub>Si<sub>2</sub>-Al, and UN-Al. *J. Nucl. Eng. Radiat. Sci.* 4, (2018).
  24. Ranasinghe, J. I., Malakkal, L., Jossou, E., Szpunar, B. & Szpunar, J. A. Density functional theory study of the structural, mechanical and thermal conductivity of uranium dialuminide (UAl<sub>2</sub>). *J. Nucl. Mater.* 540, (2020).
  25. Wang, T. Qiu, N., Wen, X., Tian, Y., He, J., Luo, K., Zha, X., Zhou Y., Huang, Q., Lang, & Du, S.. First-principles investigations on the electronic structures of U<sub>3</sub>Si<sub>2</sub>. *J. Nucl. Mater.*, 469, (2016).
  26. Durazzo, M., Souza, J. A. B., Carvalho, E. F. U. De & Riella, H. G. Effect of porosity on

- the manufacturing of  $U_3O_8$ -Al dispersion fuel plates. *Prog. Nucl. Energy* 99, (2017).
27. Saoudi, M., Barry, A., Lang, J., Boyer, C., Rogge, R. B., Corbett, S., & Wang, X., Post-irradiation examination of U-7Mo/Mg and U-10Mo/Mg dispersion fuels irradiated in the NRU reactor. *J. Nucl. Mater.* 558, (2022).
  28. Kim, Y. S. Modeling of interaction layer growth between U-Mo particles and an Al matrix. *Nucl. Eng. Technol.*, 45, (2013).
  29. Kim, Y. S. Uranium intermetallic fuels (U-Al, U-Si, U-Mo)., *Comprehensive Nuclear Materials*, 3, (2012).
  30. Bhattacharya, S., Mo, K., Mei, Z., Seidman, D., Stepnik, B., Pellin, M. J., & Yacout, A. M., Improving stability of ALD ZrN thin film coatings over U-Mo dispersion fuel. *Appl. Surf. Sci.* 533, (2020).
  31. Jeong, G. Y., Kim, Y. S., Jeong, Y. J., Park, J. M. & Sohn, D. S. Development of PRIME for irradiation performance analysis of U-Mo/Al dispersion fuel. *J. Nucl. Mater.* 502, (2018).
  32. Ye, B., Hofman, G.L., Leenaers, A., & Wallin, H., A modelling study of the inter-diffusion layer formation in U-Mo/Al dispersion fuel plates at high power. *J. Nucl. Mater.* 499, (2018).
  33. Betzler, B. R., Chandler, D., Evans, T.M., Davidson, G.G., Daily, C. R., Wilson, S. C., & Mosher, W., As-Built Simulation of the High Flux Isotope Reactor. *J. Nucl. Eng.* 2, (2021).
  34. Martin, M. M. High-Uranium-loaded  $U_3O_8$ -Al fuel element development program. Oak Ridge National Laboratory, U.S. DOE.
  35. Piro, M. H. A. Thermodynamic predictions of CANDU fuel volatilization and fission product behaviour under severe accident conditions. *J. Nucl. Mater.* 558, (2022).
  36. Szpunar, B. Investigation of uranium within LDA+U method. *J. Phys. Chem. Solids* 73, (2012).
  37. Pillai, C. G. S., Dua, A. K. K. & Raj, P. Thermal conductivity of  $U_3O_8$  from 300 to 1100 K. *J. Nucl. Mater.*, 288, (2001).

38. Hideaki, I., Hisashi, S. & Keiji, N. Lambda-type heat capacity anomalies in  $U_3O_8$ . *J. Nucl. Mater.*, 64, 66–70, (1977).
39. Noda, Yasuo., Keiji, N. The thermal conductivity of  $U_3O_8$ -z from 200 to 750 K. *J. Nucl. Mater.*, 80, (1979).
40. Yeo, S., McKenna, E., Baney, R., Subhash, G. & Tulenko, J. Enhanced thermal conductivity of uranium dioxide-silicon carbide composite fuel pellets prepared by Spark Plasma Sintering (SPS). *J. Nucl. Mater.*, 433, (2013).
41. Chen, S. & Yuan, C. Neutronic study of  $UO_2$ -BeO fuel with various claddings. *Nucl. Mater. Energy*, 22, 100728, (2020).
42. Tulenko, J. Development of Innovative Accident Tolerant High Thermal Conductivity  $UO_2$ -Diamond Composite Fuel Pellets. *NEUP Final Progress Report*, University of Florida, (2016)
43. Kim, D. J., Rhee, Y. W., Kim, J. H., Kim, K. S., Oh, J. S., Yang, J. H., Koo, Y.H., Song, K. Fabrication of micro-cell  $UO_2$ -Mo pellet with enhanced thermal conductivity. *J. Nucl. Mater.*, 462, (2015).
44. Haire, M. J., Roedern, B. G. von, Meek, T. T., Tesmer, J. & Wetteland, C. The effect of ion implantation of selected dopants on some of the electrical properties of  $UO_2$ . in *WM'03 Conference., February 23-27, 2003, Tucson, AZ, 3–9*, (2003).
45. Meek, T. T. & von Roedern, B. Semiconductor devices fabricated from actinide oxides. *Vacuum*, 83, 226–228, (2008).
46. Meek, T., Hu, M. & Haire, M. J. Semiconductive properties of uranium oxides. Waste Management 2001 Symposium, *February 25-March 1, 2001, Tucson, AZ, 0–6*, (2001).
47. Durazzo, M., Conturbia, G. L. C. R. & Urano de Carvalho, E. F. Increasing productivity in the manufacture of  $UAl_2$ -Al dispersion-plate targets for Mo-99 production. *Prog. Nucl. Energy*, 140, (2021).
48. Ryu, H. J., Kim, C. K., Sim, M., Park, J. M. & Lee, J. H. Development of high-density u/al dispersion plates for Mo-99 production using atomized uranium powder. *Nucl. Eng.*



- Technol.* 45, (2013).
49. Alexander, G. & Zia, M. Fissile material stocks and production. *Bull. At. Sci.* 65, 35–47 (2009).
  50. Stahl, D. *Fuels for research and test reactors; status review (ANL--83-5)*. Argonne National Laboratory (1982).
  51. Kang, S. Y., Gao, T. & Tian, X. F. First-principles study of electronic structure and elasticity of  $UAl_x$  ( $x=1,2,3$ ) system. *Phys. B Condens. Matter* 407, (2012).
  52. Mei, Z. G. Kim, Y. S., Yacout, A. M., Yang, J., Li, X., & Cao. Y., First-principles study of thermal conductivities of uranium aluminides. *Materialia*, 4, (2018).
  53. Wedemeyer, H. With Metals of 3rd Main Group. in *U Uranium*, Springer Berlin Heidelberg, (1989).
  54. Argaman, N. & Makov, G. Density functional theory: An introduction. *Am. J. Phys.*, 68, (1999).
  55. Sholl, David, S. & Janice, A, S. Density Functional Theory: A Practical Introduction. *John Willey & Sons Inc.*, (2009).
  56. Li, W. Katcho, N. A., & Mingo, N.. ShengBTE: A solver of the Boltzmann transport equation for phonons. *Comput. Phys. Commun.*, 185, (2014).
  57. Madsen, G. K. H. & Singh, D. J. BoltzTraP. A code for calculating band-structure dependent quantities. *Comput. Phys. Commun.* 175, (2006).
  58. Poncé, S., Margine, E. R., Verdi, C. & Giustino, F. EPW: Electron–phonon coupling, transport and superconducting properties using maximally localized Wannier functions. *Comput. Phys. Commun.* 209, (2016).
  59. Togo, A. & Tanaka, I. First principles phonon calculations in materials science. *Scr. Mater.* 108, (2015).
  60. Giannozzi, P., Baroni S., Bonini, N., Calandra, M., Car, R., Cavazzoni, C., Ceresoli, D., Chiarotti, G.L., Cococcioni, M., Dabo, I., Dal Corso, A., Gironcoli, S., Fabris, S., Fratesi, G., Gebauer, R., Gerstmann, U., Gougoussis, C., Kokalj, A., Lazzeri, M., Martin-Samos,

- L., Marzari, N., Mauri, F., Mazzarello, R., Paolini, S., Pasquarello, A., Paulatto, L., Sbraccia, C., Scandolo, S., Sclauzero, G., Seitsonen, A.P., Smogunov, A., Umari, P., Wentzcovitch, R.M. QUANTUM ESPRESSO: A modular and open-source software project for quantum simulations of materials. *J. Phys. Condens. Matter.*, 21, (2009).
61. Suryanarayana, C. & Norton, M. G. X-Ray Diffraction: A practical Approach. Springer, Boston, MA, (1998).
  62. Russ, J. C. Fundamentals of energy dispersive x-ray analysis. *Butterworths*, (1984).
  63. Corbin, S. F. & Turriff, D. M. Thermal Diffusivity by The Laser Flash Technique. John Wiley & Sons, Ltd, (1987).
  64. Fitts, D. D. Principles of Quantum Mechanics. *Cambridge University Press*, (1999).
  65. Kittel, C. Introduction to Solid State Physics. *John Wiley & Sons*, (2005).
  66. Hohenberg, P. & Kohn, W. Inhomogeneous Electron Gas. *Phys. Rev.*, 136, (1964).
  67. Born, M. & Oppenheimer, R. On the quantum theory of molecules. *Ann. Phys.*, 84, 1–24 (1927).
  68. Hettema, H. Quantum Chemistry. World scientific, (2000).
  69. Hartree, D. R. The calculation of atomic structures. *Reports Prog. Phys.*, 11, 113–143 (1947).
  70. Amusia, M. Y., Msezane, A. Z. & Shaginyan, V. R. Density Functional Theory versus the Hartree–Fock Method: Comparative Assessment. *Phys. Scr.*, 68, (2003).
  71. Fock, V. Näherungsmethode zur Lösung des quantenmechanischen Mehrkörperproblems. *Zeitschrift für Phys.*, 61, (1930).
  72. Giustino, F. Materials modelling using density functional theory: properties and predictions. Oxford University Press, (2014).
  73. Kohn, W. & Sham, L. J. Self-Consistent equations including exchange and correlation effects. *Phys. Rev.*, 140, (1965).
  74. Chen, J., Xu, Z. & Chen, Y. Introduction of density functional theory. in *Electronic*

*Structure and Surfaces of Sulfide Minerals*, Elsevier Inc., (2020).

75. Perdew, J. P. & Zunger, A. Self-interaction correction to density-functional approximations for many-electron systems. *Phys. Rev. B*, 23, (1981).
76. Vosko, S. H., Wilk, L. & Nusair, M. Accurate spin-dependent electron liquid correlation energies for local spin density calculations: a critical analysis. *Can. J. Phys.* 58, (1980).
77. Perdew, J. P., Burke, K. & Ernzerhof, M. Generalized Gradient Approximation Made Simple. *Phys. Rev. Lett.* 77, (1996).
78. Burke, K., Perdew, J. P. & Wang, Y. Derivation of a Generalized Gradient Approximation: The PW91 Density Functional. *Electron. Density Funct. Theory*, (1998).
79. Perdew, J. P., Ruzsinszky, A., Csonka, G. I., Vydrov, O. A., Scuseria, G. E., Constantin, L. A., Zhou, X., & Burke, K. Restoring the Density-Gradient Expansion for Exchange in Solids and Surfaces. *Phys. Rev. Lett.*, 100, 136406, (2008).
80. Lee, C., Yang, W. & Parr, R. G. Into a Functional of the Electron Density F F. *Phys. Rev. B*, 37, (1988).
81. Alex D. Beck. Density-functional thermochemistry. III. The role of exact exchange. *J. Chem. Phys.*, 98, (1993).
82. Perdew, J. P., Ernzerhof, M. & Burke, K. Rationale for mixing exact exchange with density functional approximations. *J. Chem. Phys.*, 105, (1996).
83. Adamo, C. & Barone, V. Toward reliable density functional methods without adjustable parameters: The PBE0 model. *J. Chem. Phys.*, 110, (1999).
84. Heyd, J., Scuseria, G. E. & Ernzerhof, M. Hybrid functionals based on a screened Coulomb potential. *J. Chem. Phys.* 118, (2003).
85. Zhao, Y. & Truhlar, D. G. Density functional for spectroscopy: No long-range self-interaction error, good performance for Rydberg and charge-transfer states, and better performance on average than B3LYP for ground states. *J. Phys. Chem. A* 110, (2006).
86. Zhao, Y. & Truhlar, D. G. The M06 suite of density functionals for main group thermochemistry, thermochemical kinetics, noncovalent interactions, excited states, and

- transition elements: Two new functionals and systematic testing of four M06-class functionals and 12 other function. *Theor. Chem. Acc.* 120, (2008).
87. Hubbard, J. Electron correlations in narrow energy bands. *Proc. R. Soc. London. Ser. A. Math. Phys. Sci.* 276, (1963).
  88. Georges, A., Kotliar, G., Krauth, W. & Rozenberg, M. J. Dynamical mean-field theory of strongly correlated fermion systems and the limit of infinite dimensions. *Rev. Mod. Phys.* 68, (1996).
  89. Ziman, J. M. *Electrons and Phonons*, Oxford University Press, (2001).
  90. Srivastava, G. P. *The Physics of Phonons*. CRC press, (2019).
  91. Lindsay, L. & Broido, D. A. Three-phonon phase space and lattice thermal conductivity in semiconductors. *J. Phys. Condens. Matter*, 20, (2008).
  92. Omini, M. & Sparavigna, A. An iterative approach to the phonon Boltzmann equation in the theory of thermal conductivity. *Phys. B Phys. Condens. Matter*, 212, (1995).
  93. Deumens, E. *The Principles of Quantum Mechanics*. Oxford university press, (2018).
  94. Chen, G. P. *Nanoscale energy transport and conversion : a parallel treatment of electrons, molecules, phonons, and photons*. Oxford University Press, (2005).
  95. Franz, R. & Wiedemann, G. Ueber die Wärme-Leitungsfähigkeit der Metalle. *Ann. der Phys. und Chemie.*, 165, (1853).
  96. Cavaliere, P. *Spark Plasma Sintering of Materials*. *Spark Plasma Sintering of Materials*. Springer, (2019).
  97. Locci, A. M., Cincotti, A., Todde, S., Orrù, R. & Cao, G. A methodology to investigate the intrinsic effect of the pulsed electric current during the spark plasma sintering of electrically conductive powders. *Sci. Technol. Adv. Mater.*, 11, 045005, (2010).
  98. Malakkal, L. Prasad, P., Jossou, E., Ranasinghe, J., Szpunar, B., Bichler, L., Szpunar, J.. Thermal conductivity of bulk and porous ThO<sub>2</sub>: Atomistic and experimental study. *J. Alloys Compd.*, 798, (2019).

99. Malakkal, L. Prasad, P., Jossou, E., Ranasinghe, J., Oladimeji, D., Szpunar, B., Bichler, L., Szpunar, J. The effect of SPS processing parameters on the microstructure and thermal conductivity of ThO<sub>2</sub>. *J. Nucl. Mater.*, 527, 151811, (2019).
100. Malakkal, L. Atomistic and Experimental Determination of the Structural and Thermophysical Properties of the Accident Tolerant Fuel Materials. *Doctoral thesis, University of Saskatchewan*, (2020).
101. Ge, L. Processing of uranium dioxide nuclear fuel pellets using spark plasma sintering. *Doctoral thesis, University of Florida*, (2014).
102. Ge, L., Subhash, G., Baney, R. H. & Tulenko, J. S. Influence of processing parameters on thermal conductivity of uranium dioxide pellets prepared by spark plasma sintering. *J. Eur. Ceram. Soc.*, 34, (2014).
103. Ironman, T. An exploration of the viability of spark plasma sintering for the commercial fabrication of nuclear fuel pellets. *Doctoral thesis, University of Florida*, (2017).
104. Chen, Z., Subhash, G. & Tulenko, J. S. Master sintering curves for UO<sub>2</sub> and UO<sub>2</sub>-SiC composite processed by spark plasma sintering. *J. Nucl. Mater.*, 454, (2014).
105. Tummalapalli, M. K., Szpunar, J. A., Prasad, A., Malakkal, L. & Bichler, L. Evaluation of thermophysical properties of UO<sub>2</sub>-10 Vol% Mo nuclear fuel pellets. *J. Nucl. Mater.*, 559, (2022).
106. Tummalapalli, M. K., Szpunar, J. A., Prasad, A. & Bichler, L. EBSD studies on microstructure and crystallographic orientation of UO<sub>2</sub>-Mo composite fuels. *Nucl. Eng. Technol.*, 53, (2021).
107. Chen, Z., Subhash, G. & Tulenko, J. S. Spark plasma sintering of diamond-reinforced uranium dioxide composite fuel pellets. *Nucl. Eng. Des.*, 294, (2015).
108. Weisensee, P. B., Feser, J. P. & Cahill, D. G. Effect of ion irradiation on the thermal conductivity of UO<sub>2</sub> and U<sub>3</sub>O<sub>8</sub> epitaxial layers. *J. Nucl. Mater.*, 443, (2013).
109. Schulz, B. Thermal expansion anomaly and thermal conductivity of U<sub>3</sub>O<sub>8</sub>. *Rev. Int. Hautes Temp. Refract.*, 12, (1975).

110. Sheykhi, S. & Payami, M. First-principles study of  $\text{UO}_2$  lattice thermal-conductivity: A simple description. *Iranian Journal of Science and Technology, Transactions A: Science*, 44, (2020).
111. Kaloni, T. P., Onder, N., Pencer, J. & Torres, E. DFT+U approach on the electronic and thermal properties of hypostoichiometric  $\text{UO}_2$ , *Annals of Nuclear Energy*. 144, (2020).
112. Torres, E., Cheiknjifon, I., Kaloni, T. P. & Pencer, J. A comparative analysis of the phonon properties in  $\text{UO}_2$  using the Boltzmann transport equation coupled with DFT + U and empirical potentials. *Computational Materials Science*, 177, (2020).
113. Lu, Y., Yang, Y. & Zhang, P. Thermodynamic properties and structural stability of thorium dioxide. *J. Phys. Condens. Matter* 24, (2012).
114. Liu, J., Dai, Z., Yang, X., Zhao, Y. & Meng, S. Lattice thermodynamic behavior in nuclear fuel  $\text{ThO}_2$  from first principles. *J. Nucl. Mater.*, 511, (2018).
115. Kaloni, T. P. & Torres, E. Thermal and mechanical properties of  $\text{U}_3\text{Si}_2$ : A combined ab-initio and molecular dynamics study. *J. Nucl. Mater.*, 533, 152090, (2020).
116. Jossou, E. Rahman, M. D. J., Oladimeji, D., Beeler, B., Szpunar, B., & Szpunar, J. Anisotropic thermophysical properties of  $\text{U}_3\text{Si}_2$  fuel: An atomic scale study. *J. Nucl. Mater.*, 521, (2019).
117. Szpunar, B. & Szpunar, J. A. Thermal Conductivity of Uranium Nitride and Carbide. *Int. J. Nucl. Energy*, 2014, (2014).
118. Kim, Y. S. A thermodynamic evaluation of the  $\text{U}\pm\text{O}$  system from  $\text{UO}_2$  to  $\text{U}_3\text{O}_8$ , 279, (2000).
119. b, Y., Rusz, J., Suzuki, M. T. & Oppeneer, P. M. First-principles investigation of higher oxides of uranium and neptunium:  $\text{U}_3\text{O}_8$  and  $\text{Np}_2\text{O}_5$ . *Phys. Rev. B - Condens. Matter Mater. Phys.*, 83, (2011).
120. Wen, X., Martin, R. L., Scuseria, G. E., Rudin, S. P., Batista<sup>1</sup>, E. R., & Burrell, A. K. Screened hybrid and DFT + U studies of the structural, electronic, and optical properties of

- $U_3O_8$ . *J. Phys. Condens. Matter*, 25, 025501, (2013).
121. Ranasinghe, J. I., Malakkal, L., Jossou, E., Szpunar, B. & Szpunar, J. A. Comprehensive study on the electronic and optical properties of  $\alpha$ - $U_3O_8$ . *Comput. Mater. Sci.*, 171, (2020).
  122. Yun, Y., Kim, H., Kim, H. & Park, K. Atomic diffusion mechanism of Xe in  $UO_2$ . 378, (2008).
  123. Yun, Y., Eriksson, O., Oppeneer, P. M., Kim, H. & Park, K. First-principles theory for helium and xenon diffusion in uranium dioxide. *J. Nucl. Mater.*, 385, (2009).
  124. Freyss, M., Vergnet, N. & Petit, T. Ab initio modeling of the behavior of helium and xenon in actinide dioxide nuclear fuels. 352, (2006).
  125. Wen, X., Martin, R. L., Henderson, T. M. & Scuseria, G. E. Density Functional Theory Studies of the Electronic Structure of Solid State Actinide Oxides. *American Chemical Society*, 2, 113, (2013).
  126. Copeland, G. L., Martin, M., Development of High-Uranium-Loaded  $U_3O_8$ -Al fuel plates. *Nuclear Technology*, 56:3, (1982).
  127. Martin, M. M. High-Uranium-loaded  $U_3O_8$ -Al fuel element development program. Oak Ridge National Laboratory, U.S. DOE.
  128. Peacock, H.B. Properties of  $U_3O_8$ -Aluminum cermet fuel (WSRC-RP-89-981). Westinghouse Savannah River Co., Aiken, SC (USA), (1989).
  129. Martin, M. M., Richt, A. E., Martin M. W. *Irradiation behavior of aluminum base fuel dispersions (ORNL-4856)*. (1973).
  130. Ge, L., Processing of  $UO_2$  nuclear fuel pellets using spark plasma sintering, *PhD dissertation*, University of Florida, (2014).
  131. Ironman, T., Tulenko, J. & Subhash, G. Exploration of Viability of Spark Plasma Sintering for Commercial Fabrication of Nuclear Fuel Pellets. *Nucl. Technol.*, 200, (2017).
  132. Cartas, A., Wang, H., Subhash, G., Baney, R. & Tulenko, J. Influence of Carbon Nanotube Dispersion in  $UO_2$ -Carbon Nanotube Ceramic Matrix Composites Utilizing Spark Plasma

- Sintering. *Nucl. Technol.*, 189, (2015).
133. Subhash, G., Development of Innovative High Thermal Conductivity UO<sub>2</sub> Ceramic Composites Fuel Pellets with Carbon Nano-Tubes Using Spark Plasma Sintering, *Technical report*, University of Florida, USA, (2014).
  134. Shepherd, D. Spark plasma sintering research in nuclear technology-UO<sub>2</sub>-ZrN. (2018).
  135. Mishra, A.K., Shelke, B.K., Yadav, M.K., Afzal, Mohd, Kumar, Arun, & Prasad, G. J. Developments in fabrication of annular MOX fuel pellet for Indian fast reactor. International Atomic Energy Agency (IAEA), (2015).
  136. Singh, A. K., Zunjarrao, S. C. & Singh, R. P. Silicon Carbide and Uranium Oxide Based Composite Fuel Preparation Using Polymer Infiltration and Pyrolysis. *Proceedings of the 14th International Conference on Nuclear Engineering*. Miami, Florida, USA. July 17–20, 427-433. ASME, (2006).
  137. Raftery, A. M., Seibert, R., Brown, D., Trammell, M., Nelson, A., & Terrani, K. Fabrication of UN-Mo CERMET nuclear fuel using advanced manufacturing techniques. *Nuclear and Emerging Technologies for Space*, TN, April 6-9, (2020).
  138. Buckley, J., Turner, J. D. & Abram, T. J. Uranium dioxide - Molybdenum composite fuel pellets with enhanced thermal conductivity manufactured via spark plasma sintering. *J. Nucl. Mater.*, 523, (2019).
  139. Loopstra, B. O. Neutron Diffraction Investigation of U<sub>3</sub>O<sub>8</sub>. *Acta Crystallogr.* 17, (1964).
  140. Ackermann, R.J., & Chang, A.T., Thermal expansion and phase transformations of the U<sub>3</sub>O<sub>8-z</sub> phase in air., *J. inorg. nucl. Chem.*, 39, (1977).
  141. Landau, L.D.E., Theory of elasticity. *Pergamon Press*, (1970).
  142. Jochym, P. T. & Parlinski, K. Ab initio lattice dynamics and elastic constants of ZrC. *Physical Journal B.*, 268, (2000).
  143. Mauhat, F., & Coudert, F., Necessary and sufficient elastic stability conditions in various



- crystal systems. *Physical Review B*, 90, 224104, (2014).
144. Brincat, N. A., Parker, S. C., Molinari, M., Allen, G. C. & Storr, M. T. Density functional theory investigation of the layered uranium oxides  $U_3O_8$  and  $U_2O_5$ . *Dalt. Trans.* 44, 2613–2622, (2015).
  145. Voigt, W. *Lehrbuch der Kristallphysik.*, Vieweg & Teubner Verlag, (1966).
  146. Reuss, A. Berechnung der Fließgrenze von Mischkristallen auf Grund der Plastizitätsbedingung für Einkristalle. *J. Appl. Math. Mech. / Zeitschrift für Angew. Math. und Mech.* 9, (1929).
  147. Hill, R. The Elastic Behaviour of a Crystalline Aggregate. *Proceedings of the Physical Society. Section A*, 65, (1952).
  148. Ondracek, G. & Schulz, B. The porosity dependence of the thermal conductivity for nuclear fuels. *J. Nucl. Mater.* 46, (1973).
  149. Blasinski, H. & Heim, A. The influence of porosity on the thermal conductivity of granular layers. *Zesz. Nauk. Politech. Łódzkiej- Chem.* 24, (1973).
  150. Naito, K., Inaba, H., & Takashi, S., Phase transitions in  $U_3O_8$ -z:I, Heat capacity measurements, *J. Nucl. Mater.*, 110, (1982).
  151. George, A. M. & Karkhanavala, M. D. Studies of the electrical properties of uranium oxides-I. Electrical conductivity of  $\alpha$ - $U_3O_8$ . *J. Phys. Chem. Solids* 24, (1963).
  152. Kövér, M., Behúlová, M., Drienovský, M. & Motyčka, P. Determination of the specific heat using laser flash apparatus. *J. Therm. Anal. Calorim.*, 122, (2015).
  153. Westrum, E. F. & Grønvald, F. Low Temperature Heat Capacity and Thermodynamic Functions of Triuranium Octoxide. *J. Am. Chem. Soc.*, 81, (1959).
  154. Hideaki, I., H., Shimizu, H., & Naito, K. Lambda-type heat capacity anomalies in  $U_3O_8$ , *J. of Nuc. Mat.*, 64, (1977).
  155. Girdhar, H. L. & Westrum, E. F.  $\lambda$ -Type Thermal Anomaly in Triuranium Octaoxide at

- 482.7°K. *J. Chem. Eng. Data*, 13, (1968).
156. Konings, R. J. M., Benes, O., Kovacs, A., Manara, D., Sedmidubsky, D., Gorokhov, L., Irosh, V. S., Yungman, V., Shenyavskaya, E., & Osina, E. The Thermodynamic Properties of the f-Elements and their Compounds: Part 2. The Lanthanide and Actinide Oxides. *J. Phys. Chem. Ref. Data*, 43, (2014).
  157. Ioffe, A. F., & Regel, A. R., Non-crystalline, amorphous and liquid electronic semiconductors. *Prog. Semicond*, 4, (1960).
  158. Yin, Q. & Savrasov, S. Y. Origin of Low Thermal Conductivity in Nuclear Fuels. *Phys. Rev. Lett.*, 100, 225504, (2008).
  159. Kopp, H., Investigations of the Specific Heat of Solid Bodies. *Philosophical Transactions of the Royal Society of London*, 155, (1865).
  160. Rasor, N. S. & McClelland, J. D. Thermal properties of graphite, molybdenum and tantalum to their destruction temperatures. *J. Phys. Chem. Solids* 15, (1960).
  161. Brooks, C. R. & Bingham, R. E. The specific heat of aluminum from 330 to 890°K and contributions from the formation of vacancies and anharmonic effects. *J. Phys. Chem. Solids* 29, (1968).
  162. Gibson, G. W. & De Boisblanc, D. R. The Use of Uranium Aluminide Powders in Nuclear Reactor Fuel Elements. *Modern Developments in Powder Metallurgy*, (1966).
  163. Ryu, H. O. J. I. N., Kim, C. K. Y. U., Sim, M., Park, J. M. A. N. & Lee, J. H. Development of high-density U/Al dispersion plates for Mo-99 production using atomized uranium powder. *Nucl. Eng. Technol.* 45, (2013).
  164. Thümmeler, F., Lilienthal, H. E. & Nazare, S. UAl<sub>2</sub>-Al instead of UAl<sub>3</sub>-Al in fuel-element plates for advanced test-reactors. *Powder Metall.*, 12, (1969).
  165. Dienst, W., Nazaré, S. & Thümmeler, F. Irradiation behaviour of UAl<sub>x</sub>-Al dispersion fuels for thermal high flux reactors. *J. Nucl. Mater.* 64, (1977).

166. Brown, K. R. Irradiation Program of Highly Loaded  $UAl_2$ -Al Fuel Plates (ANL/RERTR/TM--4). *International Atomic Energy Agency (IAEA)*, (1980).
167. Taleyarkhan, R. P. Analysis & Modeling of Fission Product Release From Heated Uranium-Aluminum Plate-Type Reactor Fuels (CONF-900917--4), (1990).
168. *Research reactor core conversion guidebook Volume 4: Fuels (Appendices I-K)*. IAEA-TECDOC-643, 4, IAEA. (1992).
169. Lundberg, L. B. & Croson, M. L. Corrosion of spent advanced test reactor fuel (CONF-941207--9). *Spent nuclear fuel meeting: challenges and initiatives*, USA, (1994).
170. Kaminski, M. D. *Aqueous corrosion of aluminum-based nuclear fuel*. (ANL-CMT-01/1), Argonne National Lab., IL, USA, (2003)
171. *Uranium alloys with metals of 3rd Main Group*. Chapter 3, Springer, (1989).
172. Meyer, M. K. Irradiation performance of U-Mo Monolithic fuel. *Nucl. Eng. Technol.* 46, (2014).
173. Hu, S., Burkes, D., Lavender, C. A. & Joshi, V. Effect of grain morphology on gas bubble swelling in UMo fuels - a 3D microstructure dependent Booth model. *J. Nucl. Mater.* 480, (2016).
174. Finlay, M. R., Hofman, G. L. & Snelgrove, J. L. Irradiation behaviour of uranium silicide compounds. *J. Nucl. Mater.*, 325, (2004).
175. Harp, J. M., Lessing, P. A. & Hoggan, R. E. Uranium silicide pellet fabrication by powder metallurgy for accident tolerant fuel evaluation and irradiation. *J. Nucl. Mater.* 466, (2015).
176. Copeland, G. L. & Martin, M. M. Development of High-Uranium-Loaded  $U_3O_8$ -Al Fuel Plates. *Nucl. Technol.* 56, (1982).
177. Peacock, H. B. Properties of  $U_3O_8$ -aluminum cermet fuel. *Westinghouse Savannah River Co., Aiken, SC, USA*, (1989).

178. Palancher, H., Martin, P., Nassif, V., Tucoulou, R., Proux, O., Hazemann, L., Tougait, O., Lahera, E., Mazaudier, F., Valot, C., & Dubois, S. Evidence for the presence of U–Mo–Al ternary compounds in the U–Mo/Al interaction layer grown by thermal annealing: a coupled micro X-ray diffraction and micro X-ray absorption spectroscopy study. *J. Appl. Crystallogr.*, 40, (2007).
179. Leenaers, A., Detavernier, C. & Van den Berghe, S. The effect of silicon on the interaction between metallic uranium and aluminum: A 50 year long diffusion experiment. *J. Nucl. Mater.*, 381, (2008).
180. Mei, Z. & Yacout, A. M. First-principles study of structural, elastic, electronic, vibrational and thermodynamic properties of uranium aluminides. *Comput. Mater. Sci.*, 158, (2019).
181. Modak, B., Ghoshal, K., Srinivasu, K. & Ghanty, T. K. Exploring the electronic structure and thermal properties of  $UAl_3$  using density functional theory calculations. *J. Phys. Chem. Solids*, 136, 109179, (2020).
182. Gordon, P. & Kaufmann, A. R. The alloy systems uranium-aluminum and uranium-iron. *JOM*, 2, (1949).
183. Rundle, R. E. & Wilson, A. S. The structures of some metal compounds of uranium. *Acta Crystallogr.* 2, (1949).
184. Katz, G. & Jacobs, A. . Lattice constants of the intermetallic compounds  $UAl_2$  and  $UFe_2$ . *J. Nucl. Mater.*, 5, (1962).
185. Kassner, M. E., Adler, P. H., Adamson, M. G. & Peterson, D. E. Evaluation and thermodynamic analysis of phase equilibria in the U-Al system. *J. Nucl. Mater.* 167, (1989).
186. Burzo, E. & Lucaci, P. Magnetic properties of  $U(Co_xAl_{1-x})_2$  compounds. *Solid State Commun.*, 56, (1985).
187. Narasimham, A. V, Roth, S., Renker, B., Käfer, K. & Buerkin, J. Elastic constants of  $UAl_2$ . Temperature and magnetic field dependence. *Phys. Status Solidi*, 57, K75–K78, (1980).

188. Wire, M. S., Stewart, G. R. & Roof, R. B. Properties of some pseudobinary alloys based on  $\text{UAl}_2$ . *J. Magn. Magn. Mater.*, 53, (1985).
189. Togo, A., Chaput, L., Tanaka, I. & Hug, G. First-principles phonon calculations of thermal expansion in  $\text{Ti}_3\text{SiC}_2$ ,  $\text{Ti}_3\text{AlC}_2$ , and  $\text{Ti}_3\text{GeC}_2$ . *Phys. Rev. B*, 81, 174301 (2010).
190. Birch, F. Finite Elastic Strain of Cubic Crystals. *Phys. Rev.* 71, (1947).
191. Ackland, G. J., Huang, X. & Rabe, K. M. First-principles thermodynamics of transition metals: W, NiAl, and PdTi. *Phys. Rev. B*, 68, 214104, (2003).
192. Swift, D. C., Ackland, G. J., Hauer, A. & Kyrala, G. A. First-principles equations of state for simulations of shock waves in silicon. *Phys. Rev. B*, 64, 214107, (2001).
193. Huang, X. Thermal equation of state of Molybdenum determined from in situ synchrotron X-ray diffraction with laser-heated diamond anvil cells. *Sci. Rep.* 6, 19923, (2016).
194. Dengg, T. *Computation of Temperature Dependent Elastic Constants within the Framework of Density-Functional Theory*. PhD thesis, Karl-Franzens-University, (2017).
195. Snyder, M. & Tripler, A. *Some Refractory Uranium Compounds Preparation and Properties*. *ASTM International*, (1960).
196. Pang, J. W. L. Phonon Lifetime Investigation of Anharmonicity and Thermal Conductivity of  $\text{UO}_2$  by Neutron Scattering and Theory. *Phys. Rev. Lett.*, 110, 157401 (2013).
197. Malakkal, L., Prasad, P., Jossou, E., Oladimeji, D., Ranasinghe, J., Szpunar, B., Bichler, L., Szpunar, J.. Atomistic and experimental study on thermal conductivity of bulk and porous cerium dioxide. *Sci. Rep.* 9, 6326, (2019).
198. Arko, A. J., Brodsky, M. B. & Nellis, W. J. Spin Fluctuations in Plutonium and Other Actinide Metals and Compounds. *Phys. Rev. B*, 5, (1972).
199. Armbrüster, H., Franz, W., Schlabit, W. & Steglich, F. Transport properties, susceptibility and specific heat of  $\text{UAl}_2$ . *Le J. Phys. Colloq.*, 40, (1979).

200. Wire, M. S., Thompson, J. D. & Fisk, Z. Influence of spin fluctuations on the electrical resistance of  $\text{UAl}_2$  and  $\text{UPt}_3$  at high pressures and low temperatures. *Phys. Rev. B*, 30, (1984).
201. Park, J. S., Woo, U. M., Kim, K. H., Park, J. M. & Kim, C. K. The evaluation of thermal conductivity in  $\text{UAl}_2$  rod manufactured by powder metallurgy method. *Transactions of the Korean Nuclear Society Spring Meeting*, (2007).
202. Zhou, W., Liu, R. & Revankar, S. T. Fabrication methods and thermal hydraulics analysis of enhanced thermal conductivity  $\text{UO}_2\text{-BeO}$  fuel in light water reactors. *Annals of Nuclear Energy*, 81, (2015).
203. Kurata, M. Research and Development Methodology for Practical Use of Accident Tolerant Fuel in Light Water Reactors. *Nucl. Eng. Technol.* 48, (2016).
204. Kim, H., Yang, J., Kim, W. & Koo, Y. Development Status of Accident-tolerant Fuel for Light Water Reactors in Korea. *Nucl. Eng. Technol.*, 8, (2015).
205. Rahman, M. J., Cooper, M. W. D., Szpunar, B. & Szpunar, J. A. Primary radiation damage on displacement cascades in  $\text{UO}_2$ ,  $\text{ThO}_2$  and  $(\text{U}_{0.5}\text{Th}_{0.5})\text{O}_2$ . *Comput. Mater. Sci.*, 154, (2018).
206. Yu, J., Devanathan, R. & Weber, W. J. First-principles study of defects and phase transition in  $\text{UO}_2$ . *J. Phys. Condens. Matter*, 21, 435401, (2009).
207. Sonoda, T. Transmission electron microscopy observation on irradiation-induced microstructural evolution in high burn-up  $\text{UO}_2$  disk fuel. *Nucl. Instruments Methods Phys. Res. Sect. B Beam Interact. with Mater. Atoms* 191, (2002).
208. Herranz, L. E. & Feria, F. Spent fuel rod splitting due to  $\text{UO}_2$  oxidation during dry storage: Assessment of the database. *Prog. Nucl. Energy*, 51, (2009).
209. Comsan, M. N. H. Status of Nuclear Power Reactor Development. *6th Conf. Nucl. Part. Phys.* 79–89, (2007).

210. Chollet, M., Belin, R. C., Richaud, J.-C., Reynaud, M. & Adenot, F. High-Temperature X-ray Diffraction Study of Uranium–Neptunium Mixed Oxides. *Inorg. Chem.*, 52, 2519–2525, (2013).
211. Szpunar, B., Szpunar, J. A., Milman, V. & Goldberg, A. Implication of volume changes in uranium oxides: A density functional study. *Solid State Sci.*, 24, (2013).
212. Snelgrove, J., Hofman, G., Meyer, M., Trybus, C. & Wiencek, T. Development of very-high-density low-enriched-uranium fuels. *Nucl. Eng. Des.*, 178, (1997).
213. Marra, J. E. & Peacock, H. B. Reactions During the Processing of U<sub>3</sub>O<sub>8</sub>-Al Cermet Fuels. *J. Am. Ceram. Soc.*, 74, (1991).
214. Loopstra, B. O. The structure of  $\beta$ -U<sub>3</sub>O<sub>8</sub>. *Acta Crystallogr. Sect. B Struct. Crystallogr. Cryst. Chem*, 26, (1970).
215. Price, R. R., Haire, M. J. & Croff, A. G. Depleted -Uranium uses R&D program, WM'01 Conference, February 25-March 1, 2001, Tucson, AZ., 204, (2001).
216. Marks, D. L., Vinegoni, C., Bredfeldt, J. S. & Boppart, S. A. Interferometric differentiation between resonant Coherent Anti-Stokes Raman Scattering and nonresonant four-wave-mixing processes. *Appl. Phys. Lett.*, 85, 5787, (2004).
217. Glazoff, M. V., van Rooyen, I. J., Coryell, B. D. & Parga, C. J. Comparison of Nuclear Fuels for TREAT: UO<sub>2</sub> vs U<sub>3</sub>O<sub>8</sub>. Idaho National Laboratory, USA, (2016).
218. Pasto, A. E., Copeland, G. L., & Martin, M. M. A quantitative differential thermal analysis study of the U<sub>3</sub>O<sub>8</sub>-Al thermite reaction. *INIS 12*, CONF-800460--5 (1980).
219. He, H., Andersson, D. A., Allred, D. D. & Rector, K. D. Determination of the Insulation Gap of Uranium Oxides by Spectroscopic Ellipsometry and Density Functional Theory. *J. Phys. Chem. C*, 117, (2013).
220. Magnuson, M., Butorin, S. M., Werme, L., Nordgren, J., Ivanov, K.E., Guo, J. H., Shuh, D. K., Uranium oxides investigated by X-ray absorption and emission spectroscopies. *Appl.*

- Surf. Sci.* 252, (2006).
221. Kohn, W. & Sham, L. J. Self-Consistent Equations Including Exchange and Correlation Effects. *Phys. Rev.*, 140, (1965).
  222. Ebraheem, S. & El-Saied, A. Band Gap Determination from Diffuse Reflectance Measurements of Irradiated Lead Borate Glass System Doped with TiO<sub>2</sub> by Using Diffuse Reflectance Technique. *Mater. Sci. Appl.* 04, (2013).
  223. Yang, L. & Kruse, B. Revised Kubelka–Munk theory I Theory and application. *J. Opt. Soc. Am. A* 21, 1933 (2004).
  224. Murphy, A. Band-gap determination from diffuse reflectance measurements of semiconductor films, and application to photoelectrochemical water-splitting. *Sol. Energy Mater. Sol. Cells* 91, (2007).
  225. Schwarz, K. & Blaha, P. Solid state calculations using WIEN2k. *Comput. Mater. Sci.* 28, (2003).
  226. Ernzerhof, M. & Scuseria, G. E. Assessment of the Perdew–Burke–Ernzerhof exchange–correlation functional. *J. Chem. Phys.*, 110, (1999).
  227. Dorado, B., Amadon, B., Freyss, M. & Bertolus, M. DFT+U calculations of the ground state and metastable states of uranium dioxide. *Phys. Rev. B* 79, 235125, (2009).
  228. Watson, G. W., Kelsey, E. T., de Leeuw, N. H., Harris, D. J. & Parker, S. C. Atomistic simulation of dislocations, surfaces and interfaces in MgO. *J. Chem. Soc. Faraday Trans.* 92, 433, (1996).
  229. Momma, K. & Izumi, F. VESTA : a three-dimensional visualization system for electronic and structural analysis. *J. Appl. Crystallogr.* 41, (2008).
  230. Vargas, W. E. & Niklasson, G. A. Applicability conditions of the Kubelka–Munk theory. *Appl. Opt.*, 36, 5580, (1997).
  231. Tauc, J., Grigorovici, R. & Vancu, A. Optical Properties and Electronic Structure of



- Amorphous Germanium. *Phys. status solidi*, 15, (1966).
232. Viezbicke, B. D., Patel, S., Davis, B. E. & Birnie, D. P. Evaluation of the Tauc method for optical absorption edge determination: ZnO thin films as a model system. *Phys. status solidi*, 252, (2015).
  233. Wang, W., Sun, J. & He, J. Spin-orbit coupling and electron correlation effects on phonon anharmonicity of  $\text{KOs}_2\text{O}_6$ . *AIP Adv.*, 9, 025214 (2019).
  234. Kang, C., Kim, K. & Min, B. I. Phonon softening and superconductivity triggered by spin-orbit coupling in simple-cubic  $\alpha$ -polonium crystals. *Phys. Rev. B*, 86, 054115, (2012).
  235. Hudson, E. A., Rehr, J. J. & Bucher, J. J. Multiple-scattering calculations of the uranium L3-edge x-ray-absorption near-edge structure. *Phys. Rev. B*, 52, (1995).
  236. Kvashnina, K. O., Butorin, S. M., Martin, P. & Glatzel, P. Chemical State of Complex Uranium Oxides. *Phys. Rev. Lett.*, 111, 253002, (2013).
  237. Hummer, K., Harl, J. & Kresse, G. Heyd-Scuseria-Ernzerhof hybrid functional for calculating the lattice dynamics of semiconductors. *Phys. Rev. B*, 80, 115205, (2009).
  238. Kumar, D. & Gupta, N. M. An overview of studies on the highly dispersed uranium oxide species occluded within mesoporous MCM-41 and MCM-48 host materials. *Catal. Surv. from Asia*, 9, (2005).
  239. Schoenes, J. Optical properties and electronic structure of  $\text{UO}_2$ . *J. Appl. Phys.*, 49, 1463–1465, (1978).
  240. Young, C., Petrosky, J., Mann, M., Hunt, M. E., Turner, D., & Kelly, T., The work function of hydrothermally synthesized  $\text{UO}_2$  and the implications for semiconductor device fabrication, *Phys. Status Solidi*, 10, (2016).
  241. Umebayashi, T., Yamaki, T., Itoh, H. & Asai, K. Band gap narrowing of titanium dioxide by sulfur doping. *Appl. Phys. Lett.*, 81, (2002).
  242. Johnson, K. W. & Bell, E. E. Far-Infrared Optical Properties of KCl and KBr. *Phys. Rev.*,

- 187, (1969).
243. Davis, E. A. & Mott, N. F. Conduction in non-crystalline systems V. Conductivity, optical absorption and photoconductivity in amorphous semiconductors. *Philos. Mag.*, 22, (1970).
244. Shuffler, C., Trant, J., Malen, J. & Todreas, N. Thermal hydraulic analysis for grid supported pressurized water reactor cores. *Nucl. Eng. Des.*, 239, (2009).
245. *Nuclear Fuel Safety Criteria Technical Review*. 2<sup>nd</sup> Ed., Nuclear Energy Agency. (2012).
246. Allen, T., Busby, J., Meyer, M. & Petti, D. Materials challenges for nuclear systems. *Mater. Today*, 13, (2010).
247. Matos, J.E. & Snelgrove, J.L. Selected thermal properties and uranium density relations for alloy, aluminide, oxide, and silicide fuels. IAEA-TECDO, (1992).
248. Zhou, W., Liu, R. & Revankar, S. T. Fabrication methods and thermal hydraulics analysis of enhanced thermal conductivity UO<sub>2</sub>-BeO fuel in light water reactors. *Ann. Nucl. Energy* 81, (2015).
249. Kegler, P., Klinkenberg, M., Bukaemskiy, A., Murphy, G. L., Deissmann, G., Brandt, F., & Bosbach, D. Chromium doped UO<sub>2</sub>-based ceramics: Synthesis and characterization of model materials for modern nuclear fuels. *Materials (Basel)*, 14, (2021).
250. *Incorporation of Chromia-Doped fuel properties in AREVA approved methods*, ANP-10340NP, (2016).
251. Van Den Berghe, S. & Lemoine, P. Review of 15 years of high-density lowenriched UMO dispersion fuel development for research reactors in Europe. *Nucl. Eng. Technol.*, 46, (2014)
252. Agata, E. D., Knol, S, Fedorov, A.V., Fernandez, A., Somers, J., Klaassen, F., The behaviour under irradiation of molybdenum matrix for inert matrix fuel containing americium oxide ( CerMet concept ). *J. Nucl. Mater.* 465, (2015).
253. Ranasinghe, J. I., Malakkal, L., Szpunar, B., Prasad, A., Jossou, A., Spunar, J., & Bichler, L. DFT and experimental study on the thermal conductivity of U<sub>3</sub>O<sub>8</sub> and U<sub>3</sub>O<sub>8</sub>-X; (X=Al

- and Mo). *J. Nucl. Mater.*, 549, 152900, (2021).
254. Zeng, Z. Y., Hu, C. E., Cai, L. C., Chen, X. R. & Jing, F. Q. Lattice dynamics and thermodynamics of molybdenum from first-principles calculations. *J. Phys. Chem. B*, 114, (2010).
255. Dwight, A. E. The uranium-molybdenum equilibrium diagram below 900° C. *J. Nucl. Mater.* 2, (1960).
256. Ikehata, H., Nagasako, N., Furuta, T., Fukumoto, A., Miwa, K., & Saito, T. First-principles calculations for development of low elastic modulus Ti alloys. *Phys. Rev. B - Condens. Matter Mater. Phys.* 70, (2004).
257. Rafaja, D., Kostenbauer, H., Muhle, U., Loffler, C., Schreiber, G., Kathrein, M., Winkler, J., Effect of the deposition process and substrate temperature on the microstructure defects and electrical conductivity of molybdenum thin films. *Thin Solid Films*, 528, (2013).
258. Zarestky, J., Stassis, C., Harmon, B. N., Ho, K. M. & Fu, C. L. Temperature dependence of the vibrational modes of molybdenum. *Phys. Rev. B*, 28, (1983).
259. Desai, P. D., Chu, T. K., James, H. M. & Ho, C. Y. Electrical Resistivity of Selected Elements. *J. Phys. Chem. Ref. Data*, 13, (1984).
260. Martin, F. & Mattsson, T. R. Thermoelectric transport properties of molybdenum from *ab initio* simulations. *Phys. Rev. B - Condens. Matter Mater. Phys.*, 90, (2014).
261. Tye, R. P. Preliminary measurements on the thermal and electrical conductivities of molybdenum, niobium, tantalum and tungsten. *J. Less-Common Met.*, 3, (1961).
262. Taylor, R. E. & Finch, R. A. The specific heats and resistivities of Molybdenum, Tantalum, and Rhenium. *J. less-common Met.*, 6, (1964).
263. Wen, S., Ma, J., Kundu, A. & Li, W. Large lattice thermal conductivity, interplay between phonon-phonon, phonon-electron, and phonon-isotope scatterings, and electrical transport in molybdenum from first principles., *Phys. Rev. B* 102, (2020).

264. Cutler, M. & Cheney, G. T. Measurement of thermal conductivity at high temperatures. *J. Appl. Phys.* 34, (1963).
265. Wang, J., Carson, J. K., North, M. F. & Cleland, D. J. A new approach to modelling the effective thermal conductivity of heterogeneous materials. *Int. J. Heat Mass Transf.*, 49, (2006).
266. Miller, J. V. *Estimating thermal conductivity of cermet fuel materials for nuclear reactor applications*. NASA technical note (1967).
267. Liu, M., Lee, Y. & Rao, D. V. Development of effective thermal conductivity model for particle-type nuclear fuels randomly distributed in a matrix. *J. Nucl. Mater.*, 508, 168–180, (2018).

# APPENDIX A

## COPYRIGHT AGREEMENTS

### A.1 Copyright permission for the manuscript presented in Chapter 3.



The screenshot shows a web browser window with the URL <https://s100.copyright.com/AppDispatchServlet#formTop>. The page header includes the CCC RightsLink logo and navigation links: Home, Help, Email Support, Sign in, and Create Account. The main content area displays the following information:

**DFT and experimental study on the thermal conductivity of U3O8 and U3O8-X; (X=Al and Mo)**

**Author:** Jayangani I. Ranasinghe, Linu Malakkal, Barbara Szpunar, Anil Prasad, Eric Moore Jossou, Jerzy A. Szpunar, Lukas Bichler

**Publication:** Journal of Nuclear Materials

**Publisher:** Elsevier

**Date:** June 2021

*© 2021 Elsevier B.V. All rights reserved.*

**Journal Author Rights**

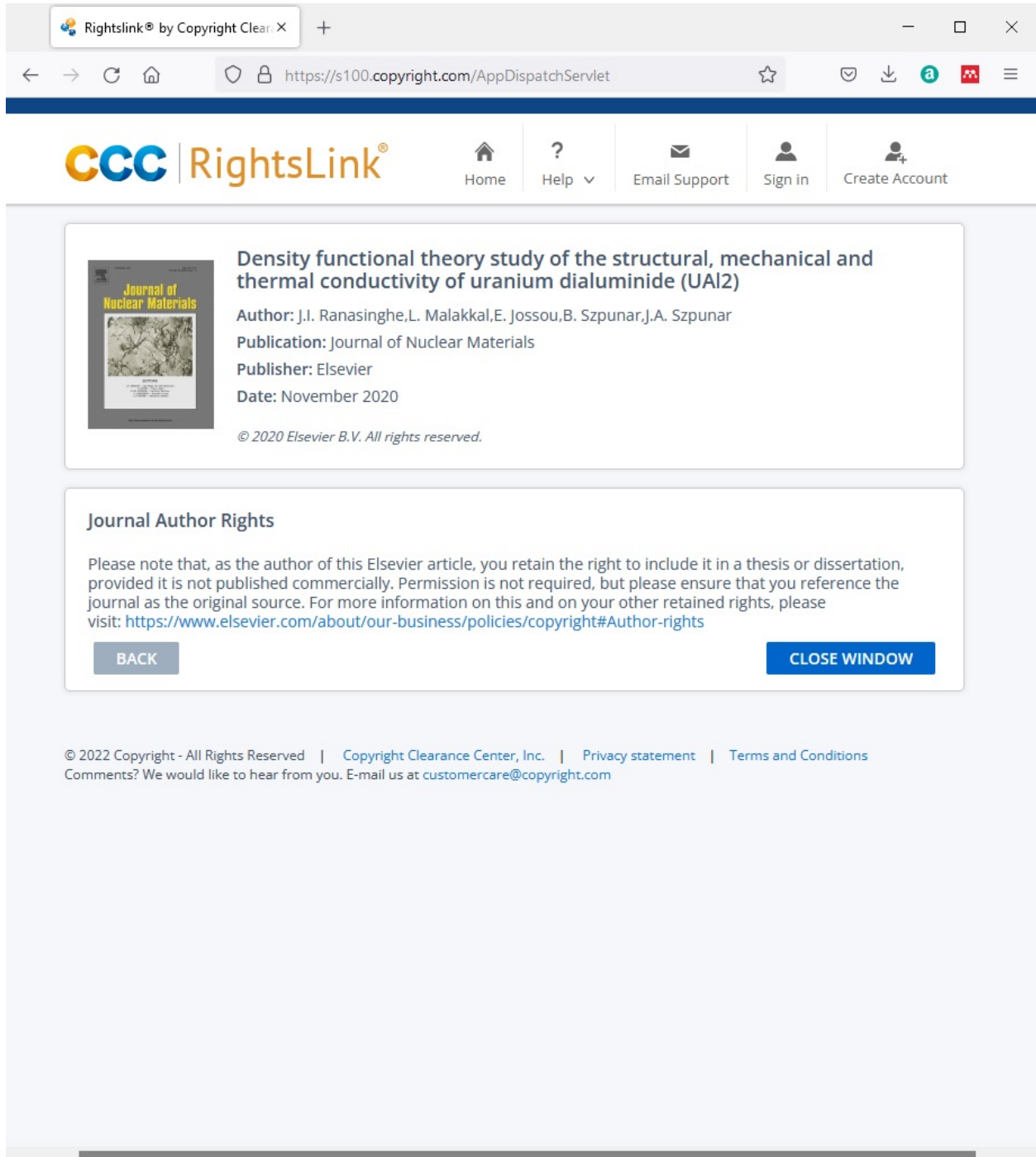
Please note that, as the author of this Elsevier article, you retain the right to include it in a thesis or dissertation, provided it is not published commercially. Permission is not required, but please ensure that you reference the journal as the original source. For more information on this and on your other retained rights, please visit: <https://www.elsevier.com/about/our-business/policies/copyright#Author-rights>

Buttons: BACK, CLOSE WINDOW

© 2022 Copyright - All Rights Reserved | Copyright Clearance Center, Inc. | [Privacy statement](#) | [Terms and Conditions](#)  
Comments? We would like to hear from you. E-mail us at [customer care@copyright.com](mailto:customer care@copyright.com)

Page 4 of 18 26 of 4328 words English (United States) Text Predictions: On Accessibility: Investigate

## A.2 Copyright permission for the manuscript presented in Chapter 4.



The screenshot shows a web browser window with the URL <https://s100.copyright.com/AppDispatchServlet>. The page header features the CCC RightsLink logo and navigation links for Home, Help, Email Support, Sign in, and Create Account. The main content area displays the following information:

**Density functional theory study of the structural, mechanical and thermal conductivity of uranium dialuminide (UAl<sub>2</sub>)**

**Author:** J.I. Ranasinghe, L. Malakkal, E. Jossou, B. Szipunar, J.A. Szipunar  
**Publication:** Journal of Nuclear Materials  
**Publisher:** Elsevier  
**Date:** November 2020

*© 2020 Elsevier B.V. All rights reserved.*

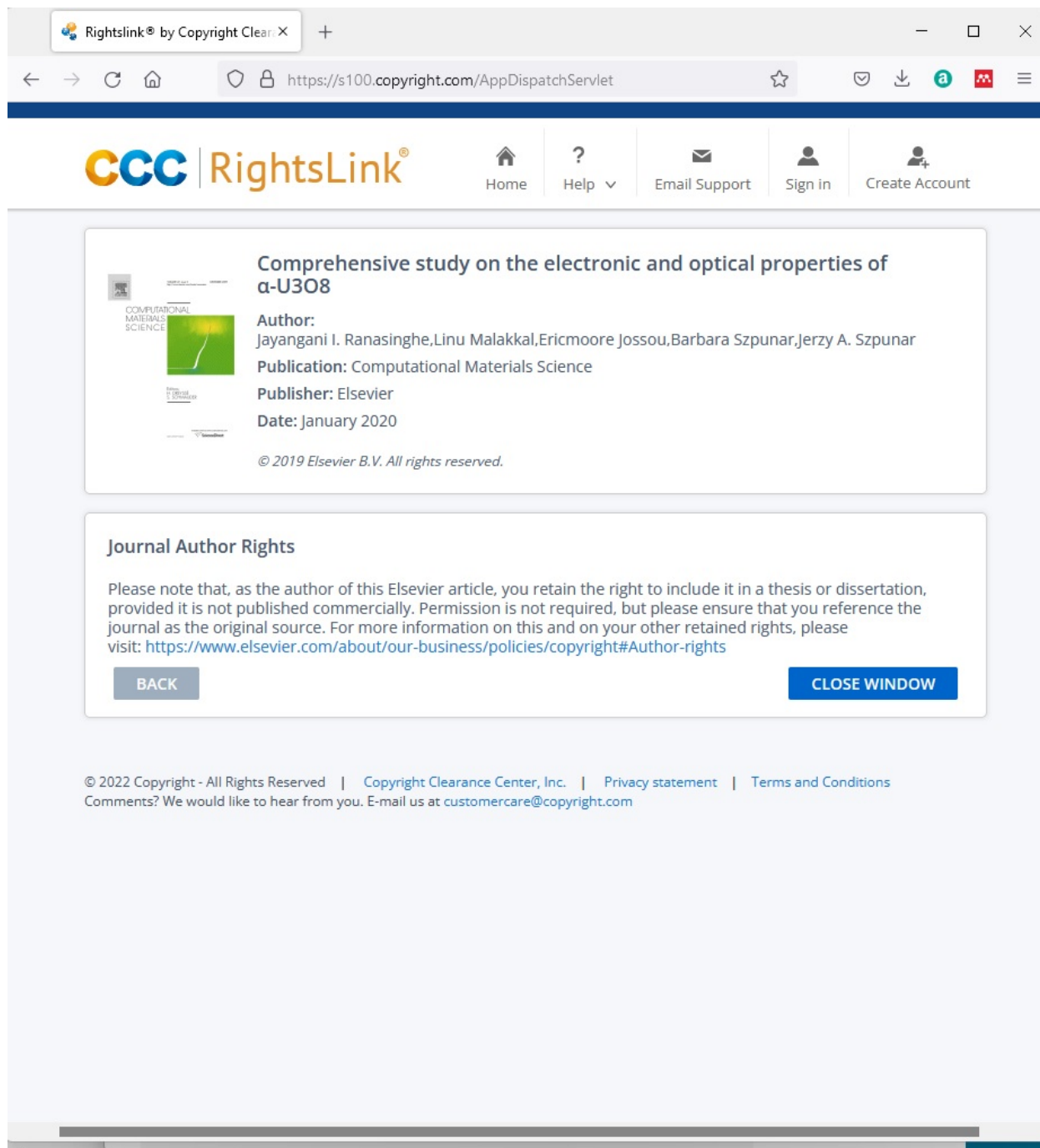
**Journal Author Rights**

Please note that, as the author of this Elsevier article, you retain the right to include it in a thesis or dissertation, provided it is not published commercially. Permission is not required, but please ensure that you reference the journal as the original source. For more information on this and on your other retained rights, please visit: <https://www.elsevier.com/about/our-business/policies/copyright#Author-rights>

Buttons: **BACK** and **CLOSE WINDOW**

© 2022 Copyright - All Rights Reserved | [Copyright Clearance Center, Inc.](#) | [Privacy statement](#) | [Terms and Conditions](#)  
Comments? We would like to hear from you. E-mail us at [customer@copyright.com](mailto:customer@copyright.com)

### A.3 Copyright permission for the manuscript presented in Chapter 5.



The screenshot shows a web browser window with the URL <https://s100.copyright.com/AppDispatchServlet>. The page header features the CCC RightsLink logo and navigation links: Home, Help, Email Support, Sign in, and Create Account. The main content area displays the following information:

**Comprehensive study on the electronic and optical properties of  $\alpha$ -U3O8**

**Author:** Jayangani I. Ranasinghe, Linu Malakkal, Ericmoore Jossou, Barbara Szpunar, Jerzy A. Szpunar

**Publication:** Computational Materials Science

**Publisher:** Elsevier

**Date:** January 2020

*© 2019 Elsevier B.V. All rights reserved.*

**Journal Author Rights**

Please note that, as the author of this Elsevier article, you retain the right to include it in a thesis or dissertation, provided it is not published commercially. Permission is not required, but please ensure that you reference the journal as the original source. For more information on this and on your other retained rights, please visit: <https://www.elsevier.com/about/our-business/policies/copyright#Author-rights>

Buttons: **BACK** and **CLOSE WINDOW**

© 2022 Copyright - All Rights Reserved | [Copyright Clearance Center, Inc.](#) | [Privacy statement](#) | [Terms and Conditions](#)  
Comments? We would like to hear from you. E-mail us at [customer-care@copyright.com](mailto:customer-care@copyright.com)